University of Plymouth

PEARL **https://pearl.plymouth.ac.uk**

04 University of Plymouth Research Theses 01 Research Theses Main Collection

2021

Lithological and climatic controls on fluvial landscape evolution of a post-orogenic dryland mountain belt

Zondervan, Jesse Ruben

http://hdl.handle.net/10026.1/17061

http://dx.doi.org/10.24382/1027
University of Plymouth

All content in PEARL is protected by copyright law. Author manuscripts are made available in accordance with publisher policies. Please cite only the published version using the details provided on the item record or document. In the absence of an open licence (e.g. Creative Commons), permissions for further reuse of content should be sought from the publisher or author.

© 2021 Jesse Zondervan

This copy of the thesis has been supplied on condition that anyone who consults it is understood to recognise that its copyright rests with its author and that no quotation from the thesis and no information derived from it may be published without the author's prior consent.

UNIVERSITY OF
PLYMOUTH

Lithological and climatic controls on fluvial landscape evolution of a post-orogenic dryland mountain belt

by

Jesse Ruben Zondervan

A thesis submitted to the University of Plymouth in
partial fulfilment for the degree of

DOCTOR OF PHILOSOPHY

School of Geography, Earth and Environmental Sciences

April 2021

COLOPHON

This thesis was typeset inspired by Robert Bringhurst's seminal book on typography "*The Elements of Typographic Style*". Robert Slimbach's Minion Pro acts as both the text and display typeface. Chapter numbers are typeset in Hermann Zapf's AMS Euler; monospaced text uses Jim Lyles's Bitstream Vera Mono ("Bera Mono"). Equations are typeset in Donald Knuth's Computer Modern Math.

Acknowledgements

The last three years and a bit have been a true rite of passage. Indeed, I could write a whole book, but here I will keep things a bit shorter by only mentioning and thanking some of the main characters of the story, who in many different ways helped bring this thesis to fruition. My head reels as I try to reconstruct my path here, and my heart aches at the loss of so many places and people who have been home for me along the way. Undoubtedly there will be many people who have meant much to me but who have not made these pages. To you I say, thank you, you are not forgotten.

As I'm writing my acknowledgements, we are still in the full throes of the global pandemic that 2020 is known for. In fact, most of this thesis was written during social isolation. Especially because of these circumstances, I would like to express my deepest appreciation to my supervisory team, and in particular my director of studies Martin Stokes, who managed to consistently offer support throughout the last three and a half years. Through many zoom calls and marked digital documents he and the rest of the team, including Sarah Boulton, Anne Mather, and Matt Telfer, offered guidance without which I would not have been able to produce the thesis you're about to read. My PhD was funded by the School of Geography, Earth and Environmental Sciences at the University of Plymouth, supplemented by numerous awards and grants from institutions listed in the author's declaration below.

I've had the pleasure of working with a diverse supervisory team, as well as many collaborators, each bringing their own expertise within the fields of geomorphology and Quaternary science. Sarah Boulton helped me with all things GIS and topographic analysis, and also proved invaluable in supporting my sedimentological descriptions and interpretations. Matt Telfer introduced me into the magical world of optically stimulated luminescence and introduced me to some top-notch Danish OSL wizards. Anne Mather has always supplied me with insightful suggestions in the field and while constructing my arguments. Martin did not only teach me all I needed to know about doing fieldwork on terraces, his constructive criticism and unparalleled ability in developing narrative has been instrumental in the success I've had so far communicating my ideas. He taught me how to translate the mess of connections that constitute my ideas and insight into a linear story, and kept me focussed when I had wondered off to another interesting idea, perspective, or approach. If your success in life largely depends on your ability to speak, your ability to write, and the quality of your

ideas, in that order, then indeed I would hate to think what this thesis would have looked like without this stellar team.

As I had alluded to already, in addition to my thesis supervisors, I'm deeply indebted to the crew at Risø in Denmark. Jan-Pieter Buylaert, Mayank Jain and Andrew Murray have given their unwavering support and patience in transforming me into a true apprentice of OSL/IRSL and its exciting future. I have felt incredibly welcomed by them as well as the numerous visiting PhD students, postdocs, and staff at the lab. Of course, the help of many early career staff and lab technicians cannot be underestimated. A special thanks to Vicki Hansen, Warren Thompson, Henrik Olesen, Reza Sohbati, Kristina Thomsen, Eike Rades, Alistair Cunningham and Nasrin Karimi.

Most of the data in this thesis relies heavily on field work, and thus could not have been done without the many collaborators and field assistants that helped me. I'm extremely grateful for the unrelenting support from Professor Alaeddine Belfoul and his PhD students. Without them I would have been unable to navigate the depth of the Moroccan High Atlas and its people as I have done. In particular, Nawfal Taleb has been a rock-solid support in the field for many weeks, and even enlisted the help of a local farmer who was keen to put in physical effort to sample rocks and gravels, and organised an impromptu off-road taxi when I had underestimated the walking distance for the day. Of course, I cannot mention field work without acknowledging Madeleine Hann. She has seen me through some of the most challenging as well as exciting times while working in the field for weeks on end. She has had to put up with my unrelentless drive as well as high standard of comfort in the field, and has thus proven herself to be one of the most tolerant and caring people on the planet.

I've seen many people come and go in the offices I've worked in, and I'd like to thank all for putting up with my constant exclamations, be that of consternation, wonder or frustration to the content on my computer screen, my pacing and roaming which helps me think, or indeed the proliferation of an out-of-control spider plant jungle. In particular I have to mention Kilian Eichenseer, who suffered my rumbling thoughts on drainage reorganisation in many jacuzzi chats, and who (amongst many other things) was always up for philosophical debates. A big thanks to Josh Jones, who was keen for squash or board games, and Wycliff Tupiti for his unstoppable thirst for marine adventures.

I'd finally like to thank everyone who supported me throughout my time at university, from my parents and family who wholeheartedly supported me from the start to Houssine Azabi and his family who provided much appreciated hospitality during fieldwork in Bou Tharar. Special thanks to my lecturers at Imperial who programmed my brain to such a degree that I don't know where to start applying it next, and Lorraine Craig for masterminding it all. In particular I need to acknowledge Sanjeev Gupta for inspiring me to follow the path of geomorphology, and John Cosgrove for teaching me all there is to know about rock engineering and structural geology, and for sending me his new book which is a treasure trove of insight that could inspire the rest of my research career. Both have been supportive of my ideas and led me to the thesis that I wrote during my PhD. I also wish to thank Alex Whittaker and Becky Bell from Imperial College, my masters supervisors, for teaching me how to collect and interpret quantitative field data and how to write a paper; staff at the Australian National University and the University of Amsterdam who taught me research skills and insights which will be useful throughout my career, in particular Brad Pillans, Janelle Stevenson, Crystal McMichael and Suzette Flantua; the faculty in Plymouth who always offered encouragement; everyone I shared interesting discussions with at various conferences around the world; my housemates at Devon Terrace, especially Ashleigh Sladen and Simon Grant who have become true friends; João Lourenço at Chaddlewood Avenue who has become my crypto partner in crime; Madeleine Vickers for generously sharing her Copenhagen flat with me; landlord and chef Mimo for his generous dinners; my sister Sarah Zondervan for suffering me throughout an extended quarantine; my grandparents Wil and Hans Zondervan, and Rein and Fokje Schuiten for supporting my London education; the University of Plymouth Yacht Club for teaching me the ropes on the water; people at the Friday bar at Risø and the JSV in Plymouth; the Improv crew under the direction of Rolando Yunquera who helped me channel my creativity and who offered me a glimpse into the true depths of the wonder that is humanity; and my friends from London who kept me connected to the world while I was hiding far away in the provinces. The final lines I would like to dedicate to my parents Paul and Nicole, who drove me to the geological society meetings in the Netherlands when I was in school, and without whom I could not have come so far.

Jesse Zondervan
Eelde
December 2020

Author's Declaration

At no time during the registration for the degree of Doctor of Philosophy has the author been registered for any other University award without prior agreement of the Doctoral College Quality Sub-Committee.

Work submitted for this research degree at the University of Plymouth has not formed part of any other degree either at the University of Plymouth or at another establishment.

This study was financed by an internal studentship from the School of Geography, Earth and Environmental Sciences. Optically Stimulated Luminescence was conducted at the Nordic Centre for Luminescence Research supported by the Technical University of Denmark (DTU) and Aarhus University.

Costs related to conference attendance, field and lab work was funded through the University of Plymouth scholarship, as well as through several grants awarded to the author:

BSRG STEVE FARRELL FUND | 250 GBP | *to attend the BSRG AGM* | 2020

BSG POSTGRADUATE CONFERENCE GRANT | 500 GBP | *to attend the EGU General Assembly in Vienna* | 2020

QRA QUATERNARY CONFERENCE FUND | 750 GBP | *to attend the AGU Fall Meeting in San Francisco* | 2019

INTERNATIONAL ASSOCIATION OF SEDIMENTOLOGISTS POSTGRADUATE GRANT | 1000 EUR | *to extend my PhD lab work to do more experimental geochronology* | 2018

BRITISH SOCIETY FOR GEOMORPHOLOGY POSTGRADUATE RESEARCH GRANT | 1000 GBP | *to extend my PhD field sampling campaigns* - "Experimental luminescence dating of Quaternary river terraces, High Atlas Mountains, Morocco" | 2018

QUATERNARY RESEARCH ASSOCIATION NEW RESEARCH WORKERS AWARD | 1000 GBP | *to extend my PhD lab work to do more experimental geochronology* | 2018

GEOLOGICAL REMOTE SENSING GROUP STUDENT AWARD | 1000 GBP | *to extend my PhD remote sensing activities by carrying out field surveys* | 2018

INTERNATIONAL ASSOCIATION OF SEDIMENTOLOGISTS STUDENT TRAVEL GRANT | 450 EUR | *to attend the 4th Meeting of the Working Group on Sediment Generation* | 2018

Presentations at conferences related to the work in this thesis:

2020 Asynchronous strath terrace formation in a collisional mountain belt.
Zondervan JR, Stokes M, Boulton SJ, Mather AE, Telfer M, Buylaert JP, Jain M, Murray AS, Belfoul A, Hann MG, Taleb N.
AGU Fall Meeting

2020 Eccentricity forcing of Saharan climate drives fluvial strath terrace formation in the High Atlas.
Zondervan JR, Stokes M, Telfer MW, Boulton SJ, Buylaert JP, Jain M, Murray AS, Belfoul A, Mather AE, Taleb N, Hann MG.
EGU General Assembly

2019 Changes in mountain valley widening, river incision and sediment transport in North-West Africa during the last 180 ka of Saharan climate.
Zondervan JR, Stokes M, Boulton SJ, Mather AE, Telfer M, Buylaert JP, Jain M, Murray AS, Belfoul A, Hann MG, Taleb N.
AGU Fall Meeting, San Francisco

2019 A North-West African river terrace record spanning 180 ka of Saharan Climate, High Atlas Mountains, Morocco.
Zondervan JR, Stokes M, Boulton SJ, Mather AE, Telfer M, Buylaert JP, Jain M, Murray AS, Belfoul A, Hann MG, Taleb N.
Earth Sciences Research Conference, University of Plymouth

2019 Quaternary river terrace-climate relationships on the NW Sahara Desert margin (Morocco).
Stokes M, *Zondervan JR*, Mather AE, Boulton SJ, Telfer MW & Belfoul A.
Congress of the International Union for Quaternary Research (INQUA), Dublin

2018 Lithological controls on drainage divide dynamics.
Zondervan JR, Stokes M, Boulton SJ, Mather AE & Telfer MW.
Earth Sciences Research Conference, University of Plymouth

2018 Chronology for mountainous river terraces: OSL/IRSL and rock dating techniques applied to carbonate-rich terraces in the Atlas Mountains.
Zondervan JR, Stokes M, Jain M, Buylaert J-P, Telfer MW & Murray AS.
UK Luminescence and ESR Dating Meeting

2018 Palaeo river long profile reconstruction in a fold-and-thrust belt: river terraces as archives of Quaternary incision and aggradation in the Atlas Mountains.
Zondervan JR, Stokes M, Boulton SJ, Mather AE & Telfer MW.
Fluvial Archives Group Meeting, Belgium

2018 Catchment changes in response to tectonics and climate: using river terraces and DEM data in the southern High Atlas Mountains (Morocco).
Zondervan JR, Stokes M, Boulton SJ, Mather AE & Telfer MW.
Meeting of the Working Group on Sediment Generation, Dublin

2017 Fluvial archives of NW African climate and tectonic evolution, Atlas Mountains, central Morocco.
Zondervan JR, Stokes M, Mather AE & Boulton SJ.
Earth Sciences Research Conference, University of Plymouth

Peer-reviewed publications related to the work in this thesis:

2020 Rock strength and structural controls on fluvial erodibility: implications for drainage divide mobility in a collisional mountain belt.
Zondervan J.R., Stokes M., Boulton S.J., Telfer M.W., Mather A.E.
Earth and Planetary Science Letters
DOI: 10.1016/j.epsl.2020.116221

Word count of main body of thesis: 41,620

Signed

....

Date

01 Apr 2021

Lithological and climatic controls on fluvial landscape evolution of a post-orogenic dryland mountain belt

Jesse Ruben Zondervan

Many mountain ranges in the world are in post-orogenic decay, a stage in which erosion is dominant over crustal thickening. The dominance of regional isostatic and mantle controls on rock uplift over localised fault uplift means climatic changes and intrinsic properties such as drainage capture and lithological variations are principal drivers of landscape evolution. In addition, dryland conditions in low to mid latitude settings with negligible glacial ice cover result in fluvial processes forming a primary agent of erosion. This thesis investigates the lithological and structural control on long-term fluvial mountain landscape evolution, using a synthesis of detailed field observations and topographic analysis of rivers draining the post-orogenic dryland High Atlas Mountains, and field and geochronological studies on strath terraces in a catchment draining into its foreland basin. In the first part of this thesis, I assess the progressive mobility of the drainage divide in three lithologically and structurally distinct groups of bedrock in the High Atlas (NW Africa). Collection of field derived measurements of rock strength using a Schmidt hammer and extraction of river channel steepness from a digital elevation model allowed me to estimate contrasts in fluvial erodibilities of rock types. I show that fluvial erodibility between the weakest and strongest lithological units in the central High Atlas varies up to two orders of magnitude. The derived range in erodibilities in horizontal stratigraphy of the sedimentary bedrock cover leads to changes in erosion rates as rivers erode through strata, leading to drainage divide migration with a timescale on the order of 10^6-10^7 years. In contrast, I show that the faulted and folded metamorphic sedimentary rocks in the centre of the mountain belt coincide with a stable drainage divide. Finally, where the strong igneous rocks of the crystalline basement are exposed after erosion of the covering meta-sediments, there is a decrease in fluvial erodibility of

up to a factor of three, where the drainage divide is mobile towards the centre of the exposed crystalline basement. These findings demonstrate drainage divide reorganisation can be induced through rock properties alone without need for tectonic or climatic drivers, which has implications for the perception of autogenic dynamism of catchments and fluvial erosion in mountain belts.

I further present geomorphological, sedimentological, and chronological datasets of strath surfaces and bedload sediments preserved in valleys and river reaches of the Mgoun River where morphology is controlled by the high contrast in rock erodibility and passive tectonic structure. To derive a record of terrace aggradation and incision along a 30 km river reach eroding a wedge-top basin and thrust front, over 200 kyr, I: (1) extract terrace surface and river channel elevations from a digital elevation model and field mapping to reconstruct river long profiles; (2) constrain the timing of bedload aggradation within the two latest strath levels using a new approach to OSL dose rate correction of gravels. I show that only one synchronous aggradation event occurred along this reach during the last interglacial maximum MIS 5e (~124 – 119 ka), linked to more frequent penetration of high magnitude storms of subtropical origin, connecting the trunk river with ephemeral tributaries, hillslopes, and alluvial fans. Strath terrace incision nucleates and propagates as a knickpoint connecting reaches of the river at a 10^5 yr timescale over ~ 20 km river length. In addition, further than 20 km upstream an independent nucleation of river incision occurred, asynchronous from the first at a 10^4 yr timescale. Weak bedrock (10 - 14 MPa) allowed the formation of strath terraces through lateral erosion, and three gorges of strong limestone (39 – 90 MPa) slowed down knickpoint propagation and thus erosional connectivity of the trunk river channel. These results demonstrate that studies which constrain river incision by dating terraces in one reach of a river may not constrain the river's entire history of incision.

I also collected sedimentological, grain size and lithology data from these terraces to derive information on sediment source and transport over the last 200 kyr. Terraces in an

unconfined valley (3.5 km wide) record abundant gravity flow deposits, whilst terraces in confined valleys (150 – 750 m wide) preserve only completely fluvially reworked deposits. In addition, trends in grain size and clast lithological provenance reflect a low ratio of longitudinal to lateral sediment input. The dominance of lateral sediment flux enhances the effect of valley width on the timescale of buffering between hillslope and river channel response to climatic changes, by varying the accommodation for alluvial and tributary fans. These findings demonstrate lithological and structural controls on valley width influence the sensitivity of river reaches to external perturbations such as climate and internal dynamics spurred on by stochastic events, thus explaining the asynchronous independent incision of terraces along the river channel at a 10^4 yr timescale.

Overall, the findings presented in this thesis demonstrate that lithological and structural properties of mountain belts affect the controls of internal dynamics and climatic changes on geomorphic response, at spatial scales which translate into landscape evolution over 10^4 – 10^7 yr timescales.

In dieser großen Kette von Ursachen und Wirkungen kann keine Tatsache isoliert untersucht werden

(In this great chain of causes and effects no single fact can be considered in isolation)

--- *Friedrich Wilhelm Heinrich Alexander von Humboldt*

CONTENTS

LIST OF FIGURES

CHAPTER 1

CHAPTER 2

CHAPTER 3

CHAPTER 4

CHAPTER 5

LIST OF TABLES

CHAPTER 2

CHAPTER 3

CHAPTER 4

LIST OF EQUATIONS

1

Introduction

1.1 OVERVIEW

This thesis investigates the lithological and structural controls on post-orogenic fluvial dryland mountain landscape evolution over 10^4 – 10^7 yr timescales. Chapter 2 explores this at the scale of drainage organisation of a 10^6 – 10^7 yr order at the mountain belt scale. Chapters 3 and 4 investigate a catchment's responses to orbital changes in climate – a temporal scale of 10^4 – 10^5 yr. To this end, I use a synthesis of topographic analyses of digital elevation models (DEMs) and field measurements of rock strength throughout the dryland post-orogenic High Atlas Mountains. These data are then integrated with field and geochronological data on strath terrace stratigraphy and sedimentology in a catchment draining into the Ouarzazate foreland basin. The main body of the research takes the form of three chapters, with distinct objectives. In this introduction I firstly present the broad rationale for research on lithological and structural controls on landscape evolution, and secondly discuss the particular research needs that motivated this work. I finish with a detailed outline of the thesis structure.

1.2 RATIONALE

Mountain belts form the erosional source of the Earth's surface, coupling surface erosion with tectonic and climatic forces. In addition, rock type (lithology) and the structural control on the strength and configuration of bedrock geology affect the processes of hillslope and river erosion in mountain belts. Many studies have shown the importance of rock types on the morphology of modern rivers and hillslopes at a reach-specific scale (Wohl and Merritt, 2001; Hurst et al., 2013; Chittenden et al., 2014), and lithological and structural variability in bedrock is expected to play a key role in post-orogenic mountain belt settings (Gallen, 2018; Bernard et al., 2019). However, very few have attempted to characterise the influence of lithology on 10^4 – 10^7 yr evolution of entire mountain belts or catchments, and the extent to which lithological and structural variability affect landscape evolution on the timescale of climatic and tectonic changes is still relatively unexplored.

Decoding sedimentary records of mountain erosion proves particularly challenging, as routing of sediment from the mountain front to depositional basins may modify or completely shred the original erosion signal (Castelltort and Van Den Driessche, 2003; Jerolmack and Paola, 2010; Simpson and Castelltort, 2012; Armitage et al., 2013; Romans et al., 2016). Instead of deriving erosional histories from downstream stratigraphy, direct information on the interrelationships between erosion, climate and tectonic histories comes from the study of fluvial archives within mountain belts, which include both erosional topography and fluvial depositional sequences. In particular, information on uplift and climatic changes is embedded in incisional landforms such as river long profiles (Stock and Montgomery, 1999; Whipple and Tucker, 1999; Crosby and Whipple, 2006; Kirby and Whipple, 2012; Whittaker, 2012; Whittaker and Boulton, 2012; Boulton et al., 2014), river channel geometry (Whittaker et al., 2007a; Attal et al., 2008), strath treads (Seidl and Dietrich, 1992; Howard et al., 1994; Zaprowski et al., 2001; Jansen et al., 2011; Finnegan, 2013), terraces (Bridgland and Westaway, 2008; Rixhon et al., 2011; Bridgland and Westaway, 2014; Demoulin et al., 2017; Stokes et al., 2017), and fluvial deposits such as in modern river channels (Attal and Lavé, 2006; Attal et al., 2015; Dingle et al., 2016; Quick et al., 2019). Thus, understanding the extent of lithological controls in the context of long-term landscape evolution requires integration of fluvial archives with lithological and structural characterisation of river valley bedrock. The results of such an inquiry would have implications for interpreting the fluvial archives of mountain erosion for climatic and tectonic signals, and for understanding processes of landscape evolution.

The growing recognition of the importance of lithological and structural control on mountain landscape evolution has led to numerous field and modelling studies on fluvial archives. Before all else, the landscape of a mountain belt is controlled by the organisation of the drainage system. Field and modelling studies show the potential of lithological variability to cause changes in the organisation of the drainage network (Bonnet, 2009; Giachetta et al., 2014; Gallen, 2018; Bernard et al., 2019; Strong et al., 2019), which subsequently causes changes in lower order fluvial archives such as river long profiles, hillslopes, and water and sediment discharge (Bonnet, 2009; Giachetta et al., 2014). The next spatial and temporal scale down from drainage divides is that of catchments. Within those, numerous fluvial archives exist and those have been the subject of studies investigating lithological controls. Field studies have shown lithological effects on river channel steepness (Brocard and van der Beek, 2006; Gallen, 2018; Bernard et al., 2019), river long profile evolution in response to tectonic perturbations (Cook et al., 2009; DiBiase et al., 2018; Zondervan et al., 2020), river gravel bedload grain size (Attal and Lavé, 2006; Dingle et al., 2016; Quick et al., 2019), the coupling of hillslopes and river channels through tributary fans (Stokes and Mather, 2015; Mather and Stokes, 2018), strath terrace formation and preservation (Montgomery, 2004; Schanz and Montgomery, 2016; Keen-Zebert et al., 2017; Stokes et al., 2017). These studies demonstrate that fluvial archives that can be used for reconstructing tectonic and climatic histories, often reflect a lithological effect on the temporal evolution of the landscape. Isolated, some of these archives and lithological effects are relatively simple and thus an easy target for numerical modelling to understand underlying processes such as for river long profiles (Forte et al., 2016; Perne et al., 2017) and drainage reorganisation (Scherler and Schwanghart, 2020). However, many questions remain: for example, how do bedrock strength and structural weaknesses affect the fluvial erodibility of river channels? How common is lithologically induced drainage mobility within mountain belts? Do lithological controls affect the timing of strath terrace formation in response to climatic changes? How do lithological and structural controls affect valley morphology, and how does that affect sediment recycling and delivery to river channels?

Developing the tools to decode fluvial archives of mountain landscape change is one of the most exciting challenges in the field of Earth Sciences. However, it is clear that if we are to come closer to reaching this aim, we need a detailed understanding of the controls of lithological and structural variability on landscape evolution, and the effects on fluvial archives.

In this thesis I focus on a post-orogenic, dryland mountain belt where the controls of lithological variability and climatic changes on fluvial processes of landscape evolution can be more clearly isolated from the influence of tectonic advection and ice sheets on topography. Many mountain ranges in the world are in post-orogenic decay, a stage in which erosion is dominant over crustal thickening, such as the Appalachians, Canadian and Southern Rockies, Lachlan fold belt of south-eastern Australia, Ural Mountains, several Palaeozoic ranges in central Asia, the Pyrenees, the European Alps and the Atlas Mountains (Baldwin et al., 2003; Tucker and van der Beek, 2013). Unlike in more active mountain belts, the dominance of regional isostatic and mantle controls on rock uplift over localised fault uplift in such post-orogenic belts means intrinsic properties such as drainage capture and lithological variations together with climatic changes are principal drivers of landscape evolution (Valla et al., 2012; Flowers and Ehlers, 2018). Furthermore, in contrast to mid to high latitude northern hemisphere mountain belts that evolved under glacial, periglacial and humid climatic conditions in proximity and connectivity to ice sheets (Bridgland and Westaway, 2008, 2014), lower latitude settings evolved in environments with minimal direct ice sheet influence under more arid continental conditions (Stokes et al., 2017).

1.3 RESEARCH NEEDS

To understand the lithological controls on fluvial landscape evolution, firstly I consider the challenges in defining and quantifying the relationship between lithology, rock strength and bedrock erodibility, and the controls of structural geology on the distribution, stratigraphic orientation, and magnitude of erodibility differences in natural landscapes. Once the definition and relationship between lithology and fluvial erosion has been established, processes of landscape evolution and their dependence on lithology and structure are addressed. At the largest scale drainage divide organisation is a process that controls landscape evolution, which may cascade down to affect smaller scale processes. Here I consider the lithological and structural controls on bedrock erodibility and drainage divide migration at a mountain belt scale. At the next spatial and temporal scale down from drainage organisation, I consider lithological and structural controls on catchment response to climatic changes. Strath terraces are archives which connect multiple processes of fluvial landscape evolution at the catchment scale, and enable integration with chronology on the timescale of orbitally induced climatic changes. To answer how lithological and structural controls affect catchment response to climatic changes, I address the concept of strath terrace formation and finally consider the challenges and opportunities in dating such landforms.

1.3.1 *Bedrock erodibility and structural geology*

Lithology is a rock unit description of physical characteristics including colour, texture, grain size and composition. The concept of lithology is one that is used widely within geology and geomorphology as it is the basis of subdividing rock sequences which can be correlated for the purposes of mapping on landscape scales. At a first order, the strength of rock defined as the ability of rock to resist deformation by compressive, tensile or shear stresses is affected by the cohesion of the rock (Selby, 1993). The cohesion of rock is intrinsically related to the lithology of rock, as it affects the chemical and electrostatic bonds inside and between crystals of crystalline rocks and between grains in weak rocks with rigid cementing materials (Selby, 1993). In addition, capillary stresses and interlocking particles contribute to apparent cohesion which depends on grain size distribution and roughness. As such, the cohesion of rock as a product of its lithology affects the ability of geomorphic action to result in erosion of intact rock, as well as affecting the rock's natural fracture patterns. As the resistance of rock to failure in geomorphic settings is often dominantly controlled by the resistance along natural partings, this second effect may even be more crucial to understand (Selby, 1993). Lithological boundaries inherent in rocks, as well as partings

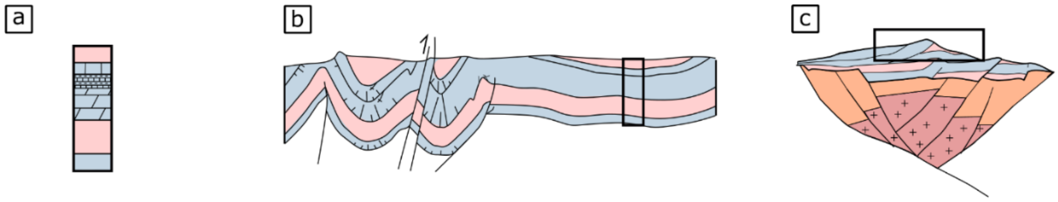

Cohesive limestone and non-cohesive marls

Primary structures (e.g. bedding thickness) affect structural strength

Dipping contacts

Tectonic structural weakening

Horizontal contacts

Minimal tectonic structural weakening

Relatively intact sedimentary cover vs heavily deformed metamorphic rocks & lithologically strong basement

Figure 1.1– Lithological and structural control on fluvial erodibility and landscape morphology from the unit scale to mountain scale. (a) At the unit and stratigraphic scale, lithology and primary structures are the primary control on the erodibility of bedrock. Lithology determines the cohesion of material: e.g., marls have overall weaker cohesion than limestones. Primary structures, such as bedding thickness, contribute to weaknesses in the rock that are exploited in plucking and cavitation, or in rock sliding and toppling. (b) The tectonic structure of stratigraphy determines the order and orientation of lithologies of variable erodibilities, and thus the erodibility of rock in space and time. On top, folding and faulting and corresponding stress and strain leads to brittle weakening of rocks through joints and fracture formation. Thus, tectonic structural control can weaken strong rocks and decrease the contrast in erodibility between units. (c) At a mountain belt scale, older metamorphosed units in the core of the mountain belt have gone through more deformation which tends to decrease contrasts in erodibility, and result in different orientation of such variations, compared to younger sedimentary cover units. Basement geology usually contains lithologically stronger crystalline rocks.

formed during sedimentation such as bedding can be considered primary fabrics (Fig. 1.1a), on top of which secondary fabrics such as joints and faults may be introduced into the rock mass after its formation (Fig. 1.1b). Here, the lithology of rock affects the possible fracture patterns introduced within it through properties including cohesion as well as others which affect the stress distribution within it, such as the compressibility of rock (Poisson's ratio), its rheology (Young's modulus) and coefficient of thermal expansion (Cosgrove and Hudson, 2016).

In the context of landscape formation, many attempts at characterising rock strength have been made. In particular, approaches of geomorphologists often include measuring the compressive or tensile strength of *in situ* or sampled rock. These range from Schmidt hammer rebound measurements (Goudie, 2006), the Equotip (Aoki and Matsukura, 2007; Viles et al., 2011), the slake-durability test (Franklin and Chandra, 1972; Anton et al., 2015) and the Brazilian splitting test (Vutukuri et al., 1974) among others (Goudie, 2016). In addition, the effect of structural discontinuities such as joints and other fractures are integrated in assessments such as the Selby Rock Mass strength index (Selby, 1980). Despite the many methods of testing and measuring mechanical rock mass strength, understanding, and characterising the impact of rock strength on the ease of river erosion and other geomorphic processes remains a major challenge.

Lithology and its influence on rock mass strength influence landscape evolution at a first order by affecting the ability of rivers to erode into bedrock, determined by fluvial erodibility. River erosion through bedrock over timescales of 10^4 – 10^7 years is commonly modelled using the stream power model. In its simplest form, the erosion rate at any particular point in a bedrock river channel is defined by:

$$E = KA^m S^n \qquad \text{Eq. 1}$$

where K is an erodibility constant which depends on the rock-type over which the river channel flows as well as the climatic setting, A is upstream drainage area and S is local channel gradient, and m and n are constants that depend on basin hydrology, channel geometry, and erosion processes (Whipple and Tucker, 1999). A major challenge is deriving the constant K, as field sites with sufficient constraints on boundary conditions are not common. A classic lab experiment by Sklar and Dietrich (2001) showed that the ease with which water flow erodes rock, the erodibility, K, is related to the inverse square of tensile rock strength ($\sigma_\tau{}^{-2}$). A major drawback of this simple abrasion mill experiment is that it does not account for structural discontinuities in the rock mass, nor for the dynamics of bedload and suspended sediment (Lamb et al., 2008; Lamb et al., 2015), or channel geometry (Whittaker et al., 2007a; Attal et al., 2008; Lamb et al., 2015). Deriving measures of fluvial erodibility from field studies requires constraints on the geological timing of river evolution, which has been done with some success (Stock and Montgomery, 1999; Whipple et al., 2000; Kirby and Whipple, 2001; Attal et al., 2008; Pechlivanidou et al., 2019; Zondervan et al., 2020). However, such well-constrained sites are not common and estimating a full range of erodibility variation within a lithologically diverse mountain belt remains a challenge.

In addition to the lithological control on fluvial erodibility, structure is a major, though often underplayed control. Not only does geological structure affect erodibility of rock and its spatial and temporal distribution within a landscape, it also affects which physical processes of erosion occur as well as landscape-scale emergent patterns. First of all, at a lithological unit scale (Fig. 1.1a), primary structures such as bedding thickness, together with secondary microstructures such as joints and fractures, affect the ease with which rivers erode through bedrock through plucking and cavitation (Miller, 1991). In particular, knickpoint retreat in the passive margin of Australia were found to be dependent on rock structure primarily (Weissel and Seidl, 1997). Through field observations of passive margin escarpment retreat, Weissel and Seidl (1997) found that the orientation of joints to the hillslope of the Apsley River Gorge results in rock toppling on one side of the river channel, and rock sliding on the other. With the peak stream discharge transporting the dropped blocks in the river channel, these hillslope processes are the rate-controlling processes of knickpoint propagation in this setting. Structural weaknesses can be caused by the tectonic structure of bedrock geology, which in addition controls the orientation and distribution of lithologies and their boundaries within a landscape (Fig. 1.1b). Folding and thrusting through tectonic activity and unroofing weakens rocks through joints and fractures formed in response to associated stress and strain, thus decreasing the magnitude of variation in erodibility between units (Molnar et al., 2007). Furthermore, the orientation of units with variable strength has been recognised as a controlling factor on landscape evolution through time (Forte et al., 2016; Perne et al., 2017; Gallen, 2018; Ward, 2019). In particular, using numerical simulations Forte et al. (2016) and Perne et al. (2017) showed that horizontal and shallowly dipping beds of variable strength produce an ongoing transient change in river channel slopes and the river long profile, whilst steeper dipping strata in a landscape tends towards equilibrium conditions. In addition, at a mountain belt scale (Fig. 1.1c), the strength of units is affected by metamorphism of lithologies, ductile and brittle deformation which tend to decrease the magnitude of variation in erodibilities between units. Instead, sedimentary cover units are more likely to preserve large differences in erodibility and to have horizontal stratigraphy preserved. Studies of the Atlas Mountains, the Eastern Cordillera of Colombia and the Pyrenees demonstrate river drainage networks change from longitudinal networks following the structure of folded and faulted sedimentary cover to transverse drainage as the more homogeneous metamorphic or igneous basement is exposed (Babault et al., 2012; Babault et al., 2013; Struth et al., 2015). At a catchment scale, field observations have shown that structural configuration controls valley morphology (Stokes and Mather, 2015; Stokes et al., 2017; Ward, 2019) and consequently affects the coupling of hillslopes to river channels through tributaries (Stokes and Mather, 2015; Mather and Stokes, 2018), and the formation and preservation of river terraces (Stokes et al., 2017). These studies demonstrate that rock erodibility and the orientation of bedrock geology directly affect fluvial processes of bedrock erosion, as well as indirectly through the coupling with hillslope and alluvial processes. However, they also demonstrate the challenge of incorporating structural controls on fluvial erodibility and estimating a magnitude of erodibility variation within natural landscapes. In addition, understanding the effect of lithological and structural controls on the coupling between hillslopes and river channels, and thus their sensitivity to external forcing such as climate, is a key emerging challenge.

1.3.2 *Lithological and structural controls on drainage divide mobility*

The central drainage divide of a mountain belt is the topographic boundary between river catchments draining either flank. Any movement of the drainage divide can result in the rearrangement of catchments, rejuvenation of topography, and changes in erosion rates and sediment flux (Bonnet, 2009; Giachetta et al., 2014). Bedrock erodibility is expected to play a significant role in drainage divide reorganisation since heterogeneous exhumation of weak and strong substrates can enhance and suppress erosion respectively (Giachetta et al., 2014; Gallen, 2018) and cause topographic rejuvenation, for example through the exhumation of a basement palaeosurface (Strong et al., 2019). This is especially the case in post-orogenic settings where erosion is dominant over crustal thickening (Gallen, 2018; Bernard et al., 2019). However, the magnitude of erodibility variation within a mountain belt, and the mobility of the drainage divide as rivers erode through its stratigraphy are still relatively unexplored.

Collisional orogens are characterised by bedrock rivers eroding through variable rock strength and tectonic architectures, such as very strong crystalline basement, deformed strong meta-sediments, and sedimentary cover composed of weak as well as stronger strata. Recent numerical modelling studies show the complexity of incision into horizontal or gently dipping strata of varying erodibility (Forte et al., 2016; Perne et al., 2017), and also suggest steady-state denudation is more likely to develop in tilted and /or faulted strata that have been highly deformed (Forte et al., 2016). The results of these models imply drainage mobility might be prevalent during incision in sedimentary cover but not in more deformed components of a collisional mountain belt. In a field study, Gallen (2018) modelled the erosion of a hard horizontal rock layer in the Appalachians. This model predicts that a geologically instantaneous capture of the Upper Tennessee River catchment by the Lower Tennessee River occurred at 9 Ma, which has led to a shift in the drainage divide and explains observed subsequent topographic rejuvenation in the landscape visible today. In the Pyrenees, Bernard et al. (2019) show the drainage divide follows the position of high-strength, high-elevation plutons in the crystalline basement in the centre of the belt, suggesting a direct lithological control on the position of the central drainage divide. These field studies demonstrate the drainage divide can be mobile in near-horizontal sedimentary stratigraphy of mountain belts and is likely to move to the centre of highly resistant plutons as they get exhumed in the axis of a collisional mountain belt. However, both studies also demonstrate the challenge of documenting drainage mobility, which is often only recognisable in instantaneous capture events which leave pervasive topographic evidence. In addition, whilst numerical simulation studies are instrumental in predicting long-term processes in geomorphology which are hard to derive from observations of modern-day landscapes alone, these involve simplifications and it is challenging to model the full complexity of lithologies and structural geology of a collisional mountain belt. Furthermore, the fluvial erodibility of rock, which depends on rock mass strength as well as jointing and weathering, is challenging to measure quantitatively (Bursztyn et al., 2015) and consequently the range of erodibility inputs in modelling studies vary widely (Roy et al., 2015; Forte et al., 2016; Yanites et al., 2017).

Consequently, while theory and numerical models predict a role for bedrock erodibility in driving drainage divide mobility, where and when this is expected to occur in the evolution of mountain belts needs to be understood from a range of settings with varying rock strength conditions. The challenges of measuring and characterising bedrock erodibility (Bursztyn et al., 2015) and drainage divide dynamics in field settings (Willett et al., 2014; Forte and Whipple, 2018) remain key problems. Addressing this challenge requires a dataset on rock erodibility that is combined with topographic measures of drainage divide mobility in a mountain belt where erosion is dominant over tectonic advection, and where rivers erode through a lithologically variable landscape.

1.3.3 Climatic, lithological, and structural controls on the formation of strath terraces

At the next spatial and temporal scale down from drainage divide organisation, the responses to climatic changes of the river channel network and its connection to hillslopes in catchment systems control fluvial erosion. In turn, such responses within catchments have the potential to affect the mobility and organisation of catchment divides through changes in erosion rates. To understand the relationship between climatic changes and responses of the catchment system which affect fluvial bedrock incision and aggradation, lithological and structural controls on fluvial erosion need to be understood on the spatial scale of a catchment system and temporal scale of orbitally induced climatic changes.

At a catchment scale, strath terraces have the potential to integrate multiple fluvial archives: river long profile reconstruction through the correlation of strath surfaces (Seidl and Dietrich, 1992; Howard et al., 1994; Zaprowski et al., 2001; Jansen et al., 2011; Finnegan, 2013); fluvial depositional setting through facies of overlying terrace sediments (Bryant, 1983; Bridgland, 2000; Lin et al., 2005; Cordier et al., 2006; Lewin and Gibbard, 2010); grain size (Paola and Mohrig, 1996) and provenance from those same deposits (Lindsey et al., 2007; Marsaglia et al., 2010); and the terrace geomorphological stratigraphy which records changes in river vertical incision, horizontal erosion and aggradation (Maddy, 1997; Hancock and Anderson, 2002; Bridgland and Westaway, 2008; Burbank and Anderson, 2011). In addition, strath terraces provide a record of fluvial evolution through time in response to climatic changes, especially when supplied with chronological control.

Strath terraces form in response to changes in sediment to discharge ratios, changing rates of lateral and vertical erosion rates by varying the amount of sediment cover on the riverbed (Hancock and Anderson, 2002; Starkel, 2003; Finnegan et al., 2007; Johnson and Whipple, 2010). Changes in climate induce transient responses of sediment delivery to river channels and thus trigger the formation of strath terraces (Bull, 1990, 1991; Hancock and Anderson, 2002). In particular, terraces record erosion rates dependent on orbitally forced climate fluctuations, which have also been argued to control rates of crustal uplift in epeirogenic regions (Bridgland and Westaway, 2008, 2014). A key question for understanding terrace formation in this context is: when during the cycle of interglacial to glacial cycles do rivers aggrade to build terraces, and when do they incise to abandon these terraces? Terrace formation in many high latitude European studies find a major eccentricity signal (Bridgland and Westaway, 2008), but what about lower latitude regions where there are no ice sheets with a significant influence on sediment generation?

The timing of sediment aggradation and incision in response to glacial-interglacial changes varies globally (Bridgland and Westaway, 2008; Schanz et al., 2018), and formation and preservation of terraces is noticeably controlled by bedrock lithology (Montgomery, 2004; Wegmann and Pazzaglia, 2009; Schanz and Montgomery, 2016; Keen-Zebert et al., 2017; Stokes et al., 2017). For example, strath terraces form only in bedrock that is weak enough to allow lateral erosion (Johnson and Finnegan, 2015; Schanz and Montgomery, 2016; Stokes et al., 2017), the presence and orientation of which is controlled by structural geology in collisional mountain belts (Stokes et al., 2017). Furthermore, local conditions can strongly control the sensitivity of a river to orbital fluctuations, as Foster et al. (2017) demonstrated using cosmogenic profiles that strath terraces along Lefthand Creek in Colorado represent occupation during multiple 100 kyr cycles of glacial interglacial climate. In addition, their results indicated terraces from neighbouring catchments draining into the Denver basin formed asynchronously.

To understand the asynchronous nature of strath terrace formation demonstrated by these studies, both the timing of terrace aggradation and terrace incision need to be considered. First of all, when a decrease in sediment flux exposes the river bedrock to erosion, incision of the river abandons its previous vertical position (Hancock and Anderson, 2002). In an insightful experiment, Baynes et al. (2018) found that strath terraces may form by downstream stripping of bedload sediment, and a local start of incision which propagates upstream as a knickpoint. Cosmogenic studies of strath terraces have demonstrated progressive abandonment in the form of knickpoint migration (Brocard et al., 2003; Ward et al., 2005; Jansen et al., 2011). Whilst the timescale for knickpoint migration to equilibrate over the length of the river can be up to ~10^6 to 10^7 years (Whittaker et al., 2007b;

Zondervan et al., 2020) which is very dependent on bedrock strength (Zondervan et al., 2020), it is likely that local stripping of bedload sediment leads to multiple nucleation points of incision along the length of the river on such long timescales. Thus, whilst incision in the form of kinetic waves is expected to play a role in asynchronous terrace development within landscapes, ultimately the timing of bedload stripping is a key control that needs to be considered. On what timescale do rivers in a mountain belt strip their channels of bedload and can this be assumed to be synchronous on the timescale of its response to orbital changes in climate?

To understand the timing and process of bedload sediment stripping of the river channel leading to incision, an integrated view of catchment architecture needs to be considered. In addition to the direct control on terrace occurrence, lithological and structural controls on valley morphology affect the sediment routing system. For example, in a field study in the Dades River of the High Atlas, Stokes and Mather (2015) show that the position of tributary fans in the valley are controlled by lithological and structural variables and that these determine the degree of coupling with the active river channel. In addition, Mather and Stokes (2018) show that the connectivity of hillslope sediment generation to the river channel is affected by the structural configuration of bedrock within tributaries. Furthermore, other larger sources of sediment, such as alluvial fans, have longer temporal scales of interaction with the river channel and the presence of these is expected only in wider valleys (Mather et al., 2017). These studies demonstrate that the amount of sediment that a river channel receives is expected to vary as a function of its structural and lithological controls, and thus that these affect the temporal sensitivity of the river bedload to climatic perturbations. To assess the extent of the control of such local conditions in comparison to headwater-derived sediment fluxes, it is worth noting that Dingle et al. (2016) and Quick et al. (2019) found that local sources of conglomerate recycling in wedge-top basins and the thrust front of the Himalayas upstream of the Ganga Plain override signals of headwater sediment output. Thus, following the conclusion that sediment input can be highly dependent on local lithological and structural controls in mountain belts, it is likely that strath terrace formation is asynchronous along rivers draining collisional mountain belts. This thesis will explore the spatial and temporal extent to which strath terraces form asynchronously.

The approach taken here is to integrate fluvial archives of sediment deposition and bedrock incision with the terrace record, and provide chronology of both sediment deposition and incision to evaluate the synchronicity of mountain erosional response to orbital changes in climate. Consequently, results from this study will reflect the lithological and structural controls on fluvial archives of landscape change on the scale of climatic response. This has implications for interpreting archives of long-term climatic forcing of landscape change and downstream stratigraphy.

1.3.4 Geochronological tools for integrating fluvial archives

To evaluate the timescales at which lithological and structural controls can cause asynchronous terrace formation, chronological control on strath terrace occupation by dating its sedimentary cover is needed. In particular, the ~50 ka limit of radiocarbon dating is too short to date landscape evolution on orbital timescales and may be especially challenging due to the poor preservation potential of organic material in dryland settings. Optically stimulated luminescence (OSL) dating has advantages over other Quaternary dating techniques because 1) it uses quartz and feldspar grains, which are commonly found in sedimentary environments across the Earth's surface, 2) it has a dating range of tens to several hundred thousand years (Wintle and Murray, 2006; Rixhon et al., 2017), and 3) it provides a direct estimate of the timing of sediment deposition, rather than a minimum age as provided by cosmogenic surface exposure dating (e.g. Gosse and Phillips, 2001; Arboleya et al., 2008; Schanz et al., 2018). Strath terrace formation integrates periods of strath planation, gravel deposition and incision and abandonment (Schanz et al., 2018). As the river incises into the terrace and starts to abandon the strath surface, overbank sands topping over this surface (e.g. Stokes et al., 2017) allow conventional OSL approaches to dating sand lenses, and dates the onset of incision. However, to date the full occupation of the terrace and integrate the archives of bedload gravels OSL dating needs to be applied to silt- and sand-sized grains of feldspar and quartz in the gravel matrix. The matrix between the coarser clasts often contains sufficient sand-sized quartz or feldspar grains suitable for OSL dating, but estimating dose rate for deposits with a wide range of grain sizes and lithologies remains a key challenge in the application of OSL to fluvial settings. In a study of alluvial fan deposits offset by a fault in Iran, Rizza et al. (2011) approach the problem by collecting matrix material and surrounding representative bulk samples in a portable darkroom. They found the 180-250 μm sand fraction produced the lowest overdispersion, suggesting a majority of well-bleached grains, and their calculated fault slip rates are consistent with GPS data. In a similar but more detailed study of gravel matrix dating in alluvial fans in Idaho, Kenworthy et al. (2014) examined the contributions of different grain-size fractions to calculated dose-rates. Their results indicate higher contribution to dose rates from the <2 mm fraction, and using bulk dose rates where available, they derived ages that preserve stratigraphic and geomorphic order, and show some agreement to independent ages from tephra correlation and U-series dating of pedogenic carbonate. These studies demonstrate that OSL dating can be applied to coarse-grained deposits with some success. However, both studies also highlight the challenges of collecting and analysing sufficient material for dose rate measurement in material with a wide range of grain sizes and lithologies. Neither consider the differential attenuation of beta and gamma dose rates (Aitken, 1985). One of the key objectives of this thesis is to develop the necessary OSL methods to date and integrate the fluvial archives locked in strath terraces.

1.4 THE HIGH ATLAS STUDY AREA

1.4.1 Introduction to the High Atlas

This thesis focuses on the High Atlas post-orogenic dryland mountain belt, as the negligible to minor influence of local fault-related uplift or ice sheets enable isolation of lithological controls on fluvial landscape evolution. The Moroccan High Atlas is a SW-NE oriented collisional mountain belt formed by the inversion of a Mesozoic intracontinental rift system by regional thrust faulting and folding (e.g., Gomez, 2000) and thermal-related isostatic uplift (e.g. Missenard et al., 2006). Thus, the belt is made up of crystalline basement, older Palaeozoic cover sequences which have undergone metamorphic and multiple structural transformations, and rift basin infill sedimentary rocks which have subsequently been uplifted. The High Atlas is in a post-orogenic state, with long-term isostatic rock uplift rates of 0.17-0.22 mm yr^{-1} since 15 Ma related to lithospheric thinning (Babault et al., 2008). The lack of recent tectonic deformation is apparent in the undeformed continuous Quaternary river terraces along the Dades River forming parallel river long profiles throughout the fold-thrust belt and thrust front (Stokes et al., 2017). Rivers eroding the central High Atlas drain south into the Ouarzazate foredeep basin and north into the Haouz basin. From there rivers eventually run into the

Atlantic Ocean 800-1000 km from the mountain front. Chapter 2 will explore the geological control on lithological and structural variability of the central High Atlas in relation to its drainage divide, and will establish the first order controls on drainage network evolution. Chapter 3 will explore the geology of the Mgoun catchment draining the southern flank of the High Atlas, and its control on valley morphology.

1.4.2 *Quaternary climate of NW Africa and the Mgoun River catchment*

The High Atlas in northwest Africa forms an orogenic boundary between three major climatic regimes. Moisture influx comes from Atlantic westerlies in the northwest, Mediterranean cyclones in the northeast and from tropical influxes south of the Sahara in the south (Fig. 1.2). Chapters 3 and 4 will investigate how orbital climatic changes affect incision and aggradation in a catchment draining the High Atlas. In these chapters I focus on the flank draining southward into the Ouarzazate basin, in the drainage basin of the River Mgoun near the town of M'Gouna (Fig. 1.2). The Mgoun River runs through the most variable lithologies and passive tectonic structures of the High Atlas, and thus forms an ideal study setting to examine the roles of lithology and structure on the river response to climatic changes within one catchment. In catchments draining into the Ouarzazate basin, winter- spring storm tracks from the Mediterranean dominate the steady but diminishing perennial discharge along trunk rivers (Schulz et al., 2008). Whilst this winter-spring precipitation generates frequent storms through the catchments that contribute to some flow in the river, rare precipitation events linked to incursions of tropical moisture (Fig. 1.2a; Fink and Knippertz, 2003; Knippertz, 2003; Knippertz et al., 2003b) are of more significant geomorphic impact. These events activate entire catchments, generating flow in the ephemeral tributaries (Fink and Knippertz, 2003; Schulz et al. 2008;

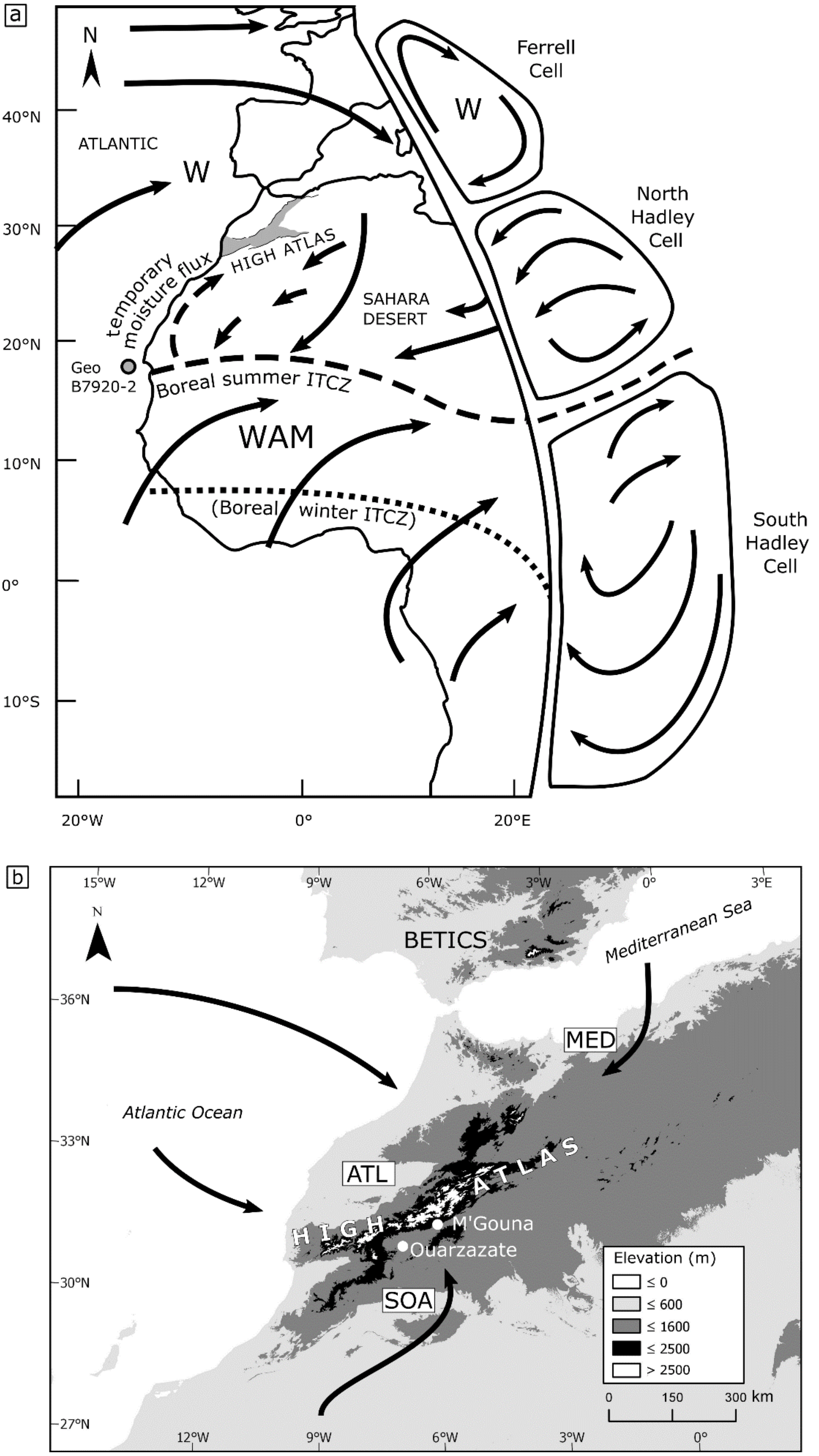
a
N
40°N
30°N
20°N
10°N
0°
10°S
20°W
0°
20°E
ATLANTIC
W
temporary moisture flux
HIGH ATLAS
SAHARA DESERT
Geo B7920-2
Boreal summer ITCZ
WAM
(Boreal winter ITCZ)
Ferrell Cell
W
North Hadley Cell
South Hadley Cell
b
15°W
12°W
9°W
6°W
3°W
0°
3°E
N
BETICS
Mediterranean Sea
36°N
33°N
30°N
27°N
MED
Atlantic Ocean
ATL
HIGH ATLAS
M'Gouna
Ouarzazate
SOA
Elevation (m)
≤ 0
≤ 600
≤ 1600
≤ 2500
> 2500
0
150
300 km
12°W
9°W
6°W
3°W
0°

Figure 1.2 - Climatic setting of the High Atlas. (a) Overview map of northwest Africa showing the prevailing wind directions and the position of the ITCZ during boreal summer and winter. Meteorological features are after Rossignol-Strick (1985); Nicholson (1996); Reichart (1997). The map includes the borehole location from which the humidity index for NW Africa in Fig. 1.3b derives (Tjallingii et al., 2008). Extent of the High Atlas is from Stokes et al. (2017). WAM: West African Monsoon; ITCZ: inter-tropical convergence zone. (b) overview of the High Atlas and main climatic zones based on precipitation correlations of weather stations by Knippertz et al. (2003a). ATL: Atlantic dominated climate; MED: Mediterranean dominated climate; SOA: South-of-Atlas dominated climate.

Dłużewski et al., 2013). These infrequent rare (>10 year) regional events drive the resetting of tributary-junction fans, providing connectivity between hillslopes and the trunk stream of the Dades River (Stokes and Mather, 2015). On orbital timescales, shifts in the Earth precession and the position of the ITCZ (Fig. 1.2a) affect the humidity of the Sahara (Fig. 1.3a-c; Tjallingii et al., 2008), resulting in Green Sahara Periods (Kutzbach, 1981; Ziegler et al., 2010; deMenocal and Tierney, 2012; Larrasoaña et al., 2013; Skonieczny et al., 2019; Pausata et al., 2020). In particular, northwest African sub-tropical driven precipitation of the last glacial cycle shows a strong control of precessional cycles (~26 kyr) albeit still paced by eccentricity (Fig. 1.3b-c; Tjallingii et al., 2008; Larrasoaña et al., 2013; Dixit et al., 2020). Compared to the global climatic curve derived from stacked marine oxygen isotope records (Lisiecki and Raymo, 2005), this regional precipitation record has a more prominent precession signal (Fig. 1.3a-c). Thus, such precessional-driven shifts would especially affect the geomorphic conditions of catchments south of the High Atlas divide by increasing the frequency of tropical incursions leading to geomorphic work in ephemeral tributaries and trunk streams. At present, the Mgoun River has two perennial trunk streams joining in the thrust front, fed by ephemeral tributaries. Flood hydrology is influenced by a semi-arid mountain climate with an altitudinal zonation where annual precipitation varies from 500 mm/yr in the headwaters to less than 200 mm/yr in the downstream reaches (Fig. 1.4).

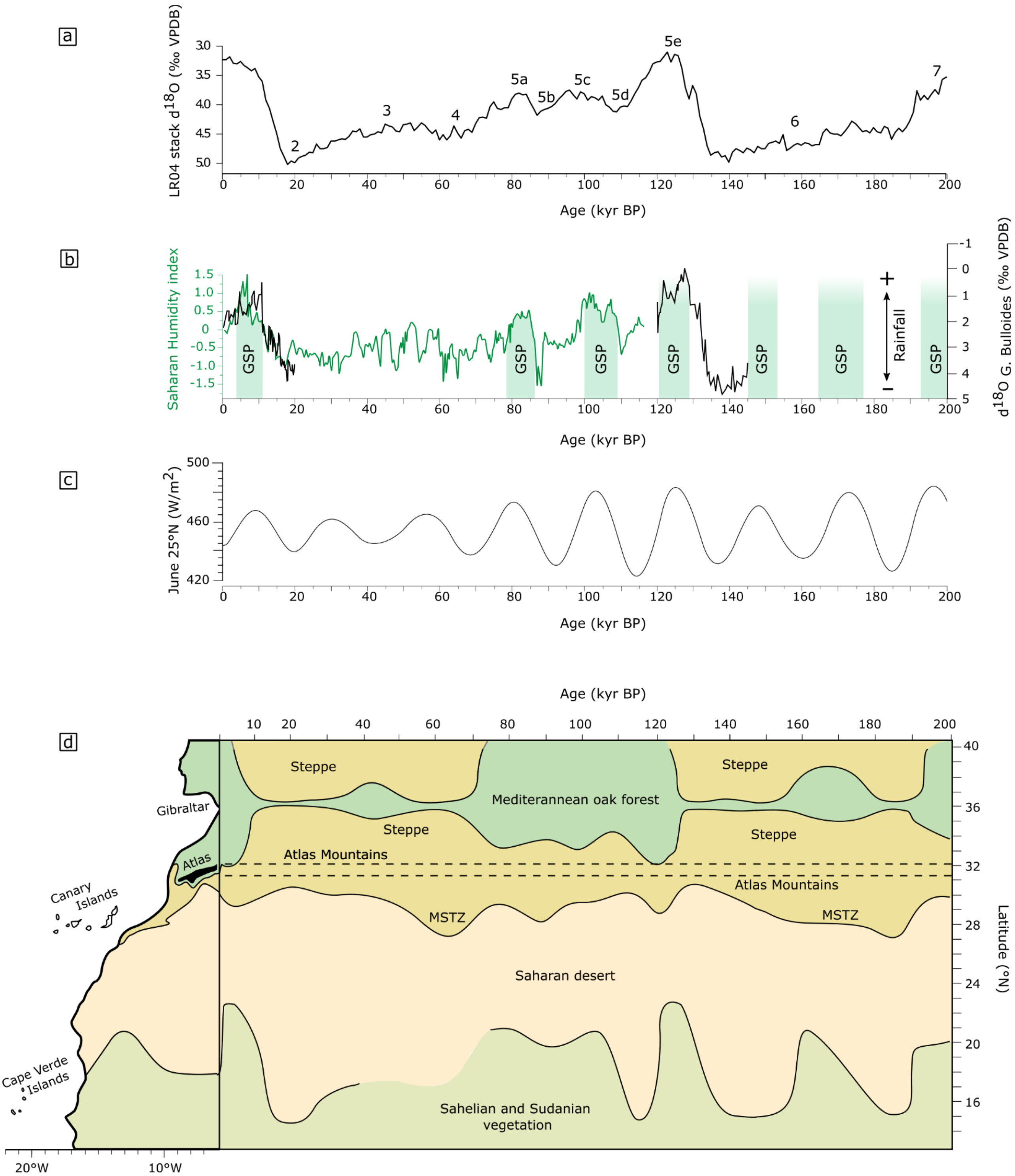

Figure 1.3– Quaternary palaeoclimatic history of NW-Africa. (a) The marine oxygen isotope (MIS) record for the last 200 ka, based on the LR04 benthic δ^{18}O stack constructed by Lisiecki and Raymo (2005), with MIS stages labelled. (b) Green Sahara periods are after Larrasoaña et al. (2013), the Saharan humidity index is from borehole GeoB7920 (see Fig. 1.1) after Tjallingii et al. (2008), and the δ^{18}O record of relative rainfall is from Dixit et al. (2020).(c) The 25 N June insolation curve is calculated using orbital parameters from Laskar et al. (2004). (d) Latitudinal position of Mediterranean to Sahelian vegetation zones based on marine pollen records, after Agwu and Beug (1982), Dupont and Hooghiemstra (1989), Dupont and Agwu (1992), Hooghiemstra et al. (1992) and Dupont (1993). Left: the present position of NW African vegetation zones.

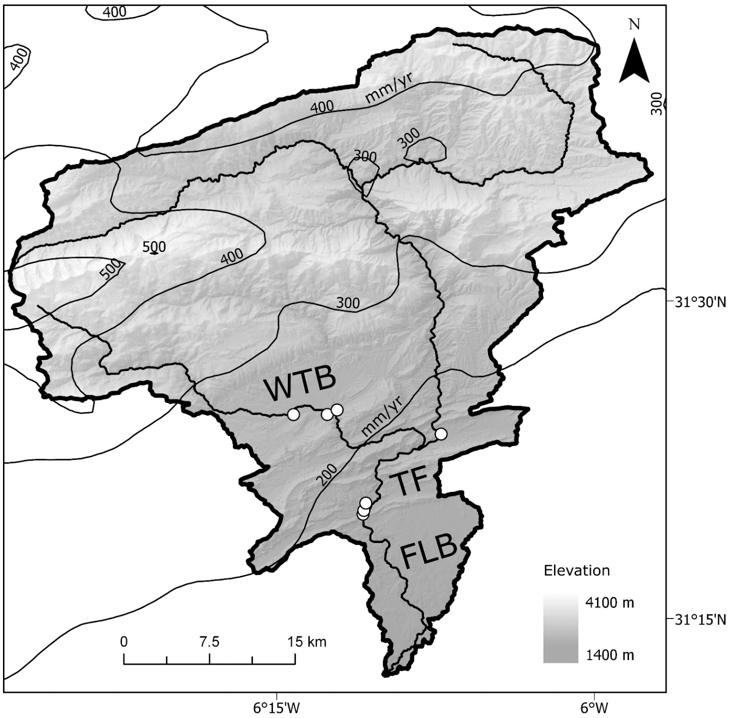

Figure 1.4– Elevation map of the Mgoun drainage basin from ALOS AW3D 30 m data. Contour lines show distribution of annual precipitation in mm/yr (precipitation from Worldclim (Hijmans et al., 2005). WTB: wedge-top basin; TF: thrust-front; FLB: foreland basin. Dots show locations of terraces sampled in this study.

In addition to the influence of NW African palaeoclimate on the hydrology of the Mgoun catchment, local lake and marine pollen records provide a window into the Quaternary vegetation history of NW Africa (Fig. 1.3; Agwu and Beug, 1982; Dupont and Hooghiemstra, 1989; Lamb et al., 1989; Dupont and Agwu, 1992; Hooghiemstra et al., 1992; Dupont, 1993; Dupont, 2011). While the reconstruction of vegetational zones (Fig. 1.3d) based on key species does not directly demonstrate changes in vegetation within the High Atlas, it must be noted that the interpretation of this diagram relies on the concept that vegetational zones are gradational. Thus, any nearby shift in e.g. the line of Mediterranean oak forests will influence the vegetation south of this boundary too. In addition to the continental-scale reconstruction, local lake sediments from the Middle Atlas demonstrate transitions from herb-rich grasslands to oak forests at 1626 m elevation (Lamb et al., 1989). Of particular interest is the declining influence of precession on vegetation from the tropics northward, where obliquity and eccentricity-forced northern hemisphere glaciation are increasing influences on the migration of vegetational zones (Dupont, 2011). Whilst for geomorphic action the magnitude and frequency of tropical rainstorm incursions is an important driver (Fink and Knippertz, 2003; Knippertz, 2003; Knippertz et al., 2003b), for the High Atlas vegetation annual precipitation linked to Mediterranean influence is a main variable (Hooghiemstra et al., 1992). Thus, whilst the Sahelian-Saharan boundary to the south of the Sahara reaches its southernmost extent during MIS stages 6, 5d and 2 (Dupont, 1993), the Mediterranean oak forests were widespread, penetrating far southwards into the Atlas region, across interglacial MIS 5 and 1 (Hooghiemstra et al., 1992). The transition from herb-rich grasslands to oak forests during the last interglacial (MIS 1) is also recorded in lake sediment from the Middle Atlas at 1626 m elevation (Lamb et al., 1989). During interglacial stages 6 and 4-2 small remnants of oak forests may have survived in protected areas during glacial phases, but mostly steppes reached across the northern Mediterranean to the Saharan border during periods when Europe was glaciated (Hooghiemstra et al., 1992). Noticeably, a large Mediterranean-Saharan transitional steppe existed between 74 – 59 kyr (MIS 4) reaching as far south as 25 to 30 N south of the Atlas mountains (Hooghiemstra et al., 1992). Time-transgressive shifts of vegetational zones is common during drier (cooler) to more humid (warmer) conditions, lagging behind climatic changes up to 3 to 5 kyr (Dupont, 1993). The non-parallel transitions between palaeo-hydrologic and vegetational conditions is likely to exert an influence on the development of strath terraces.

Figure 1.5– Landscape of the southern High Atlas. The village of Agouti el Ettahtani in the Mgoun River catchment (see also Fig. 3.1). Hillslopes are bare of soil and vegetation, with cultivated vegetation limited to irrigated fill terraces in the flood plain. Strath terraces elevated ~ 10 to 15 m above the modern river plain are often covered by villages constructed of adobe – baked clay, and leave a well-preserved terrace deposit relatively untouched. Strath terraces without any development are also common throughout the Mgoun River catchment.

Unlike the hydrological controls on hillslope and fluvial erosion, and the vegetational control on hillslope weathering and erosion, the extent of ice in the High Atlas landscape has been very limited over the course of Quaternary climate. Glacial features related to Pleistocene glaciation set the snowline during glacials at ~ 3300 m (Hughes et al., 2004), which only covers rare peaks, as the main topographic divide of the High Atlas lies at 2500 to 3000 m.

Since 1100 BP, humans have influenced the vegetation of the mountains, such that goat herding has led to hillslopes that are almost completely bare in the southern High Atlas (Fig. 1.5; McGregor et al., 2009). Vegetation is lush on irrigated fill terraces ~ 1-3 m above the modern river plain which are used for the cultivation of crops, fig trees and roses, whilst more elevated strath terraces ~ 10 m above the modern river plain, bare of vegetation like the hillslopes, function as the foundation of many adobe (baked clay) villages (Fig. 1.5). Limited development of such housing means the surface and deposits of many strath terraces are well-preserved. In addition, human influence post-dates the formation of terraces examined in this thesis.

1.4.3 Why study the High Atlas?

The overall aim of this thesis is to investigate the lithological and structural controls on fluvial mountain landscape evolution. During the Quaternary, climatic influences are a major top-down control on this evolution. The geological and climatic setting of the High Atlas post-orogenic dryland mountain belt provides a study setting which is different from many high-rate actively building mountain belts, those in high-latitude settings or those with eustatic base-level control. In particular, it allows isolation and observable characteristics of lithological, structural and climatic influences on landscape evolution:

1. The High Atlas is in a post-orogenic state, with long-term isostatic rock uplift rates of 0.17-0.22 mm yr^{-1} since 15 Ma related to lithospheric thinning (Babault et al., 2008).This isolates the effect of climatic changes and lithological control on fluvial archive formation.
2. The inland setting of the central High Atlas (800-1000 km from the coast) results in an absence of eustatic base-level control on drainage development. Thus, climatic controls on strath terrace formation are limited to top-down controls of precipitation patterns and vegetation cover through time.
3. The combination of highly heterogeneous rock strength of the mountain belt allows a focus on rock strength control on erosion. Since hillslopes are bare, the geology of the catchment is easily identifiable in the field and in remote sensing. Outcrops allowing the *in-situ* measurement of rock strength are also abundant.

4. The geological age of bedrock and its associated tectonic architecture in the mountain belt increases from east to west in the study area, allowing the tracking of both variations in rock strength and structural configuration which influence drainage mobility during erosion through an exhuming mountain belt.
5. The mountain belt is situated at a low latitude, is positioned next to the Saharan Desert, and has had limited to no influences of glacial ice restricted to the highest peaks above 3300 masl. This forms an opportunity to explore the effect of orbital climatic changes in a low latitude dryland landscape, and allows the isolation of fluvial process of mountain landscape formation.
6. Strath terraces in the High Atlas, due to its dryland setting and limited human development, have much or all of their overlying sediment preserved. This allows integration of erosional and depositional fluvial archives of landscape evolution and provides material to date erosional and depositional processes using innovative approaches.

Further details about the tectonic, structural, and geological controls on geomorphological evolution of the High Atlas are explored in later chapters of this thesis.

1.5 AIMS AND OBJECTIVES

The goal of this thesis is to evaluate to what extent lithological and structural variability affect fluvial archives originating in mountain belts, which include both erosional topography and depositional sequences. To address this aim, I have outlined two major objectives that I will address in this thesis:

OBJECTIVE **1.** Where and when does bedrock erodibility drive drainage divide mobility during the evolution of a collisional mountain belt?

OBJECTIVE 2. To what extent do lithological and structural variability within a catchment draining a collisional mountain belt affect the timing of fluvial incision and aggradation in response to climatic changes on orbital timescales?

Objective 1 requires knowledge of how rock mass strength affects fluvial erodibility and of the mobility of the drainage divide in litho-stratigraphic units of a mountain belt. The sub-objectives of objective 1 are:

1.1 Determine the magnitude of variation in erodibility between rock types within the High Atlas.
    a. Quantify mechanical rock strength of geological units in the High Atlas.
    b. Quantify the fluvial erosional response to geological units.
    c. Compare mechanical rock strength and fluvial response to quantify bedrock erodibility throughout the High Atlas.

1.2 Quantify the mobility of the central drainage divide crossing multiple litho-stratigraphic units.

Objective 2 focuses on the catchment-scale process of river channel aggradation and incision. This objective focuses on the controls on the timing of fluvial incision and aggradation within the Mgoun catchment which runs through a wedge-top basin and thrust front. Sub-objectives for this objective are:

2.1 Determine the effect of lithological and structural variation on incisional and depositional landforms of valley aggradation and incision.
    a. Establish terrace stratigraphy in the study area and its relationship to lithology.

    b. Reconstruct the fluvial depositional system recorded in sedimentary cover of strath terraces.
    c. Assess the effect of conglomerate recycling on sediment delivery to river channels and terraces.
    d. Reconstruct paleo-river long profile evolution from a digital elevation model and terrace treads.

2.2 Constrain the timing of river channel aggradation and incision throughout the catchment.

    a. Develop and apply methods of optically stimulated luminescence dating on coarse fluvial gravel terrace deposits.
    b. Constrain the timing of aggradation, incision, and strath terrace formation along the length of the studied river.

1.6 THESIS OUTLINE AND STRUCTURE

This thesis has three research chapters, a discussion, and a conclusion. The following section briefly describes the content of each of the chapters presented in this thesis.

CHAPTER 2 investigates the control of lithological and structural variability on fluvial erodibility and drainage divide mobility in the High Atlas (objective 1). To quantify the magnitude of variation in erodibility between rock types (objective 1.1) I: (a) collect mechanical measurements of rock strength in the field; (b) extract the normalised river channel steepness of rock units from a digital elevation model; and (c) derive constraints on the stream power model of bedrock river erosion and fluvial erodibility by integrating the combined dataset of mechanical rock strength and river channel steepness. I then quantify the mobility of the main drainage divide using topographic metrics (objective 1.2). Because the High Atlas exhibits different stages of orogenic landscape evolution, from erosion through gently dipping sedimentary cover to exhumed crystalline basement along the length of the main drainage divide, the measures of rock erodibility and stratigraphic orientation are then used to quantitatively assess when and where a drainage divide will move in response to erodibility variation during the evolution of a collisional mountain belt (objective 1). The results have implications for understanding long-term trends in the geomorphology and erosion of mountain belts owing to the rock types and their structural configuration, and quantitatively constrain the magnitude of contrasts in erodibility within a mountain belt which enables integration of field and modelling studies.

IN CHAPTER 3 the enquiry on the effects of lithological and structural variability is then extended to the effective unit of a mountain belt: a catchment draining into the foreland basin. This chapter establishes a geomorphological and sedimentological framework of fluvial archives of the Mgoun River in context of the lithological and structural variability throughout the wedge-top basin and thrust front (objective 2.1). To do this I derive both the incisional and depositional fluvial archives and try to integrate them. Incisional archives include the river long profile, strath treads and valley morphology. Depositional archives include the fluvial depositional system including terrace and river channel sediments and their grain size and provenance. These archives are linked by processes of river channel aggradation, lateral and vertical bedrock erosion. By integrating these archives, I assess the effect of lithological and structural variability along the Mgoun River on these processes and the subsequent signals preserved in the fluvial archives.

CHAPTER 4 follows on to address objective 2 by constraining the timing of river aggradation and incision in the catchment (objective 2.2) using OSL. To apply this technique, I develop methods of dose rate calculation for gravel sediments on fluvial terraces, which bring challenges of dosimetric heterogeneity and transient water saturation levels. To constrain the timing of aggradation and incision within the catchment I sample terraces along the length of the Mgoun River in three reaches separated by gorges.

CHAPTER 5 forms responses to the two objectives by discussing the results from chapters 2-4 and by synthesising the conclusions to address the overall aim of evaluating to which extent lithological and structural variability affect fluvial archives originating in mountain belts, from the mountain belt to the catchment scale. Two new conceptual models arise from this discussion: lithologically induced drainage divide mobility during the long-term erosion of a collisional mountain belt; and an asynchronous model of strath terrace formation in a collisional mountain belt.

FINALLY, CHAPTER 6 summarises the main conclusions that this thesis contributes to the field of fluvial archive studies.

2

Rock strength and structural controls on fluvial erodibility: implications for drainage divide mobility in a collisional mountain belt[*]

2.1 INTRODUCTION

In the central High Atlas Mountains (Fig. 2.1) different stages of orogenic landscape evolution, from erosion through gently dipping sedimentary cover to exhumed crystalline basement occur along the length of the main drainage divide, forming a natural experiment in drainage divide mobility during the erosion of a collisional mountain belt. Furthermore, the continental inland setting, low weathering rates and lack of influence from ice sheets associated with an arid climate and low rates of post-orogenic tectonic activity mean rock strength controls on topography are more clearly isolated, and can be

---

[*] A version of this chapter and the ensuing discussion in chapter 5 (5.2) has been published as the following paper:

Zondervan, J.R., Stokes, M., Boulton, S.J., Telfer, M.W. and Mather, A.E., 2020. Rock strength and structural controls on fluvial erodibility: Implications for drainage divide mobility in a collisional mountain belt. Earth and Planetary Science Letters, 538, p.116221. doi:10.1016/j.epsl.2020.116221

JRZ wrote the text, prepared all of the figures and developed the intellectual arguments therein. J.R.Z., M.S., A.E.M. and S.J.B. performed the Schmidt hammer measurements in the field, J.R.Z. performed the topographic analysis. All authors discussed the science and commented on the manuscript.

resolved as a lack of vegetation enables complete observation of the geology and geomorphology. Thus, this post-orogenic mountain range is an ideal setting to study erodibility-induced drainage divide mobility. I aim to derive data and present it in a form that is useful for both field geologists and numerical modellers alike. In this chapter, I quantify the magnitude of variation in erodibility between rock types by: (i) extracting the normalised river channel steepness of rock units from a digital elevation model; (ii) collecting mechanical measurements of rock strength in the field, and (iii) quantifying the mobility of the drainage divide using topographic metrics. The measures of rock erodibility and stratigraphic orientation are then used to quantitatively assess when and where a drainage divide will move in response to erodibility variation in the evolution of a collisional mountain belt in which rivers erode first through sedimentary cover, secondly through meta-sediments and finally through crystalline basement. The following results have implications for understanding long-term trends in the geomorphology and erosion of mountain belts owing to the rock types and their structural configuration, and quantitatively constrain the magnitude of contrasts in erodibility within a mountain belt which enables integration of observation and modelling studies.

2.2 STUDY AREA

The study area is located in the centre of the High Atlas Mountains, focussed on the 250 - 300 km length of the drainage divide bounded by the Ouarzazate Basin to the south and the Haouz Basin in the north (Fig. 2.1). The drainage divide strikes along the structural grain of the mountain belt, inherited by the configuration of a pre-existing rift (Babault et al., 2012). The age of exposed bedrock and its associated tectonic architecture in the mountain belt increases from east to west in the study area (Fig. 2.1). The along strike trends allows

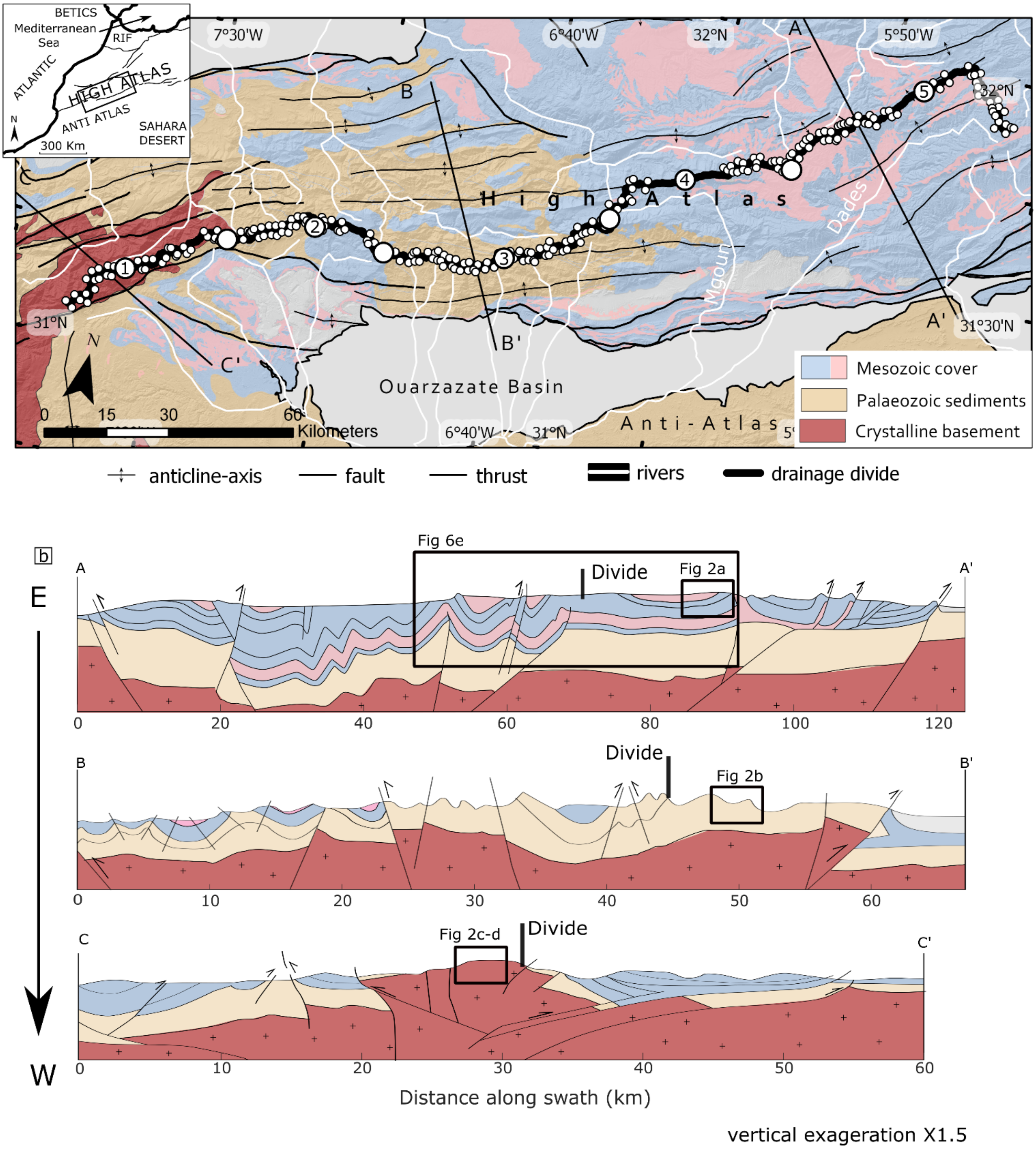

Figure 2.1– Overview of the central High Atlas. a) Geological map of the central High Atlas, showing the distribution of Mesozoic sedimentary cover consisting of limestones (blue) and continental clastic sedimentary rocks (pink), Palaeozoic meta-sediments (orange) and crystalline basement (red). The chain is flanked by sedimentary basins: the Ouarzazate Basin to the south and the Haouz Basin to the North. Three cross-sections labelled A to C show the locations of cross-sections in b). Headwater channel locations used for calculating drainage divide mobility start at a reference drainage area of 1 km2, marked as white dots (see methods 3.3). The drainage divide is marked on as a black line and is segmented into five equal lengths (Fig. 2.5). (b) Cross-sections based on seismic sections modified from Errarhaoui (1998); Teixell et al. (2003). These cross-sections are vertically exaggerated by a factor of 1.5. The location of the drainage divide is marked on as black markers on the structural cross sections.

Table 2.1- Chronostratigraphic packages labelled on Fig 2.1 with details of lithologies and structure

Chronostratigraphic package	Lithologies	Structure	Rock strength (see Table 2.2 for definitions)
Mesozoic sedimentary cover	massive marine platform limestones; continental red marls with gypsum; marine and continental conglomerates, sandstones, siltstones and micro-conglomerates	horizontal stratigraphy, gently deformed with spaced-out faults and thrust-top folds offsetting strata vertically	very weak – moderately strong
Palaeozoic meta-sediments	sandstones, shales, siltstones, schists	closely spaced faults, abundant jointing, steeply dipping and folded strata	moderately strong
Crystalline basement	granite, granodiorite, gabbro, dolerite, migmatite	massive outcrops of igneous rock, vertical or sheet fracturing in some outcrops	strong

me to use location as a proxy for time in understanding the mobility of the main drainage divide as river erosion exposes sedimentary cover to metamorphic sedimentary rock, to crystalline basement. The sedimentary cover, older meta-sediments and underlying crystalline basement have distinct lithologies with varying hardness and structural weaknesses owing to the tectonic architecture of the mountain belt (Table 2.1). Thus, each chronostratigraphic package has its own potential for drainage divide mobility which I investigate in this study.

Figure 2.2– field photos showing the lithologies and stratigraphic configuration of units within the three lithostratigraphic packages of the Atlas. (a) In the Mesozoic weathering-resistant competent limestone beds dip at sub-horizontal angles. Within the interlayered limestones and weaker clastic rocks, variations in rock strength and weathering exist. (b) In the Palaeozoic meta-sediments steeply dipping, sub-vertical strata are common. Road on the flood plain for scale. (c) Massive crystalline basement exposed in is sometimes found jointed in vertical planes or (d) as dome-shaped or massive igneous outcrops with vertical or sheet fracturing. House for scale at the bottom.

From east to west the drainage divide crosses first a landscape dominated by gently dipping beds of Mesozoic carbonates and clastic sedimentary rock (Table 2.1) configured into low-amplitude long-wavelength folds punctuated by spaced-out thrusts (Fig 2.1, Fig 2.2a) at an elevation of 2600 to 3000 m. In this length of the divide, the Dades catchment lies to the south and incises into a long-wavelength syncline exhibiting gently dipping strata, whereas directly north of the divide is a concentration of folding and thrust offset strata dipping at higher angles to the surface (Fig. 2.1b). Next the drainage divide decreases in elevation to ~2500 m, as it crosses a zone of dipping strata of faulted meta-sediments (Table 2.1, Fig. 2.2b) in the centre of the study area

(Fig. 2.1). Finally, in the west, the divide rises back up to elevations > 2800 m as it runs over the edge of the exhumed crystalline basement consisting of igneous rocks with vertical or sub-vertical fracturing (Fig. 2.1, Table 2.1, Fig 2.2c-d).

The inland setting of the central High Atlas (800-1000 km from the coast) results in an absence of eustatic base level control on drainage development. Though localised base level fluctuations are likely to have occurred, studies of basin fill sediments and river profiles suggest that such fluctuations were small to negligible over the Plio-Quaternary (Boulton et al., 2014; Boulton et al., 2019). The High Atlas is in a post-orogenic state, with long-term isostatic rock uplift rates of 0.17-0.22 mm yr^{-1} since 15 Ma related to lithospheric thinning (Babault et al., 2008). The lack of recent tectonic deformation is apparent in the undeformed continuous Quaternary river terraces forming parallel river long profiles throughout the fold-thrust belt and thrust front (Stokes et al., 2017). Therefore, unlike in active mountain belts where divide migration is expected in response to changes in the uplift field (Willett et al., 2001), the Plio-Quaternary divide mobility of the High Atlas is not expected to reflect tectonic advection. Recorded glacial features related to Pleistocene glaciation establish that the snowline was at c. 3300 m in the High Atlas (Hughes et al., 2004). Since the main drainage divide varies in elevation between 2500 and 3000 m it has not been affected significantly by glacial activity. Thus, for our purposes the main control on the Plio-Quaternary evolution of the High Atlas river network is the incision through the inherited tectonic architecture of lithological units and their contrasting strengths. Drainage development in the High Atlas is considered to be primarily the product of the exhumation of structurally distributed lithologies with different hardness, controlling where river terraces develop (Stokes et al.,

2017) and affecting the occurrence of diffusive and advective slopes (Mather and Stokes, 2018). The High Atlas is set in a semi-arid climate, which means that the effect of weathering on rock erodibility is expected to be low. Thus, intact rock strength measurements are likely to reflect the effective bedrock strength.

2.3 METHODS

I measure two proxies of fluvial bedrock erodibility to constrain the contrast between lithological units. These data allow me to compare field observations of drainage divide mobility with numerical models of river erosion through variable lithology. I systematically: 1) derive the normalised river channel steepness index from a digital elevation model (DEM) as a measure of a river channel's power to erode rock; 2) record compressive rock strength using a Schmidt hammer in the field as another measure of fluvial erodibility, and 3) extract topographic metrics of drainage divide mobility from the DEM along the length of the main drainage divide.

2.3.1 *River profile analysis, rock type and fluvial erodibility*

Rock type influences the river network by affecting the ability of rivers to erode into bedrock, determined by the fluvial erodibility. Numerical models that describe river erosion through bedrock often use the stream power model, in which the erosion rate at any particular point in a bedrock river channel is defined by:

$$E = KA^m S^n \qquad \text{Eq. 1}$$

where K is an erodibility constant which depends on the rock-type over which the river channel flows as well as the climatic setting, A is upstream drainage area and S is local channel gradient, and m and n are constants that depend on basin hydrology, channel geometry, and erosion processes (Whipple and

Tucker, 1999). Any change in the erodibility of rock type exposed will force the river to adjust its stream power by changing river channel slopes and thus can cause divide mobility as river networks respond. The use of this formula in field studies proves problematic because of the lack of data and robust methodology to determine the erodibility constant, *K*. However, equation 1 can be written as:

$$S = (\frac{E}{K})^{\frac{1}{n}} A^{-(m/n)} \qquad \text{Eq. 2}$$

which may be recognised as a form of the empirical power law scaling local channel gradient (*S*) and drainage area (*A*):

$$S = k_{sn} A^{-\theta} \qquad \text{Eq. 3}$$

$$k_{sn} = \ (\frac{E}{K})^{\frac{1}{n}}$$

$$\theta = m/n$$

where *S* is the local channel slope (dimensionless), k_{sn} is normalised steepness index ($m^{2\theta}$) and θ is the concavity index (dimensionless). I assume that erosion is proportional to specific stream power and inversely proportional to bedrock erodibility, so that n > 1 (Perne et al., 2017), and k_{sn} is inversely proportional to erodibility, *K*:

$$K \propto \frac{1}{{k_{sn}}^{n}} \qquad \text{Eq. 4}$$

Unlike *K*, the k_{sn} of river channels can be readily determined from digital elevation models (DEMs) (e.g. Boulton et al., 2014; Gallen, 2018; Bernard et al., 2019). I therefore use k_{sn} as a measure of fluvial erodibility of geological units over which river channels flow in the High Atlas, provided that spatial variability in long term rock uplift is low, which is likely, for reasons outlined above (§2.2). Consequently, a factor of difference in k_{sn} between geological units will be an estimate of the factor of difference in their fluvial erodibility, *K*. I normalise k_{sn} values to the most erodible rock-type (see §2.4.1), and then use Eq. 4 to convert these normalised average k_{sn} values to normalised *K* values. To do this, I calculate normalised *K* for three feasible values of n: n=1, n=2 and n=4. Perne et al. (2017) show that to obtain a stream-power-model generated river profile in which the slopes of river channels are steeper in low erodibility, strong rock, n must be > 1. Lague (2014) demonstrate that, fully calibrated with slope information from field locations, n ~ 2 in most cases, and this could be as high as n ~ 4. Calculating normalised *K* values from the k_{sn} data enables a quantification of contrasts in erodibility *K* between rock-types in the High Atlas and their control on changes in river erosion rates and consequent mobility of the drainage divide.

I performed k_{sn} analysis using the Topographic Analysis Kit (Forte and Whipple, 2019), a series of MATLAB functions based on TopoToolbox (Schwanghart and Scherler, 2014) which uses the chi approach to calculate k_{sn} smoothed over 1000 m segments (Perron and Royden, 2013). Tests using the criteria proposed by Perron and Royden (2013) show that θ is ~ 0.45 for a range of catchments covering the extent of the drainage divide in the central High Atlas, which is the same value as used for the High Atlas by Boulton et al. (2014). This gives k_{sn} units of $m^{0.9}$. I use the ALOS Digital Elevation Model with a resolution of 30 m from the Japan Aerospace Exploration Agency (http://www.eorc.jaxa.jp/ALOS/en/aw3d30/index.htm) to perform the analysis following recommendations of Boulton and Stokes (2018). Finally, I extract the average and standard deviation k_{sn} of each rock type using the digitised 1: 1 000 000 geological map of Morocco (Saadi et al., 1985; see Supplementary Fig. S2.1 at the end of the thesis). Formations are grouped into lithological units that collectively comprise three groups: Mesozoic sediments, Palaeozoic meta-sediments and crystalline basement over which the drainage divide crosses from east to west (Fig. 2.1). For each of those packages I group lithological units (Table 2.1): (i) gently folded massive marine platform limestone; (ii) interbedded red beds consisting of mud and siltstone; (iii) interbedded sand-siltstones and conglomerates; (iv) folded and faulted meta-sedimentary rocks such as schist and shale, and (v) faulted massive outcrops of igneous units. The contrasts in k_{sn} of river channels flowing over rock-types (Supplementary Fig. S2.1) includes the effects of both rock strength and structural weaknesses on the resulting erodibility of bedrock.

2.3.2 *Mechanical rock strength measurements, rock type and erodibility*

A further approach to determine the fluvial erodibility of rock-types is measuring their mechanical strength. The classic experiment by Sklar and Dietrich (2001) showed that erodibility of rock, K, in the stream power model for bedrock river erosion is related to the inverse square of tensile strength ($\sigma_{\tau}{}^{2}$). Thus, a measure of tensile strength and the difference between units enables the calculation of contrasts in erodibility, K. However, measurements of tensile strength cannot be achieved easily in the field, and the most commonly applied method of rock strength assessment in geomorphology is the Schmidt hammer because of its portability (Goudie, 2006). The Schmidt hammer records the rebound distance of a weighted spring that strikes the rock surface and uses a range from 10 – 100. With the Schmidt hammer, measurements of *in situ* uniaxial compressive rock strength in the landscape can be taken in large quantities, making it a very versatile instrument in landscape studies. The higher the rebound value, the higher the elastic strength of the rock, which is a measure of the uniaxial compressive strength (UCS) of a rock. Tensile strength (TS) represents the resistance to sediment impacts on the riverbed and its use has been advocated based on the stronger correlation of fluvial metrics with tensile strength than compressive strength (Bursztyn et al., 2015). But since compressive and tensile strength are correlated (UCS ~ 10*TS; Kahraman et al., 2012; Nazir et al., 2013), K is effectively also proportional to the inverse square of UCS:

$$K \propto \frac{1}{UCS^2} \quad \text{Eq. 5}$$

Thus, similar to the approach in 2.3.1, I normalise UCS values to the most erodible rock-type, and then use Eq. 5 to convert these normalised average UCS values to normalised K values. To produce a map of rock strength I digitised the 1:1 000 000 geological map of Morocco (Saadi et al., 1985) for the study area and assigned an average rock rebound value to each stratigraphic unit. Typically, ten to twenty Schmidt hammer measurements were taken at each location, totalling 690 readings throughout the central High Atlas with up to 132 readings per geological unit (Supplementary materials). Where rock strength measurements for geological units from field measurements were absent, I supplemented this with an existing database of Schmidt rebound values for lithological units reported from around the world (Goudie, 2006). This database contains Schmidt rebound measurements for 111 lithological units, in mostly arid environments similar to the High Atlas. For each stratigraphic unit without field measurements the average of values reported in the literature for the lithology of that unit is used. Units are combined in the same lithological groups as the k_{sn} data. The standard deviation of Schmidt hammer measurements and the range of values reported in the literature reflect the variation of rock strengths within the lithological units (Supplementary material Table 2.1, Figure S2.2). Mean and standard deviation of Schmidt hammer rebound values (SHV) are then converted to UCS using the conversion which was derived by Katz et al. (2000) ($UCS =$

$2.21e^{(0.07SHV)}$) for a range of carbonate rocks, sandstone, marble and igneous rocks with UCS values similar to those found in the study area. In contrast to the k_{sn} approach, the UCS of lithological units only takes into account the internal rock mass strength of bedrock, and thus does not account for structural weaknesses imposed by discontinuities such as bedding or jointing. Consequently, estimating variation in erodibility between rock-types using this approach may be expected to underestimate the erodibility of folded and faulted shales and schists and jointed igneous rock (Table 2.1).

2.3.3 *Topographic analysis of the drainage divide*

To determine the mobility of the drainage divide in response to erodibility variation and its structural configuration, I perform topographic analysis of the main drainage divide along the study length. The mobility and potential direction of movement of the drainage divide depends on erosion rates either side, and whilst the chi method of mapping drainage divide instabilities (Willett et al., 2014) is used widely, Forte and Whipple (2018) demonstrated that this method is especially problematic when integrating across multiple lithologies with different strengths. Alternatively, Forte and Whipple (2018) coined the term Gilbert Metrics, based on the assumption that contrasting stream gradients either side of a divide will drive divide migration. Where divides are bounded by different channel gradients either side they are mobile, with higher erosion rates on the steeper sides leading to migration towards the side with lower channel gradients (Fig. 2.3). The topographic proxies for erosion rates across divides defined by Forte and Whipple (2018) are differences in headwater channel elevation, local headwater hillslope gradient and local headwater relief, which have proven useful for interpreting the relative mobility of catchment divides (Forte and Whipple, 2018). Headwater channel elevation, local headwater hillslope gradient and local

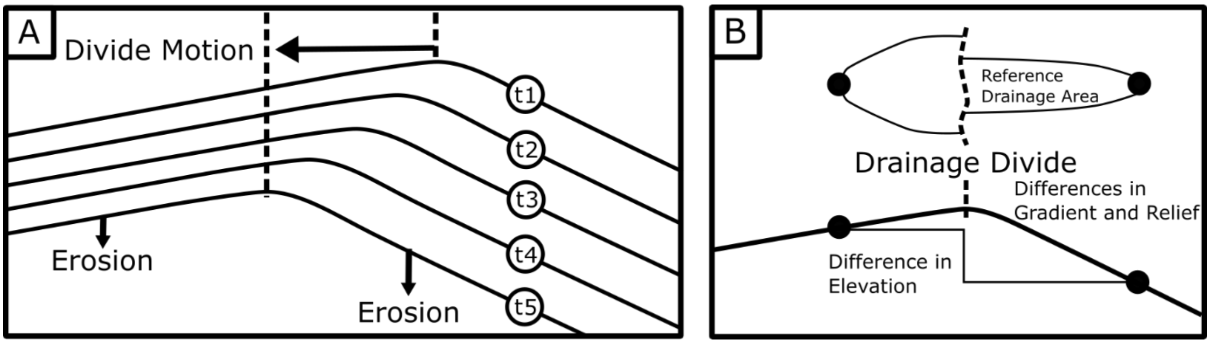

Figure 2.3– principles of the Gilbert metrics for drainage divide stability, modified after Forte and Whipple (2018). (a) Where channels are steeper on one side of the divide compared to the other, divide motion will be in the direction of low gradients where erosion is lower. (b) Similarly, erosion will progress towards those channels with higher headwater channel elevations.

headwater relief were extracted from the ALOS DEM using methods outlined in Forte and Whipple (2018), at a reference drainage area 1 km^2. While the upstream area required to initiate channel flow varies on settings (Clubb et al., 2014), this drainage area is the critical threshold area downstream of which stream-flow-dominated fluvial channels are expected to dominate over debris-flow-dominated colluvial channels in most settings (Wobus et al., 2006). In a numerical landscape evolution model, Forte and Whipple (2018) test the applicability of the Gilbert metrics in a setting with erodibility contrasts across a drainage divide, and conclude that divide migration rate approximates a linear relationship with cross-divide differences in erosion rates and all three Gilbert metrics. To assess the mobility of the drainage divide I define five equal lengths of about 50 km each where boundaries align with those of the three lithological packages described earlier (Fig. 2.1), and in each the mean, standard deviation, standard error, and bootstrap confidence interval of headwater channel values are calculated either side of the drainage divide.

2.4 RESULTS

In plan view (Fig 2.1a), the drainage divide follows a sinuous form, with lengths mostly configured to ENE-WSW and WNW-ESE orientations. The divide tends to occupy central positions in relation to the topography of the range apart from a notable southerly segment in the middle of the study area. Only in the eastern end is there a marked deviation in divide orientation where a small length (20 km) changes to NW-SE.

With respect to erodibility, the drainage divide from east to west runs over bedrock of differing erodibilities, quantified through k_{sn} and UCS measurements.

2.4.1 *K_{sn} and fluvial erodibility*

From east to west, the drainage divide runs over moderately resistant to erodible and very erodible sedimentary cover, moderately resistant meta-sediments, and resistant crystalline basement (Fig. 2.1). Red beds, other clastic sediments and limestones in the Mesozoic cover have mean k_{sn} values of 37, 59 and 74 $m^{0.9}$ with standard deviations of 25, 42 and 49 $m^{0.9}$ respectively (Fig. 2.4c). Palaeozoic meta-sediments average at 85 $m^{0.9}$ with a standard deviation of 41 $m^{0.9}$, whilst the crystalline basement has the highest k_{sn} at 146 with a standard deviation of 52 $m^{0.9}$ (Fig. 2.4c). Fluvial erodibility K values based on Eq. 4 and k_{sn}, normalised to the Mesozoic red beds (the weakest lithology: §2.3.2), vary by a factor of four (Fig. 2.4d). The normalised K value for red beds is 1.0, with other clastics 0.40 or 0.63 and limestone in the Mesozoic cover at 0.25 or 0.50, depending whether $n = 2$ or $n = 1$ (Fig. 2.4d). Normalised K for Palaeozoic meta-sediments is 0.19 or 0.44 whilst crystalline basement has the lowest normalised K at 0.066 or 0.26, about four to fifteen times less erodible than the Mesozoic red beds. Categories of erodibility suggested based

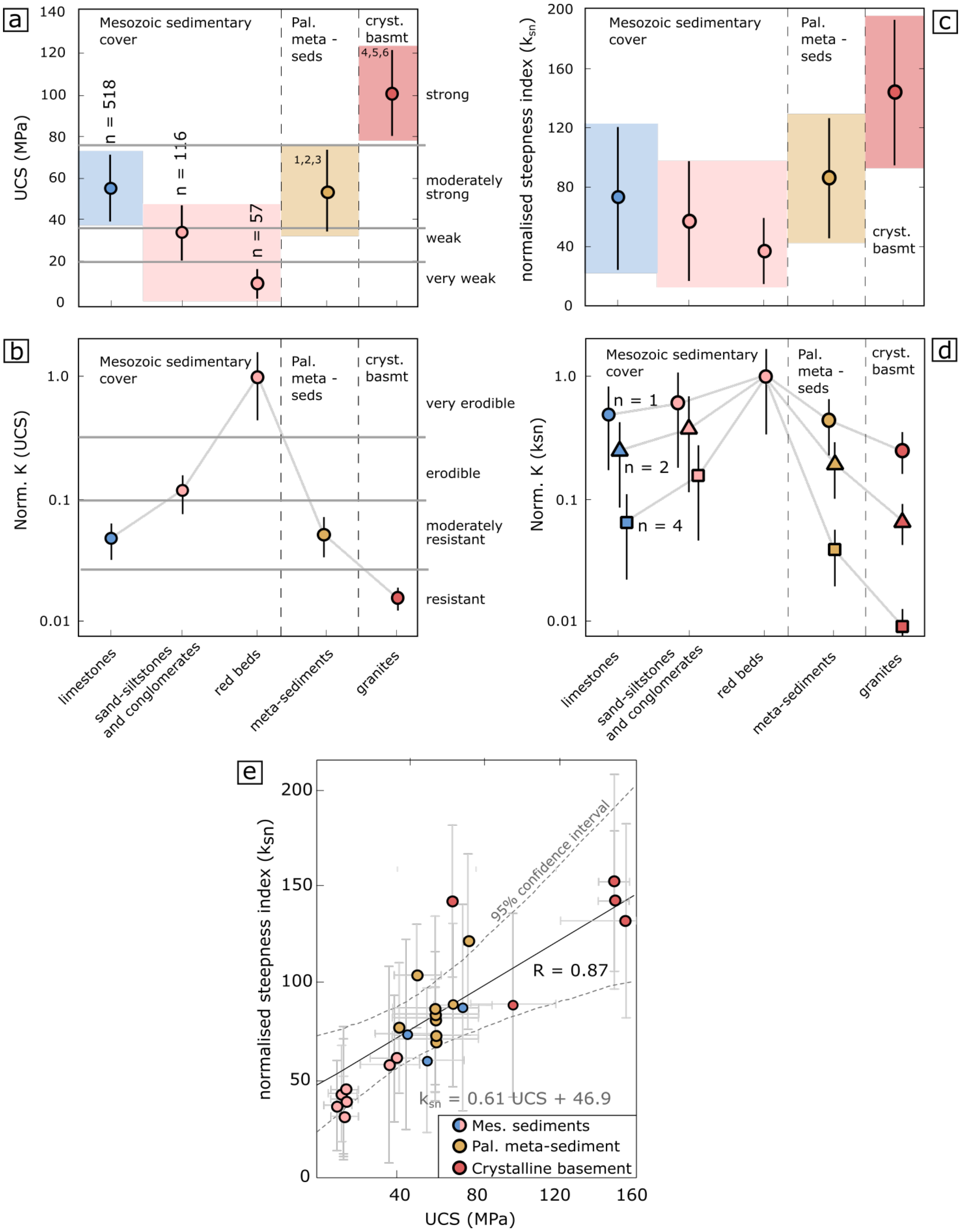

Figure 2.4– Average and standard deviation of (a) uniaxial compressive strength and (b) normalised *K*, (c) k_{sn} and (d) normalised *K* for every chronolithological unit. The number of values analysed for each lithology is displayed above the plots. Colours in graphs are in accordance with Fig. 2.1. Sources of compressive strength data: 1) Gokceoglu and Aksoy (2000) 2) Goudie (2006) & references cited therein 3) Goktan and Gunes (2005) 4) Karakus et al. (2005) 5) Pye et al. (1986) 6) Kahraman et al. (2002). Fluvial erodibility *K* for each chronolithological unit normalised against the weakest rock type derived from relative UCS values (b) and relative k_{sn} values (d). In (d), values of normalised K derived from k_{sn} depend on the value of variable *n* in the stream power equation (Eq. 4). (e) Linear regression of values of k_{sn} and UCS for every geological unit (geological map 1:100 000) with a 95 % confidence envelope in dashed grey lines and points coloured by chronolithological membership. R is the correlation coefficient. Classification of rock strength is based on Schmidt hammer values and other measures of rock strength summarised in Table 2.2, modified from Goudie (2006). Erodibility classification is based on rock strength (Table 2.2).

Table 2.2– Classification of rock-type, strength, and fluvial erodibility

Description	Schmidt hammer value	Uniaxial Compressive strength	Characteristic rocks	Fluvial erodibility
Very weak rock – crumbles under sharp blows with geological pick point, can be cut with pocket knife	10-30	1-20	Weathered and weakly compacted sedimentary rocks – rock salt, marls	Very erodible
Weak rock – shallow cuts or scraping with pocket knife with difficulty, pick point indents deeply with firm blow	30-40	20-35	Weakly cemented sedimentary rocks – siltstones and conglomerates	Erodible
Moderately strong rock – knife cannot be used to scrape or peel surface, shallow indentation under firm blow from pick point	40-50	35-75	Competent sedimentary rocks – limestone, dolomite, sandstone, shale, slate, schist	Moderately resistant
Strong rock – hand-held sample breaks with one firm blow from hammer end of geological pick	> 50	> 75	Competent igneous and metamorphic rocks – granite, migmatite, granodiorite, basalt	Resistant

Rock strength classification and descriptions modified from Table 2 in Goudie (2006)

on the lithological grouping into rock strengths (Table 2.2) and their respective normalised *K* based on k_{sn} values are defined in Fig. 2.4d.

2.4.2 *UCS and fluvial erodibility*

Similar to the k_{sn} of rock units, the fluvial erodibility of bedrock along the length of the drainage divide based on UCS varies from alternating very erodible to moderately resistant rock in the sedimentary cover, to moderately resistant in the meta-sediments and resistant in the crystalline basement. The Mesozoic sedimentary cover has the largest range in UCS of the three chronostratigraphic packages, with red beds, other clastic sediments and limestones averaging 12, 36 and 57 MPa respectively, with standard deviations of 7, 12 and 18 MPa (Fig. 2.4a). UCS values for the Palaeozoic meta-sediment averages at 55 MPa with a standard deviation of 19 MPa, similar to the Mesozoic limestones (Fig. 2.4a). The igneous rocks of the crystalline basement have the highest UCS values with a mean and standard deviation of 101 and 20 MPa. Grouping of rocks into five classes is based on a table from Goudie (2006) which is based on Schmidt hammer values and other measures of rock strength (Table 2.2), and classes are marked on the UCS graph (Fig. 2.4a). Fluvial erodibility K values based on Eq. 5 and UCS, normalised to the weakest unit, vary by two orders of magnitude (Fig. 2.4b). The normalised K value for red beds is 1.0, with other clastic and limestone in the Mesozoic cover at 0.1 and 0.05, respectively. Normalised K for Palaeozoic meta-sediments is 0.05 whilst crystalline basement has the lowest normalised K at 0.015, about two orders of magnitude less erodible than the Mesozoic red beds. Categories of erodibility suggested based on the lithological grouping into rock strengths (Table 2.2) and their respective normalised K values based on UCS are defined in Fig. 2.4b.

2.4.3 *Drainage divide mobility*

Normalised cross-divide delta values of the Gilbert metrics following Forte and Whipple (2018) show the magnitude and direction of mobility varies along the divide and that the divide is stable in the central length of the divide (Fig. 2.5). Elevation of the drainage divide is high in both the east and west, around 2600-3000 m in DIV 1 and DIV 4-5, and lowest in the middle length

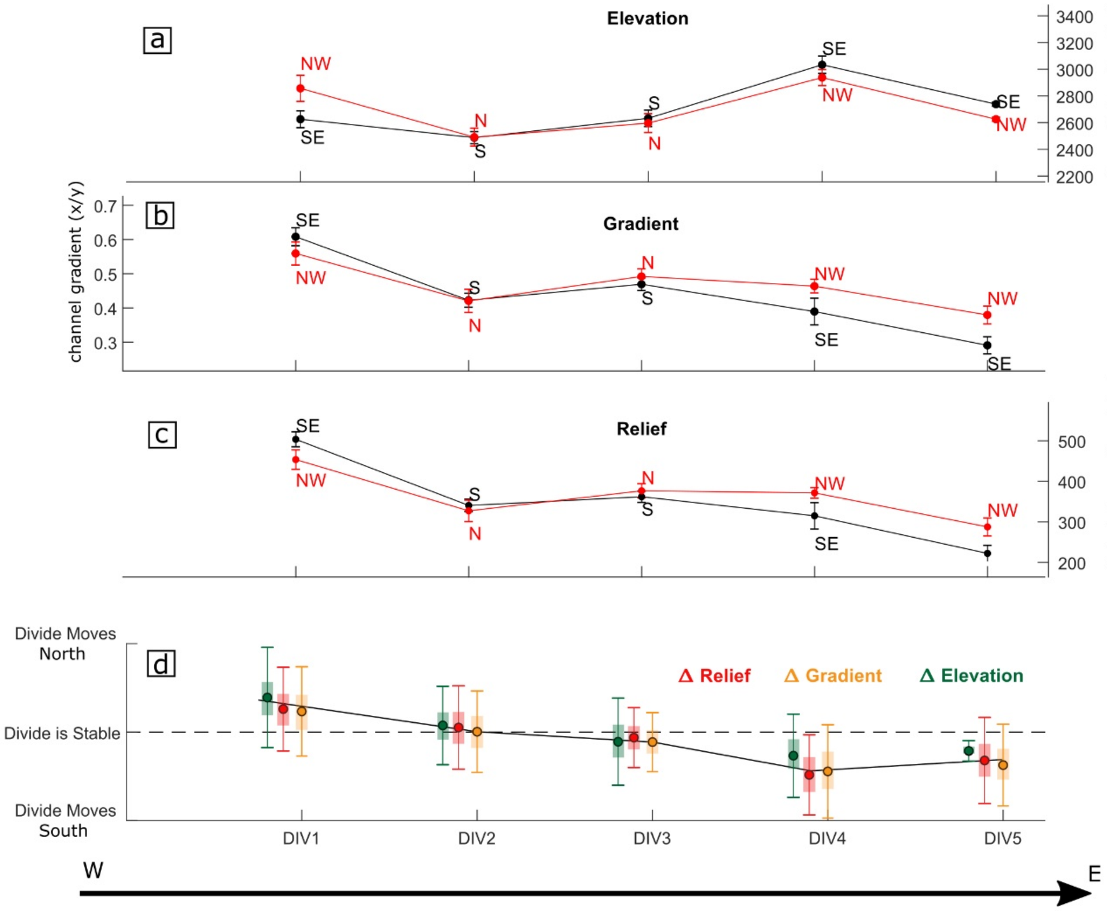

Figure 2.5 – Gilbert metrics for each length of the drainage divide (Fig. 2.1) from west to east. (a-c) headwater channel mean and standard error elevation, gradient, and relief, respectively. (d) Potential direction of divide migration indicated by the direction of mobility of the divide from the Gilbert metrics. Values are standardized to show the direction of mobility. Bars show the standard deviation and shaded boxes show bootstrap confidence intervals.

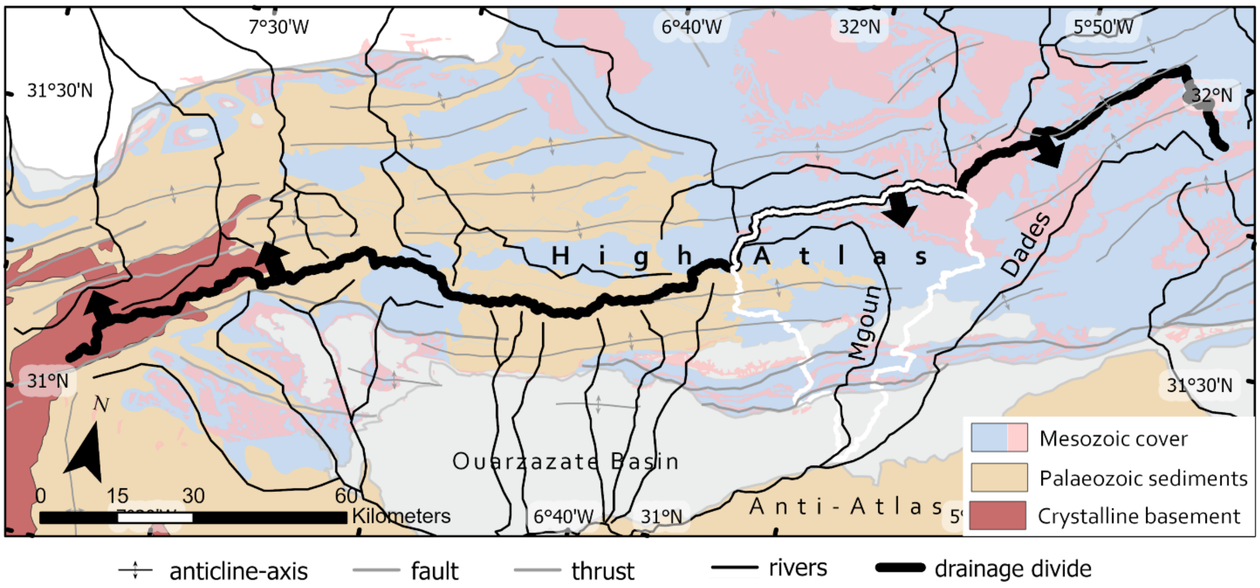

Figure 2.6 - Direction of central drainage divide mobility in the High Atlas as determined from Fig. 2.5. The Mgoun catchment erodes through the Mesozoic cover, which has the highest contrast in rock strength and k_{sn}, and is likely to have experienced drainage migration southward, thus decreasing catchment size.

at ~ 2500 m (Fig. 2.5a). This low elevation length (DIV 2-3) of the divide in the centre of the study area has equal headwater hillslope gradients and relief on both sides of the divide (Figs. 2.5b-c) suggesting a stable drainage divide in the meta-sedimentary rocks (Figs. 2.1, 2.5d). From west to east, headwater hillslope gradients and relief decrease from 0.6 (35°) and 500 m in in the crystalline basement of DIV 1 to 0.3 (15°) and 220 m in the Mesozoic sedimentary cover of DIV 5. Values of headwater channel elevation, hillslope gradient and relief differ either side of the drainage divide in the eastern (DIV 1) and western (DIV 4-5) lengths (Figs. 2.5b-c). In DIV 1, the Gilbert metrics indicate northward movement of the divide (Fig. 2.5d) towards the centre of the exposed crystalline basement. This mobility is based on headwater values which are on average 169 m higher in elevation to the north, with lower hillslope gradients and relief, which differ by 0.06 (3.4°) and 50 m of relief (10%) across the divide (Fig. 2.5a-c). In DIV 4 and 5 in the Mesozoic cover the divide is significantly mobile towards the south (Fig. 2.5d), with headwater channel elevation contrasts of 96-113 m, a difference in hillslope gradients of 0.07-0.09 (4-5°) and relief 44-55 m (14-30%) (Figs. 2.5a-c).

2.5 SUMMARY

The ENE-WSW and WNW-ESE oriented central drainage divide of the central High Atlas runs over bedrock of differing erodibilities. These include, from east to west, moderately resistant to erodible and very erodible horizontally bedded Mesozoic sedimentary cover, moderately resistant steeply dipping Palaeozoic meta-sediments, and resistant crystalline basement. k_{sn} values range from 37 ± 25 $m^{0.9}$ in Mesozoic red beds to 146 ± 52

$m^{0.9}$ in river draining crystalline basement. These values are higher by a factor of two compared to similar lithologies within the post-orogenic setting of the southern Appalachians (Gallen, 2018), but within a similar range to the Pyrenees (Bernard et al., 2019). Values of k_{sn} for crystalline basement are slightly higher than in the Pyrenees, where Bernard et al. (2019) found an average k_{sn} for plutonic rocks of 129, although Strong et al. (2019) found k_{sn} values up to an order of magnitude higher in rivers responding transiently to exhumation of crystalline basement in the Eastern Himalayan foreland. Thus, k_{sn} appears to be dependent on local setting, which could include climate as well as structural setting and whether the landscape is responding transiently in active tectonic settings or closer to equilibrium. Normalised erodibilities range by a factor of four to fifteen depending on the choice of $n = 2$ or $n = 1$. Next to rock strength control on k_{sn}, orographic enhancement of precipitation with greater precipitation on the northern and western sides of the drainage divide may lead to a decrease of k_{sn} values from south to north or east to west (Supplementary Fig. S2.3). However, there is no evidence to suggest a significant difference in k_{sn} values between north and southern or east and western portions of the High Atlas (Supplementary Fig. S2.4). Values of uniaxial compressive strength range from 12 ± 7 MPa in Mesozoic red beds to 101 ± 20 MPa in crystalline basement, resulting in two orders of magnitude in erodibility. The difference in the range of erodibilities calculated through k_{sn} and UCS and their relationship is discussed in chapter 5. Gilbert metrics following Forte and Whipple (2018) show the position of the drainage divide is shifting northwards towards the centre of this exposed resistant rock in the High Atlas; is stable in the metasedimentary bedrock; and is shifting southwards in the Mesozoic sedimentary cover. Chapter 5 will present models of drainage divide reorganisation in response to erosion through lithostratigraphic units of the High Atlas. The mobility towards the south of the divide in the eastern High Atlas means that the Mgoun River catchment has likely suffered losses in catchment area (Fig. 2.6), in which case sediment and water discharge has reduced over time. Whether any divide migration occurred as steady headward migration or capture is not resolved in this study, but any potential impact from capture-style migration could induce pulses of decreased discharge. Thus, it is possible that the geomorphic process of drainage migration has induced a stochasticity of sediment and water discharge down the catchment, potentially affecting the correlation between valley floor aggradation-incision and climatic changes in the Mgoun catchment. In addition, the contrast in rock strength of the sedimentary cover represents the highest contrasts in the High Atlas, and constitutes the substrate of the Mgoun catchment. Consequently, this catchment is the ideal location to test the influence of lithologic and structural controls on river erosion and terrace formation.

3

Geomorphological and sedimentological framework of strath terraces in the Mgoun River catchment

3.1 INTRODUCTION

After the drainage divide consideration in chapter 2, chapters 3 and 4 focus on the next spatial and temporal level of landscape evolution, addressing the timing of fluvial incision and aggradation of a catchment draining the High Atlas in response to orbital climatic changes, lithological and structural variability (objective 2). In particular this chapter provides the geomorphological and sedimentological framework needed to investigate the effect of lithological and structural variation on incisional and depositional landforms of valley aggradation and incision (objective 2.1). Chapter 2 demonstrated that contrasts in erodibility are highest in the sedimentary cover through which the Mgoun catchment erodes. In addition, of all rivers draining the High Atlas, the Mgoun catchment exhibits the longest along-stream distance through a wedge-top basin and thrust front, in which the contrasts in rock erodibility and their passive structural configuration are most pronounced. In this chapter I introduce the geological controls on the valley morphologies exhibited along several reaches of the Mgoun River; next, I explore fluvial archives of valley aggradation and incision in three reaches along the Mgoun River which exhibit strath terraces. First, I constrain a stratigraphic framework of terraces and reconstruct the evolution of river long profiles to constrain the process of terrace abandonment and bedrock incision. Subsequently, strath terrace sedimentary facies, grain size and clast provenance analysis help to constrain the sediment flux within and between each reach. The stratigraphic model and the qualitative and quantitative framework of incisional and depositional archives then form the basis for OSL dating presented in chapter 4 and the conceptual discussion on fluvial incision and aggradation in response to climatic changes, and lithological and structural variability.

3.2 GEOLOGY AND GEOMORPHOLOGY OF THE MGOUN RIVER

The headwaters of the modern Mgoun River lie at altitudes of up to 4,000 m above sea level, with the river entering the Ouarzazate basin at ~ 1500 m. The river flows from a high relief (1900 – 4100 m) fold-thrust belt (FTB) into the study area where it flows first through an intermediate relief (1840 – 1960 m) wedge-top basin (WTB), subsequently enters a high relief (1500 - 2000 m) thrust front zone (TF) and finally drains into a low relief (1400 – 1500 m) foreland basin (Fig. 3.1).

As the river exits the FTB mountain front through a gorge in Jurassic limestones (Fig. 3.2a) it enters the open valley (~3.5 km wide) of the wedge-top basin dominated by Cretaceous red beds (Fig. 3.2b). Cretaceous red beds dipping shallowly to the south make up the valley floor, with valley walls of Jurassic folded interbedded limestones and marls that grade into massive limestones. The river flows southeast obliquely across the wedge-top basin, flanked by low slopes on the eastern banks and high slopes leading to a platform of Pliocene conglomerates elevated ~100 m above the modern river on its western side. In the downstream part of the wedge-top basin the Mgoun cuts a deeply incised (> 200 m), ~ 2.5 km long and 20 to 50 m wide meandering gorge into structurally thickened Jurassic limestones (Fig. 3.2c).

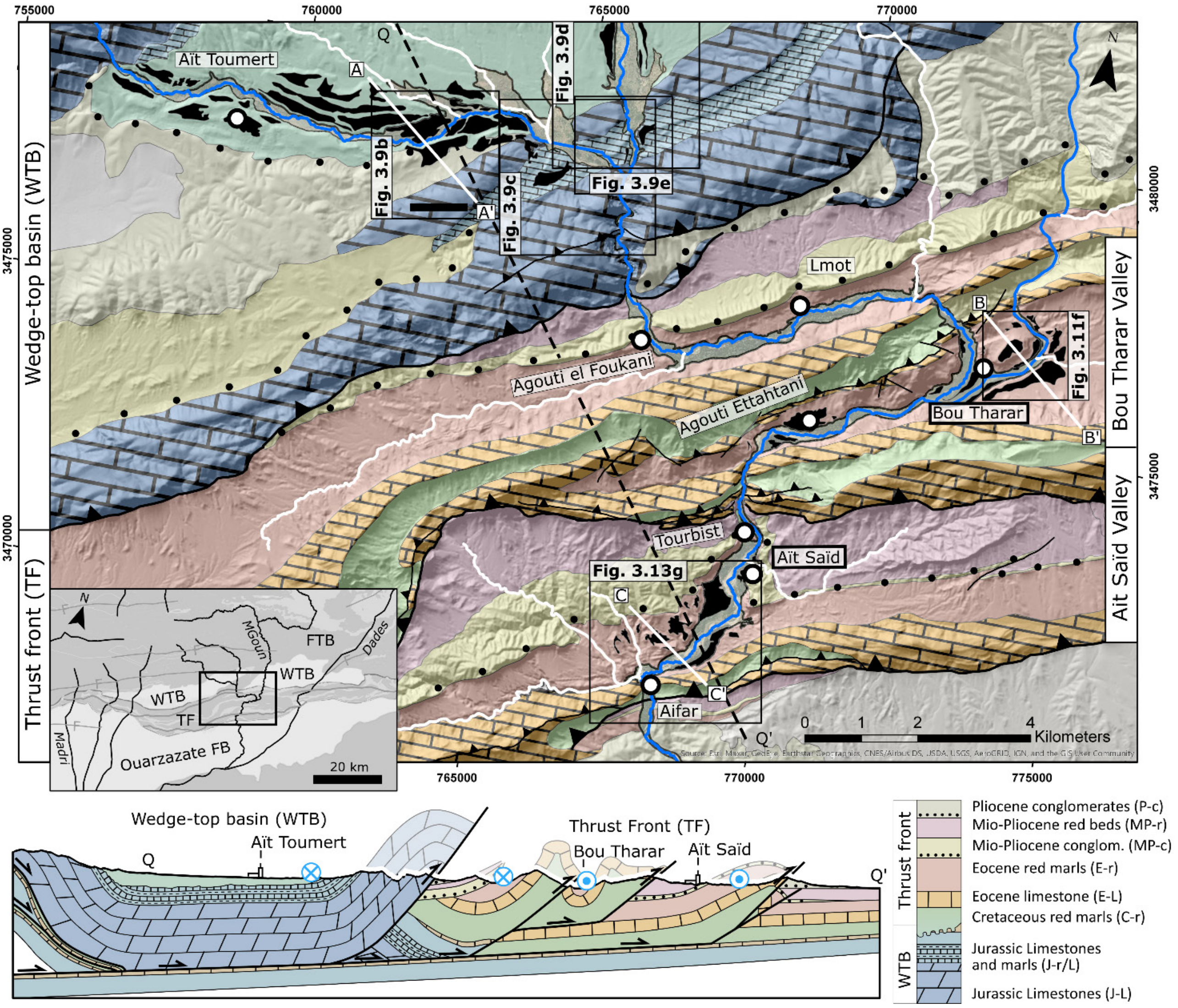

Figure 3.1 – Geology of the study area within the High Atlas, the Mgoun River from the town of Aifar in the thrust front to Aït Toumert in the wedge-top basin. Ephemeral tributaries are marked in white and the perennial trunk streams in blue. Terraces are marked in black. Map and cross section modified from Carte Géologique du Maroc (1975); Tesón and Teixell (2008); Tesón et al. (2010). See table 3.1 for details of lithologies and their rock strength. Cross sections of lines A-A', B-B' and C-C' in Fig. 3.5.

The Mgoun River emerges from the gorge into the structurally complex ENE-WSW striking southward verging folded and oblique thrust-faulted sequence of Mesozoic and Cenozoic lithologies (Fig. 3.2). The first valley contains a relatively confined flood plain (~150 to 375 m wide), running along strike through weak Eocene red beds, constrained by a valley wall of Mio-Pliocene conglomerates to the north and Eocene limestones to the south (Fig. 3.2d).

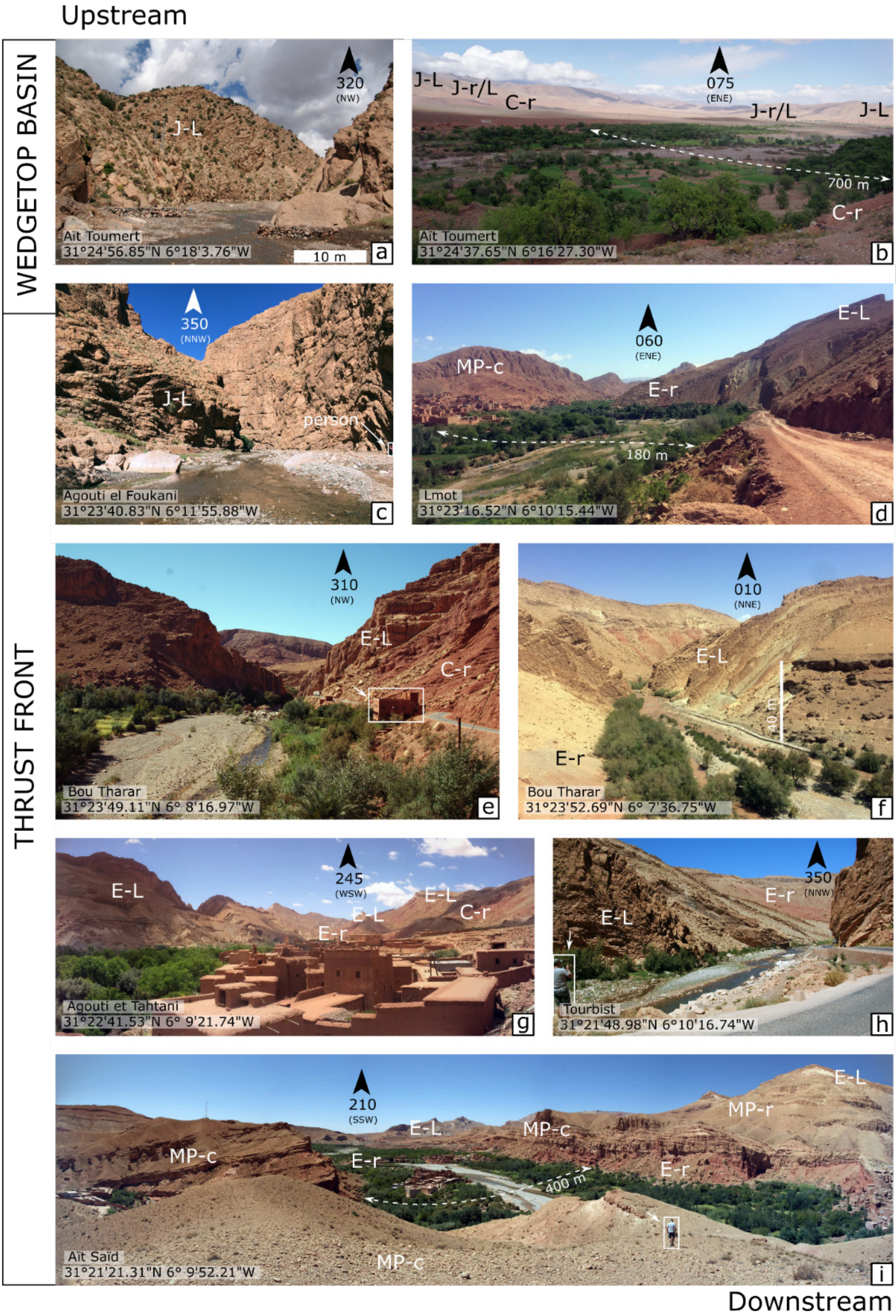
Upstream
WEDGETOP BASIN
THRUST FRONT
320
(NW)
J-L
Aït Toumert
31°24'56.85"N 6°18'3.76"W
10 m
a
J-L
J-r/L
C-r
075
(ENE)
J-r/L
J-L
700 m
C-r
Aït Toumert
31°24'37.65"N 6°16'27.30"W
b
350
(NNW)
J-L
person
Agouti el Foukani
31°23'40.83"N 6°11'55.88"W
c
060
(ENE)
E-L
MP-c
E-r
180 m
Lmot
31°23'16.52"N 6°10'15.44"W
d
310
(NW)
E-L
C-r
Bou Tharar
31°23'49.11"N 6° 8'16.97"W
e
010
(NNE)
E-L
40 m
E-r
Bou Tharar
31°23'52.69"N 6° 7'36.75"W
f
245
(WSW)
E-L
E-L
E-L
C-r
E-r
Agouti et Tahtani
31°22'41.53"N 6° 9'21.74"W
g
350
(NNW)
E-r
E-L
Tourbist
31°21'48.98"N 6°10'16.74"W
h
210
(SSW)
E-L
E-L
MP-c
MP-r
MP-c
E-r
400 m
E-r
Aït Saïd
31°21'21.31"N 6° 9'52.21"W
MP-c
i
Downstream

Figure 3.2 – Bedrock geology and geomorphology of the study area, with photos ordered from the uppermost gorge near Aït Toumert in the wedge-top basin, to the most downstream reach in the thrust front up until Aifar. Town names refer to those in Fig. 3.1. The perennial river trunk flows through at least four valleys formed in weak red beds, separated by confined gorges made from limestone bedrock. (a) Gorge in strong Jurassic Limestone. (b) Open valley form of the wedge-top basin in the weak Cretaceous red beds bounded on either side by Jurassic strong limestone and mixed-strong limestones and marls. (c) Gorge in strong Jurassic limestone. (d) Confined valley in weak Eocene red beds bounded by strong Mio-Pliocene conglomerates and Eocene Limestones. (e,f) Gorge in strong Eocene limestones opening up into a confined valley in weak Eocene red beds. (g) Confined valley formed in weak Eocene red beds and bounded by strong Eocene limestones interbedded with weak Cretaceous red beds. (h) River flowing from a confined valley in Eocene red beds into a gorge in strong Eocene limestones. (j) Confined to open valley in weak Eocene red beds bounded by strong Mio-Pliocene conglomerates, weak Mio-Pliocene red beds, and strong Eocene limestones. See table 3.1 for details of lithologies and rock strength.

Through a short gorge cutting through Eocene limestone the river joins the Bou Tharar valley (150 to 650 m wide; Fig. 3.2e), where the second pernennial trunk stream of the Mgoun catchment joins through a similar gorge (Fig. 3.2f) to join in a confluence (Fig. 3.1). The valley runs along-strike through weak Eocene red beds and is confined by high Eocene limestone cliffs either side (Fig. 3.2g). Through another straight gorge cut into Eocene limestones (Fig. 3.2h) the river enters the Ait Saïd Valley contained by more widely spaced Eocene limestone thrust stacks (~ 2 km apart) through which the river cuts an oblique transverse route (Fig. 3.2i). Mio-Pliocene conglomerates line the northern side of the valley, and the valley floor (~ 250 to 750 m wide) incises through weak Eocene red beds.

The Mgoun emerges through a short gorge at the end of the thrust-front passing southwards into the Ouarzazate foreland basin, eventually joining the Dades River 20 km downstream from the mountain front (Fig. 3.1). In this part of the basin, Plio-Quaternary terrestrial fluvial distributary fan conglomerates form a top surface ~ 100 m above the Mgoun River valley. Further west in the central and western parts of the basin, this surface is

Table 3.1 - Lithostratigraphic packages labelled in Figure 3.1 and 3.2, with details of lithologies and rock strength

Formation	Lithologies	N	Schmidt hammer value (mean, stdev)	UCS in MPa (mean, stdev)	Strength*
Pliocene conglomerates (P-c)	Continental fluvial conglomerates	50	33, 9	22, 6	Erodible
Mio-Pliocene red beds (MP-r)	Continental fluvial sandstone and siltstone	10	27, 7	14, 4	Very erodible
Mio-Pliocene conglomerate (MP-c)	Continental fluvial and fan conglomerate	-	-	-	Erodible**
Eocene red beds (E-r)	Continental and marine marl	47	22, 15	10, 7	Very erodible
Eocene limestone (E-L)	Marine limestone	64	41, 12	39, 11	Moderately resistant
Cretaceous red marls (C-r)	Continental red sandstone, shale, and gypsum	70	26, 13	14, 7	Very erodible
Jurassic limestones and marls (J-r/L)	Continental and marginal marine silts, marls, sandstone, and limestone	60	43, 16	45, 17	Moderately resistant
Jurassic Limestones (J-L)	Massive marine platform limestone	90	53, 11	90, 18	Resistant

*as defined by classifications in Table 2.2; **similar to P-c

incised and extensively covered by inset fan and terrace surfaces (Arboleya et al., 2008; Pastor et al., 2012a) resulting in more relief (1100 - 1600 m).

3.3 METHODS

3.3.1 *Rock strength measurements*

To quantify the rock strength of lithostratigraphic units affecting valley morphology and terrace occurrence, I use published geological maps and *in situ* measurements of compressive strength. Typically, ten to twenty Schmidt hammer measurements (Goudie, 2006) were taken at each location, totalling 434 readings throughout the study area with up to 90 readings per geological unit (Table 3.1). The standard deviation of Schmidt hammer measurements reflect the variation of rock strengths within the lithological units (Table 3.1). Mean and standard deviation of Schmidt hammer rebound values (SHV) are then converted to estimates of uniaxial compressive strength using the conversion which was derived by Katz et al. (2000) ($UCS = 2.21e^{(0.07\ SHV)}$) for a range of carbonates, sandstone and other rocks with a range of UCS values similar to those found in the study area.

3.3.2 *Terrace stratigraphy and sedimentology*

Strath terraces along the Mgoun River were mapped from the town of Aït Toumert in the WTB (Fig. 3.1) downstream to the confluence with the neighbouring Dades River using remote topographic analysis. In addition, field observation and measurements from Aït Toumert upstream in the WTB down to Aifar at the end of the TF (Fig. 3.1) supplemented digital topographic analysis. Strath terraces were identified using standard morphological and geological criteria such as flat surfaces, bedrock strath surfaces, rounded and imbricated clasts (Fig. 3.3a; Stokes et al., 2012; Mather et al., 2017) and where slope material covered the top of fluvial conglomerates this contact was identified using differences in sediment textures and fabrics (Mather et al., 2017). Topographic analysis of the 12 m per pixel TanDEM-X supplied by the German Aerospace Centre (https://tandemx-science.dlr.de/) helped to map flat-lying bedrock strath and terrace top surfaces in the catchment next to the trunk river. Surfaces with slopes of less than 5° were used to map the terrace top surfaces, which were subsequently targeted for field investigation (Fig. 3.1). Where possible, the height above the active channel of both the strath surface and the top surface of the overlying fluvial sediments was recorded in the field using a Trupulse 360B laser range finder and Geo-X7 GPS. Using these field measurements terrace stratigraphy was constructed for three

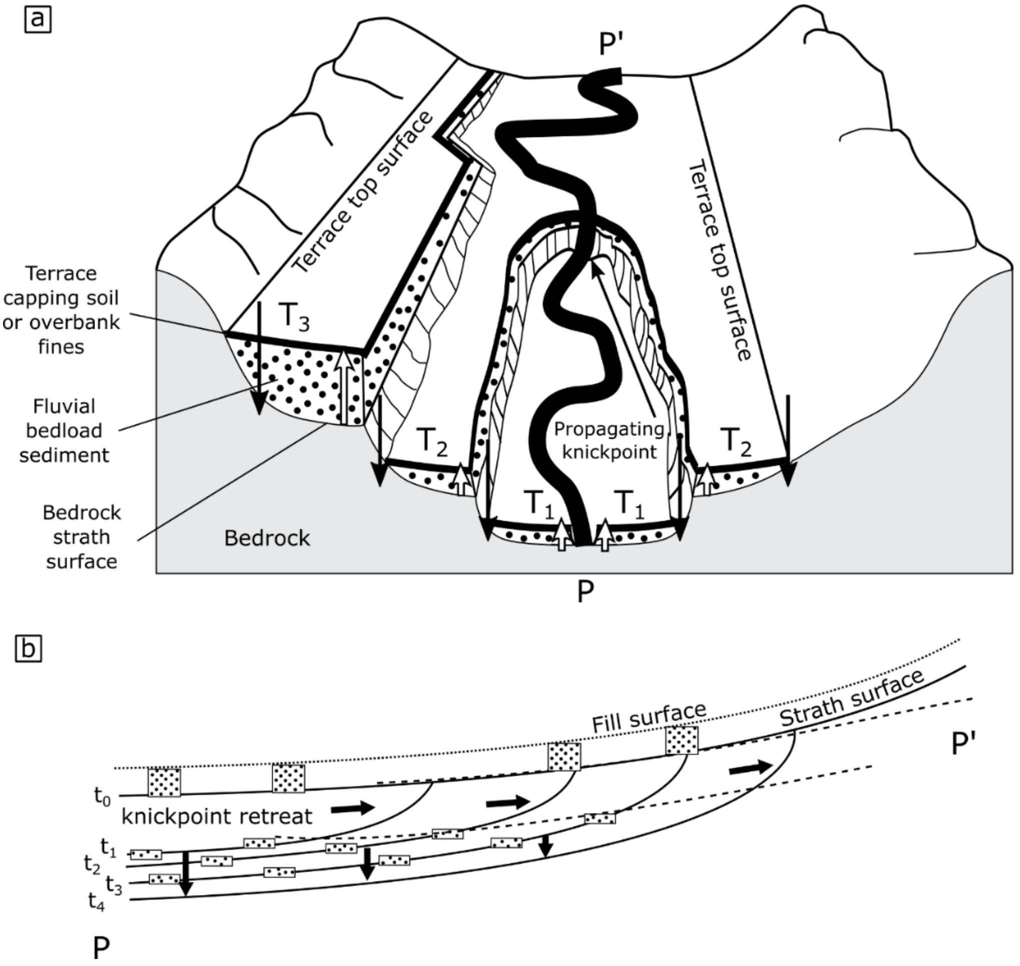

Figure 3.3 – Components of strath terraces and terrace treads in bedrock-alluvial rivers. (a) Conceptual overview of terrace creation through knickpoint propagation. Strath terraces have several distinctive features, including the bedrock strath surface, fluvial bedload sediment and the terrace capping soils and/or fine overbank sediments. Terraces form sequences by progressive incision and planation in bedrock followed by fill episodes to create strath terraces. After Finnegan (2013) and Lewin and Gibbard (2010). (b) Sketch of river incision and terrace treads associated with knickpoint propagation, showing simplified parallel terrace tread interpretations can lead to inaccurate incision histories of the river. Where terrace deposits are thick enough the strath tread and fill tread can be distinguished on river long profiles. After Demoulin et al. (2017).

reaches separated by gorges, aided by topographic profiles extracted from the DEM (Fig. 3.1). A letter and numbering system names terraces with T1 the lowest and youngest strath terrace, with subsequent higher straths corresponding to T2 and T3 etc. A combination of terrace strath and fill-top heights extracted from the DEM and measured in the field, together with the modern river long profile, was used to compare terrace positions along the length of the modern river (Fig. 3.3b). Based on evaluation of available DEMs to extract hydrological networks in mountainous terrain (Boulton and Stokes, 2018), the ALOS world AW3D (Tadono et al., 2014) 30 m digital elevation model (DEM) was used to derive the river long profile. Terrace-top heights above the river profile were extracted from the DEM at 10 m intervals along the inner valley terrace margins (closest to the modern river) and verified using field data. Prominent terraces with accessible and well-preserved sections from strath to fluvial top were targeted for OSL sampling (Ch. 4) and were described and logged using sediment facies analysis (Miall, 1978) to enable the interpretation of depositional environments. For each terrace and modern riverbed locality, I measured clast imbrication of 100 clasts over an area of 1 m^2 to constrain downstream flow direction. For more detail on Wolman point counts of clasts see the section below.

3.3.3 *Grain size and clast lithology*

The coarse sediment fraction in terraces and the modern channel may be derived from bedrock sources in the FTB upstream of the study reach, notably Triassic red sandstone, Triassic igneous rocks, and Jurassic grey limestone, together with local sources of Eocene limestone and Pliocene and Mio-Pliocene conglomerates in the TF containing a range of these lithologies (Tesón and Teixell, 2008; Tesón et al., 2010). To constrain sediment provenance and transport dynamics within the catchment I measured the grain size distribution and lithologies of clasts in terraces and the modern river channel by Wolman point counting (Wolman, 1954; Attal and Lavé, 2006; Whittaker et al., 2010; Whittaker et al., 2011), recording clast lithology for each grain size measurement (100 per count, Brozovic and Burbank, 2000; Dubille and Lavé, 2015; Quick et al., 2019). Because many sediment sections present time-averaged stratigraphy, I collected grain size from the full vertical extent of individual conglomerate deposits – usually 2 to 3 m – which allows for the effects of individual flows and high-frequency variations in deposition rates to be averaged out. High-flow channel bars were selected for measurements in the modern channel, as these are assumed to represent the deposition reflected in the terrace deposits. For each count, the long axes (the *a* axis) of 100 clasts measuring > 1 mm in diameter were recorded over an area of 1 m^2 to estimate the median grain size value, D_{50}, and the 84th and 96th percentiles, the D_{84} and D_{96} respectively. Clasts were selected randomly (Duller et al., 2010; Whittaker et al., 2011). Estimated sampling error for grain-size measurements are ±15%, similar to those in Whittaker et al. (2011) and Dingle et al. (2016). Downstream fining rates along the length of the surveyed river were calculated using Sternberg's exponential function:

$$D_x = D_0 e^{-ax} \qquad \text{Eq. 6}$$

Where D_0 is the predicted input or initial characteristic grain size, a is the downstream fining exponent and x is the distance downstream (Sternberg, 1875). The selective transport of particles and their abrasion control downstream fining rates in fluvial systems (Paola et al., 1992; Ferguson et al., 1996; Rice and Church, 2001; Attal and Lavé, 2006; Fedele and Paola, 2007; Duller et al., 2010). On the other hand, lateral input and recycling of sediment within valleys can disturb such fining trends (Rice and Church, 2001; Dingle et al., 2016; Quick et al., 2019).

3.4 RESULTS

3.4.1 *Strath terrace stratigraphy*

River strath terraces occur in three reaches flowing through weak bedrock (10 to 14 Mpa; Fig. 3.1; Table 3.1) separated by gorges formed in strong limestone bedrock (39 to 99 Mpa; Fig. 3.1 and Table 3.1). These reaches stretch from the upstream Ait Toumert reach in the WTB, to the midstream Bou Tharar reach and downstream Ait Said reach in the TF (Fig. 3.1). The occurrence of strath terraces coincides with the open valley forms in very erodible rock types, namely the Eocene red continental marls in the thrust front and Cretaceous red marls in the wedge-top basin (10 to 14 Mpa; Figs. 3.1 – 3.5 and Table 3.1). As terrace levels from reach to reach are not clearly correlated by height above the modern river plain, I define terrace stratigraphy in each reach.

Along the NW-SE axial channel of the Ait Toumert reach in the WTB four terrace levels can be identified (Figs. 3.4a, 3.5a). Each has a planation surface up to several hundred meters wide, topped with fluvial gravels. A staircase reaches up to 60 m above the modern river plain, in steps of four approximately evenly spaced surfaces down to the modern river channel. The isolated T2 opposite of the staircase has a well-preserved section which is targeted for OSL dating, with a strath surface ~ 14 m above the modern river plain.

In the midstream Bou Tharar reach three strath levels are preserved including the highest documented strath terrace in the study area at ~100 m above the modern river plain (T3, Figs. 3.4b, 3.5b). T2 has a bedrock strath ~20 m from the modern river plain covered by a ~10 m thick deposit. T1 is the bedrock strath level of T2 stripped of sediment (e.g. Baynes et al., 2018). Further downstream in the thrust front, along the Ait Saïd reach, three terrace levels

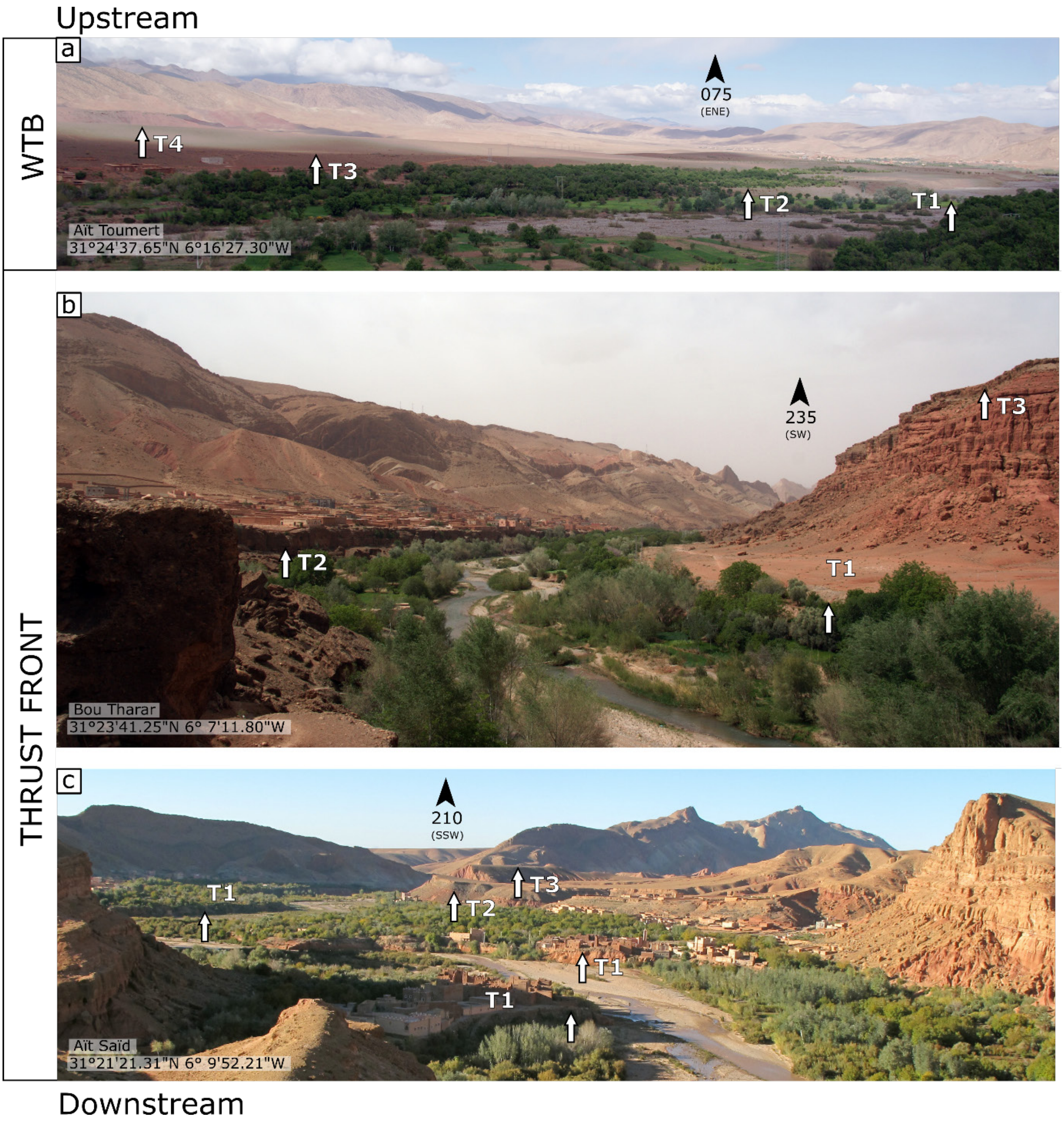

Figure 3.4– River strath terraces in three reaches of the Mgoun River, from upstream to downstream. Town names refer to those in Fig. 3.1. Photos facing downstream direction. (a) Wide top surfaces of gravel-topped strath terraces in the wedge-top basin (cross-section in Fig. 3.6a). (b) Continuous strath terrace topped by ~10 m of gravel on one side of the river (T2) with a strath surface (T1) and the highest-level strath terrace documented, topped with gravel (T3) on the other side (Fig. 3.6b). (c) high-elevation strath terrace topped with ~10 m of gravels (T2) and lower strath terraces underneath (T1) (Fig. 3.6c).

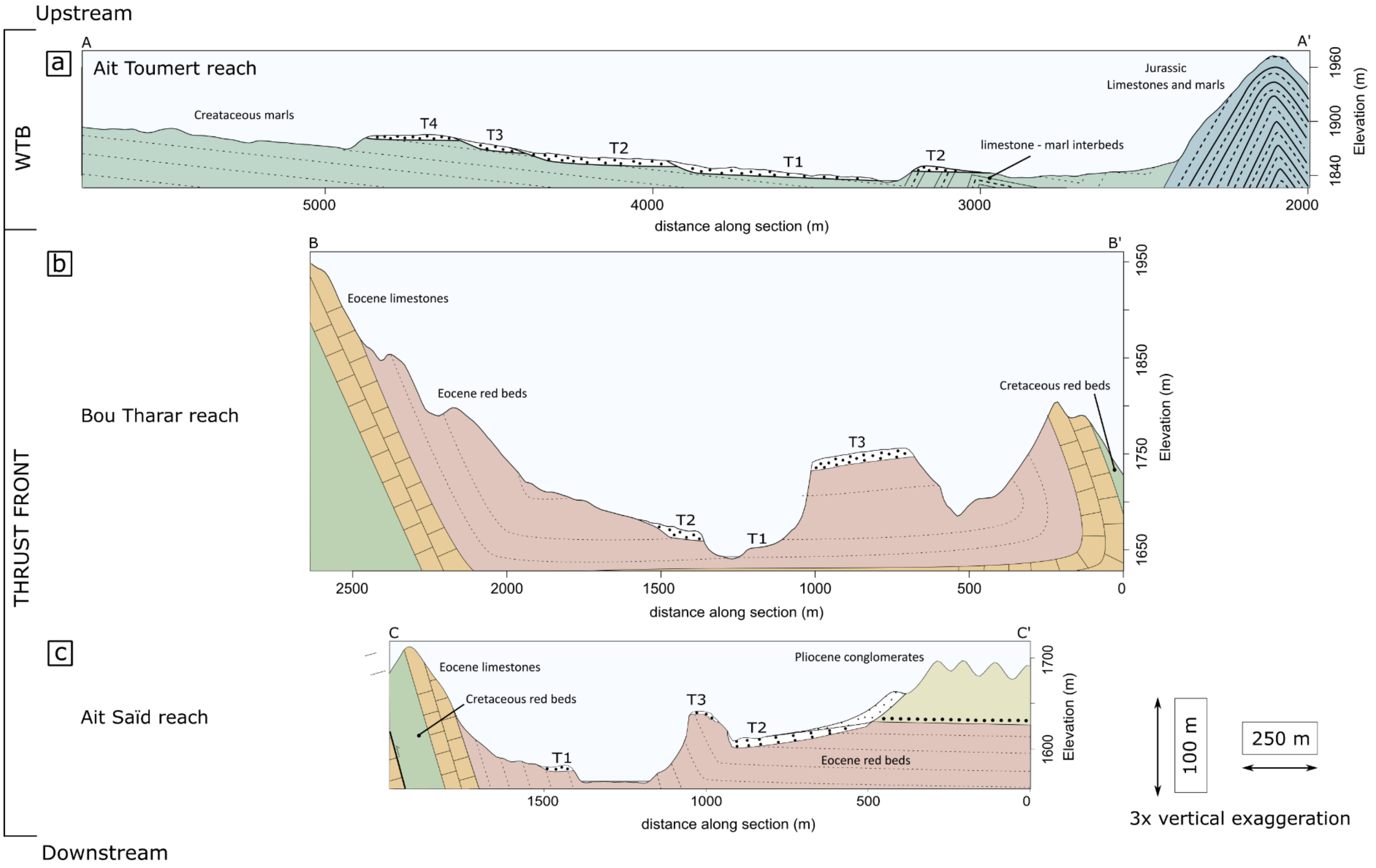
Upstream
WTB
THRUST FRONT
Downstream
A
A'
a
Ait Toumert reach
Createaceous marls
T4
T3
T2
T1
T2
limestone - marl interbeds
Jurassic
Limestones and marls
5000
4000
3000
2000
distance along section (m)
1960
1900
1840
Elevation (m)
B
B'
b
Bou Tharar reach
Eocene limestones
Eocene red beds
T3
T2
T1
Cretaceous red beds
2500
2000
1500
1000
500
0
distance along section (m)
1950
1850
1750
1650
Elevation (m)
C
C'
c
Ait Saïd reach
Eocene limestones
Cretaceous red beds
T1
T3
T2
Pliocene conglomerates
Eocene red beds
1500
1000
500
0
distance along section (m)
1700
1600
Elevation (m)
100 m
250 m
3x vertical exaggeration

Figure 3.5 - Valley cross-sections of the three river reaches with strath terraces (Fig. 3.3). Sections facing downstream direction. Cross-section lines are displayed on Fig. 3.1. (a) Staircase of strath terraces > 1km wide in the wedge-top basin, overlying weak cretaceous marls dipping in the direction of the modern river. T2 on the other bank is perched on locally mixed-strong bedrock. (b) Bou Tharar reach in the high relief thrust front with unpaired strath terraces on weak Eocene red beds, with valley walls consisting of strong Eocene limestones. The highest documented terrace is isolated from the rest of the valley by gullies and the modern river channel. (c) Valley of the Ait Saïd reach in the downstream extent of the thrust front with two strath levels, including a wide strath terrace T2 in weak Eocene red beds bordered by Pliocene conglomerates. Slope material from the Pliocene conglomerates lap onto the fluvial gravels of T2.

are found (Figs. 3.4c, 3.5c). T1 is found directly next to the modern river plain throughout the valley with a strath ~10 m elevated from the valley, with a 3 to 5 m deposit. T2 and T3 are preserved as extensive surfaces incised by gullies with bedrock straths at elevations of 40 and 60 m above the modern river plain respectively with up to 10 m thick deposits. Terraces are preserved up to the highest elevation of the weakest unit in the valley (Fig. 3.5).

3.4.2 *River long profile and terrace treads*

A combination of the valley cross-sections established from field and DEM analyses (Fig. 3.5), and a plot of terrace elevation above the contemporary river long-profile allows for correlation of terrace treads (Figs. 3.3, 3.6a). Terrace treads exhibit two distinct patterns, one in the thrust front and the other in the wedge-top basin (Fig. 3.6a). The most continuous terrace tread found in the thrust front is T2, which exhibits the thickest sedimentary cover, and which is incised to form strath terraces in the downstream Ait Said and midstream Bou Tharar reaches of the thrust front, ending against a knickpoint in the gorge leading up to the third Lmot reach in the thrust front. There, the top of the terrace fill surface has been incised, but this has not yet transitioned into bedrock incision of the T2 strath. In the downstream Ait Saïd reach, T1 forms a strath tread which merges with the strath tread of T2 in the midstream Bou Tharar reach (Fig. 3.5b-c). Incision and abandonment

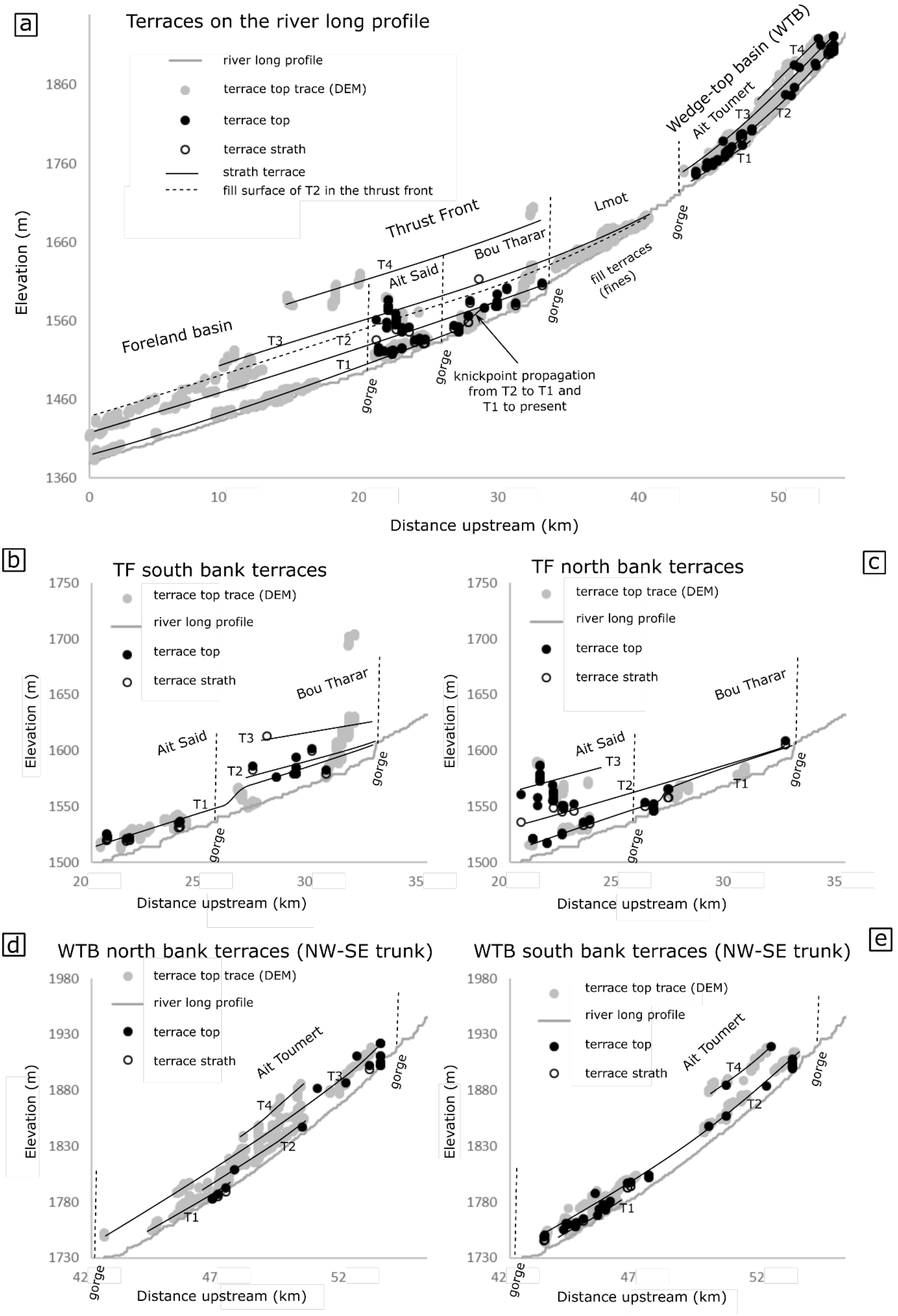
a
Terraces on the river long profile
river long profile
terrace top trace (DEM)
terrace top
terrace strath
strath terrace
fill surface of T2 in the thrust front
Elevation (m)
1360
1460
1560
1660
1760
1860
Distance upstream (km)
0
10
20
30
40
50
Foreland basin
Thrust Front
Wedge-top basin (WTB)
Ait Said
Bou Tharar
Lmot
Ait Toumert
T1
T2
T3
T4
gorge
fill terraces (fines)
knickpoint propagation from T2 to T1 and T1 to present
b
TF south bank terraces
c
TF north bank terraces
terrace top trace (DEM)
river long profile
terrace top
terrace strath
Elevation (m)
1500
1550
1600
1650
1700
1750
Distance upstream (km)
20
25
30
35
Ait Said
Bou Tharar
T1
T2
T3
gorge
d
WTB north bank terraces (NW-SE trunk)
e
WTB south bank terraces (NW-SE trunk)
Elevation (m)
1730
1780
1830
1880
1930
1980
Distance upstream (km)
42
47
52
Ait Toumert
T1
T2
T3
T4
gorge

Figure 3.6 – River long profiles with terrace surface top elevations from the DEM, and field measured heights of the strath surface and terrace sediment top surface. Treads of strath terraces and the T2 fill surface are marked. (a) The river long profile and terrace elevations from the foreland basin to the thrust front and the wedge-top basin. River gorges are marked. (b-c) River long profile with south bank (b) and north bank (c) terraces of the thrust front. (d-e) River long profile with north bank (b) and south bank (c) terraces of the wedge-top basin.

of this tread led to the modern river profile. T3 is the highest strath level preserved in the thrust front, and the tread projects against the most upstream, and widest, gorge of the study area near Agouti el Foukani downstream of the WTB. In the WTB, terrace treads T1 to T4 form parallel treads, with T2 a paired continuous terrace tread through the Ait Toumert reach, while T1 occurs only downstream and T4 upstream, and the unpaired T3 only on the left bank (Fig. 3.5c-d). Although all terraces in the TF are paired, preservation along stream is less consistent than in the WTB, with T1 present on both banks throughout the thrust front, whilst T2 and T3 are locally only preserved on either bank. Treads continue from the thrust front into the downstream foreland basin, where the paired terrace treads are parallel and continuous over the entire surveyed distance (~ 20 km).

3.4.3 *Terrace sedimentology*

Sediments overlying strath surfaces in the Mgoun catchment are characterised by a variety of conglomerates, sandstones, and mudstones collectively up to 10 m in thickness. I adopt a system of lithofacies classification from Miall (1996) and define seven genetic facies (Table 3.2) which make up three architectural elements (Table 3.3, Fig. 3.7; Miall, 1985). Differences in terrace facies are dominated by along stream, longitudinal variation, rather than vertical stratigraphic relationships of terrace levels, which is why the following sections describe the terrace facies as well as quantitative grain size and clast lithological data per reach (Fig. 3.8), to constrain the depositional environments along stream.

Table 3.2– Lithofacies and sedimentary structures of strath terrace deposits after Table 4.1 in Miall (1996). Detailed descriptions and interpretation are in the Appendix

Facies	Lithofacies	Sedimentary structures	Interpretation
Gci	Poorly-sorted, clast-supported pebble to boulder conglomerate, sub-angular to sub-rounded, disc-shaped to spherical clasts.	Inverse grading, clast imbrication	Clast-rich debris flow (high strength), or pseudoplastic debris flow (low strength), Hyperconcentrated flow
Gcm	Moderately well-sorted, clast to matrix-supported pebble-cobble conglomerate, sub-angular to well-rounded clasts, moderately well-sorted silt-sand matrix.	Massive	Pseudoplastic debris flow (inertial bedload, turbulent flow)
Gcg	Moderately poorly-sorted, clast-supported pebble-cobble conglomerate with sub-angular to well-rounded spherical to discoidal clasts. Poorly-sorted red mud-granule-sized matrix.	Weak horizontal bedding, clast imbrication, normal grading	Transverse bedforms or channel fill
Gh	Moderately well-sorted, tightly-packed, clast-supported pebble-cobble conglomerate, very well rounded clasts. Poorly-sorted mud-granule-sized matrix.	Weak horizontal bedding, clast imbrication, grain size changes abrupt and not systematic.	Gravel sheets, lag deposits and sieve deposits. Sustained reworking and low ratio of water depth to mean clast size
Gt	Clast-supported, moderately well-sorted, pebble-cobble conglomerate	Trough-stratification, clast imbrication, lenticular bodies with erosional bases	Minor channel fills
Gp	Clast-supported, moderately well-sorted, pebble-cobble conglomerate	Meter-scale planar cross beds, dipping 10° - 20° parallel to the modern flow direction,	Transverse bedforms
Fl	Red to tan-coloured sand, silt, mud	Fine lamination	Overbank, abandoned channel, or waning flood deposit

Table 3.3– Architectural elements in terrace deposits after Table 4.3 in Miall (1996)

Element	Symbol	Facies assemblage	Geometry and relationships	Interpretation
Stratified conglomerates	GB	Gcg, Gh, Gp, Gt	Bases of 2-10 m tabular bodies are sharp and erosional, laterally extensive over the extent of exposed terraces, up to 3 km in width along stream and 300 m width perpendicular to the river channel. Planar bedded conglomerates (Gp) occur as 1 to 2 m thick deposits with erosional bases directly on top of bedrock strath surfaces which transition into facies Gh. Lenticular bodies of Gt with erosional bases interbedded with Gh range from 0.3 to 1 m in thickness and typically extend 2 to 10 m laterally (Fig. 3.7a).	Braided fluvial channel gravel bars and bedforms
Inversely graded and massive conglomerates	SG	Gci, Gcm	Bases of these 1-2 m thick sequences are erosional. Lobe-shaped bodies are laterally extensive over a maximum of ~ 150 m. Facies Gcm is interbedded with facies Sh. Gcm is also found draping the hillslope and FF.	Sediment gravity flows in alluvial/tributary fans and/or slope colluvial systems
Sand-mudstone sheets	FF	Fl	1 - 2 m thick blankets which can be traced laterally for hundreds of metres in large outcrops, interbedded with GB and SG. The basal contacts of Fl units are gradational and non-erosional. Facies Fl is observed as overbank deposits in the modern river plain in the most downstream valley in the thrust front (Fig. 3.8b).	Floodplain deposits

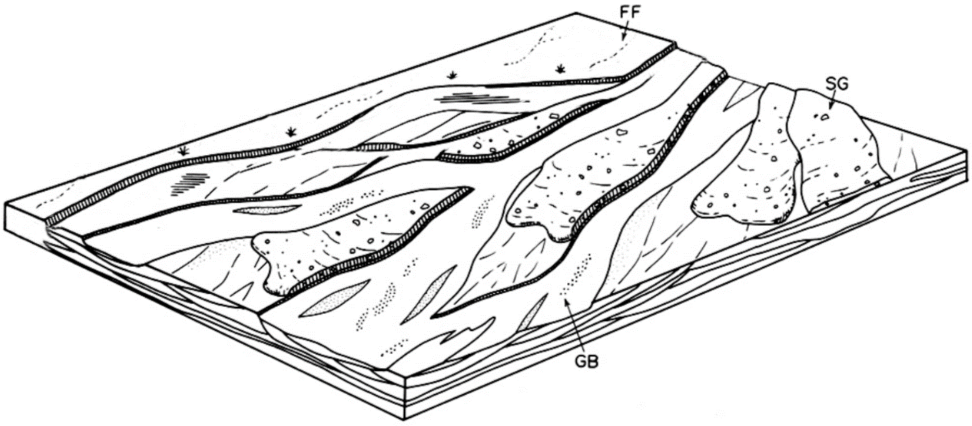

Figure 3.7– Block diagram of a braided fluvial model with the architectural elements from Table 3.3, including influence from a proximal alluvial fan with sediment gravity flow lobes. Modified from (Miall, 1985). GB: Gravel bars and bedforms; SG: Sediment gravity flows; FF: Floodplain deposits.

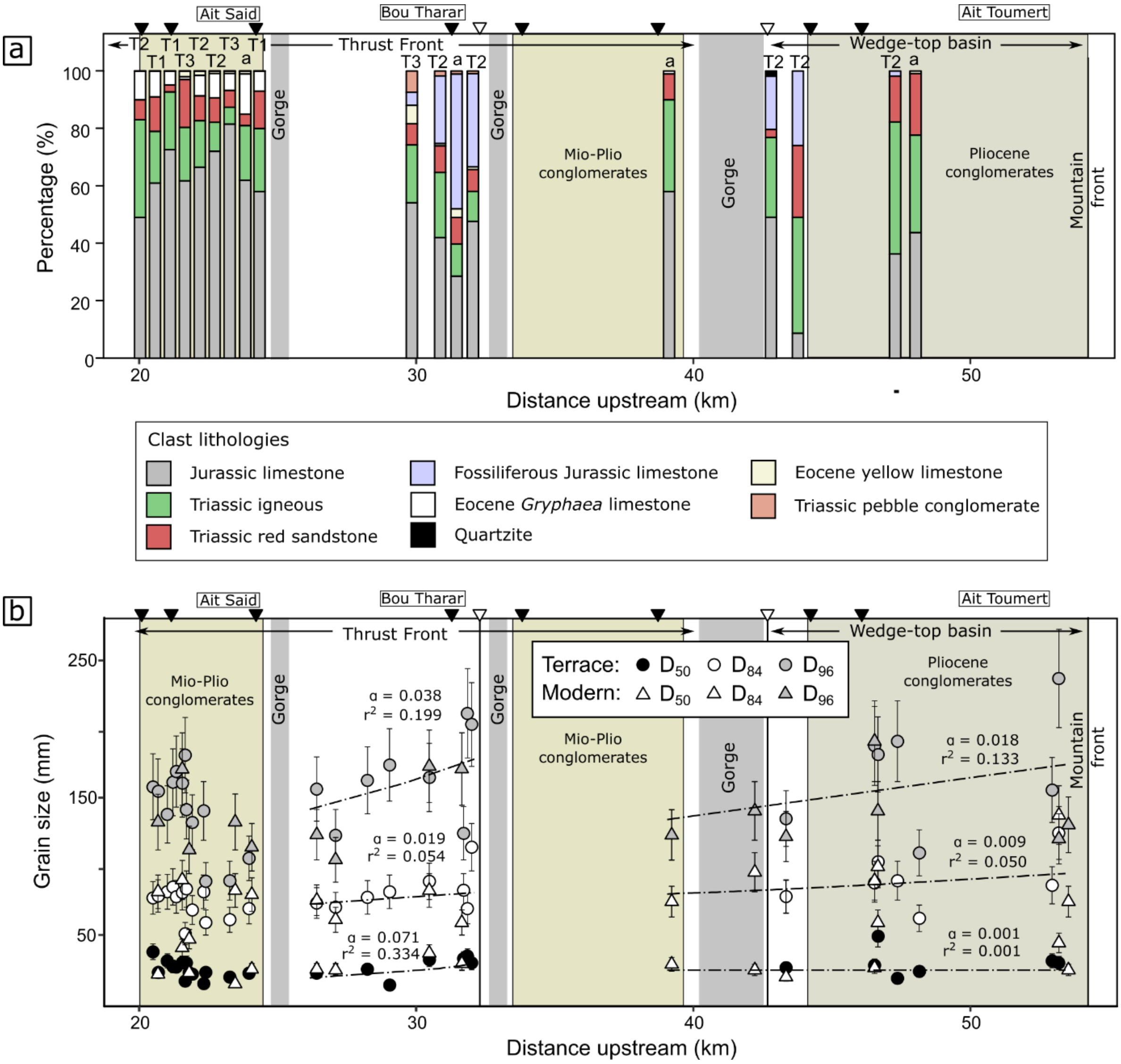

Figure 3.8 – Grain size and lithology data along the Mgoun River. (a) Bar plots of the lithological contribution to river terrace gravels and modern river bars (locations with an '*a*'). (b) Wolman point count results for each terrace and modern-river location, along the length of the surveyed trunk stream. The fining exponents from exponential fits (Eq. 8) are given together with the r-squared values. River channel confluences are marked as open triangles and ephemeral tributaries are marked as black triangles.

The upstream Ait Toumert reach (WTB)

A lateral cross-section through the stratigraphy of strath terraces and their sediments records the sequence of incision and aggradation events and their relative magnitudes experienced at its point along the river channel, as well as the sedimentary facies which characterise the process of sediment flux in the river channel (Fig. 3.9a). In the wedge-top basin, the only facies data available is of T2. Sediment facies of terrace deposits in the wedge-top basin vary along stream (Fig. 3.9a). T1 is frequently overtopped by floods and thus is often heavily used for agriculture and thus does not preserve the original terrace deposits, whilst T3 and T4 are limited spatially and similarly do not exhibit well-preserved sections through their deposits. The T2 deposits of the wedge-top basin rest on bedrock of marls and limestones and are characterised by 3 to 4 m of either gravel bedform or sediment gravity flow and floodplain facies (Table 3.3; Fig. 3.9). Four well-preserved T2 deposits that were logged and targeted for geochronological sample collection (Ch. 4) are shown in Fig. 3.9. Along the NW-SE Ait Toumert reach, the most upstream preserved outcrop of T2 is composed of 3 m of clast-supported weakly bedded conglomerates, clasts are sub-rounded to well-rounded and imbricated, assembled in 2-3 clast thick layers (Gh in Fig. 3.9b and Table 3.3). Palaeoflow directions from clast imbrication are downstream along the perennial axial river direction (Fig. 3.9a). Clast lithologies are similar to the modern perennial river channel, dominated by a trio of ~ 25% to 45% Jurassic limestone, 35% to 45% Triassic igneous and 15% to 20% red Triassic sandstone (Figs. 3.8a; 3.9b). These clast lithologies are present throughout the whole catchment

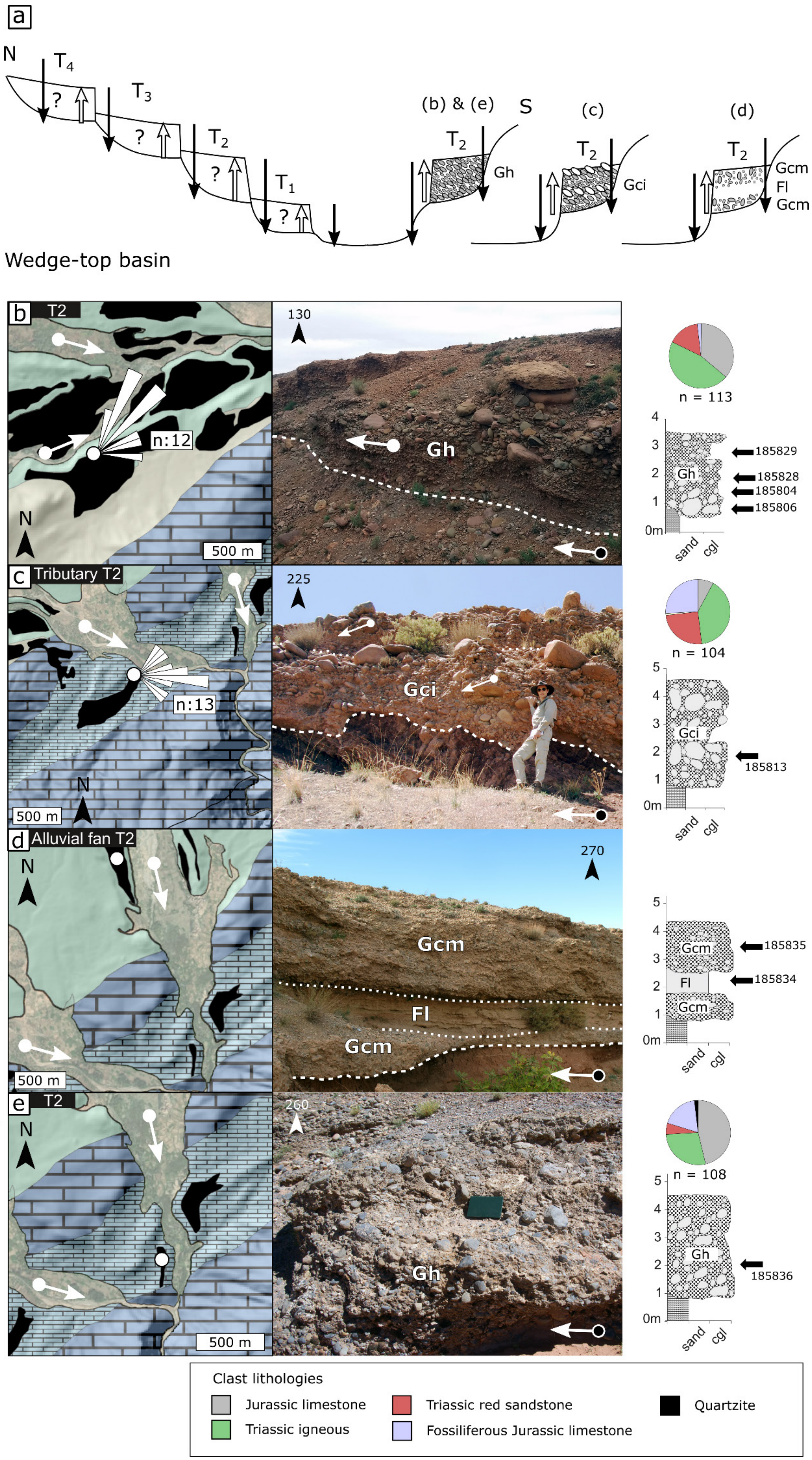
a
N
T_4
T_3
T_2
T_1
?
(b) & (e)
S
(c)
(d)
Gh
Gci
Gcm
Fl
Gcm
Wedge-top basin
b
T2
n:12
N
500 m
130
Gh
n = 113
185829
185828
185804
185806
0m
sand
cgl
c
Tributary T2
n:13
N
500 m
225
Gci
n = 104
185813
d
Alluvial fan T2
N
500 m
270
Gcm
Fl
Gcm
185835
185834
e
T2
N
500 m
260
Gh
n = 108
185836
Ait Toumert reach
N-S perennail tributary
Clast lithologies
Jurassic limestone
Triassic igneous
Triassic red sandstone
Fossiliferous Jurassic limestone
Quartzite

Figure 3.9– Terrace sedimentology of the upstream wedge-top basin including the Ait Toumert reach (b-c) and a major perennial N-S tributary (d-e). (a) Sketch stratigraphy and sedimentology which record a sequence of incision and aggradation events and their relative magnitudes. Not to scale. Only T2 facies were observable, and these vary along stream. (b-e) Maps are insets from Fig. 3.1, which includes terrace surfaces in black, geology in colour and satellite imagery of the modern floodplain. Logs of terraces show the location of samples taken for dating in chapter 4. (b) T2 with a 3 m deposit of bedform conglomerates (Gh). Clast imbrication is towards the axial perennial flow direction. (c) T2 created by a tributary channel cut-off. The photo shows the section at where the perennial channel floodplain has cut into the terrace. Clast imbrication is towards and along the axial perennial river channel direction. The inversely graded conglomerate (Gci) records sediment gravity flows from the ephemeral tributary into the axial river floodplain. (d) T2 in a lobe-shaped alluvial fan deposit next to a wide floodplain, characterised by massive clast to matrix supported conglomerate (Gcm) interbedded with tan-coloured sand and mud (Fl). (e) T2 downstream from (d) in a constricted valley with a 3 m deposit of bedform conglomerates (Gh).

(Fig. 3.8a). Further downstream along the Ait Toumert reach, an outcrop of T2 is composed of two 2 m sequences of inversely graded clast-supported conglomerates, clasts are sub-angular to sub-rounded with spherical pebbles and cobbles and more disc-shaped boulders which are imbricated (Gci in Fig. 3.9c and Table 3.2). Palaeoflow directions point from the tributary channel into the axial river channel, as well as along the axial river channel direction. Next to the trio of lithologies present in the previous terrace, a fossiliferous Jurassic limestone lithology makes up 26% of clasts (Figs. 3.8b, 3.9c). Along a perennial tributary river channel draining the wedge-top basin N-S which joins the Ait Toumert reach at a confluence, an alluvial lobe-shaped T2 deposit is located next to a ~400 m wide modern floodplain. The 3 m thick deposit is composed of ~1 m of massive clast to matrix-supported conglomerate, clasts are angular to sub-rounded (Gcm in Fig. 3.9d and Table 3.2), followed by ~1 m of finely laminated sand-mud sheets extending at least 15 m along the terrace section (Fl in Fig. 3.9d and Table 3.2), topped by ~2 m of the massive conglomerate (Gcm in Fig. 3.9d and Table 3.2). Further downstream in a constriction of the valley bottom a 3 m thick T2 deposit is composed of clast supported conglomerate; clasts are sub-rounded to well-rounded and imbricated and weak horizontal bedding is hard to

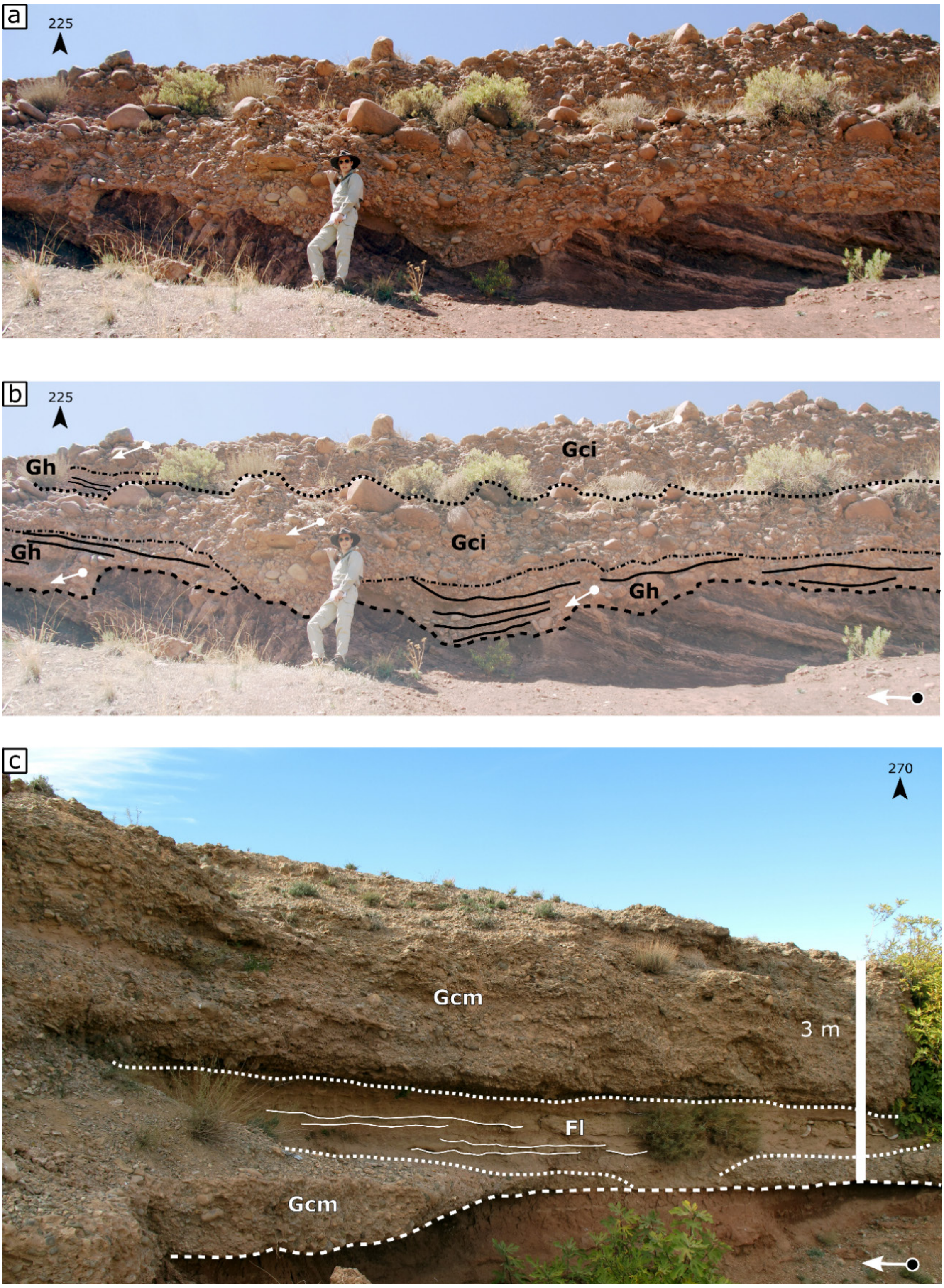
a
225
b
225
Gh
Gci
Gh
Gci
Gh
c
270
Gcm
3 m
Fl
Gcm

Figure 3.10 – Interpreted outcrops of sediment gravity flows on terraces in the upstream Ait Toumert reach in the wedge-top basin. (a-b) uninterpreted and interpreted sedimentary structures of T2 created by a tributary channel cut-off (see Fig. 3.9c). The lower unit contains sheet conglomerates (Gh) flowing obliquely out of the page with surfaces picking out lateral accretion and channel features. On top of these sheet conglomerates inversely graded conglomerate with boulders on top records a sediment gravity flow (Gci). The sequence of fluvial sheet conglomerates and inversely graded conglomerates repeats on top. Clast imbrication is towards and along the axial perennial river channel direction. (c) T2 in a lobe-shaped alluvial fan deposit next to a wide floodplain (see Fig. 3.9d). Massive clast to matrix supported conglomerate (Gcm) is interbedded with laminated tan-coloured sand and mud (Fl) representing debris and/or hyperconcentrated flows interbedded with overbank or waning flow deposits (Fig. 3.7). The general flow direction of the modern river is shown in the bottom-right corner.

observe (Gh in Fig. 3.9e and Table 3.2). Like the tributary terrace (Fig. 3.9c), this terrace deposit contains ~18 % of fossiliferous limestone, but in addition has 2 % quartzite (Fig. 3.8e). Grain size trends are compiled along the Ait Toumert reach from T2 and modern channel deposits. The downstream trend of the median grain size (D_{50}) shows a lack of fining, with a very low fining exponents (Eq. 3.8b) of 0.001 and an r-squared of 0.001. On the other hand, the fining exponents and r-squared values increase for the D_{84} and D_{96}, with fining exponents of 0.009 and 0.133 and r-squared values of 0.050 and 0.018 respectively (Fig. 3.8b).

T2 deposits in the wedge-top basin show evidence of shallow water braided fluvial processes (Figs. 3.9 - 3.10), from the presence of Gh deposits that are interpreted as gravel sheets and lag deposits (Williams and Rust, 1969; Hein and Walker, 1977; Miall, 1977, 1996). In addition, a T2 tributary terrace and an alluvial fan terrace preserve sediment gravity flows, documented by Gci and Gcm deposits (Figs. 3.9 – 3.10) which could be attributed to debris flow (*sensu* Miall, 1996) and/or hyperconcentrated flows (Pierson, 1980; Smith, 1986; Pierson, 2005) occurring in tributary channels and alluvial fans feeding into the fluvial system (Fig. 3.7). The fine sand to mud deposits in the alluvial fan terrace are assigned to overbank flows or waning flow deposits (Fig. 3.7;

Miall, 1996; Wegmann and Pazzaglia, 2002; Pazzaglia, 2013; Stokes et al., 2017). The lateral input from tributaries and alluvial fans is reflected in the clast lithologies of the terraces, with every T2 surveyed displaying a different distribution and presence of lithologies (Fig. 3.8a, 3.9), most noticeably the presence of fossiliferous Jurassic limestone in the downstream T2 deposits along the perennial tributary channel and near its confluence with the Ait Toumert reach (Fig. 3.9c,e) and the presence of quartzites in one T2 deposit along the perennial tributary (Fig. 3.9e). Consequently, the lack of a fining trend in the median grain size (Fig. 3.8b) is attributed to the lateral input and reworking of terrace, alluvial and tributary deposits as well as the Pliocene conglomerate units present in the valley (Figs. 3.1, 3.8). The D_{96} fining trend is interpreted to represent the largest boulders and cobbles being deposited at the upstream edge of the wedge-top basin once the river channel exits the FTB mountain front and enters the open alluviated WTB valley.

The midstream Bou Tharar reach (TF)

T1 in the Bou Tharar reach is characterised by down-stripping of sediment from T2 and preserves only a strath surface. Thus, the Bou Tharar depositional terrace record is dominated by an extensive, 2 km long and up to 100 m wide T2 with a strath surface 20 m above the modern river plain and a T3 ~ 100 m above the modern river plain, 1 km long and 350 m wide (Fig. 3.11a). Both T2 and T3 have well-preserved deposits, consisting solely of well-sorted gravel bar and bedform conglomerates. T2 is composed of a 10 m thick deposit of well-sorted clast support conglomerates; clasts are sub-rounded to well-rounded and imbricated with weak horizontal bedding ~ 2 – 3 clasts thick (Gh in Fig. 3.11b and Table 3.2). Within this succession, Gh is interbedded with planar stratified conglomerates (Gp in Fig. 3.11b and c and Table 3.2), dominant directly on top of the strath surface, and lenticular

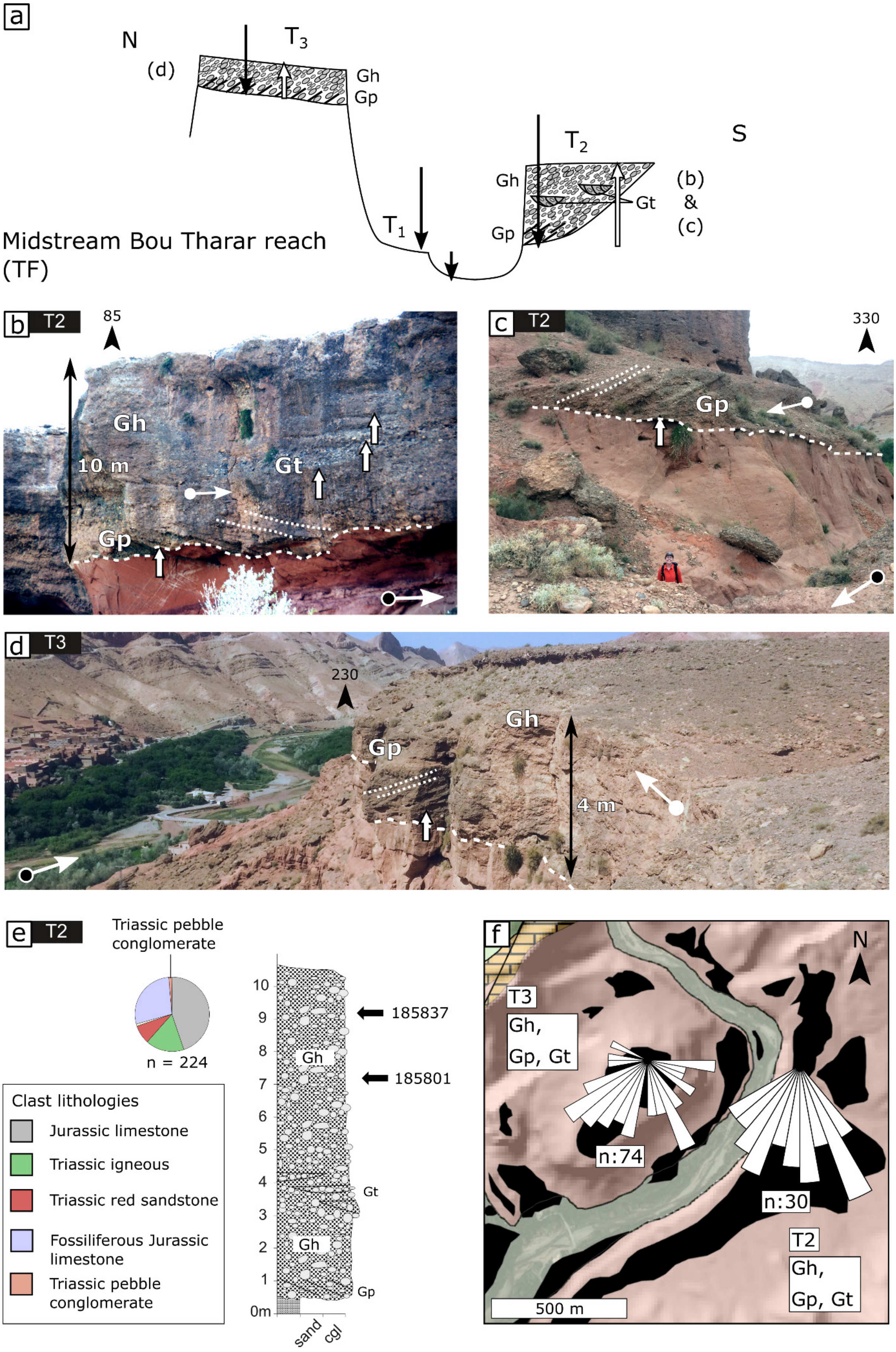
a
N
(d)
T_3
Gh
Gp
T_2
S
Gh
Gt
Gp
(b)
&
(c)
T_1
Midstream Bou Tharar reach
(TF)
b
T2
85
Gh
10 m
Gt
Gp
c
T2
330
Gp
d
T3
230
Gh
Gp
4 m
e
T2
Triassic pebble conglomerate
n = 224
Clast lithologies
Jurassic limestone
Triassic igneous
Triassic red sandstone
Fossiliferous Jurassic limestone
Triassic pebble conglomerate
10
9
8
7
6
5
4
3
2
1
0m
185837
185801
Gh
Gt
Gh
Gp
sand
cgl
f
N
T3
Gh,
Gp, Gt
n:74
n:30
T2
Gh,
Gp, Gt
500 m

Figure 3.11 – Terrace sedimentology of the midstream Bou Tharar reach in the thrust front. (a) Sketch stratigraphy and sedimentology of terraces along the Bou Tharar reach. Not to scale. (b) Section through terrace T2 showing a 10 m thick deposit of bedform conglomerates (Gh) interbedded with trough-stratified minor channel conglomerates (Gt) and planar stratified transverse gravel bar conglomerates (Gp). (c) Erosional contact of terrace T2 directly overlain by planar stratified transverse gravel bar conglomerates (Gp). (d) 4 m thick succession of terrace T3 conglomerates with basal planar stratified transverse gravel bar conglomerates (Gp) and bedform conglomerate (Gh). (e) Graphic log of terrace T2 based on (b) with the location of two samples taken for dating in chapter 4. (f) Map inset from Fig. 3.1 together with palaeoflow directions of terraces T2 and T3.

bodies of trough-stratified conglomerates (Gt in Fig. 3.11b and Table 3.2). In addition to the Jurassic limestone, Triassic igneous and Triassic red sandstone found everywhere in the catchment, gravels, and conglomerate of T2 and the modern river in the Bou Tharar reach contain 29% to 48% fossiliferous Jurassic limestone (Fig. 3.8a). This is also the only reach where the Triassic pebble conglomerate is found, with a low concentration of 1-2% in T2 and the modern river channel (Fig. 3.8a). Positions on a graphic log indicate the position of samples taken for geochronology in Ch. 4 (Fig 3.11e). Palaeoflow directions in T2, located on the outer bend of a bend in the river valley, range within 90° with a dominant direction parallel to the modern river axial flow (Fig. 3.11f). The T3 deposit, similarly to T2, is composed of a ~2 m thick base of planar stratified clast-supported conglomerate; clasts are sub-rounded to well-rounded and imbricated (Gp Fig. 3.11d and Table 3.2), overlain by 2 m of weakly horizontally bedded well-sorted clast-supported conglomerates with imbricated well-rounded clasts (Gh in Fig. 3.11d and Table 3.2). In contrast with T2 and the modern channel deposits, T3 contains only 5% of the fossiliferous limestone, but up to 7% Triassic pebble conglomerate (Fig. 3.8a). Palaeoflow directions from clast imbrication in T3 vary by as much as 180°, with the two major directions pointing along the direction of the two legs in the modern valley bend (Fig. 3.11f). The Bou Tharar reach exhibits the strongest fining trends within the study area, with a

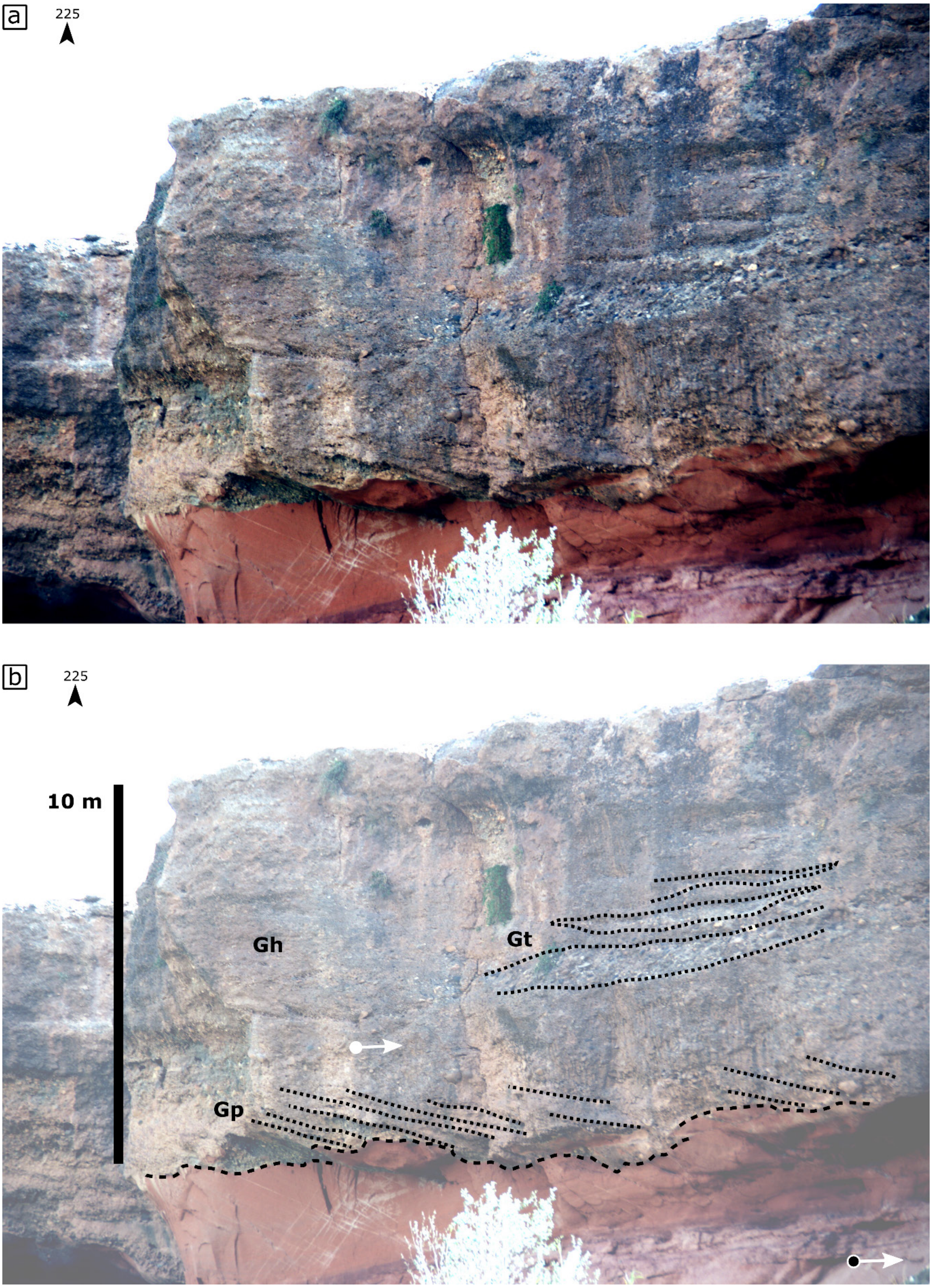
a
225
b
225
10 m
Gh
Gt
Gp

Figure 3.12 - Interpreted outcrops of braided fluvial deposits on terraces in the midstream Bou Tharar reach in the thrust front. (a-b) uninterpreted and interpreted sedimentary structures of T2 (see Fig. 3.11b). 2-3 m high planar cross-strata (Gp) represent transverse gravel bar migration on top of the strath surface in water depth of up to 3 m or more. 4 - 8 m wide lenticular trough-stratified channel cut-fill (Gt) represent minor channel flow in between bars during high or waning flow conditions. Gt is interbedded with bedform sheet conglomerates (Gh). The general flow direction from imbricated clasts and the modern river flow are indicated with arrows without and with a black dot, respectively.

fining exponent and r-squared of 0.071 and 0.334, 0.019 and 0.054, 0.038 and 0.199 for the D_{50}, D_{84} and D_{96} respectively (Fig. 3.8b). Opposite to the upstream Ait Toumert reach in the WTB, where the strongest fining trend is in the D_{96}, the strongest r-squared and fining exponent in Bou Tharar is that of the D_{50}.

T2 and T3 deposits in the Bou Tharar reach show evidence of braided fluvial processes (Figs. 3.11 - 3.12), from the presence of Gh deposits that are interpreted as gravel sheets and lag deposits (Fig. 3.6; Miall, 1996) and intercalations with Gp and Gt (Fig. 3.12) which are genetically related to transverse bar migration and minor channel fill (Massari, 1983; Miall, 1996). The transverse bar migration represented by facies Gp on top of the strath surfaces (Figs. 3.11 – 3.12), and the preservation of these sedimentary structures as well as the trough-stratified channel cut-fill facies (Gt) points to higher water depth (at least up to 3 m channel depth for 2-3 m planar cross strata) to clast size ratios than in the upstream Ait Toumert reach (Rust, 1978). This is likely a combination of the well-sorted nature of the conglomerate deposits, the confined nature of the valley and the confluence with a second perennial trunk stream in the valley which increases discharge. The Bou Tharar reach has the highest relief and most confined valley (150 to 650 m wide; Fig. 3.1) along the studied length of the Mgoun River, and is the only reach along which there is no geological hillslope source of conglomerates (Fig. 3.1). A major perennial trunk stream sourcing gravels from Pliocene conglomerates in a neighbouring wedge-top basin joins the surveyed trunk stream at a confluence in this reach, which is the likely source of the clasts of fossiliferous Jurassic limestone and Triassic pebble conglomerate not seen elsewhere (Fig. 3.8a). The strong fining trends in this reach, especially in the median grain size, reflect the dominance of longitudinal river-fed sediment flow without significant lateral sediment input.

The downstream Ait Saïd reach (TF)

Along the Ait Saïd reach, the north bank exhibits a 1 km long and ~ 50 m wide T3 with a strath 60 m above the modern river plain, an extensive ~500 m wide and ~2 km long T2 gullied and fragmented surface with a bedrock strath surface ~40 m above the modern river plain (Fig. 3.13a). The 10 m to 1 km long T1 terraces ~10 - 19 m above the modern river plain are found on both riverbanks (Fig. 3.13a). The T1 deposits lining the sides of the 250 - 740 m wide modern valley bottom are composed of 3 to 4 m of clast-supported conglomerates with sub-rounded to well-rounded imbricated clasts with weak horizontal bedding (Gh in Fig. 3.13b and c and Table 3.2). T2 deposits are composed of a ~10 m thick succession containing two sequences of 2 - 3 m thick graded clast supported conglomerates with sub-rounded to well-rounded imbricated clasts transitioning into finely laminated ~1 km by ~ 650 m extensive red and tan-coloured ~2 m thick sand to mud sheets (Gcg into Fl in Fig. 3.13d and Table 3.2). The graded conglomerate facies extend over the whole 2 km terrace length, interbedded with 20 m to 1 km wide sand-mud sheets pinching out in a downstream direction. The deposits are capped by angular to sub-angular massive clast to matrix supported conglomerate consisting of locally sourced Eocene limestone (Gcm in Fig. 3.13d and Table 3.2). T3 deposits are composed of a 3 - 5 m thick preserved clast-

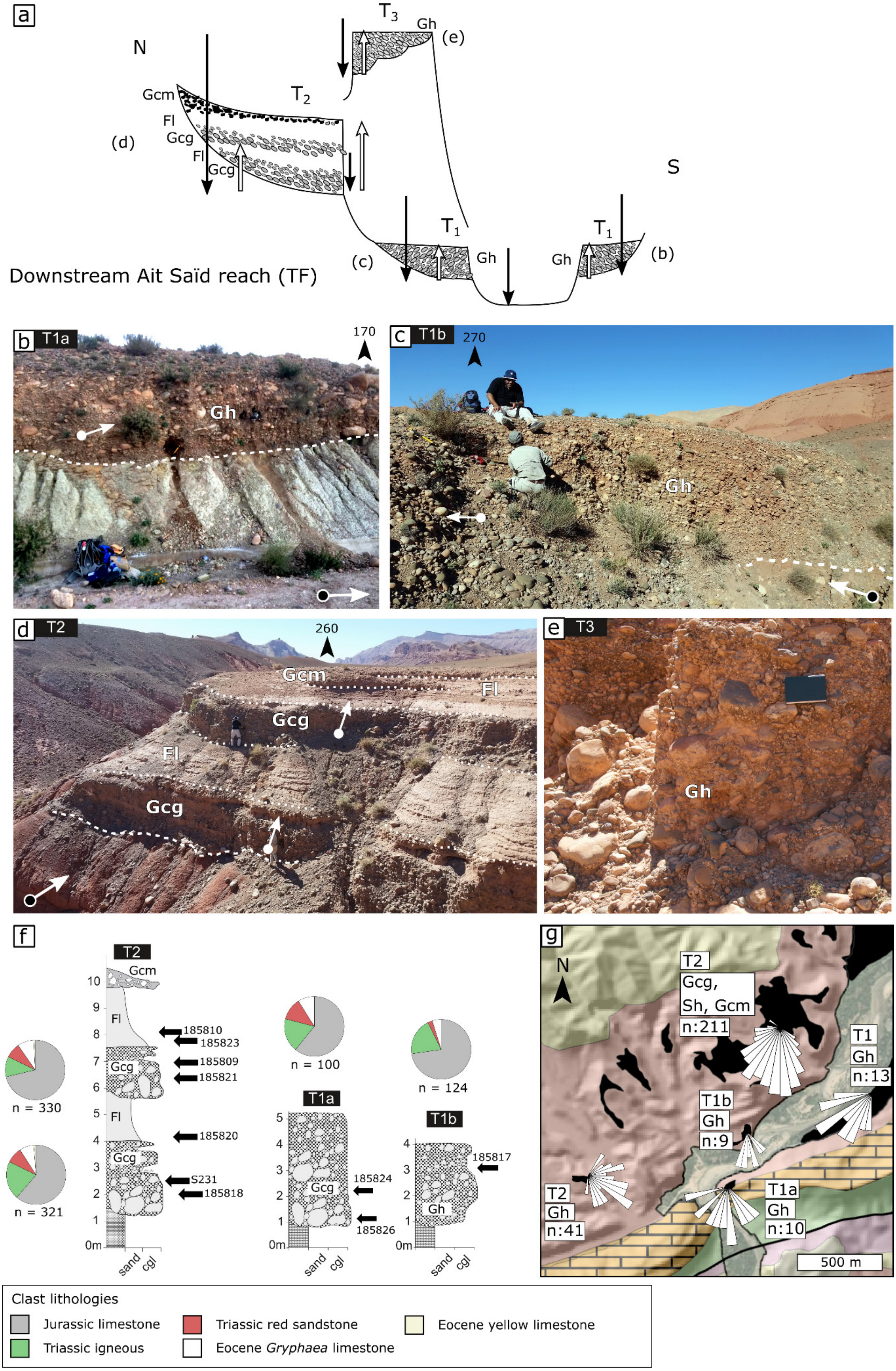
a
N
S
T3
Gh
(e)
Gcm
T2
Fl
Gcg
Fl
Gcg
(d)
T1
Gh
(c)
Gh
T1
(b)
Downstream Ait Saïd reach (TF)
b T1a
170
Gh
c T1b
270
Gh
d T2
260
Gcm
Fl
Gcg
Fl
Gcg
e T3
Gh
f
T2
Gcm
Fl
Gcg
Fl
Gcg
185810
185823
185809
185821
185820
S231
185818
n = 330
n = 321
n = 100
T1a
Gcg
185824
185826
n = 124
T1b
Gh
185817
0m
1
2
3
4
5
6
7
8
9
10
sand
cgl
g
N
T2
Gcg,
Sh, Gcm
n:211
T1
Gh
n:13
T1b
Gh
n:9
T2
Gh
n:41
T1a
Gh
n:10
500 m
Clast lithologies
Jurassic limestone
Triassic red sandstone
Eocene yellow limestone
Triassic igneous
Eocene *Gryphaea* limestone

Figure 3.13 – Terrace sedimentology of the downstream Ait Said reach in the thrust front. (a) Sketch stratigraphy and sedimentology of terraces along the Ait Said reach. Not to scale. (b-c) two T1 terraces with 3-4 m of bedform conglomerates (Gh). (d) T2 with ten meters of two sequences of graded conglomerate (Gcg) to sand-mud sheets (Fl) and capped with massive angular conglomerates (Gcm). (e) T3 with 1-3 m of bedform conglomerates (Gh). (f) Graphic logs based on (a)-(d) and samples used in chapter 4. (g) Inset map from Fig. 3.1 with palaeoflow directions of terraces.

supported conglomerates with sub-rounded to well-rounded imbricated clasts with weak horizontal bedding (Gh in Fig. 3.13e and Table 3.2). Positions on a graphic log indicate the position of samples taken for geochronology in chapter 4 (Fig 3.13f). Clast lithological distributions are markedly similar between terraces and the modern river plain (Fig. 3.8b). Conglomerates contain 49% to 82% of Jurassic limestone, 6-34% Triassic igneous, 2-17% Triassic red sandstone and 1-14% Eocene *Gryphaea*-bearing limestone (Fig. 3.8b). Palaeoflow directions of T1 deposits in the valley bottom range within 90° parallel to the river axial flow direction, whilst the extensive T2 deposits exhibit a wider range of flow directions ranging up to 180° but with a dominant river axial parallel downstream flow direction (Fig. 3.13g). There are no grain size fining trends in the Ait Said reach, with grain sizes spiking downstream where two tributaries feed into the braided valley floor (Fig. 3.8b).

T2 in the Ait Said reach shows evidence of braided fluvial processes, from the presence of Gcg to Fl deposits (Figs. 3.13 - 3.14) that are interpreted as transverse bedform or channel fill to overbank or abandoned channel backswamp deposits (Fig. 3.7; Williams and Rust, 1969; Vos and Tankard, 1981; DeCelles et al., 1991; Miall, 1996). The second such succession overlying the first in T2 (Fig. 3.14) can be interpreted to be due to active channel switching in a ~1300 m wide valley bottom or by valley bottom incision and abandonment followed by reoccupation during a renewed bout of aggradation (i.e., a cut-fill terrace). Since the Fl sheets of overbank facies

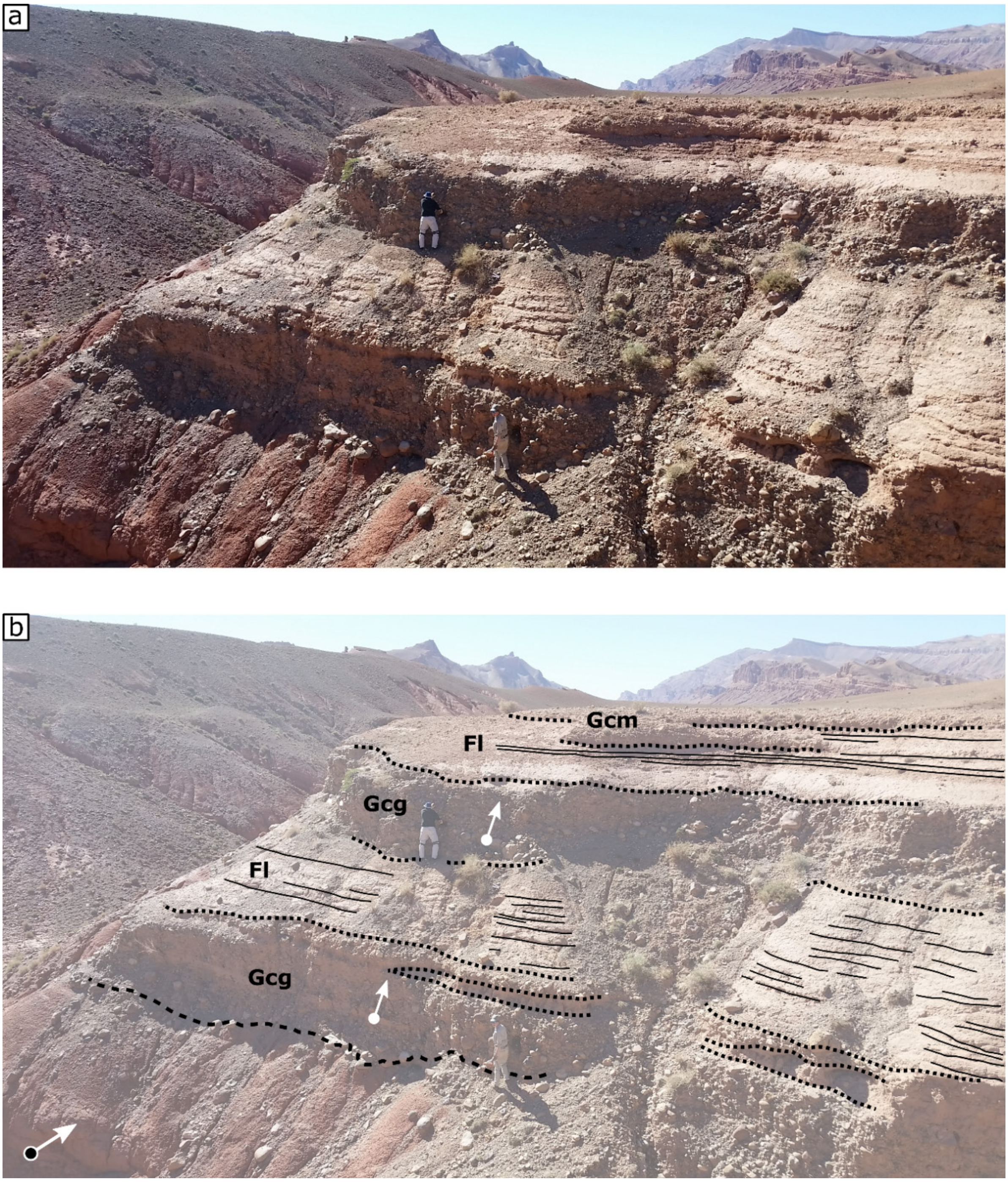

Figure 3.14 - Interpreted outcrops of braided fluvial deposits on terraces in the downstream Ait Said reach in the thrust front. (a-b) uninterpreted and interpreted sedimentary structures of T2 with ten meters of sediment (see Fig. 3.13d). Graded conglomerates (Gcg) transition into laminated sand-mud sheets (Fl), representing transverse bedform or channel fill to overbank or abandoned channel backswamp deposits. This succession is repeated on top by another sequence of graded conglomerates (Gcg) and overbank sands (Fl) and is capped with massive angular conglomerates (Gcm) of local provenance recording hillslope gravity deposits. The general flow direction from imbricated clasts and the modern river flow are indicated with arrows without and with a black dot, respectively. The modern river is to the left of the topographic high on the left side of the photo (see Fig. 3.13a).

extend over 1 km by 650 m and are up to 2 m thick, I favour a combination of these two explanations, with abandonment and successive overbank flooding and later reoccupation reflecting switching between aggradation and incision dominated environments (c.f. Stokes et al., 2017 in the neighbouring Dades catchment). The apron of clast-to-matrix supported conglomerate with angular clasts of local origin (Gcm) is interpreted as hillslope gravity deposits capping the terrace and protecting it from erosion. T1 and T3 deposits are dominated by fluvial bedform facies (Gh). The consistent clast lithological distribution between terrace levels and modern river deposits, and the lack of downstream fining point to recycling of conglomerates from terraces and the Mio-Pliocene conglomerate units. Except for the locally derived Eocene *Gryphaea*-bearing limestone, the clast lithological distribution is very similar to that in the other reach with Mio-Pliocene hillslope conglomerates. The coarser grain sizes downstream where tributaries sourced from Mio-Pliocene conglomerate headwaters join the axial river plain reflect lateral input into the fluvial system.

3.5 DISCUSSION

The overall objective of this chapter is to address objective 2.1: how do lithological and structural variation affect incisional and depositional landforms of valley aggradation and incision? In addition, the stratigraphic and sedimentologic data provide a framework for the chronology in chapter 4. The geological context of the Mgoun River has shown that the passive tectonic structure of the wedge-top basin and thrust front affects valley morphology through the spacing of resistant limestone stacks with uniaxial compressive strengths of 39 - 90 MPa (Figs. 3.1, 3.2; Table 3.1). Strath terraces form in the weak (10-14 MPa) bedrock separated by narrow gorges defining three along-stream reaches of 6 to 10 km along-stream distance with strath terraces (Figs. 3.4, 3.5, 3.6). Below I discuss the geomorphology and sedimentology of surveyed strath terraces in the context of the lithological and structural controls of the three river reaches and their connection.

3.5.1 Terrace stratigraphy and treads – lateral erosion, preservation, and longitudinal erosional connectivity

Strath terraces are characterised by planation surfaces inset on either side of the modern river plain (Figs. 3.4, 3.5), which is able to erode laterally through the weak red beds of Cretaceous and Mio-Pliocene origin. The width of the valleys and lateral coverage of terraces is determined by the width of the weak geological units: strath terraces are preserved only up to the limit of weak red beds in the valley walls (Fig. 3.5), and are absent in high-strength gorges. Thus the Mgoun river shows a clear lithological control on strath terrace formation. A maximum of four terrace levels are preserved in the studied reach of the Mgoun River, compared to up to fifteen levels recorded in the neighbouring Dades River (Stokes et al., 2017). Many of the preserved, equally spaced terraces along the Dades River have formed on valley meanders forming in mixed moderately strong-weak rocks. Johnson and Finnegan (2015) show that valley meanders such as observed in the Dades only occur in the mid-range of rock strengths between strong bedrock which allows no lateral bed mobility, and weak bedrock which allows a widening river planform such as observed in the Mgoun River. In addition, Stokes et al. (2017) showed that terrace staircases along the Dades River in the fold-thrust belt exploit weak sequences within the valley sides, and that preservation is poor in valleys with homogeneously weak bedrock. Thus, the vertical stratigraphy along the Mgoun River is less well preserved than in the neighbouring Dades catchment due to the structural and stratigraphic distribution of weaker lithologies within its valleys, but in general the lower terrace levels are more continuous along the length of reaches in weak bedrock.

Despite the continuity of strath levels within reaches of weak bedrock, the number of terrace levels, their vertical relationships and spatial extent vary significantly from reach to reach between gorges, along the 30 km length of trunk river channel surveyed. In the upstream Ait Toumert reach in the WTB terraces have lateral widths of hundreds of meters, a staircase of four terrace levels exhibits constant ~10 m vertical steps (Figs. 3.4, 3.5), and these are parallel and continuous along this reach over > 10 km. Contrastingly, terrace levels through the TF vary in elevation and number from the downstream Ait Said reach to the midstream Bou Tharar reach over a 13 km upstream distance (Figs. 3.4, 3.5). In the downstream Ait Said reach the strath of T2 lies 30 m above the strath of T1 which lies 10 m above the modern river plain, whilst in the midstream Bou Tharar reach, these straths do not differ significantly in strath elevation, where a T2 strath level at 20 m above the modern river plain covered by 10 m of fluvial deposits has been eroded to the strath level ~ 19 m above the modern river plain to form T1 (Figs. 3.4, 3.5). A longitudinal profile of the river channel and the terrace treads show that these differences in terrace stratigraphy from reach to reach is due to the upstream propagation of waves of incision through knickpoints (Figs. 3.3, 3.6).

Since the T1 to T3 thrust-front terrace treads stop against partly propagated knickpoints between and within valleys (Fig. 3.6), the incisional process of bedrock incision forming strath terraces demonstrates low erosional connectivity within the system. Over a 20 km distance surveyed in the foreland basin, terrace treads are continuous and parallel along the length of the river (Fig. 3.6), similar to the majority of strath treads upstream of the mountain front in the neighbouring Dades River (Stokes et al., 2017), which indicates *n*>>1 in the stream power equation (Eq. 1; Finnegan et al;, 2013, see also §2.3.1). Most importantly, the treads demonstrate that the partial knickpoint propagation in the 20 km length of the thrust-front is caused by the high strength obstacles of limestone with uniaxial compressive strengths of 39 to 90 MPa (Table 3.1) thrown up by the thrust stacks. Whilst the knickpoints observed today are stuck in strong rock, the partial propagation of knickpoints within long gorges, the absence of knickpoints within similar gorges of the same rock strength, the knickpoint recorded in treads in weaker bedrock, and the lack of strath incision upstream of the midstream Bou Tharar reach demonstrate the knickpoints are propagating rather than stationary and represent progressive bedrock incision upstream. Thus, these are interpreted as knickpoints generated by the slower propagation upstream of local base-level fall in high-strength gorges, which subsequently propagate at high rates through the weaker bedrock and at lower rates through gorges. Thus, the implications of low erosional connectivity between reaches in the thrust front and wedge-top basin means that the lithological and structural complexity of the collisional mountain belt in this 1200 km^2 catchment promotes asynchronous terrace formation from reach to reach separated by gorges. To explore the extent to which these deposits are asynchronous Ch. 4 will define an innovative approach to dating the deposits described and discussed in this chapter.

3.5.2 *Sedimentology*

As river strath terraces form in response to changes in sediment flux in the river channel over time (Hancock and Anderson, 2002), the role of sedimentology in defining the depositional and incisional history of the Mgoun River is to constrain the processes of sediment flux and its connectivity laterally between hillslope and river channel, and longitudinally through the river system. Below I discuss the depositional facies of terrace deposits in each reach as well as the longitudinal trends in grain size and clast lithological distributions in the context of lithological and structural controls on valley morphology.

Facies – process of sediment flux into river channels

The character of terrace deposits is most variable longitudinally along stream, with terraces in vertical staircases exhibiting facies of similar architectural elements. The biggest difference in facies is between the upstream Ait Toumert reach in the WTB, and the midstream and downstream reaches of Ait Said and Bou Tharar in the TF. T2 deposits in the Ait Toumert reach are characterised by shallow water braided fluvial channel gravel bedform elements, as well as sediment gravity flow and floodplain deposits (Fig. 3.9). On the other hand, the confined valley of the Bou Tharar reach only preserves terrace deposits exhibiting braided fluvial channel gravel bar and bedform deposits representing 2-3 m deep channel flows (Fig. 3.10). The difference in deposits can be ascribed to multiple controls: 1) The valley width of the WTB vs the confined high-relief valleys of the TF (Figs. 3.1, 3.5) 2) the increased discharge downstream in the Bou Tharar reach due to a confluence of two trunk perennial streams (Fig. 3.1); and 3) the absence of lateral sediment input from tributaries, alluvial fans, and hillslope sources of geological conglomerate in the Bou Tharar reach (Fig. 3.1). Thus, the width of the valley set by the width of passive limestone – red bed thrust stacks affects the nature of hillslope to river channel coupling. Noticeably, the wider the valley, the larger the buffering between hillslope and channel through alluvial and ephemeral tributaries which deposit sediment in the river channel through sediment gravity flows (e.g., Stokes and Mather 2015). The nature of hillslope-channel coupling is therefore likely to affect the timing of a geomorphic response to changes in climate.

Clast lithology and grain size trends – provenance and transport

The longitudinal sediment transport through the river system will affect the timescales at which reaches link their response to a change in hillslope to river channel sediment flux. Two longitudinal trends in the clast lithological distribution and grain size of modern and river terrace deposits suggest the transport connectivity along the Mgoun River has been low over the time of terrace formation. First, the clast lithological distribution changes systematically from reach to reach (Fig. 3.8a). Resistant fossiliferous limestone clasts enter the river channel and terraces at confluences with perennial tributaries which drain the eastern side of the FTB. However, after each gorge downstream of these two confluences, none of the fossiliferous limestones are found in the river or terrace deposits. These transitions also coincide with the presence of geological conglomerates in the hillslopes, recycled from previous mountain front distributary fan deposition into thrust front stacks. Grain size trends, rather than showing continuous downstream fining, are weak in the upstream Ait Toumert reach, stronger in the Bou Tharar reach which does not exhibit hillslope sources of geological conglomerates, and is non-existent in the downstream Ait Said reach where tributaries draining the hillslope conglomerates lead to coarsening downstream (Fig. 3.8b). Whilst in the Bou Tharar reach selective transport of particles and their abrasion are dominant processes of sediment transport (Fig. 3.8b; Paola et al., 1992; Ferguson et al., 1996; Fedele and Paola, 2007), reaches with hillslope sources of geological conglomerates such as in the Ait Saïd reach are characterised with a sediment flux that is dominated by recycling of coarse-grained conglomerate deposits (Fig. 3.8b). The effect of coarse-grained lateral sediment influx through conglomerate recycling on reduced fining rates in modern river channels and the position of the gravel-sand transition has been demonstrated previously in the Himalaya (Dingle et al., 2016; Quick et al., 2019). Thus, the grain size and clast lithological trends seen in the modern river and terrace deposits in the Mgoun River demonstrate that coarse sediment flux has been dominated by local lateral flux from hillslope to channel over the course of river terrace formation, and that this lateral flux is affected by the presence of geological conglomerates in the hillslopes.

3.6 SUMMARY

I have used a combination of geomorphic field and DEM surveying together with qualitative and quantitative sedimentological analysis of terrace deposits to characterise the fluvial terrace record of bedrock incision and sediment transport and deposition. These fluvial archives are set in context of the passive tectonic structure and lithologies of the thrust front and wedge-top basin in which these archives are found. The tectonic structure and lithology of the wedge-top and thrust front of the High Atlas affects the bedrock incision as well as sediment deposition within river reaches along the length of the Mgoun River. Strath terrace occurrence depends on the distribution of low strength marl units (10 - 14 Mpa) within valleys. Gorges in high strength limestone (39 - 90 MPa) separate these reaches, and are responsible for the partial propagation and preservation of knickpoints representing waves of incision travelling through the catchment. Consequently, terrace treads are discontinuous between valleys, most noticeably between the thrust front and the wedge-top basin, which is separated by a ~2.5 km long gorge in the strongest limestone unit (90 Mpa). In addition, facies, grain sizes and clast lithologies show a strong local control on sediment flux and its depositional dynamics. In particular, a wide valley morphology is characterised by sediment gravity flows entering the river channel from ephemeral tributaries and alluvial fans. Grain size and clast lithology demonstrate the ratio of longitudinal to lateral sediment flux is low, where recycling from hillslope conglomerates dominates the coarse sediment in the channel. Thus, both incisional and depositional records of the strath terraces in the Mgoun River demonstrate low longitudinal connectivity of the fluvial system within the wedge-top basin and thrust front of the southern High Atlas and a strong dependence on local lithological conditions.

4

Dating strath terrace formation using OSL

4.1 INTRODUCTION

Together with chapter 3, this chapter aims to answer to what extent lithological and structural variability within a catchment draining a collisional mountain belt affect the timing of fluvial incision and aggradation in response to climatic changes on orbital timescales (objective 2). Chapter 4 contributes to this objective by dating terraces which have been placed in a stratigraphic and sedimentological context in chapter 3, to constrain the timing of river aggradation and incision in the Mgoun catchment (objective 2.2). To constrain the timing of aggradation and incision within the catchment I sample terraces along the length of the Mgoun River in three reaches separated by gorges. Optically stimulated luminescence (OSL) dating has advantages over other Quaternary dating techniques such as radiocarbon and cosmogenic nuclides (see §1.3.4) because 1) it uses quartz and feldspar grains, which are commonly found in sedimentary environments across the Earth's surface, 2) it has a dating range of tens to several hundred thousand years (Wintle and Murray, 2006; Rixhon et al., 2017), and 3) it provides a direct estimate of the timing of sediment deposition. To apply optically stimulated luminescence, I develop methods of dose rate ($\dot{D}$) calculation for gravel sediments on fluvial terraces. These coarse-grained gravels bring challenges of dosimetric heterogeneity (see §1.4.1) and transient water saturation levels.

This chapter explores the effect of differential Ḋ contributions of grain-size fractions by taking advantage of methodological advances in dosimetry (Cunningham et al., 2018) and proposes a calculation of Ḋ values based on differential attenuation of gamma and beta Ḋ. I evaluate the efficacy of the Ḋ, and water saturation corrections developed in this chapter, and set the dates in context of the climatic context detailed in chapter 1 (§1.4.2). Next to dating bedload gravels to constrain the aggradation history of strath terraces in line with objective 2.2, I develop more experimental approaches using rock surface OSL techniques (Sohbati et al., 2012a; Sohbati et al., 2012b; Freiesleben et al., 2015) which have the potential to extract more information from strath terraces.

4.2 AN OSL APPROACH TO DATING STRATH TERRACES

Strath terrace formation integrates periods of strath planation, gravel deposition and incision and abandonment (Foster et al., 2017; Schanz et al., 2018; Fig. 4.1). The first stage of strath terrace formation is the planation of the bedrock strath surface by lateral erosion. Dating the exposure of bedrock to sunlight during planation would directly date the onset of strath formation, and establish whether there is a gap between surface planation and bedload gravel deposition. Deposition of gravel bedload during the aggradation of the strath terrace can be dated using silt- and sand-sized grains of feldspar and quartz in the gravel matrix, or by rock surface dating of the pebble, cobble, and boulder clasts (Fig. 4.1). The latter technique can expose multiple exposure-burial events (Freiesleben et al., 2015; Sohbati et al., 2015) and thus could date individual clasts histories to beyond deposition in the terrace itself. As the river incises into the terrace and starts to abandon the strath level, overbank sands capping the sequence allow conventional OSL approaches to dating sand lenses, which would constrain the onset of incision and strath level

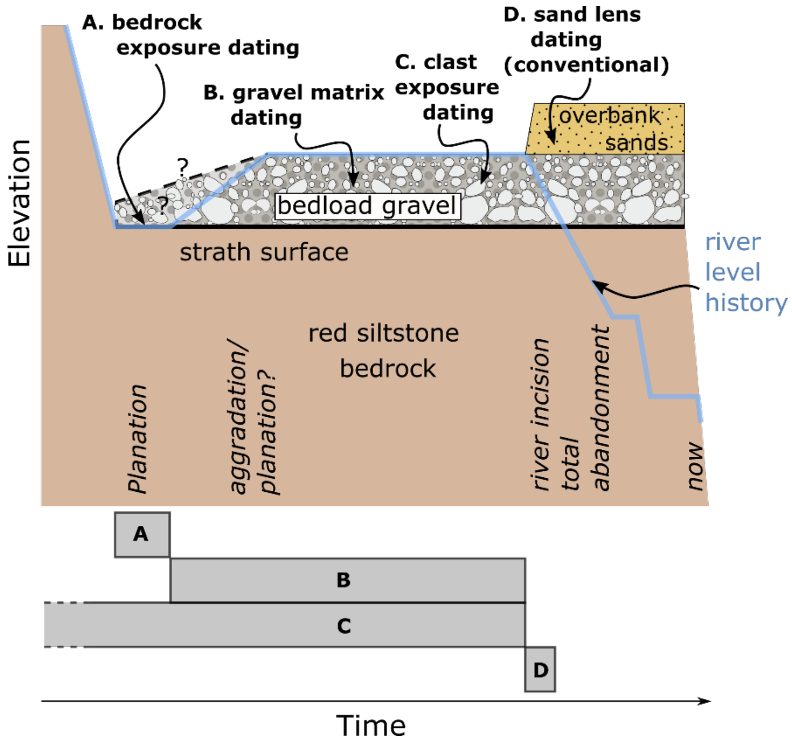

Figure 4.1 – After Foster et al. (2017). Terminology of strath terrace evolution and the application of luminescence dating techniques. The history of the river level in blue starts with bedrock incision and planation of a strath surface. Whether during planation the bedrock surface is exposed or covered by bedload is an unknown. Strath planation is followed by aggradation of bedload material and active aggradation of the terrace. The timing of active aggradation of the river on this surface can be constrained by dating bedload gravel matrix, or the clast surfaces through rock surface dating. Luminescence-depth profiles of clasts can constrain the timing of deposition in the terrace, as well as previous exposure and burial events. As the river starts incising bedrock, abandoning the strath level, the only deposition on the terrace will be fine overbank sands. Dating of the overbank sands enables timing of the onset of incision.

abandonment (e.g. Stokes et al., 2017; Fig. 4.1). The technique expected to produce the results for achieving the objective of constraining timing of incision and aggradation (objective 2.2) is the dating of gravel matrix and sand lenses. However, more experimental approaches to rock surface dating are developed here as a contribution to geochronological techniques which could unlock further information from the strath terrace record. Luminescence-depth profiles have been used to date exposure and burial events in archaeological (Chapot et al., 2012; Sohbati et al., 2012a; Freiesleben et al., 2015; Sohbati et al., 2015) and glacial contexts (Rades et al., 2018). While the light penetration of luminescence-depth profiles has been tested within modern riverbed cobbles (Liu et al., 2019), until now no attempt has been made to date fluvial gravel deposits using OSL rock exposure dating. In addition, the luminescence characteristics of bedrock can be used to trace the source of sediments within the catchment (Sawakuchi et al., 2018; Gray et al., 2019; Sawakuchi et al., 2020). Firstly, results of gravel matrix dating approaches are presented, followed by the constraints on the timing of terrace aggradation and abandonment in the context of the geomorphic framework laid out in chapter 3. Subsequently, results of the experimental bedrock surface approaches are presented and discussed in the context of strath terrace formation.

4.3 DOSE RATE IN OSL DATING

The basis for an OSL age is the following equation:

$$\text{Age} = \frac{\text{equivalent dose } (\mathrm{D_e})}{\text{environmental dose rate } (\dot{\mathrm{D}})} \qquad \text{Eq. 7}$$

where the equivalent dose (D_e in grays: 1 Gy = 1 J kg^{-1}) is the radiation energy absorbed and trapped as charge in a quartz or feldspar mineral after the source traps (i.e., electron holes in the mineral lattice) were last emptied. The environmental dose rate ($\dot{D}$ in Gy/ka) refers to the effective rate of supply of ionising radiation from nearby radioactive isotopes: dominantly potassium-40 and the products of uranium and thorium decay chains. In this chapter, I am interested in the timing of the resetting of dose by exposure to sunlight during sediment transport and bedrock exposure before sediment deposition and burial. An important challenge in OSL dating of natural sediments other than homogenous dune sands is the introduction of $\dot{D}$ heterogeneity in nonuniform sediment such as the coarse gravels studied here. The approach detailed below addresses this challenge to enable accurate dating of gravel matrix in strath terrace deposits in the High Atlas.

4.4 STUDY SITES AND SAMPLING

Strath terraces in the Mgoun catchment of the High Atlas in Morocco are characterised by bedrock strath surfaces with bedload gravels and overbank sands (chapter 3), and thus provide the perfect location to test the combination of OSL techniques for dating strath formation. The headwaters of the river erode mainly though limestone bedrock, as well as red sandstones and igneous rocks (Fig. 4.2) which together make up the majority of pebble to cobble material in the river strath terraces. Potential sources of quartz and feldspar sand are red sandstones, igneous rocks, as well as the red mudstones and siltstones forming the valley bottoms in the wedge-top basin and thrust front (chapter 3). Furthermore, Saharan dust storms are another potential source as well as recycling of Mio-Pliocene conglomerates within valleys.

Two sites were selected based on the ability to sample from the bedrock strath surface to the top of the sediment cover, positioned downstream and upstream. Site A is T2 in the downstream Ait Said reach of the thrust-front (Fig. 3.5c) and site B is T2 in the upstream Ait Toumert reach in the wedge-top basin (Fig. 3.5a). Both sites have a bedrock strath surface in red mudstones and siltstones. Site A exhibits two sequences of bedload gravels and overbank sands. Four gravel and three sand samples (Fig. 4.3) were taken from this sequence. In site B, four samples of gravels were taken within the 3 m thick gravel deposit. Where possible, samples were taken using metal tubes driven into the terrace section after cleaning a fresh exposure surface, and sealed with lightproof tape. Where gravels were too well-cemented for driving in tubes, blocks were broken off using a hammer and the outer surface spray painted. In the lab, spray-painted outer surfaces were removed for dose rate

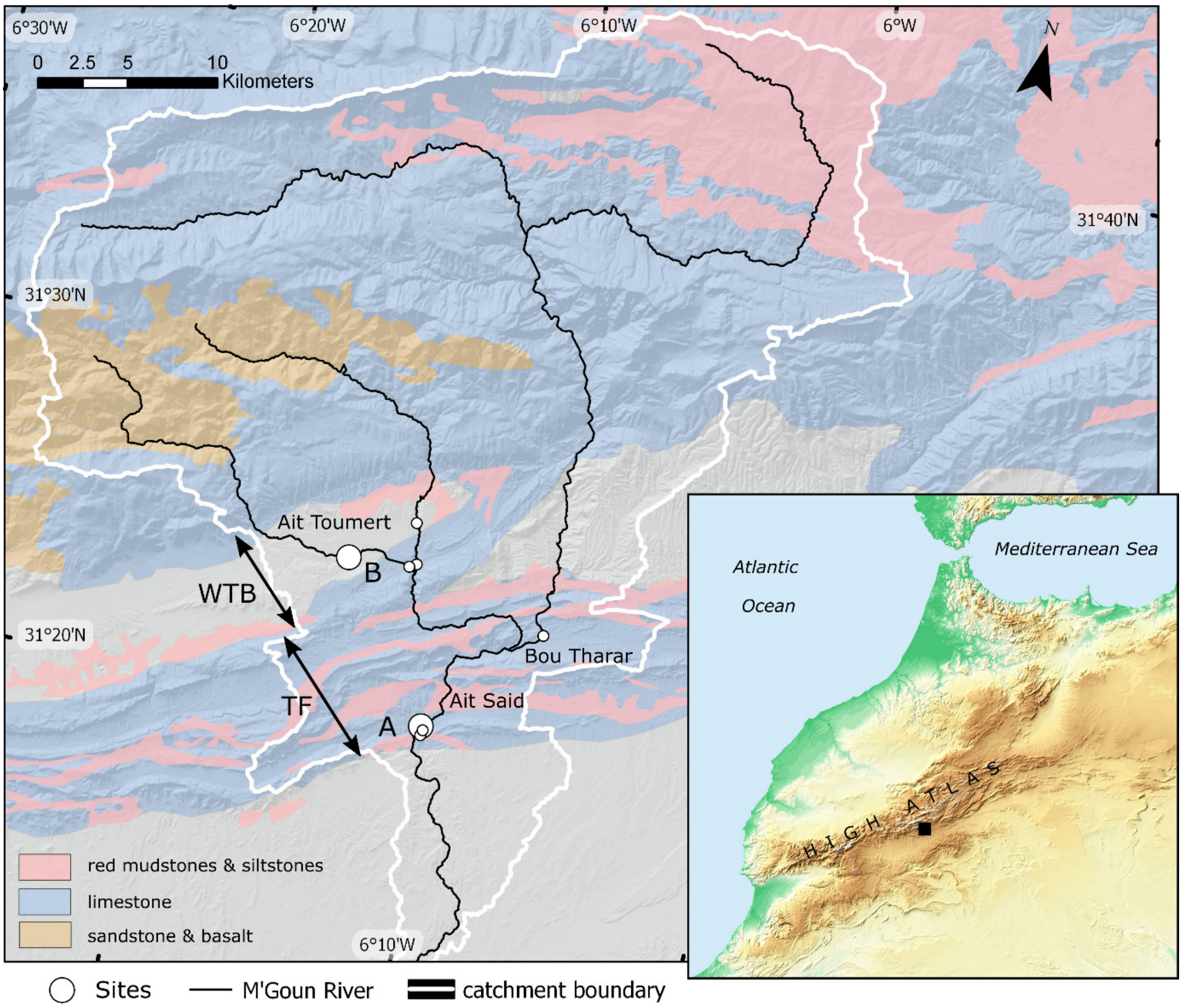

Figure 4.2 – Location of the Mgoun River within the High Atlas in northwest Africa and the sample sites. Exposed bedrock geology is displayed, with grey representing sedimentary basins. A and B are full sections highlighted in this chapter on which a full range of techniques are developed, and the other smaller dots represent sampling locations of other terraces on which I perform only gravel matrix dating. These terraces are described in detail in Ch 3. WTB – wedge-top basin; TF – thrust front.

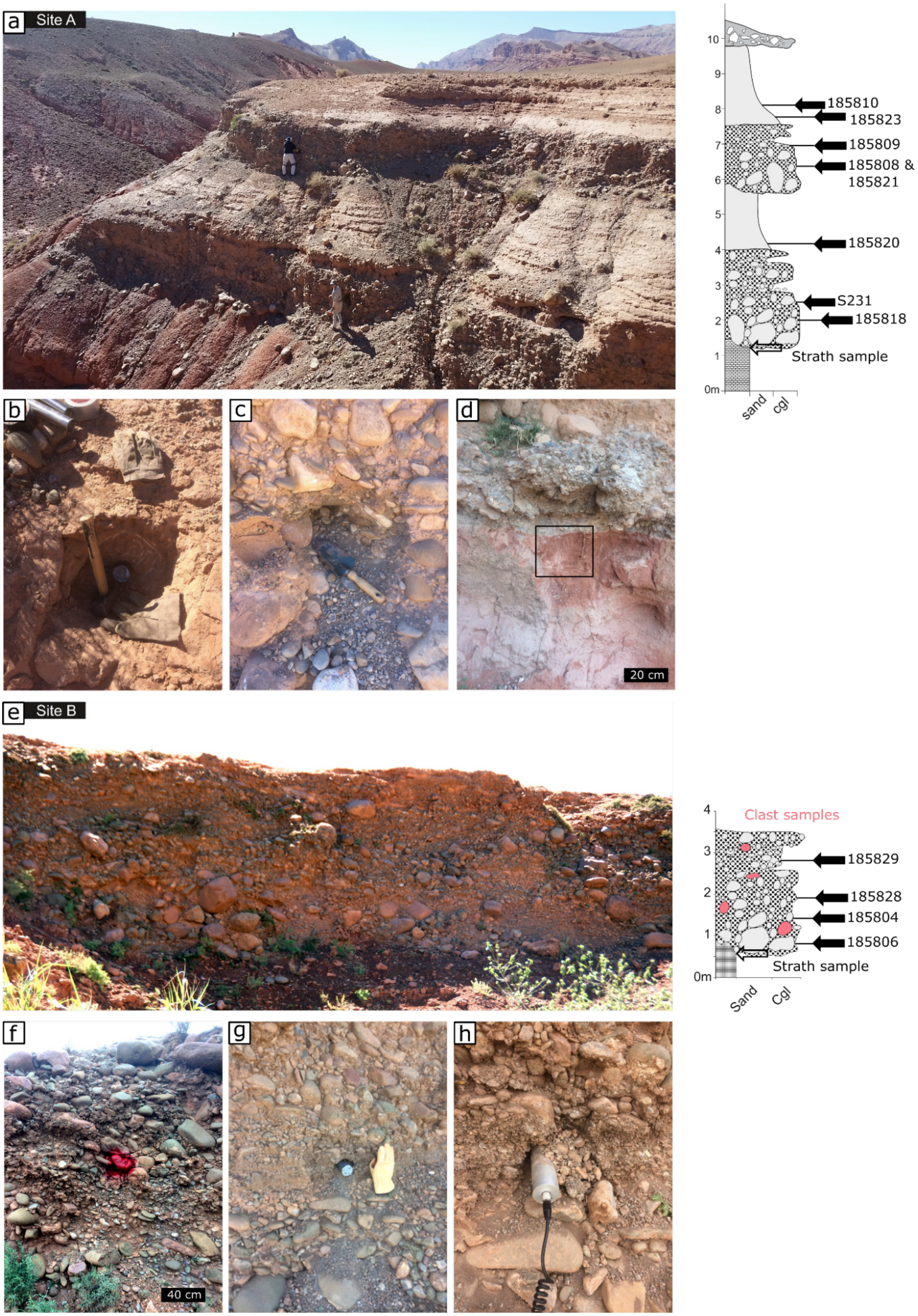
a
Site A
10
9
8
7
6
5
4
3
2
1
0m
185810
185823
185809
185808 &
185821
185820
S231
185818
Strath sample
sand
cgl
b
c
d
20 cm
e
Site B
4
3
2
1
0m
Clast samples
185829
185828
185804
185806
Strath sample
Sand
Cgl
f
40 cm
g
h

Figure 4.3 – Section logs and photos of site A and B. (a) Photo and log of T2 at site A in the thrust front. (b) Sand sampling with a metal tube. (c) Gravel dose sampling in a hole left by a tube for lab $\dot{D}$ measurements. (d) Location of removed block of bedrock including the strath surface. (e) Photo and log of T2 in the wedge-top basin at site B. (f) example of a painted and sampled cobble. (g) Gravel sampling using a metal tube. (h) in-situ gamma spectrometer inside a sampled hole. Site A (a) has an intercalation of sand and gravel material sampled from bottom to top, whilst site B (e) only has gravel material. The bedrock strath was sampled at both sites. Pebble and cobble clasts were sampled throughout the terrace in site B.

($\dot{D}$) measurements, and the inner unexposed sediment used for equivalent-dose measurements (D_e). Where gravels were sampled using the tube-method, extra material for $\dot{D}$ measurements was collected from the sampling site. A portable gamma spectrometer was used to take in-situ measurements of radiation inside the sampling holes. In addition to gravel and sand samples for quartz grain luminescence, in site A the bedrock was sampled and in site B both the bedrock strath and sandstone pebbles and cobbles exposed in the section were sampled (Fig. 4.3). Pebbles and cobbles were spray-painted before collection in the section to identify the exposed face in the lab. Strath sample collection was done using a geological hammer and part of the overlying gravel was taken as well to avoid exposing the strath surface outside the lab. The rest of the samples were gravel-matrix samples taken along the length of the river (Figs. 3.9 – 3.11, 4.2).

4.5 LUMINESCENCE SAMPLE PREPARATION

All samples used for D_e determination were processed under subdued red-orange light conditions. Material in the outer part of the tube and the outer spray-painted layer of gravel blocks were reserved as $\dot{D}$ samples. Material used for gravel-matrix and homogeneous sand dating was wet-sieved to obtain the 180-250 μm fraction, and quartz extraction was done with conventional sample preparation techniques (Aitken, 1998). The obtained fraction was then treated with HCl (10%), H2O2 (10%) and HF (10%) for 20 minutes to remove carbonates, organic material and to etch the quartz and feldspar grains. To separate quartz and feldspar an aqueous heavy liquid solution (2.58 g cm^{-3}) was used, and the quartz-rich fraction treated with concentrated HF to remove any remaining feldspar. After etching any fluoride precipitates were dissolved using HCl. Quartz was mounted as large 8 mm aliquots on stainless steel discs and feldspar in small 1-2 mm aliquots as it was much scarcer. The purity of quartz samples was tested by stimulating three aliquots per sample with IR and blue-light, with a threshold ratio of IRSL to blue-light (BLSL) ≤ 10%.

Rock sample preparation

Cores ~ 10 mm in diameter and ~ 30 – 70 mm long were drilled through the strath rock and pebble/cobble samples using a water-cooled diamond-tipped core drill. The cores were then cut into slices of ~1.2 mm thickness with a 300 µm thick water-cooled diamond wafer saw resulting in net slice spacing of ~ 1.5 mm. Adequately brittle, the slices could be broken into at least four pieces and measured in separate cups to enable standard error calculation. One strath sample was too friable for solid slicing and instead material was manually cored and sliced up using a drill core and scalpel.

4.6 LUMINESCENCE EXPERIMENTAL PROCEDURES

Luminescence measurements used Risø TL/OSL DA-OSL-15/20 readers, equipped with calibrated 90Sr/90Y beta sources (Bøtter-Jensen et al., 2010). OSL measurements were done with blue-light stimulation (470 nm; ~80 mW cm^{-2}) and photon detection through a 7.5 mm Hoya U-430 filter. IRSL measurements used infrared stimulation and photon detection through a Schott BG39/Corning 7-59 blue filter combination (2 and 4 mm, respectively). For D_e determination a standard single-aliquot regenerative (SAR) protocol was used (Murray and Wintle, 2000, 2003), including a zero-dose (recuperation) and a duplicated low regeneration dose to assess the recycling ratio. The influence of preheat temperature on the D_e value, recycling ratio and recuperation was examined using a high and low dose sample. The D_e appears to be independent of preheat temperature between 220 – 300 °C for the high dose sample (Fig. 4.4a), and between 160 and 300 °C for the low dose sample (Fig. 4.4b). The recycling ratio is independent from preheat temperature and close to unity (Fig. 4.4c,d). The recuperation for the high dose sample increases to ~ 14% for a 300 °C preheat but stays low (<5 %) over the entire 160-300 °C preheat temperature interval (Fig. 4.4c). Considering this, the final measurements used a preheat temperature of 260 °C for 10s and a 220 °C cut-heat. A clean-out was done at the end of each SAR cycle at 280 °C for 40s.

The initial 0.48 s of the quartz OSL decay curve minus an early background of the following 0.32 s was used for calculation of the net OSL signal to minimize the influence of slow and medium components (Cunningham and Wallinga, 2010). The same protocol was used on rock slices but with pieces of sliced rock instead of grain aliquots, and an extended measurement time of 100 s instead of 40 s. For rock profiles a high temperature $pIRIR_{225}$ SAR protocol (Buylaert et al., 2009) was used to measure feldspar signals, chosen over the more stable $pIRIR_{290}$ signal (Buylaert et al., 2012) as $pIRIR_{225}$ is more bleachable (Buylaert et al., 2011) and thus more likely to show a bleached profile. For rock material a background based on the last 10 s of signal was subtracted from the signal detected in the initial 2 s to give the net OSL and IRSL signal.

A critical test for the applicability of the luminescence measurement protocol is the dose recovery test (Murray and Wintle, 2003). The frequency distribution of dose recovery ratios for all samples with three aliquots each

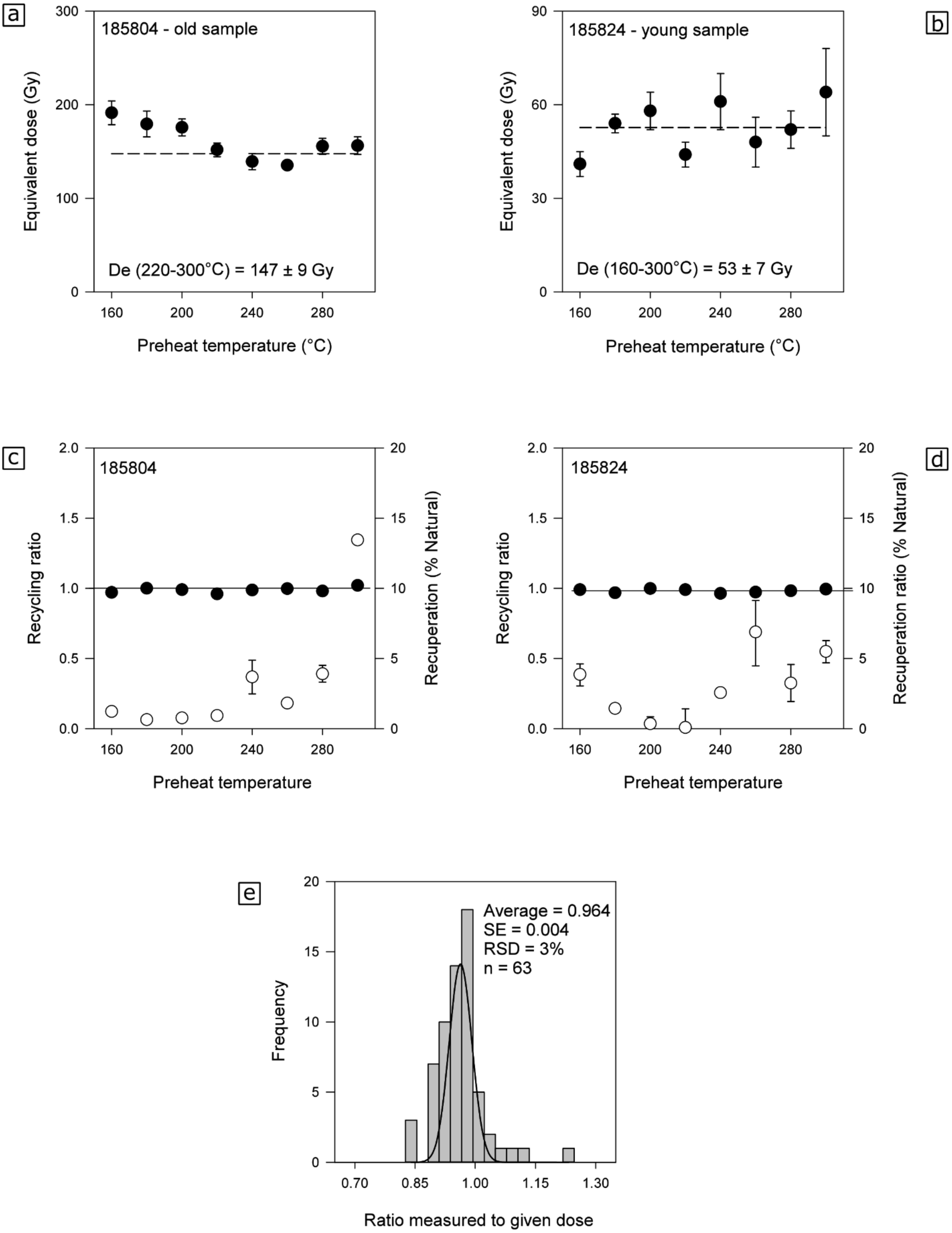
a
185804 - old sample
Equivalent dose (Gy)
300
200
100
0
De (220-300°C) = 147 ± 9 Gy
160
200
240
280
Preheat temperature (°C)
b
185824 - young sample
Equivalent dose (Gy)
90
60
30
0
De (160-300°C) = 53 ± 7 Gy
Preheat temperature (°C)
c
185804
Recycling ratio
2.0
1.5
1.0
0.5
0.0
Recuperation (% Natural)
20
15
10
5
0
Preheat temperature
d
185824
Recycling ratio
Recuperation ratio (% Natural)
Preheat temperature
e
Average = 0.964
SE = 0.004
RSD = 3%
n = 63
Frequency
20
15
10
5
0
0.70
0.85
1.00
1.15
1.30
Ratio measured to given dose

Figure 4.4– (a-d) Luminescence characteristics of an old high-dose and young low dose sample of gravel matrix and (e) a histogram of the ratio of measured to given doses for the routine dose recovery test on all samples. (a-b) D_e against preheat temperature for the old and young sample, respectively. The old sample has a preheat plateau of 220-300 °C, whilst the young sample has a wider preheat plateau of 160-300 °C. (c-d) recycling ratios and recuperation against preheat temperature for the same aliquots as in (a-b). A solid line is drawn at 1 to show a recycling ratio of unity. Six aliquots were used per sample and error bars represent 1 standard error.

(Fig. 4.4e) lies around an average of 0.964 ± 0.004 ($n=63$) indicating the SAR protocol used here is able to measure a given dose accurately.

4.7 DOSE RATE ($\dot{D}$) DETERMINATION

$\dot{D}$ measurements and calculations for gravel topped strath terraces are complicated by heterogeneity of the matrix and potentially complex water saturation histories. This study demonstrates a novel approach to both of these challenges. As gravels markedly do not conform to assumptions of an homogeneous infinite matrix (Aitken, 1985), the $\dot{D}$ of individual grains need to be explicitly considered. The ionising range of alpha, beta and gamma radiation emitted by grains are ~10 μm, ~2 mm, and ~ 30 cm respectively (Fig. 4.5; Aitken, 1985). Etching of the outer rim of gravel matrix sand grains precludes alpha radiation contamination from surrounding material. As most sand grains are in a matrix several mm wide in between cobbles and pebbles (Fig. 4.5), beta radiation comes primarily from surrounding sand grains, whilst gamma radiation integrates the bulk of sand and pebble/cobble material. To account for grain-size-dependent $\dot{D}$ variations four samples with at least 500 g of $\dot{D}$ material were wet-sieved through 500 μm, 1-, 2-, 4-, and 20-mm sieves and prepared for gamma spectrometry and beta counting.

Sample preparation and radiation measurements

$\dot{D}$ sample material was crushed (<200 μm) for homogenisation, ignited at 450 °C and cast in wax to retain ^{222}Rn. The sticks (~ 8 g of dry sample), discs

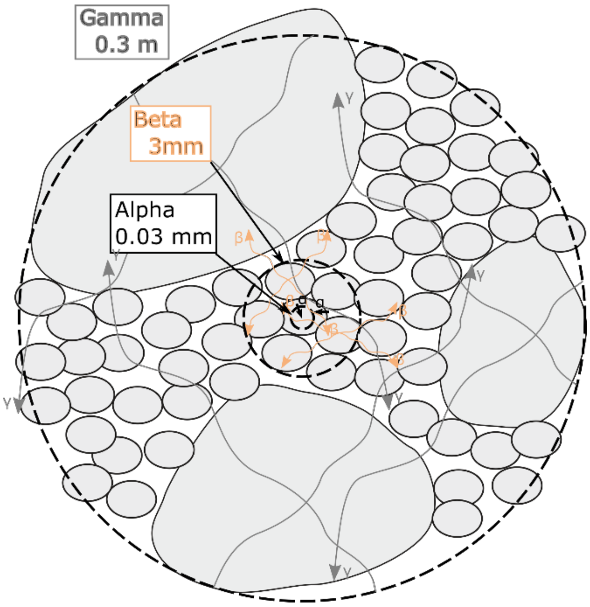

Figure 4.5 – Diagram showing texture of sampled gravels and sample homogeneity of alpha, gamma, and beta dose rates. Not to scale. Each radiation type has a different penetration depth (Aitken 1985). Alpha radiation has the shortest penetration depth and in sand size grain fraction influence from surrounding grains affect only on the outer rim which is dissolved during preparation. Since most sand grains lie within the inter-clast matrix, beta radiation comes from the surrounding sand grains mostly. Gamma radiation penetrates to around 30 cm, and thus comes from both the surrounding sand grains and larger clasts.

(>30 g) and cup-shaped (>93 g) samples for gamma spectrometry and beta buttons (>2 g) for beta-counting were stored for more than three weeks to allow ^{222}Rn to build up to equilibrium with ^{226}Ra before analysis. High-resolution spectrometry (HRGS) follows Murray et al. (1987) and radionuclide concentrations were subsequently converted to dry Ḋ values using the conversion factors from Guérin et al. (2011) or used for conversion of beta counts. Beta-counting to derive Ḋ is a relatively new approach (Cunningham et al., 2018), but instruments are simple to operate and cheap, and thus enables high quantity Ḋ testing which is useful for the grain-size dependent measurements. K concentrations from XRF, and relative proportions of K, U, Th as determined from HRGS were used in combination with beta count rates to calculate dry Ḋ values following methodology detailed in Cunningham et al. (2018).

Method 1:	Activity concentrations of K, U and Th are measured using HRGS. Beta-plus-gamma dry Ḋ is then calculated from this data. This represents the established method of Ḋ calculations.
Method 2:	Prior information on the relative proportions of K, U, Th sources measured by HRGS, together with beta count rates of these samples are used to calculate Ḋ. This represents the maximum amount of prior information, and uses both HRGS and beta counter measurements on samples, and thus is more equipment-intensive than method 1.
Method 3:	X-ray fluorescence (XRF) spectrometry of small Ḋ samples result in K weight concentrations, from which the activity concentration of K and the relative proportion of K, U, Th are estimated. I find equal ratios of K, U and Th activity concentrations between samples measured with HRGS (methods 1 and 2), which I use to calculate Ḋ from K activity.

Thus, lab-based radiation measurements resulted in three calculations of Ḋ for grain size dependent samples: 1) Ḋ HRGS, 2) Ḋ beta counter (U, Th, K) and 3) Ḋ beta counter (K).

Moisture content and dose rate calculations

As moisture content affects the absorption of dose into grains, estimation of water content is important for Ḋ calculations. Gravels of river strath terraces have two main stages of water content during their history of deposition and abandonment: saturation during perennial river aggradation, and non-saturation after incision and abandonment. Typically, both wet water content from sediment samples, and saturated water content are measured in the lab and either one is used for age calculations. However, in strath terraces dating

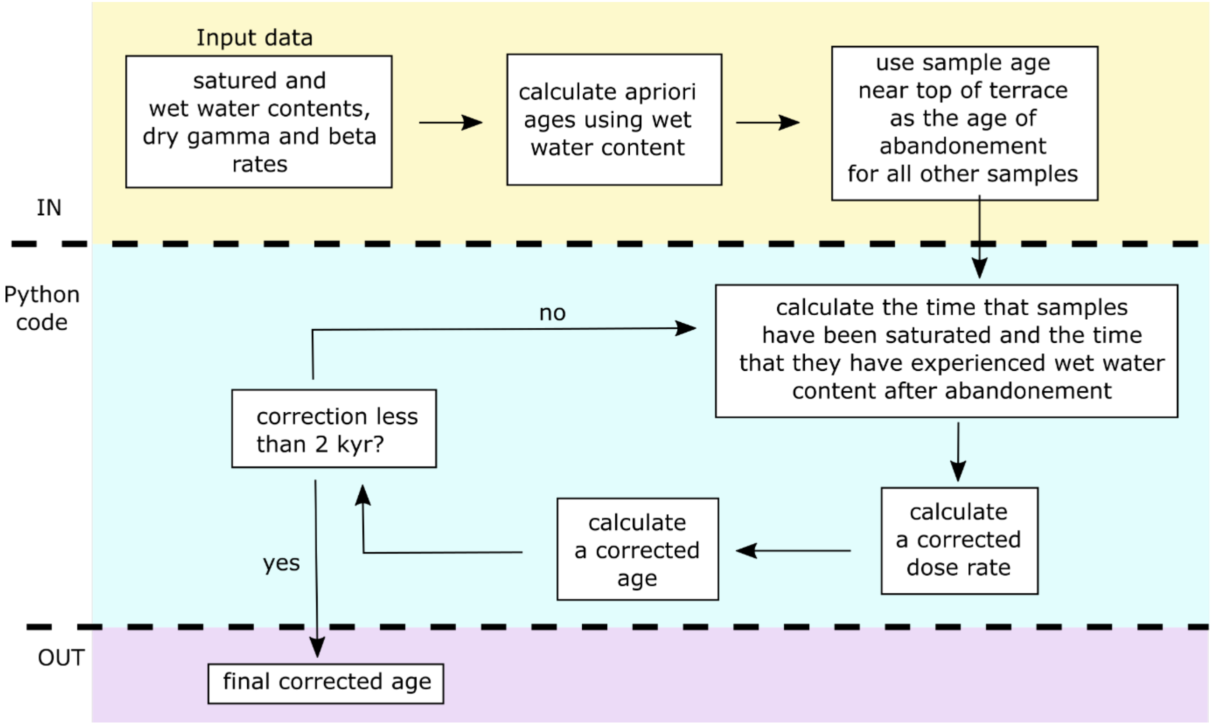

Figure 4.6 – Flow chart showing the process of iteration in calculation of $\dot{D}$ values in strath terraces. The three coloured areas correspond to the process before entering inputs into the python script, the iteration performed by the python script, and the final output.

back to several tens of thousands of years both values need to be taken into account. The natural moisture content from the field sample, together with the saturated moisture content measured in the laboratory form inputs for $\dot{D}$ calculations using an iterative python script (See supplementary material, Fig. 4.6). Where abandonment of the strath terrace is constrained by a sample towards the top of the sequence, the lengths of time underlying samples were saturated before terrace abandonment are calculated. Iteration of resulting ages continues until a correction of less than 2 kyr is reached (Fig. 4.6).

4.8 DISTRIBUTION OF D_E, $\dot{D}$ AND DERIVING A MEANINGFUL AGE MODEL - BAYESIAN STATISTICS

Common approaches to interpreting D_e distributions for finding a representative D_e of the bleaching event of interest are based on the effects of well-known problems such as incomplete bleaching and grain migration (Galbraith et al., 1999; Lepper et al., 2000; Roberts et al., 2000). In particular, characteristics such as over-dispersion (OD; Galbraith et al., 1999) and skewness (Bailey and Arnold, 2006) are often used to assess incomplete bleaching and to derive 'central' or 'minimum' ages (Galbraith et al., 1999; Galbraith and Roberts, 2012). However, Thomsen et al. (2012) have shown that over-dispersion is not a reliable indicator of incomplete bleaching, and in addition the average multi-grain residual dose from young or modern quartz samples from fluvial environments around the world is ~2 Gy (Murray et al., 2012), meaning incomplete bleaching is not of major concern for the old samples in this study (> 40 ka). More importantly, the introduction of D_e heterogeneity due to heterogeneous beta heterogeneity in sediments such as the gravels studied here means the inherent assumption of the average infinite-matrix dose rate (Aitken, 1985) does not hold. Thus, modelling efforts by Nathan et al. (2003) demonstrate the rejection of grains that contribute to 'over-dispersed' regions of the D_e distribution may lead to inaccurate date calculations. Consequently, I here calculate the arithmetic mean of D_e distributions and report the standard error to retain the full distribution for date calculation. I explicitly correct for beta heterogeneity in grain sizes and use a high number (n > 20) of multi-grain aliquots to derive a mean D_e which will be representative of the full range of dose rates experienced within the sample. To rigorously test the accuracy of date calculations and to restrict the distribution of uncertainties, I then analyse the age estimates using Bayesian statistical methods (e.g. Rhodes et al., 2003).

Bayesian analysis form a quantitative method for taking into account prior information such as the stratigraphic order of samples. Where samples are relatively closely spaced chronologically, and where age estimates overlap, stratigraphic relationships and Bayesian methods can be used to provide additional resolution. Here I use the approach described in Rhodes et al. (2003) using the radiocarbon calibration programme OxCal v 4.3 (Bronk Ramsey, 2009). The calculation of precision-only errors in age estimates is enabled in the python script accounting for water saturation (github.com/jessezondervan/corr_lum_dose_rate), the age outputs of which are fed into the OxCal programme.

4.9 GRAVEL MATRIX AND SAND LENS RESULTS

4.9.1 Luminescence characteristics

Examples of natural decay curves and a sensitivity-corrected growth curve for an aliquot of sample 185824 are shown in Fig 4.7. Blue-light stimulated OSL signals decrease quickly within the first second of stimulation, thus are dominated by the fast component. The dose response curves were fitted using an exponential function, and from this the D_0, a sample dependent constant characterising the filling rate of electron traps (Wintle and Murray, 2006), for each sample was derived. To establish the upper dose limit of the quartz samples, three to six sensitivity-corrected growth curves for each sample were generated, extending beyond 4x the estimated dose of the sample (250 - 600 Gy) with five Li/Ti points. The $2D_0$, the upper dose limit for the samples, is approximately equal for all samples and is ~260 Gy.

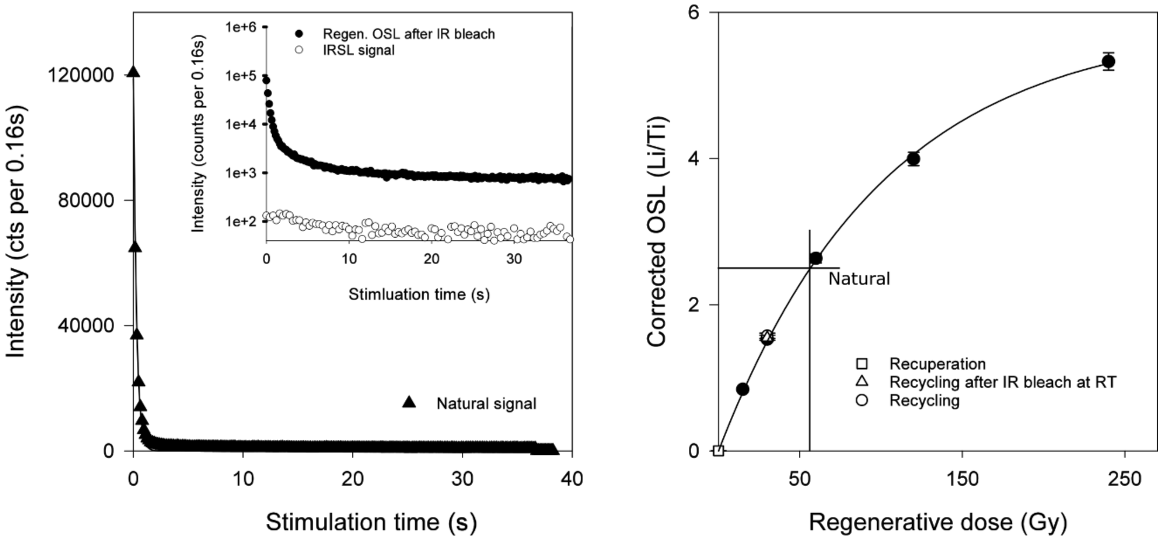

Figure 4.7 – Luminescence characteristic of gravel matrix quartz sample 185824. (a) Natural decay curve of a single disc of 180-250 µm quartz. The inset show the regenerated blue-light and infrared stimulated luminescence (IR_{50}) induced by a 30 Gy regenerative dose. (b) Sensitivity-corrected growth curve for the same aliquot as in (a). Recycled points with and without an infrared bleach before blue-light stimulation are shown as open triangles and circles, respectively. The response to a zero Gray dose (recuperation) is shown as an open square.

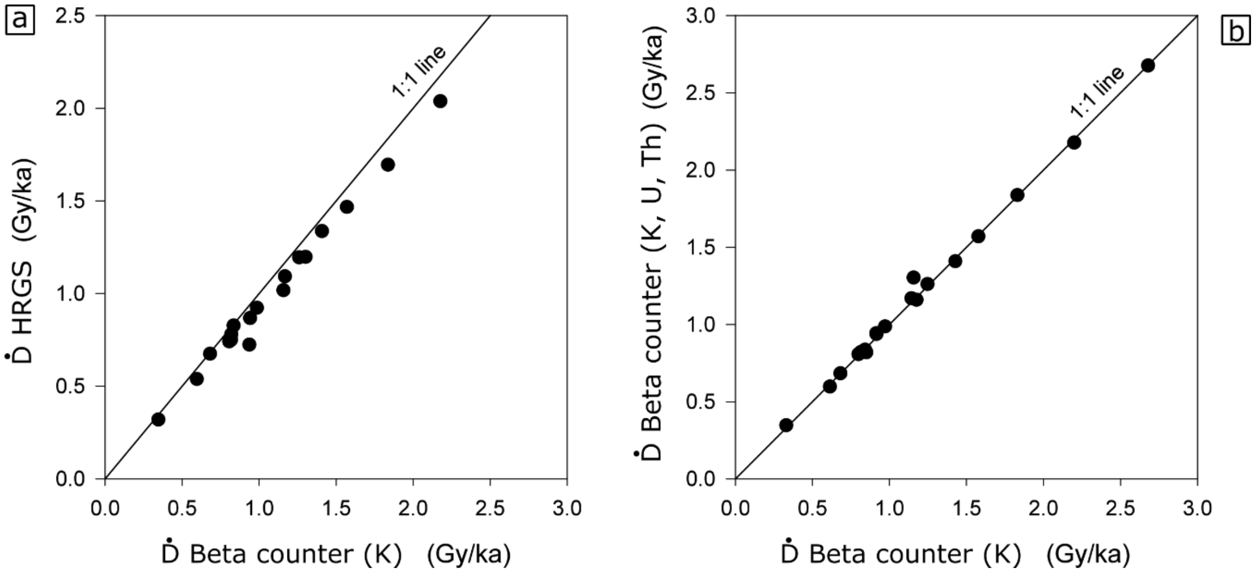

Figure 4.8 – Comparison of Ḋ measurements. (a) Plot of Ḋ values calculated from the gamma spectrometer against Ḋ calculated using the beta counter. (b) Ḋ calculated using beta counter data and K, U, Th data from HRGS against Ḋ calculated using beta counter data and K data from XRF.

4.9.2 Grain size dependent Ḋ

The benefit of using three independent measuring instruments and three Ḋ calculation approaches is that the consistency of all approaches can be tested. A plot of Ḋ HRGS (method 1) against beta counter derived Ḋ using XRF inputs of K concentration (method 2) yields a relationship close to 1:1 (Fig. 4.8a). A plot of beta counter derived Ḋ using XRF inputs of K concentration (method 3) against those calculated with HRGS prior information of K, U and Th source proportions (method 2) yields an almost perfect 1:1 relationship (Fig. 4.8b). Thus, there seems to be no benefit of the instrument-intensive method 2 over a beta-counter only method 3, though there is a slight difference in the measurement of radiation activity between HRGS and beta counter approaches as Ḋ increases.

Ḋ decreases with increasing grain size from the sand fraction to the pebble/cobble fraction (Fig. 4.9a). At site B in particular, the <500 μm fraction has a Ḋ almost three times the Ḋ of the pebble/cobble fraction. Ḋ in this sample is the highest, with values ranging between 1.1 and 2.8 Gy/ka. Nonetheless, due to the volume of pebbles/cobbles their Ḋ dominates the bulk Ḋ measurements. Absolute Ḋ, as well as the Ḋ contrasts for gravels in site A are less than in site B, with Ḋ between 0.4 and 1.2 Gy/ka and a contrast between grain sizes of a factor ~ 2. The Ḋ of grain size fractions are strongly controlled by the sample concentration of K, with higher K concentrations and Ḋ in fine grain size fractions (Fig. 4.9a,b). I find grain size by weight falls into two main groups (Fig. 4.10), grains of <500 μm (coarse sand and finer) and clasts of > 2 cm (pebbles and cobbles). Thus, based on the ratio between HRGS dry beta Ḋ of bulk sediment and the dry beta Ḋ of the <2 mm fraction a correction ratio for the sampled terraces could be calculated and applied to the dry beta Ḋ of all samples. Gamma Ḋ values were taken from bulk measurements as these a

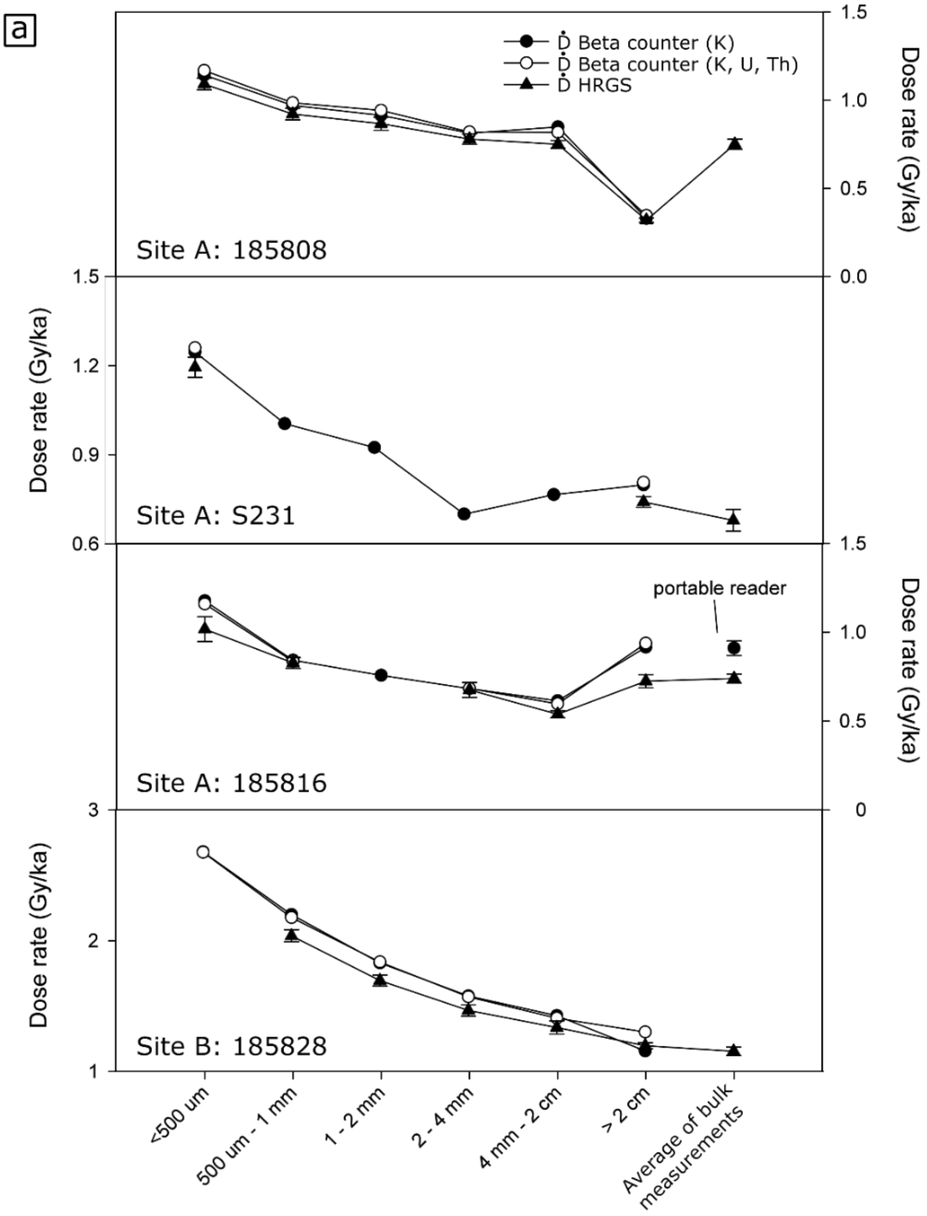
Ḋ Beta counter (K)
Ḋ Beta counter (K, U, Th)
Ḋ HRGS
Site A: 185808
Site A: S231
Site A: 185816
Site B: 185828
portable reader
Dose rate (Gy/ka)
1.5
1.0
0.5
0.0
1.2
0.9
0.6
0
3
2
1
<500 um
500 um - 1 mm
1 - 2 mm
2 - 4 mm
4 mm - 2 cm
> 2 cm
Average of bulk measurements

b

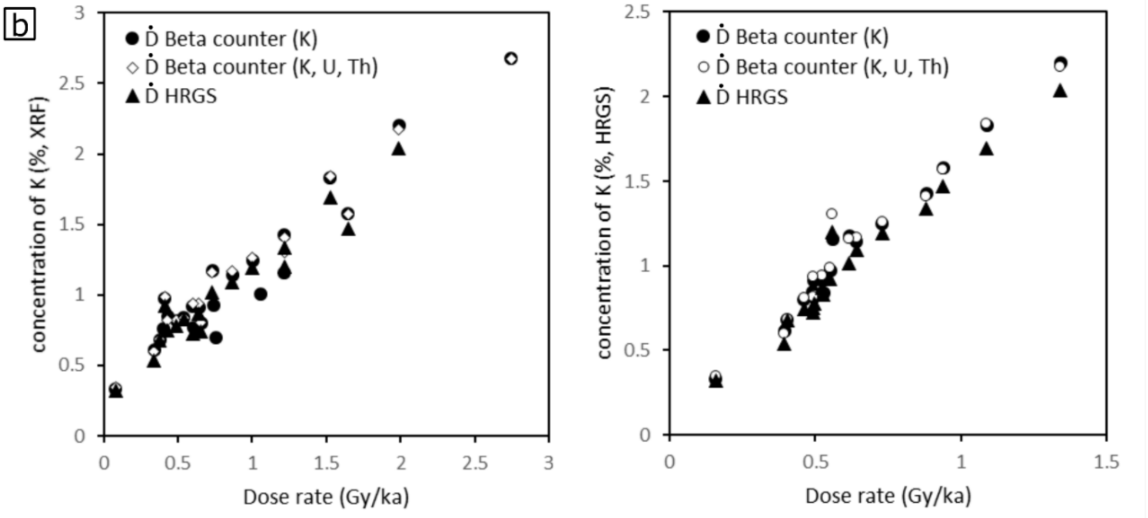
Ḋ Beta counter (K)
Ḋ Beta counter (K, U, Th)
Ḋ HRGS
concentration of K (%, XRF)
Dose rate (Gy/ka)
0
0.5
1
1.5
2
2.5
3
concentration of K (%, HRGS)
Dose rate (Gy/ka)
0
0.5
1
1.5
2
2.5

Figure 4.9 – Dependence of dry beta-plus-gamma $\dot{D}$ on grain-size fraction analysed for four samples, three from the thrust front and one from the wedge-top basin. (a) All samples show an overall trend of $\dot{D}$ decreasing with grain size. Site B in the wedge-top basin has a markedly higher contrast in $\dot{D}$ as well as overall higher $\dot{D}$. Sample 185816 has a bulk measurement using both the lab-based HRGS and the portable gamma spectrometer. (b) Dependency of samples from (a) on sample concentration of K, indicating a strong linear dependence of $\dot{D}$ on K concentration.

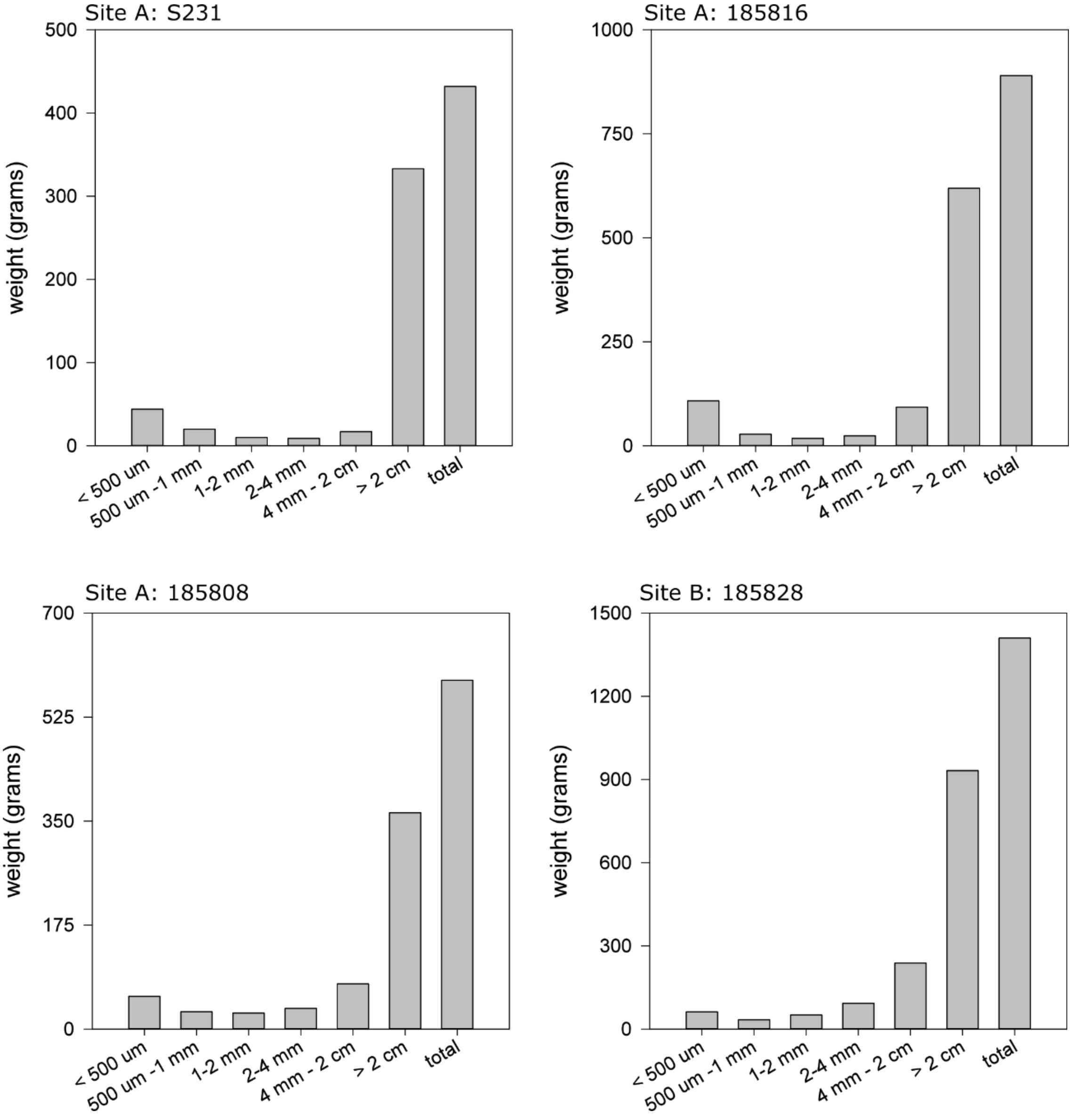

Figure 4.10 – sieved weights of grain size fractions in the sand to pebble range of four gravel samples used for grain-size dependent $\dot{D}$ measurements.

integrate over all grain sizes (Fig. 4.5). Note that the *in situ* $\dot{D}$ of sample 185816 measured by the portable spectrometer is higher than the HRGS measurement of grounded bulk material, which indicates $\dot{D}$ underestimation from grounded bulk $\dot{D}$ samples due to the grain size effect (lower activity of high-volume low surface area carbonate pebbles vs high activity of low-volume high surface area sand and silt). Noticeably, once I apply the correction ratio the bulk $\dot{D}$ estimation is consistent with the field gamma spectrometer value within uncertainties. This means that any potential disequilibrium in the uranium decay chain is likely to be of relatively low importance for dosimetry calculations at this site (Prescott and Hutton, 1995).

4.9.3 *Age models for sites A and B*

The effect of gravel $\dot{D}$ and water saturation corrections on the age-depth plot for the two detailed sections in both sites are shown in Fig. 4.11a. In site A the effect of the gravel $\dot{D}$ correction fixes the internal stratigraphic inconsistency in the uncorrected age model. From this plot, it is clear that without accounting for the grain-size dependent beta $\dot{D}$, age estimates for gravel layers in the section are significantly overestimated. This effect is also visible in the all-gravel section in site B. Water saturation corrections for the aggradation time of terraces result in significant changes to the ages of samples at the base of the sections which have been occupied for ~70 ka. On the other hand, water saturation corrections are insignificant in relation to errors for the samples in the upper parts of the sections where the time between deposition and abandonment is only a few thousand years. The final age-depth model is a function of the D_e values, corrected $\dot{D}$ values and Bayesian statistics (Fig. 4.11b). Two major phases of accumulation can be discriminated in the two sites. In site A, the first accumulation event starts at 170 ka and is followed by

Table 4.1 - OSL sample details, dosimetry data, equivalent dose (D_e) and dose rate ($\dot{D}$) estimates, luminescence ages and Bayesian age models

site	Sample	Depth (m)	Aliquots analysed	Sat water content (%)	Wet water content (%)	Dry gamma contribution (Gy/ka)	Dry beta contribution (Gy/ka)	Gravel correction**	Cosmic contribution (Gy/ka)	De ± se (Gy)	$\dot{D}$ (Gy/ka)	Age (ka)	Precision-only error	Bayesian age (ka)***
Site A	185810	2.1	17	29	1.6	0.44 ± 0.02	0.81 ± 0.03	NA	0.22 ± 0.01	121 ± 9	1.38 ± 0.07	88 ± 10	9	90 ± 8
	185823	2.4	21	21	3.1	0.49 ± 0.02	0.94 ± 0.03	NA	0.21 ± 0.01	144 ± 10	1.49 ± 0.06	97 ± 10	9	97 ± 6
	185809	3	18	18	0.1	0.34 ± 0.01	0.70 ± 0.02	1.4 ± 0.2	0.20 ± 0.01	170 ± 8	1.35 ± 0.12	126 ± 17	16	108 ± 8
	185821	3.6	21	20	1	0.29 ± 0.02	0.53 ± 0.03	1.3 ± 0.1	0.182 ± 0.009	119 ± 5	1.07 ± 0.14	111 ± 17	16	118 ± 7
	185808	3.6	21	29	0.1	0.25 ± 0.01	0.50 ± 0.02	1.32 ± 0.06	0.182 ± 0.009	136 ± 5	0.98 ± 0.09	139 ± 15	14	118 ± 7
	185820	6.3	21	36	1.4	0.39 ± 0.02	0.74 ± 0.03	NA	0.136 ± 0.007	124 ± 4	1.13 ± 0.08	110 ± 11	9	124 ± 7
	S231	7.4	21	18	0.5	0.24 ± 0.01	0.43 ± 0.02	1.6 ± 0.1	0.121 ± 0.006	152 ± 9	0.90 ± 0.11	168 ± 22	21	152 ± 16
	185818	8	21	24	0.2	0.19 ± 0.01	0.39 ± 0.03	1.4 ± 0.1	0.114 ± 0.006	122 ± 8	0.73 ± 0.15	167 ± 28	27	170 ± 21
Site B	185829	1	21	27	1	0.46 ± 0.01	0.93 ± 0.03	1.9 ± 0.2	0.25 ± 0.01	134 ± 4	2.26 ± 0.12	59 ± 8	7	57 ± 7
	185828	1.9	21	10	0.6	0.39 ± 0.01	0.77 ± 0.02	1.9 ± 0.1	0.22 ± 0.01	139 ± 7	1.87 ± 0.10	74 ± 9	8	83 ± 6
	185804	2.2	20	21	0.5	0.25 ± 0.01	0.52 ± 0.02	1.9 ± 0.2	0.21 ± 0.01	142 ± 5	1.24 ± 0.13	115 ± 16	15	96 ± 8
	185806	2.95	21	32	0.5	0.28 ± 0.01	0.59 ± 0.01	1.9 ± 0.2	0.20 ± 0.01	165 ± 9	1.29 ± 0.13	128 ± 19	18	123 ± 14

Others (Ch. 3)	185801	3.5	16	12	0.1	0.22 ± 0.01	0.42 ± 0.02	1.4 ± 0.1	0.184 ± 0.009	75 ± 5	0.90 ± 0.13	84 ± 13	12
	185813*	2.5	6	34	0.4	0.48 ± 0.01	0.89 ± 0.02	1.9 ± 0.2	0.21 ± 0.01	318 ± 33	3.03 ± 0.10	110 ± 15	14
	185817	1	19	27	1.9	0.28 ± 0.03	0.52 ± 0.06	1.4 ± 0.1	0.25 ± 0.01	82 ± 9	1.12 ± 0.27	74 ± 19	19
	185824	4.5	51	15	1.1	0.22 ± 0.01	0.44 ± 0.01	1.4 ± 0.1	0.165 ± 0.008	53 ± 3	0.93 ± 0.13	57 ± 8	8
	185826	5.5	21	17	1.6	0.23 ± 0.01	0.42 ± 0.01	1.4 ± 0.1	0.147 ± 0.007	58 ± 2	0.88 ± 0.13	66 ± 9	9
	185834	0.5	21	20	1.2	0.110 ± 0.004	0.24 ± 0.01	1.4 ± 0.1	0.28 ± 0.01	103 ± 5	0.66 ± 0.12	157 ± 21	20
	185835	1.5	21	36	4.5	0.43 ± 0.03	0.93 ± 0.06	NA	0.24 ± 0.01	105 ± 4	1.39 ± 0.10	76 ± 9	8
	185836	2	21	16	0.2	0.26 ± 0.01	0.53 ± 0.02	1.4 ± 0.1	0.22 ± 0.01	100 ± 6	1.16 ± 0.12	86 ± 12	12
	185837	1.5	21	15	0.1	0.31 ± 0.01	0.62 ± 0.02	1.4 ± 0.1	0.24 ± 0.01	148 ± 6	1.24 ± 0.12	119 ± 16	15

* feldspar IRSL ** Correction of grainsize-dependent dose rate heterogeneity of beta radiation: correction factor to account for underestimation of dry beta dose rates in bulk measurements ***1 % unshared systematic error (USS; Rhodes et al., 2003) has been added for the OSL dates from site A . Site A has an agreement index of 79.9 %, for site B this is 73.4 %, with a value of 60 % considered acceptable.

a major accumulation event from 124 to 90 ka which accounts for the majority of the 10 m terrace deposit preserved today. At site B, accumulation of ~1 m of gravel took place within 128 to 115 ka, and another ~1.5 m between 74 and 59 ka.

4.9.4 *Chronology of all terrace deposits*

The gravel-matrix dating developed in this chapter allows me to date the aggradation time of terraces and the timing of sediment aggradation along the length of the Mgoun River. Dates and sample numbers are presented in Table 4.1, which match the sample numbers on the sedimentary logs of Figs. 3.9 - 3.13. Burial ages in T2 of the downstream Ait Said reach (thrust front) start ~170 ka and continue to 90 ka, after which the strath terrace is abandoned and incised by 30 m to form T1 (Fig. 3.5) starting ~75 ka, which is then abandoned after ~ 50 ka (Fig. 4.12). The incision and abandonment of T2 to form T1 between 90 and 74 ka downstream is in contrast with continued aggradation of T2 further upstream in the midstream Bou Tharar reach (thrust-front) from 119 to 84 ka constrained by two dated samples. However, the 90-74 ka incision period leading to strath abandonment in the downstream Ait Said reach (thrust front) can be linked to a hiatus in the extensively dated T2 in the upstream Ait Toumert reach (wedge-top basin; Figs. 4.11, 4.12). Aggradation of T2 in the upstream Ait Toumert reach (wedge-top basin) occurs through 128 to 59 ka (Fig. 4.12). The start of this T2 planation correlates with the dating of overbank sands which define an incisional period for T2 in the downstream Ait Saïd reach (thrust front).

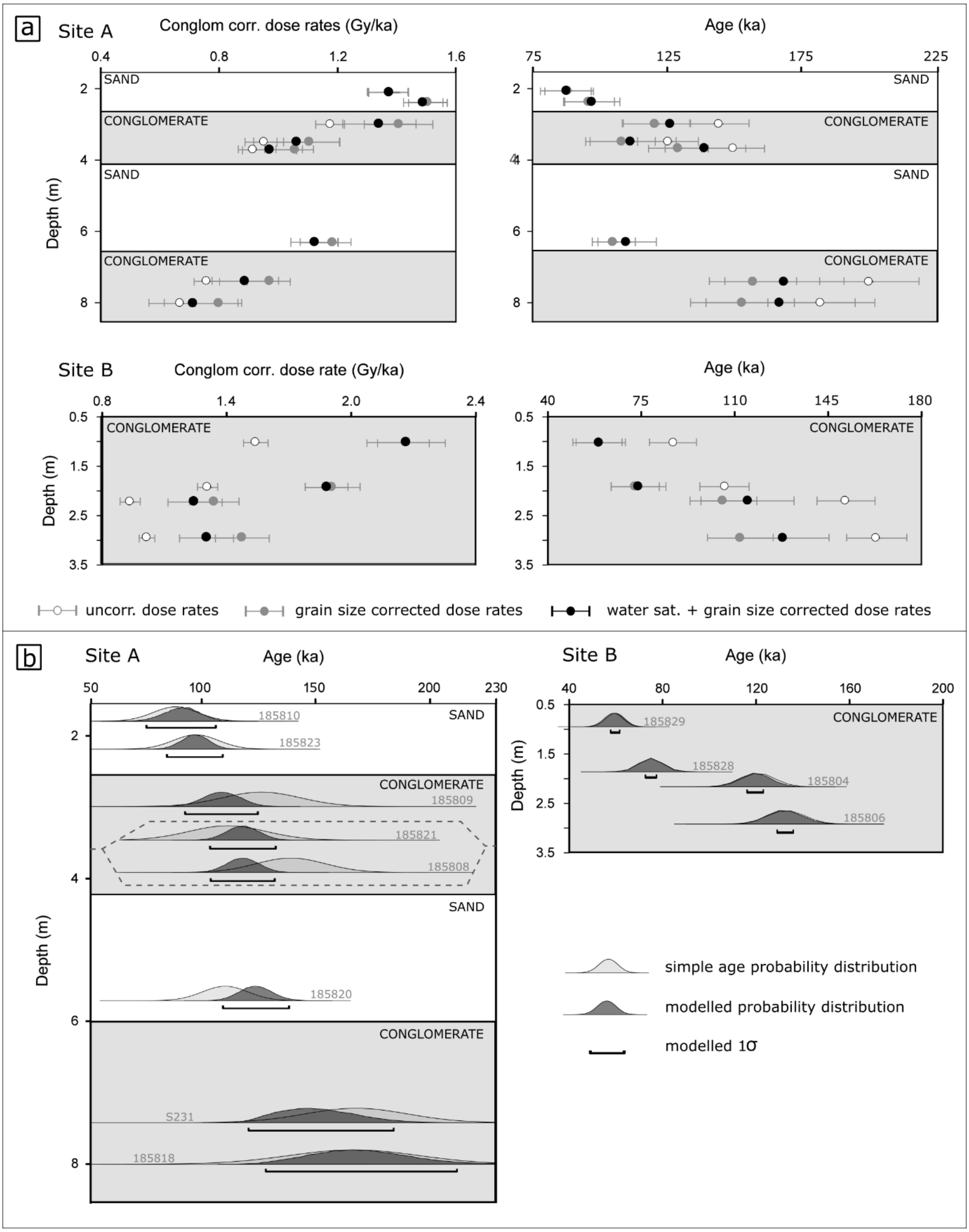

Figure 4.11 – Age-depth profiles for sites A and B. (a) Calculated $\dot{D}$ and ages against depth for sediment overlying straths of sites A and B. The graphs plot the effect of the corrections for grain size heterogeneity and water saturation history. (b) Age probability distributions and one standard deviation of Bayesian model accounting for stratigraphic information vs the data prior to Bayesian modelling.

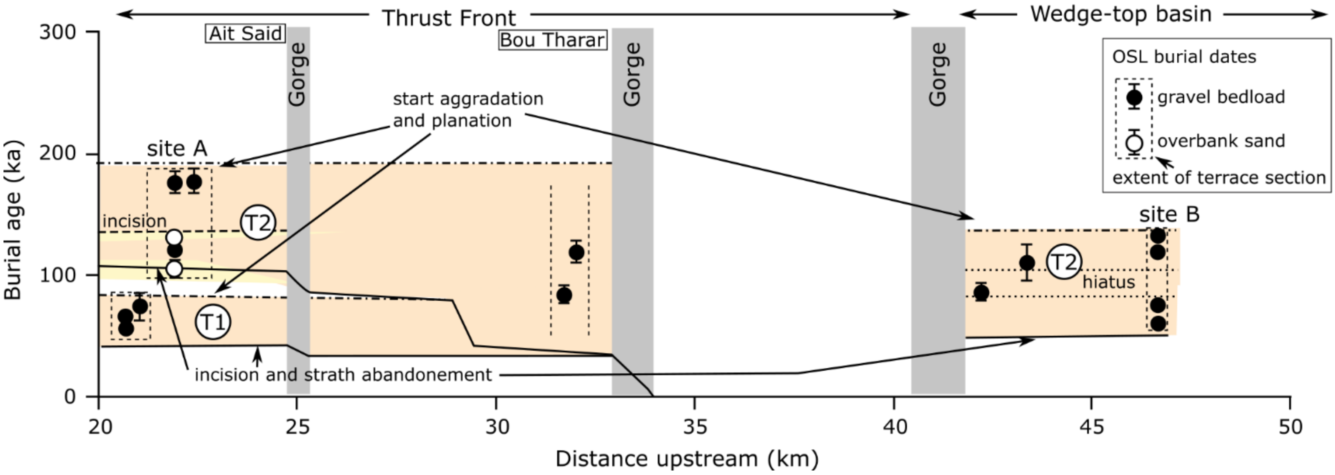

Figure 4.12– OSL burial ages against the distance upstream along the Mgoun River. Filled and open circles represent samples of gravel bedload and overbank sand material, respectively. The start of terrace aggradation and planation of a terrace level is constrained by the bedload at the base of terraces. Overbank sand deposition marks incisional phases, which may or may not lead to strath surface abandonment by bedrock incision. Bedrock incision of the strath surface is constrained by the burial chronology as well as terrace stratigraphy and river long profile form described in chapter 3. Note that a hiatus recorded at site B in the wedge-top basin correlates with incision and strath abandonment in the thrust front.

4.10 STRATH LUMINESCENCE-DEPTH PROFILE RESULTS

Results from natural and regenerative dose signals for strath samples from site A include IR_{50} and OSL decay curves (Fig. 4.13a,b). The OSL decay curves show slow as well as a fast component, and the IR_{50} curves show a slow component. The TL curve has an identifiable 110 °C quartz peak, indicating a mix of quartz and feldspar in this bedrock material (Fig. 13c). The blue-light stimulated signal is much stronger than the infrared-stimulated signal indicating a larger quartz contribution. Peaks of OSL and IR_{50} signals after a 100 Gy regenerative dose are about a factor of two lower than the natural signals, pointing to values close to saturation of the slice taken from the bottom of the strath sample.

Results from natural and regenerative dose signals for site B include IR_{50} and $pIRIR_{225}$ decay curves (Fig. 4.13d,e). Regenerative doses of 100 Gy result in lower peaks than in the natural decay curves and suggest doses approaching

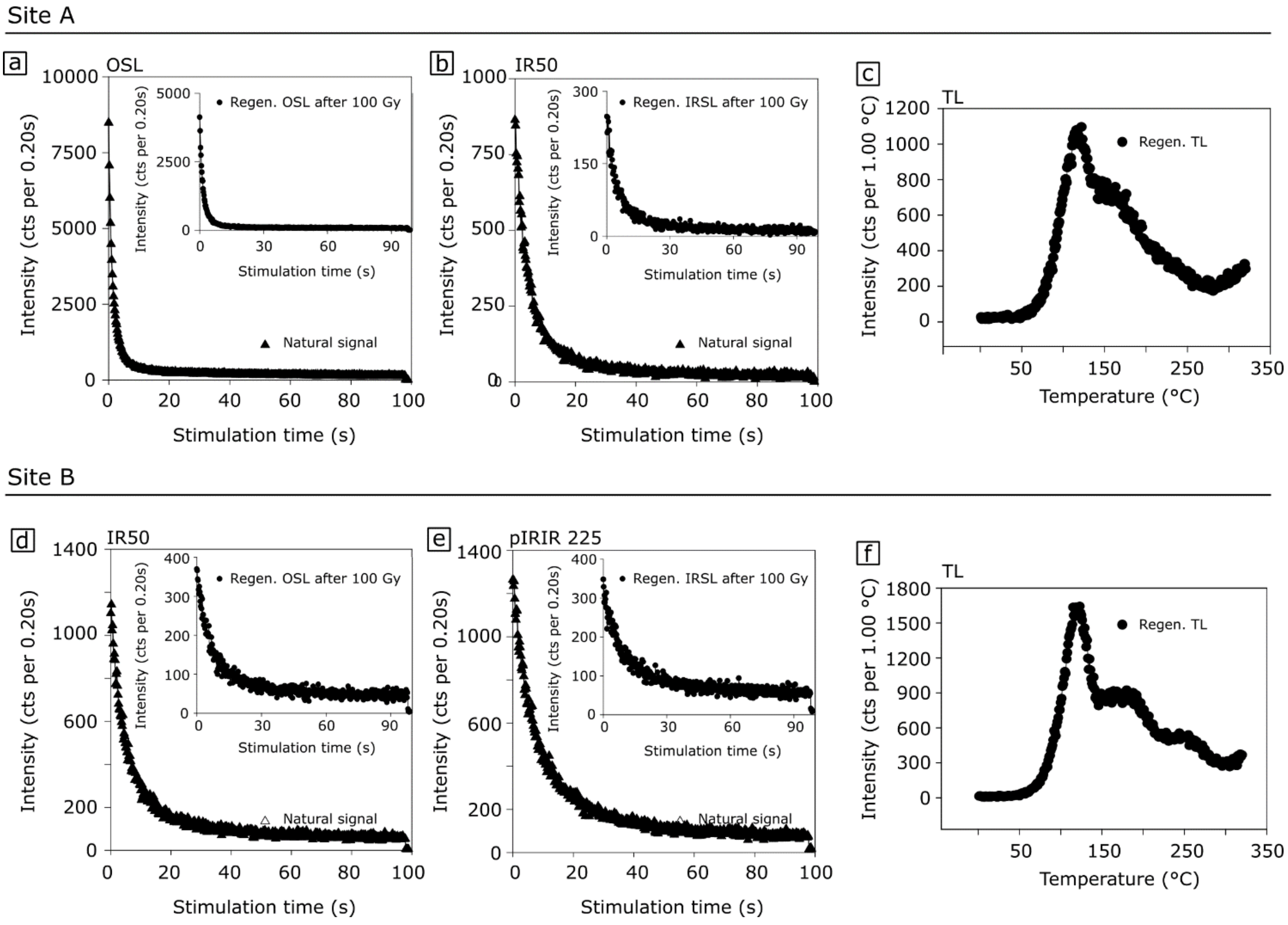

Figure 4.13 - Luminescence characteristics of bedrock strath samples. (a) Natural decay curve of a single cup of lose red sandstone grains from site A. The inset show the regenerated blue-light stimulated luminescence induced by a 100 Gy regenerative dose. (b) Natural decay IRSL curve of a single cup of lose red sandstone grains after 50 °C preheat. The inset shows the infrared stimulated luminescence (IR$_{50}$) induced by a 100 Gy regenerative dose. (c) TL curve of the same aliquot as in (b) showing a 110 °C quartz peak. (d) Natural IRSL curve of a single slice from bedrock in site B after 50 °C preheat. The inset show the infrared stimulated luminescence (IR$_{50}$) induced by a 100 Gy regenerative dose. (e) Natural decay IRSL curve the same slice as (d) after 225 °C preheat (pIRIR$_{225}$). The inset show the infrared stimulated luminescence (pIRIR$_{225}$) induced by a 100 Gy regenerative dose. (f) TL curve of the same aliquot as in (e) showing a 110 °C quartz peak.

saturation in the bottom slice of the strath sample. The TL curve shows a 110 °C quartz signal (Fig. 13f), indicating a mix of quartz and feldspar in this sample.

The sensitivity-corrected luminescence Ln/Tn (natural to test signal) OSL, IR$_{50}$ and pIRIR$_{225}$ profiles with depth for the two straths do not show any bleaching signals (Fig. 4.14). The strath surface at site A seems to be in

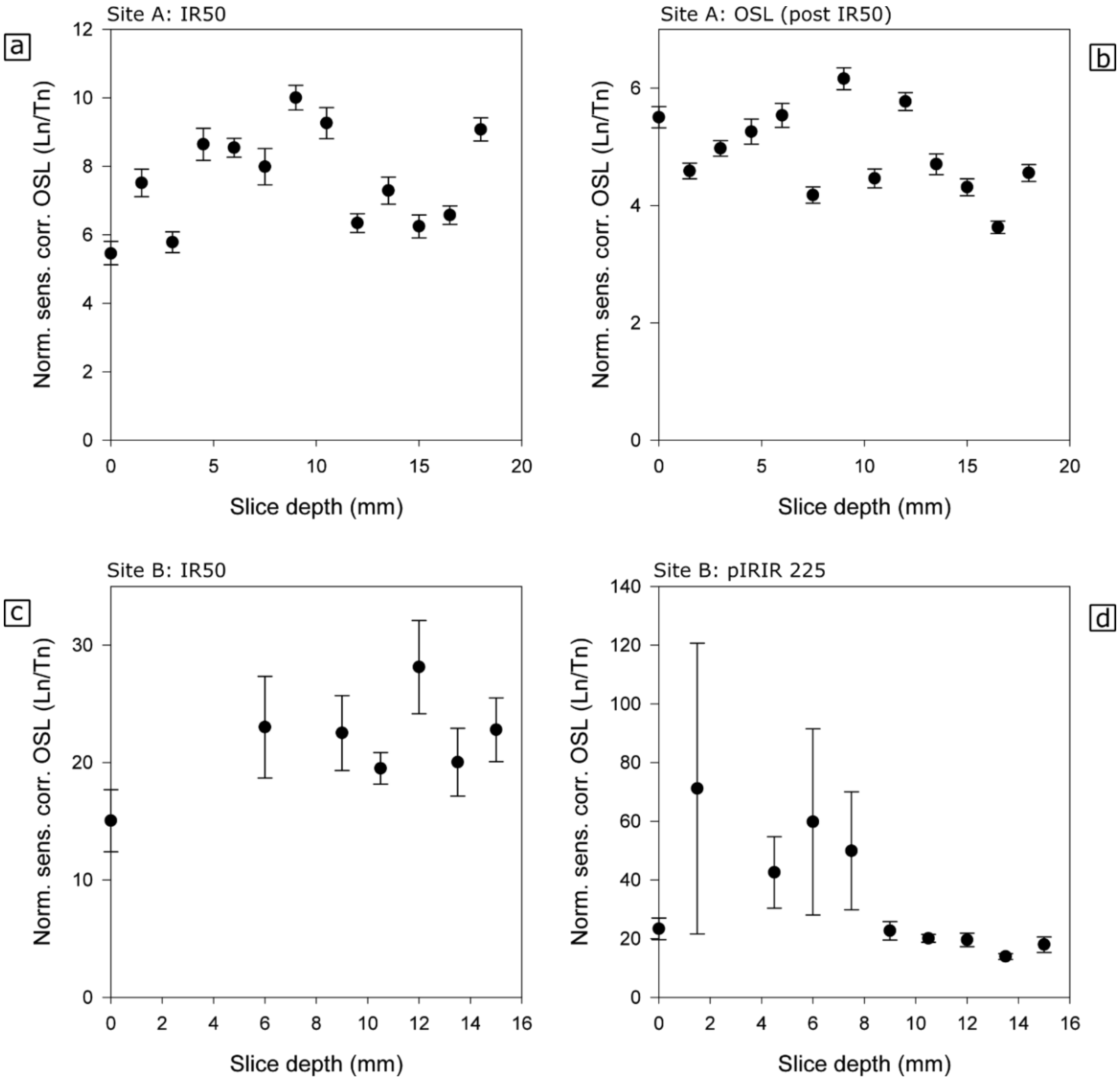

Figure 4.14 - Measured luminescence-depth profile of two bedrock straths. Depth = 0 mm is the top surface (facing the top of the strath surface). Solid rock slices were broken into a minimal of four pieces and each data point is an average of three pieces or aliquots. Error bars represent one standard error. (a) IR_{50} depth profile for site A. The first slice has a lower IRSL signal than the rest of the core. (b) OSL depth profile for site A. There is no apparent bleaching signal. (c-d) IR_{50} and $pIRIR_{225}$ depth profiles of site B. There is no apparent bleaching signal.

saturation (Fig. 4.14a,b), and the strath surface at site B has a few slices which have very low or no infrared-stimulated regenerative signals indicating feldspar-poor spots (Fig. 4.14c,d).

4.11 CLAST LUMINESCENCE-DEPTH PROFILE RESULTS

Three possible quartz and/or feldspar bearing lithologies from non-exposed material were tested for OSL and IRSL signals: a chert pebble derived from limestone units, a pebble of igneous origin and a pebble of red sandstone. None of the clasts tested showed a strong IRSL signal. The igneous quartz signal was also weak to non-existent (Fig. 4.15). Both the natural and regenerative decay curve are very weak, and the TL curve peaks at 150 °C (Fig. 4.15), instead of 110 °C which would be expected if there was a sensitive quartz presence. For the chert pebble, the regenerative curve and distinct 110 °C TL peak (Fig. 4.15) point to OSL sensitivity of the microcrystalline quartz. However, whilst the regenerative curve shows a strong signal (Fig. 4.15), it has a very slow decay rate, and the weak to non-existent natural decay signal (Fig. 4.15) suggests the signal is not stable and thus not viable for dating purposes. Red sandstone has the strongest 110 °C peak, with a strong low-rate regenerative decay curve and a natural decay signal that is stronger than that of the 70 Gy regenerative curve (Fig. 4.15). These properties point to an OSL signal that is both sensitive and stable, thus making this the only suitable lithology to perform further clast dating tests on. Site B was chosen for its abundance of red sandstone clasts. The first slice of a buried face of the pebble displays a strong natural decay signal and a regenerative signal shows minimal IR_{50} indicating low feldspar levels (Fig. 4.16). The growth curve for this slice is also shown, including the recycling, which is close to one, and the recuperation which indicates the curve goes through the origin (Fig. 4.16). Thus, the quartz in this pebble shows a very healthy OSL response. Of the twelve sandstone pebble cores explored for profiles, seven of the eight cores from the exposed faces of pebbles have completely bleached first slices, and all of the four cores from the buried faces have unsaturated first slices (Fig. 4.17). Five out of the seven bleached cores have unsaturated second slices, and

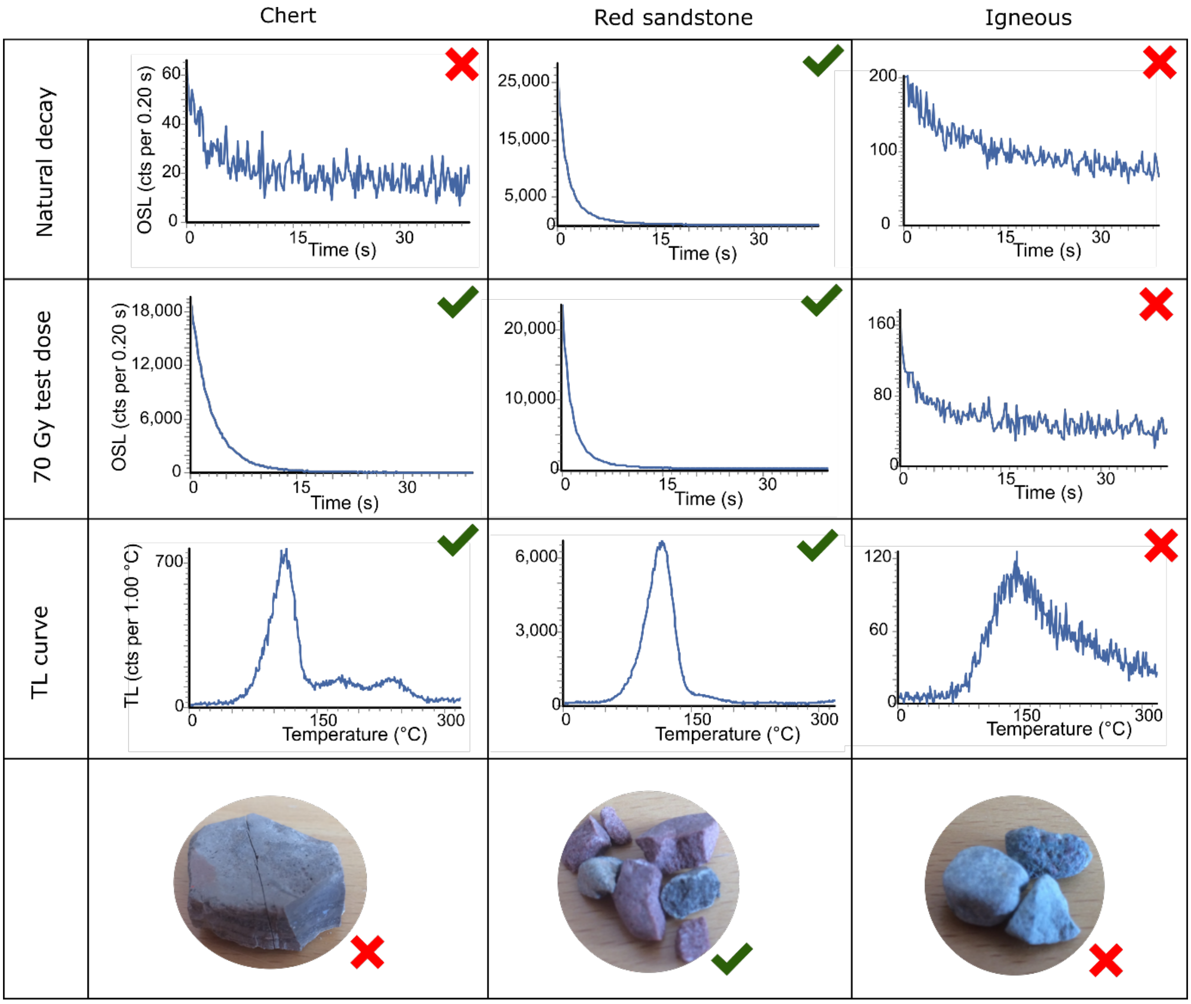

Figure 4.15 – suitability of rock types for further OSL rock exposure dating tests based on three criteria: signal presence (first row), signal stability (second row)) and presence of quartz (third row). The natural decay curve of non-exposed buried rock samples should give a luminescence signal. The regenerated blue-light luminescence signal induced by a 70 Gy regenerative dose should result in a readable fast component to noise ratio. The TL curve should show a peak at 110 °C if quartz is present.

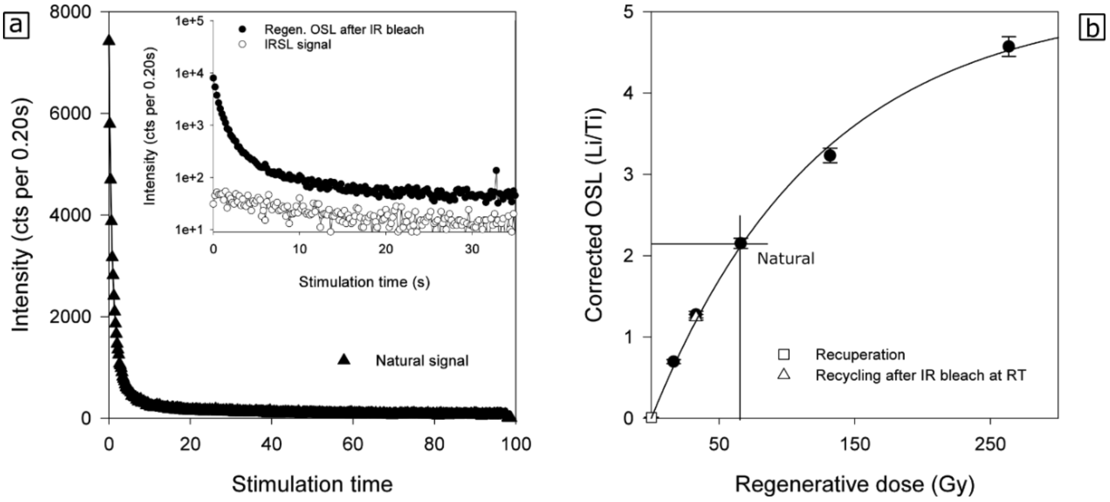

Figure 4.16 – Luminescence characteristics of red sandstone pebble samples. This pebble was taken from sediment cover on top of the strath surface. The first slice of the buried side of the clast was sampled. (a) Natural decay curve of a single slice. The inset show the blue-light and infrared stimulated luminescence (IR50) induced by a 26 Gy regenerative dose. (b) Sensitivity-corrected growth curve for the same slice as in (a). The response to a zero Gray dose (recuperation) is shown as an open square. A recycled point with an infrared bleach before blue-light stimulation is shown as an open triangle.

one has a third unsaturated slice (Fig. 4.17). One profile consisting of twelve slices, up to 16.5 mm into the buried face of a pebble, exhibits an unsaturated surface slice with a significantly lower Ln/Tn than the saturated slices behind it (Fig. 4.18). Based on these results I used the first slice of pebble surfaces facing the buried side of the section to measure D_e values. $\dot{D}$ values come from samples of the pebble and surrounding sediment. Ages determined from the first slice of the buried face of pebbles result in the majority plotting within the aggradation time of the terrace (Fig. 4.19), constrained by dating of the gravel matrix. Three slices have calculated apparent ages younger than this aggradation time (Fig. 4.19), and these might have been bleached during the process of sampling. Three points lie above the aggradation time (Fig. 4.19), and these have doses more than $4D_0$, thus significantly out of the range of the technique. Surface burial ages also vary significantly within the same clast.

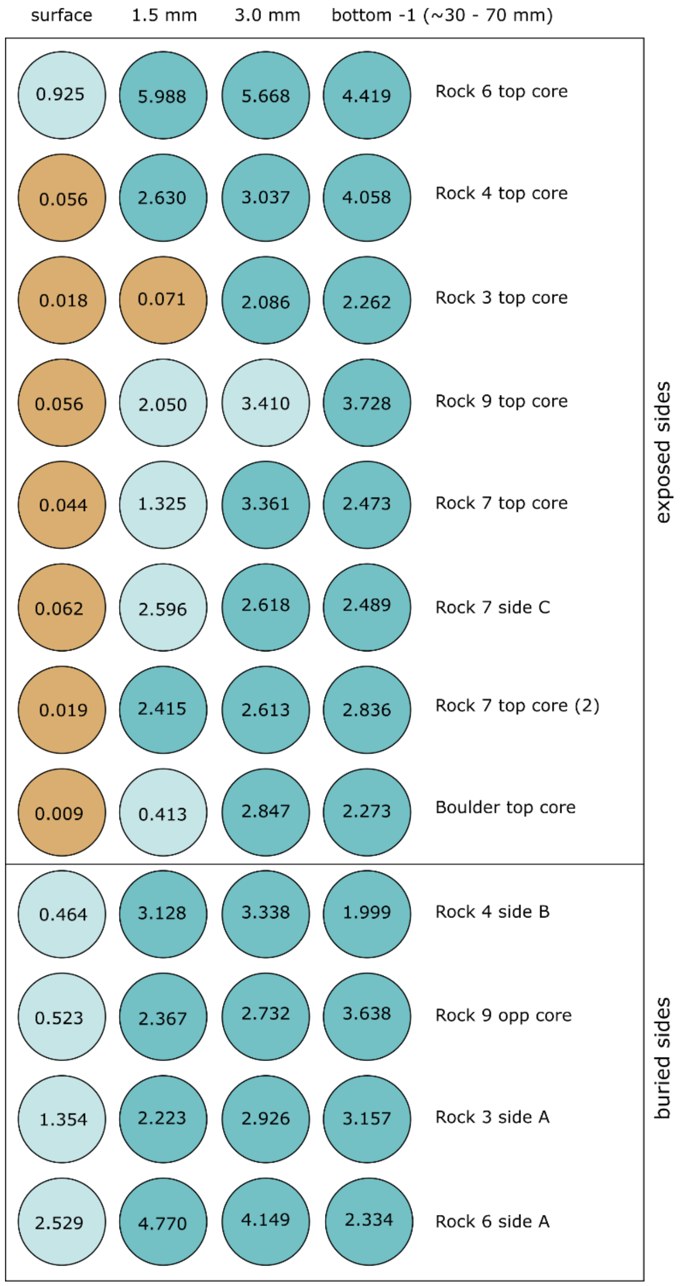

surface	1.5 mm	3.0 mm	bottom -1 (~30 - 70 mm)		
0.925	5.988	5.668	4.419	Rock 6 top core	exposed sides
0.056	2.630	3.037	4.058	Rock 4 top core	
0.018	0.071	2.086	2.262	Rock 3 top core	
0.056	2.050	3.410	3.728	Rock 9 top core	
0.044	1.325	3.361	2.473	Rock 7 top core	
0.062	2.596	2.618	2.489	Rock 7 side C	
0.019	2.415	2.613	2.836	Rock 7 top core (2)	
0.009	0.413	2.847	2.273	Boulder top core	
0.464	3.128	3.338	1.999	Rock 4 side B	buried sides
0.523	2.367	2.732	3.638	Rock 9 opp core	
1.354	2.223	2.926	3.157	Rock 3 side A	
2.529	4.770	4.149	2.334	Rock 6 side A	

Figure 4.17 – Natural signal to test signal ratio (Ln/Tn, where the test dose is 26 Gy) for twelve cores through pebbles from site B. Eight cores come from the exposed face of pebbles exposed in the terrace section. Four cores come from the face buried in the terrace. Slices are ~1.5 mm apart. The Ln/Tn of the three top slices and the bottom slice of the drilled core are displayed. Bleached slices are highlighted in orange, saturated slices in blue. Light-blue slices have values in between bleached and saturated.

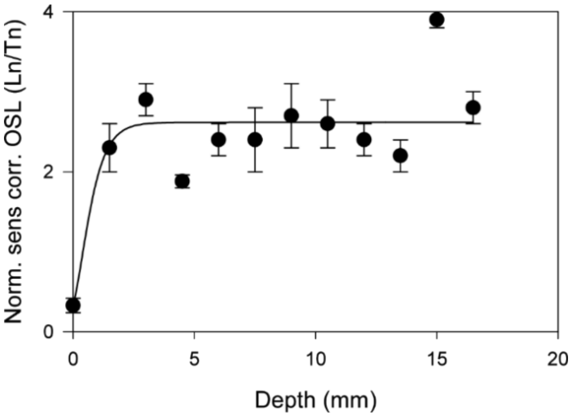

Figure 4.18– Measured luminescence-depth profile of sample 185809. Depth = 0 mm is the top surface (facing the buried surface into the terrace section). Rock slices were broken into a minimal of four pieces and each data point is an average of three pieces. Error bars represent one standard error. Only the first slice is bleached and all subsequent slices are at saturation level.

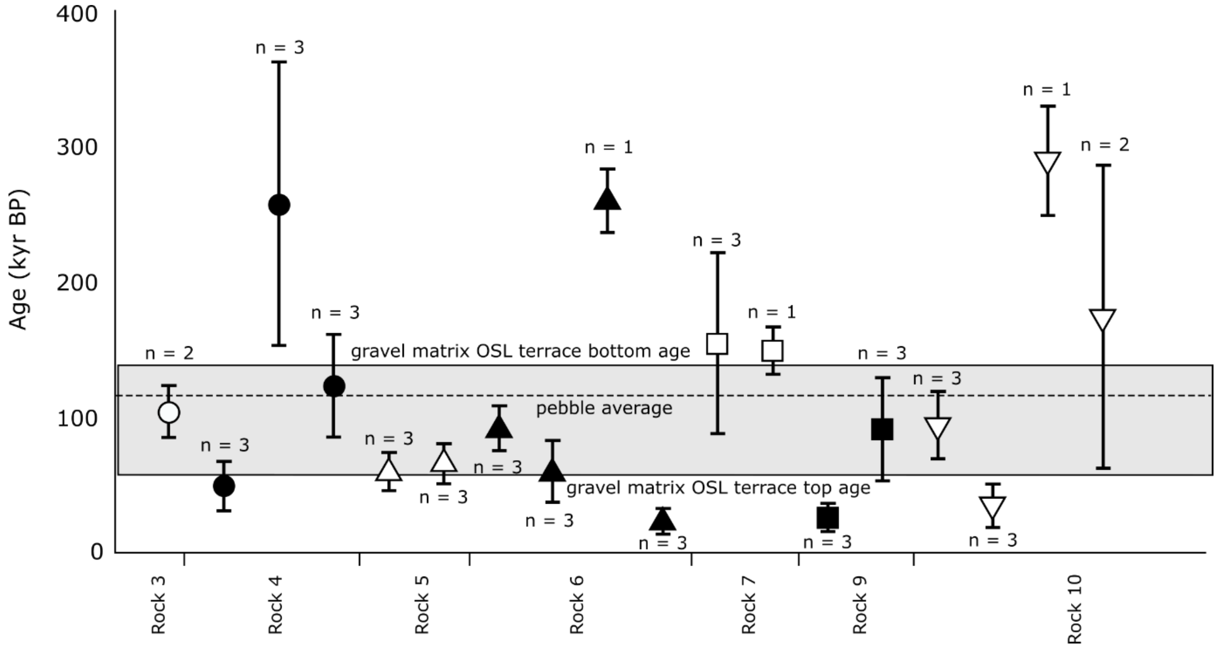

Figure 4.19– first slice ages of pebbles and cobbles in T2 in the wedge-top basin. The grey box is the aggradation time of the terrace from OSL dating of the gravel matrix. Error bars include standard error on D_e measurements, and uncertainty in sediment and rock sample derived $\dot{D}$. n: number of measurements per rock slice.

4.12 DISCUSSION

4.12.1 Gravel matrix and sand lens results

Corrections for OSL on terrace gravel matrix

The relatively high saturation level ($2D_0$ ~260 Gy) and low $\dot{D}$ for gravel matrix samples, due in part because of low gamma rates from surrounding carbonate pebbles and cobbles (Fig. 4.10), enables me to use quartz OSL up to ~ 250 ka. Thus, when coupled with beta $\dot{D}$ determination of finer material within gravels, the dating of gravels might actually be preferable over the dating of sand lenses if the material is expected to push the age limit of the OSL method. To use OSL on terrace gravel matrix, I developed approached for two necessary corrections. Firstly, $\dot{D}$ values were found to vary within a factor of two to three in grain size fractions from fine sand to cobble/boulder material (Fig. 4.9a). These $\dot{D}$ values strongly correlate with concentration of K (Fig. 4.9b), which reflects a higher presence of K feldspar in the sand fraction, and scarce K sources in the carbonate pebble and cobble material. Consequently, laboratory measurements of bulk crushed and powdered material lead to underestimations of $\dot{D}$ (Fig. 4.9a). The terrace section with intermittent gravels and sands shows an inconsistent age-depth profile before correction of gravel $\dot{D}$ values, which is fixed when the beta $\dot{D}$ values of finer grain sizes are used in combination with bulk gamma $\dot{D}$ values leading to an age model consistent with stratigraphic constraints (Fig. 4.11a). I find the grain size beta dose correction to have a more significant effect than the water saturation model corrections accounting for water fluctuations in strath terraces. The effect of prolonged water saturation during aggradation becomes more important for samples that experienced ~ 70 kyr aggradation and saturation before the river plain was abandonment and incised to create a strath terrace. In such cases the correction leads to shifts of several thousand years (Fig.

4.11a). Thus, the water saturation history correction is especially important for terraces with long aggradation times, such as in the High Atlas as well as the US Midwest (e.g. Foster et al., 2017), though probably less so in high uplift regions such as the European and New Zealand Alps where terrace levels are quickly abandoned after planation and aggradation (e.g. Brocard et al., 2003; Zinke et al., 2017).

Age models

The age-depth models (Fig. 4.11b) indicate non-linear accumulation rates, with the age-depth profiles in the thrust front and wedge-top basin both showing two main aggradation periods spaced out by 30 to 40 kyr (Figs. 4.20, 4.21). The OSL burial data presented here are able to illuminate timing of bedload aggradation of strath terraces. Thus, the aggradation time of several tens of thousands of years – 80 kyr in the thrust front – and multiple accumulation events within one terrace emerging from the chronology highlight the need and opportunities for careful and high-resolution sample collection within single strath terraces. Furthermore, a comparison of burial dates from terraces in three reaches of the Mgoun River helps to constrain the synchronicity of terrace aggradation and abandonment in the catchment in response to climatic change (§1.4.2). Summed probability density curves of gravel bedload burial ages for the downstream Ait Said reach (thrust-front), midstream Bou Tharar reach (thrust-front) and upstream Ait Toumert reach (wedge-top basin) correlate at an MIS 5e peak around 124-119 ka (Fig. 4.21). In the downstream Ait Said reach (thrust-front) this period is followed by a 20 ka long incisional event leading to the planation of a new terrace at 74 ka. This incisional period corresponds to the abandonment of foreland basin terraces recorded by cosmogenic data from Arboleya et al. (2008; Fig. 4.21a) and incision of strath terraces along the Dades River in the fold-thrust belt

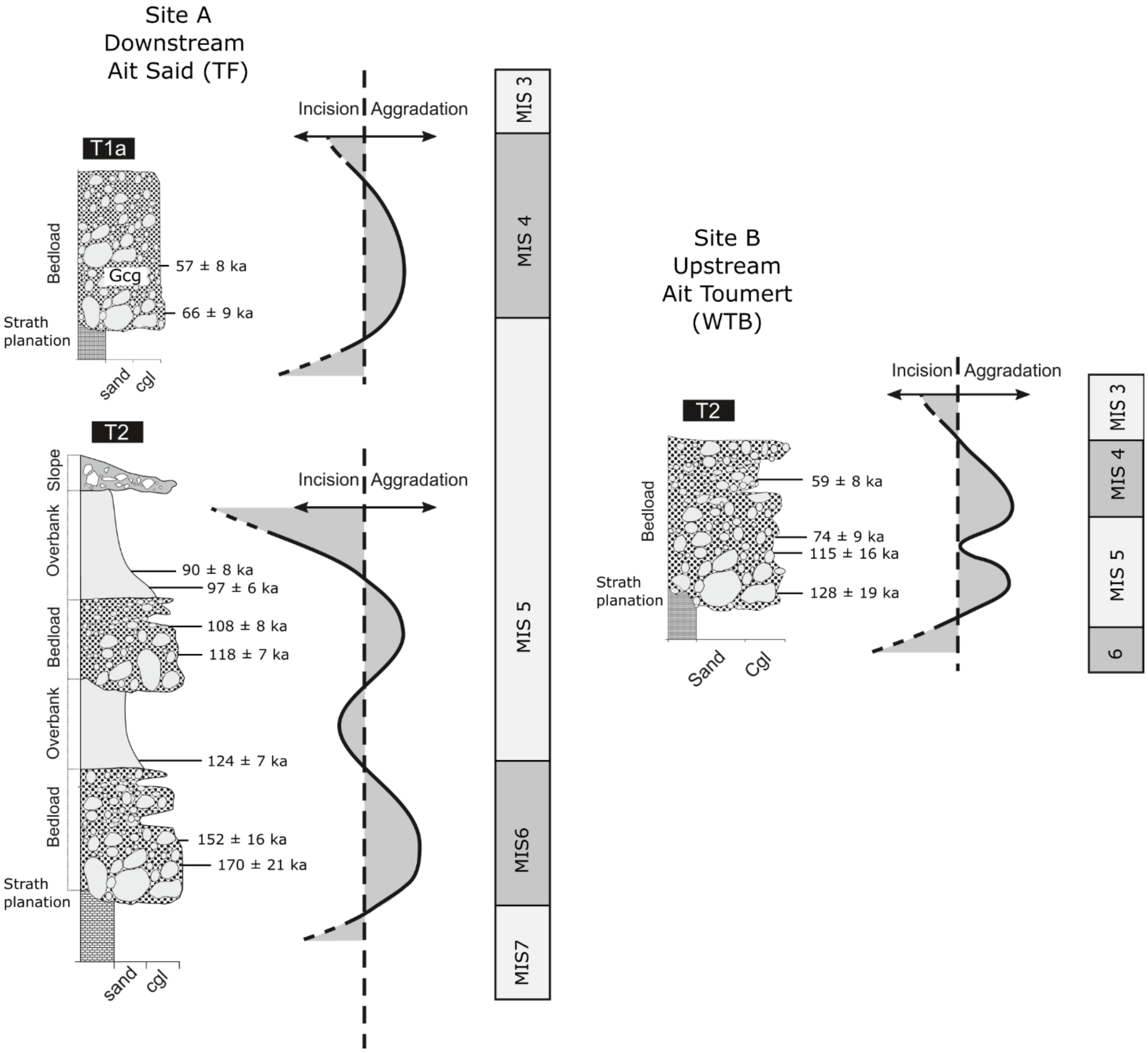

Figure 4.20 - Illustration of strath terrace deposits, chronology and the relationship between valley floor incision-aggradation and MIS stages (c.f. Stokes et al., 2017). Bedload data from this figure is used to project the age distribution of bedload aggradation through time in Fig. 4.21. Note that site A has a substantially thicker series of deposits over T2 and T1 spanning the same time as T2 in site B, and that the vertical scale is not linear with time.

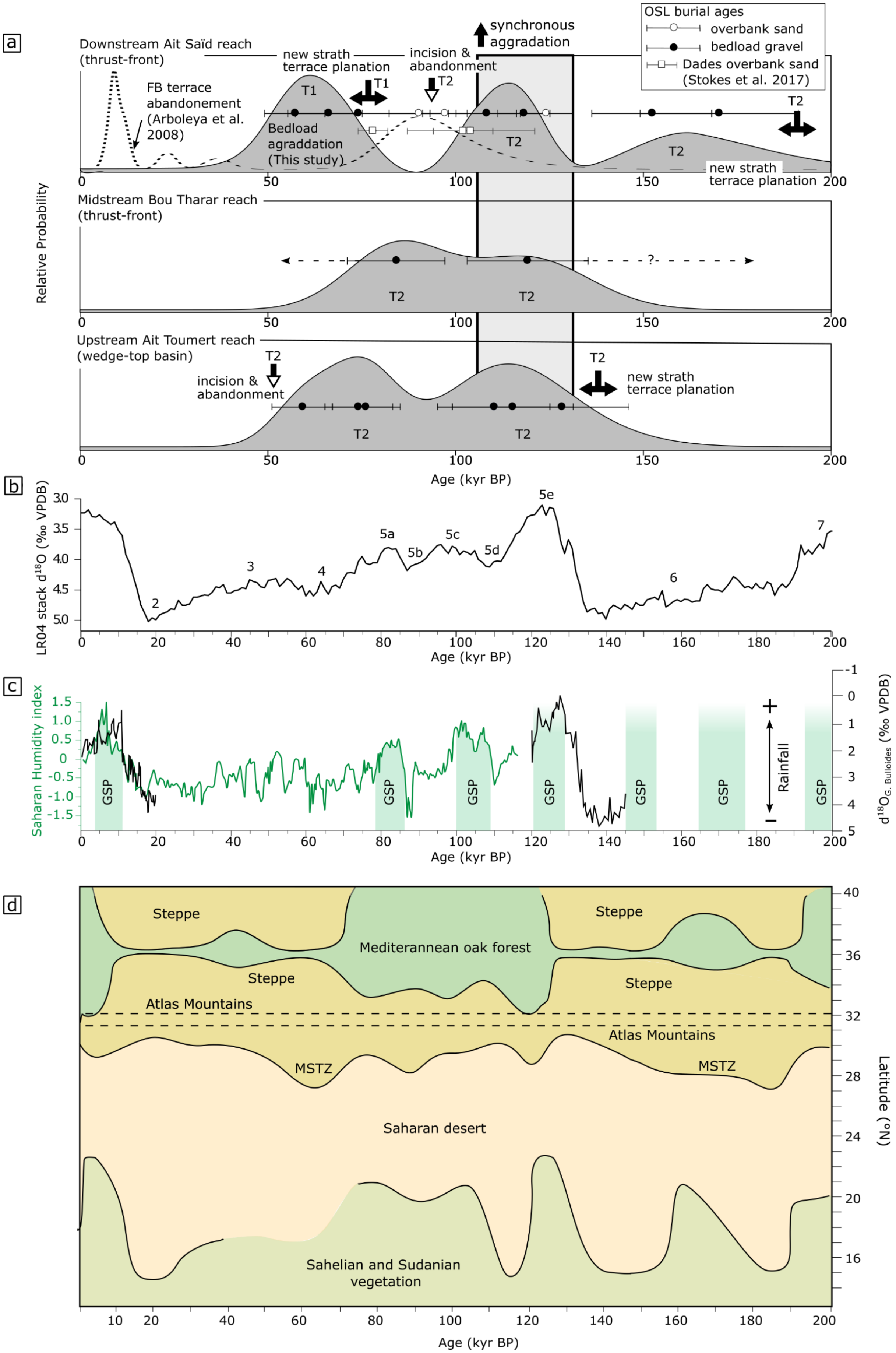
a
Downstream Ait Saïd reach
(thrust-front)
new strath
terrace planation
incision &
abandonment
synchronous
aggradation
OSL burial ages
overbank sand
bedload gravel
Dades overbank sand
(Stokes et al. 2017)
FB terrace
abandonement
(Arboleya et al.
2008)
T1
T1
T2
Bedload
agraddation
(This study)
T2
T2
T2
new strath
terrace planation
Relative Probability
Midstream Bou Tharar reach
(thrust-front)
?
T2
T2
Upstream Ait Toumert reach
(wedge-top basin)
T2
incision &
abandonment
T2
new strath
terrace planation
T2
T2
0
50
100
150
200
Age (kyr BP)
b
LR04 stack d¹⁸O (‰ VPDB)
3.0
3.5
4.0
4.5
5.0
2
3
4
5a
5b
5c
5d
5e
6
7
0
20
40
60
80
100
120
140
160
180
200
Age (kyr BP)
c
Saharan Humidity index
1.5
1.0
0.5
0
-0.5
-1.0
-1.5
GSP
GSP
GSP
GSP
GSP
GSP
GSP
+
Rainfall
−
-1
0
1
2
3
4
5
d¹⁸O G. Bulloides (‰ VPDB)
0
20
40
60
80
100
120
140
160
180
200
Age (kyr BP)
d
Steppe
Steppe
Mediterannean oak forest
Steppe
Steppe
Atlas Mountains
Atlas Mountains
MSTZ
MSTZ
Saharan desert
Sahelian and Sudanian
vegetation
40
36
32
28
24
20
16
Latitude (°N)
10
20
40
60
80
100
120
140
160
180
200
Age (kyr BP)

Figure 4.21 – Burial age data in context of orbital climate changes. (a) OSL results plotted as scatter points and summed probability distributions for bedload burial ages in terraces in three river reaches. Terrace levels based on the stratigraphy presented in Ch. 3 are labelled. In addition to plotted overbank sands dated in the Dades River (Stokes et al., 2017), the summed probability distribution of foreland basin terrace abandonment from Arboleya et al. (2008) is projected on the graph for the downstream Ait Said reach in the thrust-front. (b) The marine oxygen isotope (MIS) record for the last 200 ka, based on the LR04 benthic $\delta^{18}O$ stack constructed by Lisiecki and Raymo (2005), with MIS stages labelled. (c) Green Sahara periods are after Larrasoaña et al. (2013), the Saharan humidity index is from borehole GeoB7920 (see Fig. 1.1) after Tjallingii et al. (2008), and the $\delta^{18}O$ record of relative rainfall is from (Dixit et al., 2020). (d) Latitudinal position of Mediterranean to Sahelian vegetation zones based on marine pollen records, after Agwu and Beug (1982), Dupont and Hooghiemstra (1989), Dupont and Agwu (1992), Hooghiemstra et al. (1992) and Dupont (1993). For a description of the NW African palaeoclimate see §1.4.2.

recorded by OSL dates in overbank sands (Stokes et al., 2017). In the midstream Bou Tharar reach (thrust-front) aggradation continues during this time. In upstream Ait Toumert reach (wedge-top basin), after a depositional gap in the record centred around 90 ka, the record of gravel bedload accumulation reaches another peak around 76 – 59 ka. Abandonment of T2 in this reach and T1 in the downstream Ait Said reach (thrust-front) occurs after 59 ka. Thus, incision and aggradation are asynchronous between reaches in the Mgoun catchment, whilst one synchronous river channel aggradation event occurs throughout the basin during interglacial MIS 5e. Overall, river terrace chronology is not in sync with Green Sahara periods occurring on precessional timescales (~ 26 kyr cycles), but this does not mean these periods do not affect terrace formation. In particular, tropical incursions during the GSP of the MIS 5e interglacial maximum is likely to have penetrated further north towards the High Atlas, thus increasing geomorphic action.

4.12.2 Strath profiles

OSL as well as IRSL methods were applied to two bedrock straths, and of all the approaches blue-light generated stimulation produced the most luminous response (Fig. 4.13). Thus, any further investigation into strath terrace profiles in this study area I advise should use blue-light approaches. None of the blue-light and infrared luminescence-depth profiles through bedrock strath samples gave evidence of surface exposure, with all slices, including the top slice, at saturation (Fig. 4.14). The absence of exposure signals in IRSL profiles is important in this conclusion, as IRSL signals take significantly longer to saturate than OSL signals, up to ~ 900 kyr, and dating of the overlying sediments gives an age range of straths in the two terraces of ~ 170 to 130 ka. This means either strath planation occurred while the riverbed was fully covered by bedload, or if bedrock was exposed, gravel accumulation was paired with stripping of any exposed layer. Since the clast profiling pilot established light does not penetrate red sandstone material more than 1.5 to 3 mm, such an erosion event does not need to be very extensive to erase any record of bedrock strath exposure. Thus, any future attempts to constrain strath planation using luminescence surface dating should target translucent bedrock material, such as clear sandstone or granites.

4.12.3 Clast profiles

Of all the clast lithologies tested for a luminescence signal, the only suitable signal found was blue-light generated OSL signals in Triassic red sandstone (Fig. 4.15). This suggests that Triassic red sandstone is the source for suitable quartz used in gravel matrix dating. This finding is in agreement with studies focusing on the sensitivity of quartz (Sawakuchi et al., 2018; Gray et al., 2019; Sawakuchi et al., 2020) that find igneous quartz is unsuitable whilst quartz derived from sedimentary sources is more likely to have been reset multiple times during successive erosion-transport-burial cycles (polycyclic quartz), making it sensitive and suitable for luminescence dating. The physical drivers that induce quartz OSL sensitivity are still poorly understood (Sawakuchi et al., 2020). Similarly, the chert source, whilst formed in the sedimentary limestone deposits, is unstable, likely because of the process of recrystallization in pore fluids. Since neither the Triassic sandstone nor any other clast lithology found in the terraces supported any IRSL signal, in contrast to the Cretaceous and Mio-Pliocene red beds that made up the strath material (Fig. 4.13), the feldspar from these later Mesozoic-Cenozoic red beds is likely to come from another geological unit found regionally. Thus, the approach of tracking luminescence characteristics of bedrock and sediments trialled here shows potential for source tracking of Mesozoic – Cenozoic sedimentary rocks as well as Quaternary sediments.

Clasts are bleached in the terrace section (Fig. 4.17), exposed to direct sunlight for potentially many years. Some, but not all clasts show penetration of bleaching further than the first slice (Fig. 4.17), and thus it is likely that the red oxidization inhibits deep penetration of light (c.f. Vandenberghe et al., 2003; Lomax et al., 2007; Meyer et al., 2018). Nonetheless, since exposed clasts exhibit a bleached first slice, and all of the first slices in the non-exposed clasts show a non-saturated signal, a dating approach that uses the first slice of clasts was attempted. The resulting ages in Fig 4.19, whilst the number of 'aliquots' of solid rock slices is limited, give an indication of the dating ability of clasts in the terraces. Ages are variable, not just between but also within single clasts. Such a result suggests not all geometric faces of clasts are bleached at the same time during the history of a clast. Likely each clast has been eroded, buried, and exposed multiple times. Nonetheless, most age estimates from buried surface slices lie within the time range of terrace aggradation (Fig. 4.19), as determined from gravel matrix optical ages. Three rock faces indicate burial ages that are older than the terrace aggradation time, and these might represent faces of clasts that were exposed and buried in an earlier terrace or in the river channel, and not reset before deposition in the sampled terrace. However, the exact timing of such earlier events, is beyond the limits of the quartz OSL approach. The three slices with estimated ages younger than terrace aggradation point to the need for more scrupulous shielding from sunlight during sampling, a need that was not anticipated while looking for deeply bleached luminescence-depth profiles. Whilst the objective of deriving clast transport and burial histories from multistage, deeply bleached penetrating luminescence depth profiles was impossible due to the opaque quality of the red sandstone material, applying a first-slice approach with sampling of multiple faces of a clast might result in a similar ability to derive multiple burial and transport events. Thus, clast dating has the potential to provide information on sediment transport and aggradation over multiple climate cycles, by sampling clasts in just one terrace or modern flood plain. Where such cycles are expected to be of the order of ~100 kyr, this might only be resolved using IRSL, and thus K feldspar bearing material should be targeted in future studies.

4.13 CONCLUSIONS

Ḋ measurements of gravel size fractions indicate beta Ḋ values ~ 2 to 3 times higher in a K-rich sand fraction compared to the carbonate-dominated pebbles and cobbles. Ḋ corrections for gravels resolve internal inconsistencies within an uncorrected age-depth profile in a mixed sand-layer and gravel terrace deposit. Further Ḋ calculations using the python-enabled strath terrace water content model, and Bayesian statistics integrating stratigraphic information, enable a high-resolution robust age model for strath terraces in the Mgoun catchment. Luminescence dating of bedload gravels has enabled detailed insight into the timing of burial events within a single strath level, with accumulation during 170-150 ka, 124-90 ka and 75 – 60 ka in terraces of sites A and B. Overall, the chronology of terraces along the Mgoun river demonstrates periods of incision and aggradation are not synchronous with gaps of several tens of thousands of years, but that throughout the catchment level T2 records a period of aggradation during the MIS 5e interglacial.

In addition to providing chronology based on gravel-matrix dating, the approach to applying rock exposure techniques to bedrock straths and clasts in the overlying sediment has yielded information on strath formation processes and sources of quartz and feldspar within the river catchment. Neither OSL, nor IR_{50} or $pIRIR_{225}$ luminescence-depth profiles of strath surfaces yielded any evidence of exposure. Thus, the pilot study of bedrock luminescence profiling of straths supports a scenario of bedload-covered strath planation but cannot rule out the possibility of bedrock exposure during planation followed by ongoing erosion during bedload accumulation. Modern exposed red sandstone clasts indicate the material's opacity to light prevents deep penetration of light and establishment of a bleached luminescence-depth profile. However, sampling of multiple faces of clasts suggests multiple exposure-burial events for clasts can be resolved but are ultimately beyond the age limitations of the OSL method in this case. However, most samples from clasts indicate burial within the time of terrace aggradation dated using gravel matrix dating. Thus, rock burial dating on bedload clasts shows a promise of being able to date multiple transport-deposition events of bedload clasts within one deposit.

5

Discussion and Synthesis

5.1 OVERVIEW

This thesis has used an integrated approach of fieldwork, remote topographic analysis, and geochronology to investigate the controls of lithology and climate on Quaternary fluvial archives of landscape change in a post-orogenic dryland mountain belt. The need for understanding the lithological controls on the dynamics of the river system has been increasingly recognised as an outstanding challenge within the field of geomorphology. Firstly, chapter 2 used the High Atlas of Morocco as a natural laboratory to study the way drainage divides in a mountain belt change while eroding through lithostratigraphic units. The results presented therein quantify the relationship between rock strength and erodibility, and demonstrate that lithology is the main driver of drainage mobility in this post-orogenic mountain belt. Chapters 3 and 4 then investigate the effect of lithological and structural variability within a catchment on river channel aggradation and incision in the context of orbital climatic changes. The approach is here to look first at the lithological and structural setting of valleys and their fluvial archives within the study catchment of the Mgoun River (Ch. 3). The insights on erosional and depositional process within the catchment were then supplemented with geochronological time control in chapter 4 using new applications of established and new methods of optically stimulated luminescence. Below I discuss the results from chapters 2-4 to answer the two main objectives introduced in §1.5: 1) Where and when does bedrock erodibility drive drainage divide mobility during the evolution of a collisional mountain belt? (Objective 1, §5.2) 2) To what extent do climatic changes on orbital timescales, and lithological and structural variability within a catchment draining a collisional mountain belt affect the timing of fluvial incision and aggradation? (Objective 2, §5.3). I then synthesize the insights gained through these discussions of the results in §5.4, where I address the overarching question of this thesis: to what extent do lithological and structural variability affect fluvial archives originating in mountain belts?

5.2 WHERE AND WHEN DOES BEDROCK ERODIBILITY DRIVE DRAINAGE DIVIDE MOBILITY DURING THE EVOLUTION OF A COLLISIONAL MOUNTAIN BELT?

5.2.1 *Rock strength, k_{sn} and fluvial erodibility*

The theory and empirical relationships outlined in §2.3.1 – §2.3.2 predict that fluvial erodibility, K relates to UCS in an inverse square (Eq. 5) and to k_{sn} in an inverse relationship in which the power depends on the value of n (Eq. 4). I find a linear relationship between UCS and k_{sn}, which suggests that $n = 2$, such that k_{sn} and UCS scale according to a linear relationship. However, visual inspection of Figs. 2.4b and 2.4d suggests that normalised K values calculated from k_{sn} data where I assume $n = 4$ are more similar to the normalised K values derived from UCS data. However, since Lague (2014) found that $n \sim 2$ is most commonly observed in the field, and the regression of UCS and k_{sn} data yields a strong linear fit consistent with $n = 2$, I suggest that $n \sim 2$ and that any difference between UCS and k_{sn}-derived normalised K values is due to other effects. For example, UCS does not explicitly include other factors influencing bedrock erodibility including the degree of weathering and structural discontinuities (Table 2.1), which especially through zones of deformation, will lead to more rapid erosion of even hard rocks (high UCS) by fluvial systems. For example, Anton et al. (2015) and Baynes et al. (2015) showed that bedrock canyons can be created by flood events in granite and basalt respectively, where the presence of discontinuities enables rapid erosion through fluvial plucking and block topple. On the other hand, whilst the simple form of the stream power model of bedrock river erosion only accounts for changes in river channel slope, field studies show that rock strength correlates with channel width (Allen et al., 2013), as well as valley width (Schanz and Montgomery, 2016) and can influence the efficiency of riverbed load in eroding underlying bedrock (Brocard and van der Beek, 2006). Furthermore, there can be a dampening of k_{sn} value variations across lithological boundaries as sections of river with weak bedrock downstream of river reaches with hard bedrock can be armoured with blocks (e.g. Thaler and Covington, 2016). Based on the lithological effects on river channel and valley morphology demonstrated by these field studies, using k_{sn} as a measure of rock erodibility in the stream power model of bedrock river incision likely underestimates the effect of lithology on river erosion.

Thus, calculated through UCS measurements, K is expected to vary by two orders of magnitude (Fig. 2.4b), whereas if using k_{sn}, K is expected to vary by one order of magnitude only (Fig. 2.4d). The lack of constraints of K in natural settings have led to numerical modelling studies varying widely in the range of erodibilities, using from one (Forte et al., 2016), two (Yanites et al., 2017), to three orders of magnitude difference between rock-types (Roy et al., 2015). Such a range of inputs is often based on the experimental relationship between intact rock strength and erosion in the classic abrasion mill experiment done by Sklar and Dietrich (2001), and the five orders of magnitude difference in *K* derived through the early work of Stock and Montgomery (1999). The latter forward-modelled river paleo-profiles, constrained by bedrock strath terraces and basaltic layers, to presently observed profiles for a range of locations worldwide. Their values of *K* range from 10^{-2} to 10^{-4} $m^{0.2}$ yr^{-1} in the mudstones of humid continental Japan, to 10^{-6} - 10^{-7} $m^{0.2}$ yr^{-1} in the subtropical granite landscape of Australia (Stock and Montgomery, 1999). An issue with the experimental approach by Sklar and Dietrich (2001) is that it does not include the effects of weathering and jointing of rock in natural landscapes and their influence on fluvial erodibility. In the results from Stock and Montgomery (1999) the influence of rock-type is difficult to isolate from the variation in climatic setting owing to the spread of study locations. Thus, whilst these early studies give some first order estimates of possible absolute values of fluvial erodibility and the relationship between rock strength and erosion rates, the results in this thesis constrain more fully the contrasts in fluvial erodibility between rock types which may be expected within a mountain belt. Next to rock strength control on k_{sn}, orographic and coastal enhancement of precipitation with greater precipitation on the northern and western sides of the drainage divide may lead to in a decrease of k_{sn} values from south to north or east to west (Supplementary Fig. S2.3). However, there is no evidence to suggest a significant difference in k_{sn} values between north and southern or east and western portions of the High Atlas (Supplementary Fig. S2.4).

5.2.2 *Drainage reorganisation in sedimentary cover*

The Gilbert metrics indicate drainage divide mobility where it crosses the sedimentary cover in the east (Fig. 2.5d). Here, the Mesozoic sedimentary cover is gently deformed, resulting in gently dipping strata punctuated by

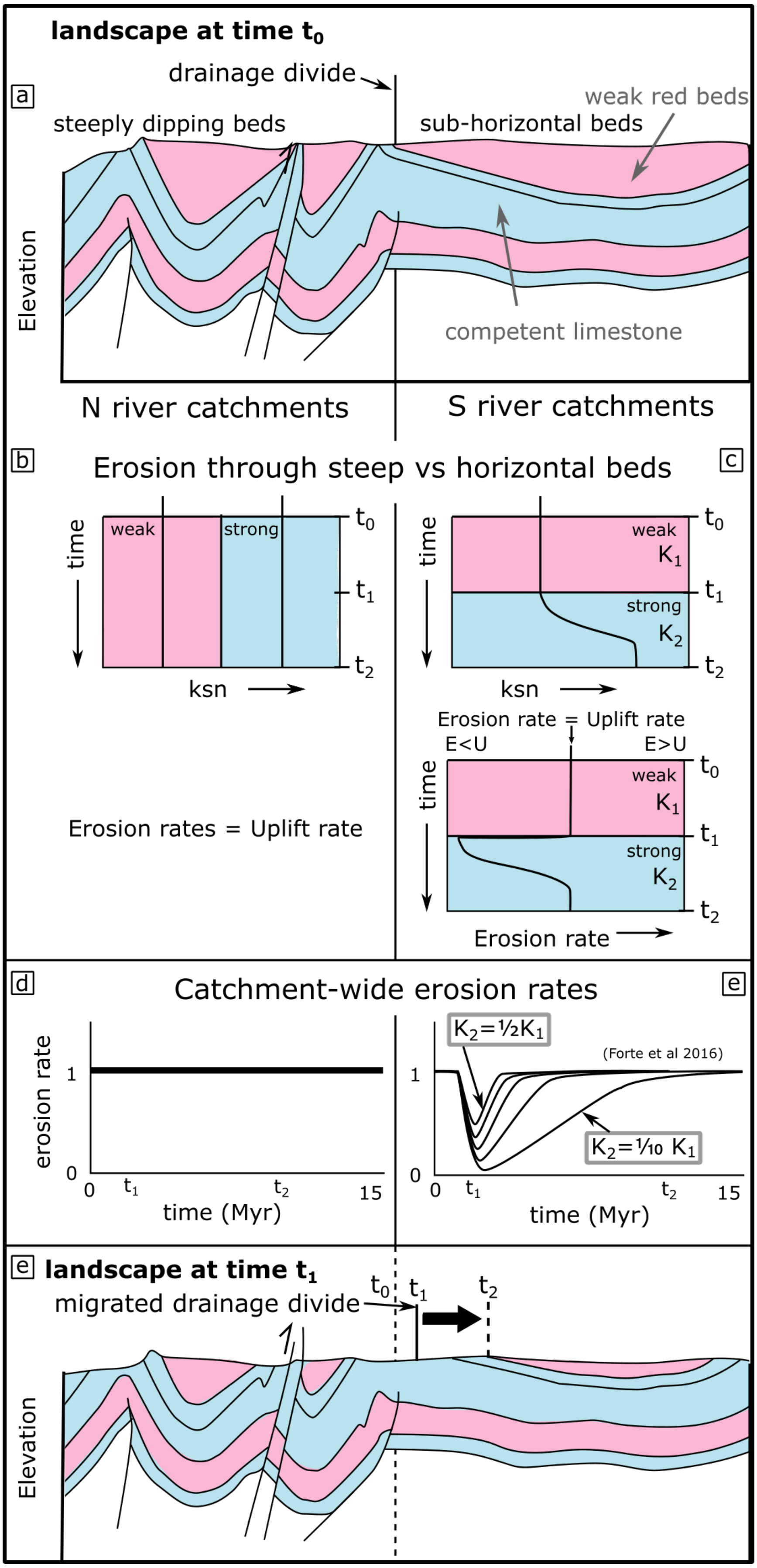
landscape at time t_0
a
drainage divide
steeply dipping beds
sub-horizontal beds
weak red beds
competent limestone
Elevation
N river catchments
S river catchments
b
Erosion through steep vs horizontal beds
c
time
weak
strong
t_0
t_1
t_2
ksn
weak
K_1
strong
K_2
Erosion rates = Uplift rate
Erosion rate = Uplift rate
E<U
E>U
Erosion rate
d
Catchment-wide erosion rates
e
erosion rate
1
0
time (Myr)
15
K_2=½K_1
(Forte et al 2016)
K_2=⅒ K_1
landscape at time t_1
migrated drainage divide

Figure 5.1 - The erosion and exposure of a hard limestone layer underneath a soft red bed layer in the Mesozoic low amplitude syncline (a) leads to a divide mobility towards the southern catchment (Fig. 2.5). (b) This is because the k_{sn} of the surface exposed needs to adjust to the new lithological strength, steepening transiently as it incises into harder limestone bedrock. (c) The graph for the southern catchments shows the results from landscape evolution modelling of the exposure of a contact between sub-horizontal soft stratigraphy on top of a hard layer (Forte et al., 2016). The resultant change in erosion rates across the divide explains the migration of the drainage divide. The response depends on the factor of difference in erodibility, *K*, between units.

widely spaced thrusts and folds (Fig 2.1b, Fig 2.2a). For example, the Dades river catchment south of the main drainage divide (Fig. 5.1a) incises into a long-wavelength syncline of slightly dipping strata composed of weak continental red beds and hard limestones, whereas directly north of the divide folding and thrusting is more closely spaced resulting in strata dipping at higher angles to the surface (Fig. 5.1a). Results show that k_{sn} is correlated to rock strength (Fig. 2.4e), and in the hard limestone k_{sn} is higher than in the weak red beds (Fig. 2.4a,c). Whereas erosion through near-vertical strata north of the divide result in near-stable k_{sn} values through time (Fig. 5.1b), the horizontal stratigraphy of the Dades river catchment to the south of the divide means k_{sn} values need to change through time to return to stable erosion rates (Fig. 5.1c) which equal rock uplift rates. Consequently, there is a period of transience when k_{sn} values adjust to the change in bedrock erodibility that occurred when erosion of soft red beds exposed hard limestone along the majority of the river catchment (Fig. 2.1a, 5.1a). This transition period explains the southwards movement of the divide (Fig. 2.5d), as erosion rates stay more or less stable in the north (Fig. 5.1d) whilst transient k_{sn} value causes a temporary decrease in erosion rates in the southern river catchments (Fig. 5.1e). The stratigraphic effect on river erosion rates presented in Fig. 5.1e was first demonstrated in a numerical modelling study of river erosion through layered stratigraphy by Forte et al. (2016), who show that for strata of variable erodibility dipping 5° or less the overall erosion rate of the landscape is expected to change by several factors during incision. Here, I show that such an effect can lead to migration of the drainage divide in the gently deformed sedimentary cover in collisional mountain settings, where exhumation of hard and soft strata is isolated or offset by faults.

Simulations by Forte et al. (2016) show the exhumation of a stratigraphic contact with a factor of two to ten difference in erodibility (Fig. 5.1e) could take 2 - 9 Ma to re-equilibrate in an area of 800 km^2 with a relatively high amount of precipitation (1 m yr^{-1}). Therefore, drainage divide migration in response to the incision through soft red beds to hard limestones in the upper half of the 1500 km^2 Dades catchment, representing a change in erodibility by a factor of 2 - 20 (Fig. 2.4), where rainfall is on the order of 0.1 - 0.5 m yr^{-1}, is expected to persist on a timescale of 10^6 – 10^7 years.

5.2.3 Divide migration driven by crystalline basement exhumation

Where crystalline basement is exposed, I find the position of the drainage divide is shifting towards the centre of this exposed resistant rock in the High Atlas (Fig. 2.5). In a numerical simulation, Giachetta et al. (2014) found that when they imposed an erodibility gradient across a drainage divide, which is representative of the exhumation of a crystalline basement such as in the High Atlas, the drainage divide responded by moving towards the side of lower erodibility over a timescale on the order of 10^6 years. Bonnet (2009) proposed that such a shift of the drainage divide is accompanied by a split of catchments, creating more and smaller catchments on the side of lower erodibility. Giachetta et al. (2014) also show that on the other side, a growth of larger catchments occurs. Similarly, Bernard et al. (2019) found that the drainage divide in the Pyrenees follows the position of strong plutons. This implies that the results of this thesis show a transient stage of drainage divide migration in response to exhumation of crystalline basement, where today's drainage divide at the edge of the crystalline basement is expected to be stable in the centre of the strong crystalline basement, or might even continue reorganising within the basement to follow the exhumation of resistant plutons. Giachetta et al. (2014) used two orders of magnitude difference in erodibility values to model this effect, and here I show divide mobility can be driven by exhumation of basement that is only a factor of two less erodible than the overlying meta-sedimentary rock if calculated through k_{sn} (Fig. 2.4d), and a factor of three less erodible if calculated through UCS (Fig. 2.4b).

5.2.4 Lithologically induced drainage divide mobility during the long-term erosion of a collisional mountain belt

The combination of estimations of contrasts in fluvial erodibility of rock types (Fig. 2.4), geomorphic indicators of drainage mobility (Fig. 2.5), and considerations of their structural configuration in the High Atlas compared to numerical simulation studies (see §5.1 - §5.3) enables the proposal of a model of lithologically-induced drainage divide mobility during the erosion of a mountain belt. The overall trend of the drainage divide, strike of faults and bedding planes follows the structural grain of the mountain belt (Fig. 2.1), for example determined by the pre-existing structure of an extensional rift such as in the High Atlas (Babault et al., 2012). I purport that changes in erosion rates as rivers incise through strata of different erodibility will drive drainage reorganisation in collisional mountain belts, where layers are close to horizontal and only gently deformed (Figs. 5.1, 5.2). This is because where strata are deformed gently and offset by faults, local exhumation of contacts between soft and hard rock leads to changes in erosion rates between catchments (Fig. 5.1). Consequent changes in erosion rates across the drainage divide will lead to the migration of the drainage divide (Fig. 5.2a) as illustrated by the mobility of the drainage divide in the High Atlas (Figs. 2.5,

a Stage 1: erosion through gently deformed sedimentary cover
of variable rock strength
persistent drainage reorganisation

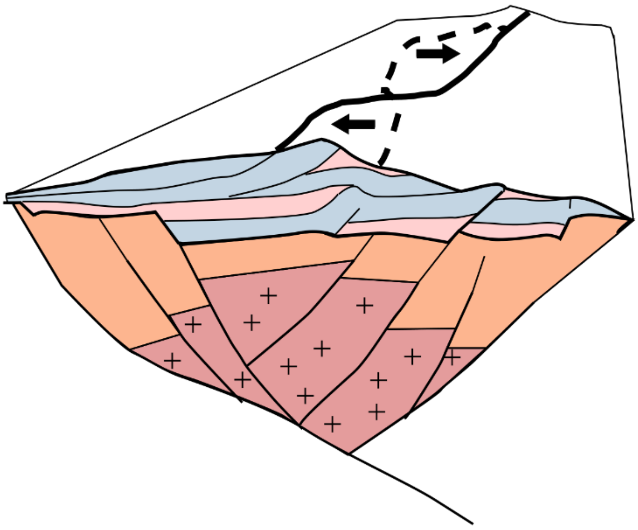

b Stage 2: erosion through strongly deformed meta-sediments
resulting in a stable divide

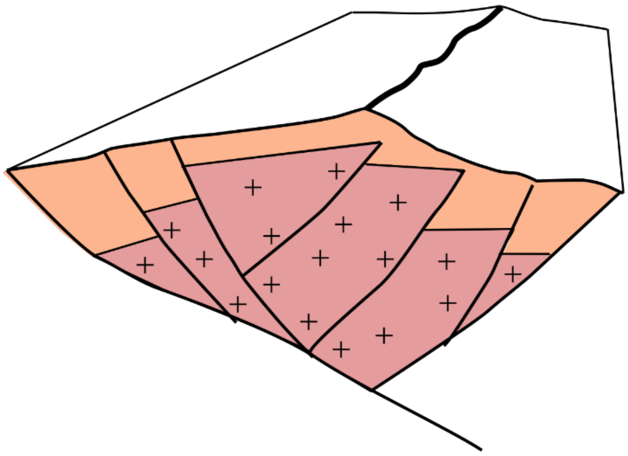

c Stage 3: exhumation of strong crystalline basement
leading to migration to the centre of
exposed highly resistant core rocks

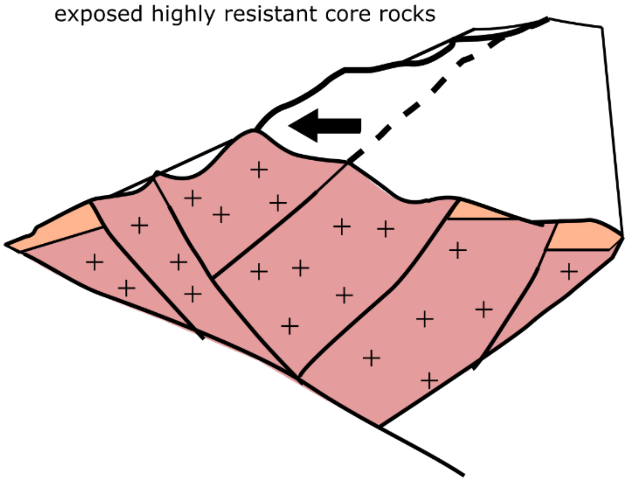

Figure 5.2 – Conceptual model of the development of a collisional mountain belt and the behaviour of the central drainage divide in response to exhumation of lithostratigraphic units.

5.1), which could lead to steady divide migration or instantaneous capture of catchments, such as shown in the Appalachians (Gallen, 2018). The effect of rock type on drainage reorganisation will be strongest in early phases of collisional mountain building before the sedimentary cover erodes in the centre of the belt. In later stages, minor reorganisation and capture could still occur closer to the thrust front on the margins of the mountain belt where Mesozoic sedimentary strata are present. When deformed meta-sediments become exhumed, the increase in dip and deformation of strata leads to more stable erosion as rivers incise (Forte et al., 2016, Fig. 5.2), resulting in stable drainage divides as witnessed in the middle of the study area (Figs. 2.5, 5.2b). When crystalline basement gets exhumed, the drainage divide will migrate into the centre of highly resistant rocks resulting in more drainage divide migration (Figs. 2.5, 5.2). The migration of the main drainage divide in a mountain belt has been shown to lead to reorganisation of river catchments (Bonnet, 2009; Giachetta et al., 2014), imposing new boundary conditions on river channels which change gradients and sediment loads (Forte et al., 2015) and the ensuing response can result in a cascading effect, impacting geomorphic and stratigraphic systems for millions to tens of millions of years (Beeson et al., 2017). The effects of lithologically-induced drainage migration here described for a post-orogenic belt could be more complex in an active mountain belt setting. Evidence for the effects of drainage reorganisation in the High Atlas are most likely to appear in the catchments draining the sedimentary cover and the transition from metamorphic sediment to crystalline basement. Whilst the investigation of drainage capture events and related changes in downstream sediment transport and geomorphology are beyond the scope of this thesis, such effects are most likely to be resolved around the headwaters which are challenging to access for field investigation

(Babault et al., 2012). In addition to catchment reorganisation on the scale of the central drainage divide, reorganisation between catchments and of the river network within single catchments are also possible and have been observed in localised areas such as a gorge in the Dades River in the sedimentary cover sequence (Stokes et al., 2008). The ensuing stochastic signals of sediment supply that such events would generate are not resolvable in the terrace record dated in this thesis, but may well be present within older river terrace records such as in the Dades River (Stokes et al., 2017). Thus, the potential effect of drainage reorganisation, occurring stochastically on timescales of 10^6 – 10^7 years needs to be considered when interpreting longer timescale terrace sequences, even if our data from the last 200 ka of terrace formation does not seem to reflect such events.

5.3 CLIMATIC, BEDROCK LITHOLOGICAL AND STRUCTURAL CONTROLS ON QUATERNARY RIVER CHANNEL AGGRADATION AND INCISION

Objective 2 of this thesis (§1.5) aims to derive the climatic and bedrock lithological and structural controls on Quaternary river channel aggradation and incision, in the Mgoun River draining the southern flank of the High Atlas collisional mountain belt. To answer this question, I must combine the results obtained from chapters 3 and 4. I will first discuss the details of the aggradation and incision histories of terraces constrained using terrace stratigraphy (Ch. 3) and OSL dates (Ch. 4). I will put these constraints on Quaternary river behaviour in context of background uplift rates and previously published High Atlas terrace studies in §5.3.1. I will then investigate the relationship between this river behaviour and the regional Quaternary climatic history of northwest Africa to shed light on geomorphic system response on orbital timescales in §5.3.2. After this discussion on the temporal dimension of climate and river response I will use the geomorphic, sedimentologic and geological data on the Mgoun catchment presented in Ch. 3 to explore the controls of lithology and passive tectonic structure on the geomorphic system in §5.3.3 – §5.3.4. To conclude, in §5.3.5 I will draw together the conclusions from these discussions to weigh the answer to the overall question written above (objective 2) and to offer perspective on the applicability of these conclusions on other geographic locations.

5.3.1 *How accurate are terraces as records of uplift and river incision?*

The Mgoun River terrace stratigraphy (Ch. 3) and OSL geochronology (Ch. 4) combine to provide the most detailed record of incision and aggradation in the downstream Ait Said reach of the thrust front. Here, dated terrace sediment on two strath levels reveal a detailed pattern of planation, aggradation, and incision (Fig. 5.3a). T2 was an active valley floor experiencing planation and aggradation over 80 kyr, while T1 was active > 20 kyr. The long terrace aggradational and shorter incisional periods do not conform to the often implicit or explicit assumption of punctuated river planation caused by perturbations in incision. Both terraces are active for significant amounts of time compared to the 30 kyr incisional time between T2 terrace abandonment and T1 planation, which is ~40% of the T2 terrace aggradation interval. Since there is no data on the aggradational and incisional history of the modern river plain, the length of the incisional period occurring after T1 abandonment remains unconstrained. Experimental OSL strath surface dating applied in Chapter 4 suggests planation - i.e., lateral erosion - and deposition of sediments might occur simultaneously. However, even if sediments are aggraded during planation, such sediments may not be preserved everywhere in which case the hiatus in the record of active terrace aggradation between T2 and T1 might contain periods of planation or

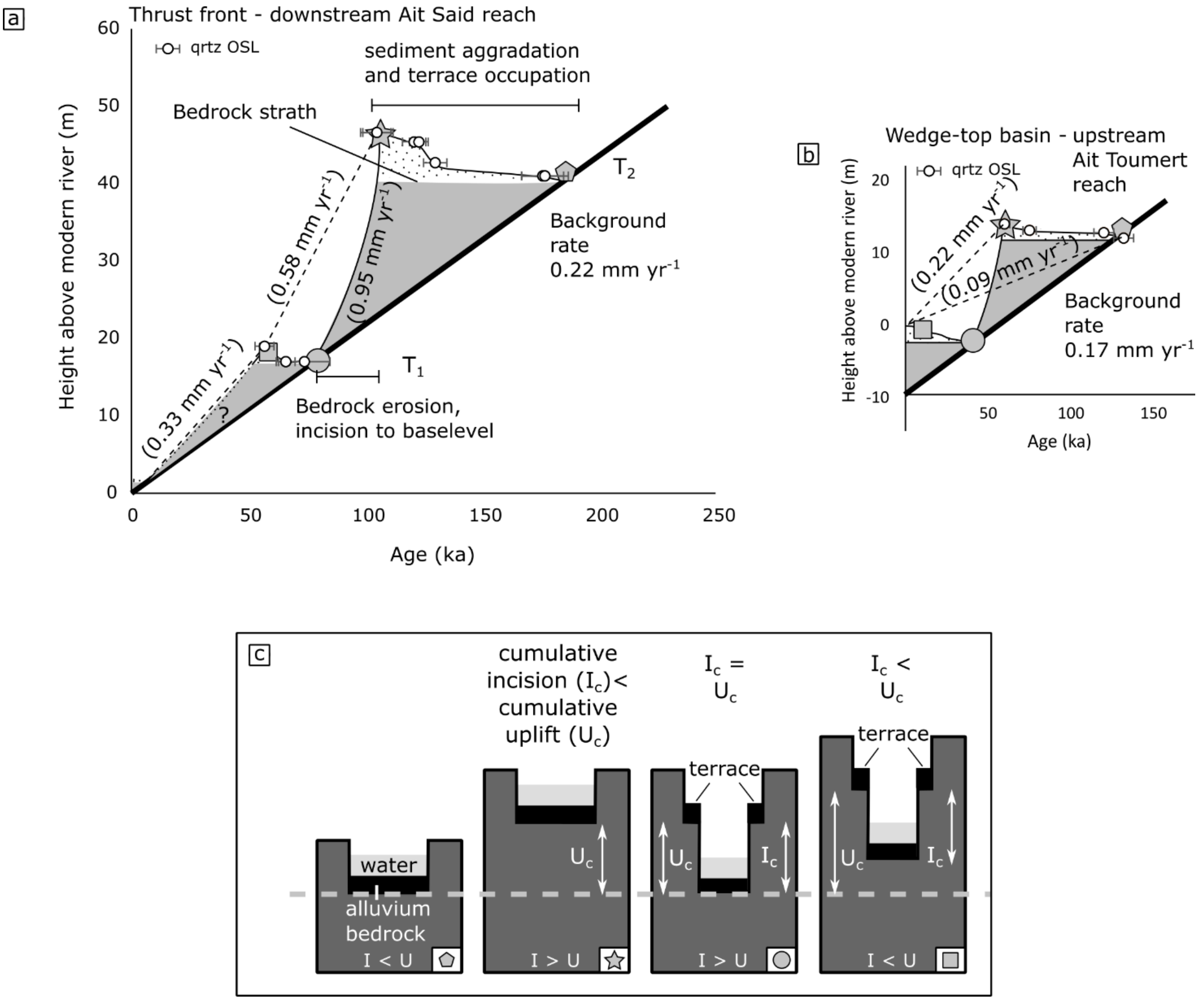

Figure 5.3 - Height of the riverbed above the modern reference stage. The curve represents the height of the riverbed over time, tracing periods of aggradation and incision superimposed on a background average incision rate. The stippled pattern represents fill deposits, with grey areas representing bedrock which is planated into a strath and cut during the incisional stages. Data points represent sample heights, dates, and error. The curve shows rates of incision between terrace abandonment and the planation and aggradation of the next terrace level. For illustration purposes, the dashed lines show rates of incision based on abandonment ages only. (a) Fully constrained terrace aggradation and incisional period in between for T2 and T1 in the Ait Said reach of the Mgoun River. The background averaged incision rate encompassing a full eccentricity cycle (100 kyr) of terrace aggradation and incision is 0.22 mm yr^{-1}. This averaged incision rate is consistent with rock uplift of 0.17 – 0.22 mm yr^{-1} averaged over the last 7.1 – 5.3 My (Babault et al., 2008). (b) The age data for the wedge-top basin constrains one terrace level above the modern riverbed. Apparent rates of incision range between 0.09 mm yr^{-1} to 0.22 mm yr^{-1}, whilst the data also fits an estimated time-averaged incision rate consistent with an uplift rate of 0.17 mm yr^{-1}. (c) Modified conceptual model of terrace formation and dynamic base level from Gallen et al. (2015). I – incision; U – uplift. Symbols match age-height points on the graphs of the thrust front (a) and wedge-top terraces (b). Depending on the stage in the incision/aggradation cycle cumulative incision will either match cumulative uplift, or cumulative incision will be less than cumulative uplift.

aggradation in addition to vertical incision. Thus, whilst the results in this thesis constrain a maximum length of time for vertical incision, the duration of incision could be shorter. The long aggradation times separated by punctuated incision found here support other field-based (Wegmann and Pazzaglia, 2002; Schanz and Montgomery, 2016; Foster et al., 2017) and numerical model studies (Hancock and Anderson, 2002) that find aggradation periods can be much longer than incisional phases. Consequently, these studies have already established that incision rates obtained from single dating points in terraces need to be treated with caution. In particular, Finnegan et al. (2014) have shown that if hiatuses in river incision have a heavy-tailed distribution, incision rates will decrease with increased measurement time, also known more generally as the Sadler effect in geology (Sadler, 1981). Using incision rates from terraces spanning a full glacial cycle (Wegmann and Pazzaglia, 2002) or using the lowest terrace as reference frame to calculate incision (Gallen et al., 2015) have been suggested as effective methods to counter the Sadler effect. However, if terraces are active for 80 kyr or longer, these approaches will not be accurate unless the full range of terrace aggradation is constrained. Studies in which the full aggradational history of terraces is constrained are rare, especially on eccentricity-driven glacial-interglacial timescales (~ 100 kyr) and in coarse gravels common in strath settings, which provide a challenge to conventional radiocarbon and OSL burial dating. Thus, the data in this thesis provide an exceptional constraint on incision, strath terrace aggradation and background incision rates in a low-rate post-orogenic mountain setting.

Rock uplift, terrace records and long-term river incision rates across the High Atlas

The incision rate between terrace aggradation in the downstream Ait Said reach (TF) is 0.95 mm yr^{-1}, which is up to an order of magnitude larger than the incision rate determined by averaging over aggradation and incisional periods (Fig. 5.3a). This time-averaged incision rate of ~ 0.22 mm yr^{-1} appears to be consistent with High Atlas long-term rock uplift rates of 0.17-0.22 mm yr^{-1} calculated from 1200 m of uplifted Messinian deposits across the Atlas area from the Middle Atlas in the north to the Anti-Atlas in the south, dated at 7.1 - 5.3 Ma (Babault et al., 2008). Whilst terrace dates are available for the Madri River, > 60 km west from the Mgoun in the Ouarzazate basin (Arboleya et al., 2008) and the neighbouring Dades River exiting the mountain front ~ 20 km east of the Mgoun River (Stokes et al., 2017), these are abandonment ages derived from cosmogenic exposure dating (Arboleya et al., 2008) and OSL dates of overbank sands (Stokes et al., 2017) marking the start of terrace abandonment. Rates calculated from the abandonment ages of terraces T2 and T1 result in rates of 0.58 and 0.33 mm yr^{-1}, which are values lower than the punctuated incision rates experienced by the river during incisional periods and higher than the time-averaged incision rate (Fig. 5.3a). In essence, the data shows that rates averaged between abandonment ages neither offer accurate insights into either long-term time-averaged incision rates nor real incision rates.

Rates of incision calculated using the abandonment age of T2 in the upstream Ait Toumert reach (WTB) appear lower than the background rate calculated in the downstream Ait Said reach (TF). In the Ait Toumert reach (WTB), rates based on abandonment ages to the modern river stream reach at least 0.23 mm yr^{-1} and time-averaged rates - including aggradation time - reach 0.09

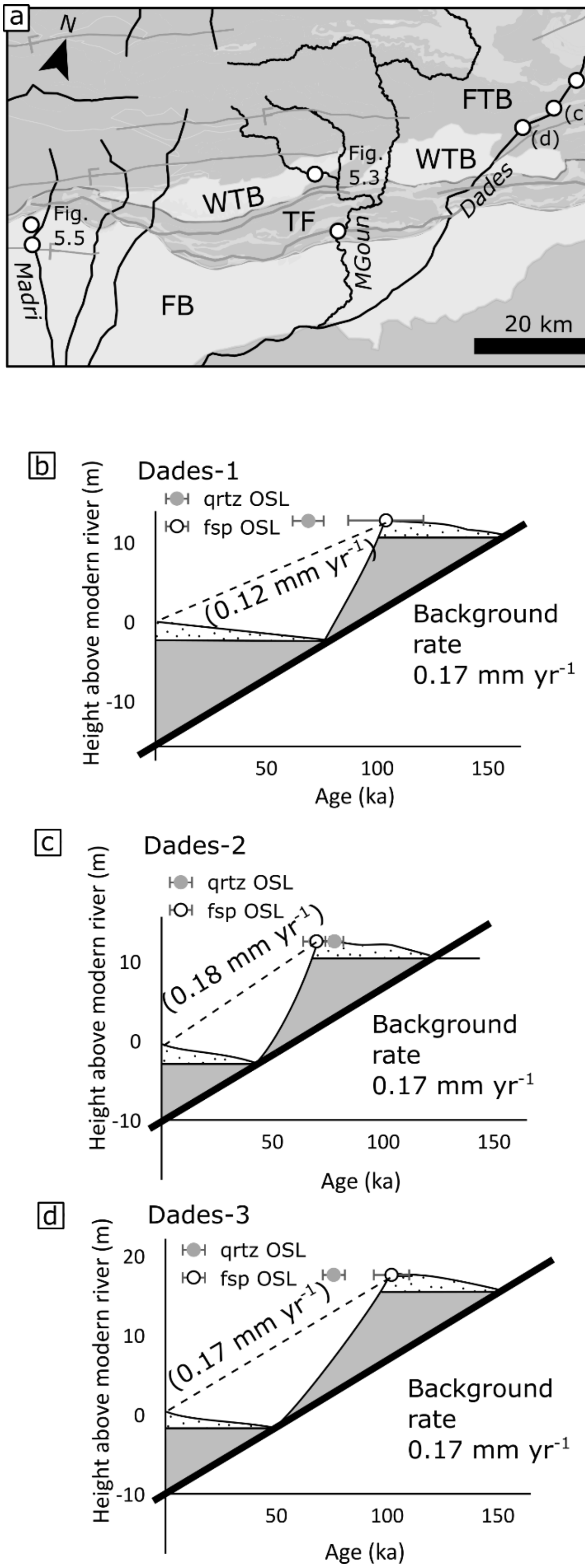
a
N
FTB
(b)
(c)
(d)
WTB
Fig. 5.3
WTB
TF
Fig. 5.5
Dades
MGoun
Madri
FB
20 km
b
Dades-1
qrtz OSL
fsp OSL
Height above modern river (m)
10
0
-10
(0.12 mm yr^-1)
Background rate 0.17 mm yr^-1
50
100
150
Age (ka)
c
Dades-2
qrtz OSL
fsp OSL
(0.18 mm yr^-1)
Height above modern river (m)
10
0
-10
Background rate 0.17 mm yr^-1
50
100
150
Age (ka)
d
Dades-3
qrtz OSL
fsp OSL
Height above modern river (m)
20
10
0
-10
(0.17 mm yr^-1)
Background rate 0.17 mm yr^-1
50
100
150
Age (ka)

Figure 5.4 – Overview of terrace locations and terrace abandonment ages for the Dades River (Stokes et al 2017). (a) Overview map of the Mgoun (Fig, 5.3) Dades, and Madri (Fig. 5.5) terrace records. FTB: fold-thrust belt. WTB: wedge-top basin. TF: thrust-front. FB: foreland basin. (b-d) Age-heigh data for terraces along the Dades River in the FTB east of the Mgoun (Stokes et al., 2017), with estimated incision rates of 0.17 mm yr^{-1}, though apparent incision rates go as low as 0.12 mm yr^{-1}.

mm yr^{-1} (Fig. 5.3b). These rates would at first glance appear inconsistent. However, the incision rate calculated in the upstream Ait Toumert reach (WTB) are based on vertical distances measured between one terrace level and the modern riverbed as reference frame. Since aggradation of the modern riverbed might have lasted several tens of thousands of years, the geodetic height of the riverbed is not steady, and thus is an arbitrary reference level (Fig. 5.3c; Gallen et al., 2015). Taking into account the effect of fluctuating riverbed elevation relative to the geoid (Fig. 5.3c), the age data from the upstream Ait Toumert (WTB) and downstream Ait Said reach (TF) both enable a fit of long-term (10^5 yr) averaged background incision rates in equilibrium with rock uplift rates of 0.17 – 0.22 mm yr^{-1} (Fig. 5.3). Similarly, dated abandonment ages of terraces east of the Mgoun, along the Dades River running through the FTB result in estimated incision rates reported at 0.12 ± 0.02 mm yr^{-1} to 0.17 ± 0.02 mm yr^{-1} (Fig. 5.4; Stokes et al., 2017), whilst these same results fit a background rate of 0.17 mm yr^{-1} consistent with long-wavelength uplift rates across the High Atlas when taking into account the reference base level effect. At such rates, the higher level terraces recorded up to 80 m above the modern river plain in the Dades catchment would record river incision and aggradation over the last 0.5 Ma, spanning the middle to late Pleistocene (Stokes et al., 2017). West of the Mgoun, abandonment ages of terraces of the Madri in the Ouarzazate foreland basin result in incision rates of 0.3 – 5.2 mm yr^{-1} (Fig. 5.5; Arboleya et al., 2008), up to an order of magnitude higher than rates seen in the Mgoun and Dades rivers. However, accounting for periods of aggradation, a rate of long-term time-averaged

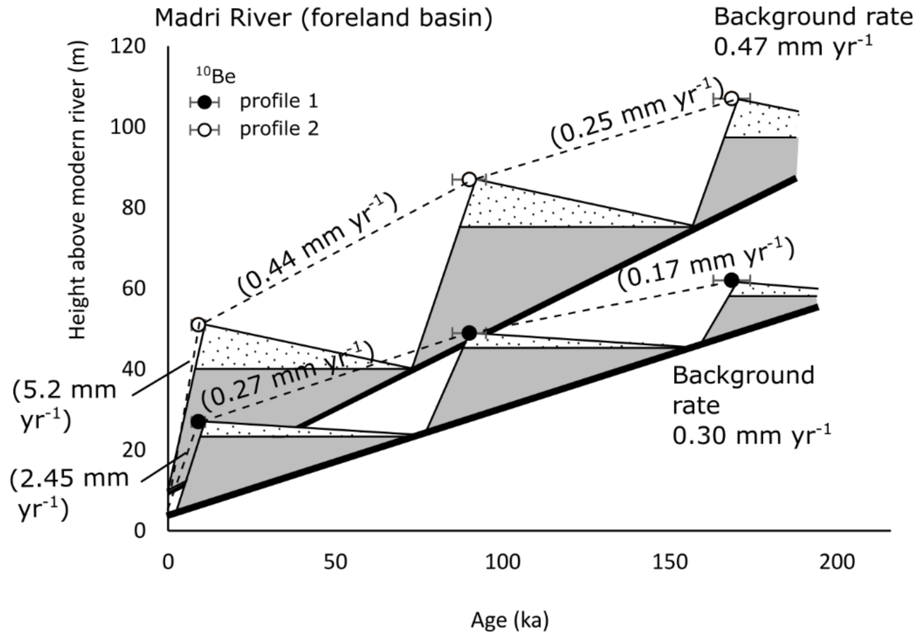

Figure 5.5 - Age-height data from two profiles along the Madri River in the foreland basin west of the Mgoun (Fig. 5.4a, Arboleya et al 2008). Estimated averaged incision rates are 0.3 and 0.5 mm yr-1 for the two profiles respectively, whilst apparent incision rates range between 0.17 and 5.2 mm yr-1.

incision can be calculated for two profiles, at 0.3 and 0.5 mm yr^{-1} (Fig. 5.5). It is likely that these rates, varying over < 3 km express additional structural rock uplift and local relative base-level fall related to low-rate active blind thrusts in the western Ouarzazate basin accounting for 0.1-0.3 mm yr^{-1} (Pastor et al., 2012b). Thus, the data in this thesis constrain punctuated incision and long terrace aggradation periods, resulting in time-averaged rates consistent with regional low-rate post-orogenic rock uplift rates. A reinterpretation of published age-height data provides a consistent understanding of low-rate rock uplift, punctuated river incision, and time-averaged river incision rates in a post-orogenic setting. At shorter 10^4 – 10^5 year timescales it appears disequilibrium represented by punctuated incision events bracketed by long aggradational periods are controlled by factors outside tectonic boundary conditions, such as climatic changes, and lithological and structural controls. Consequently, I note that in settings of slow rock uplift especially, where aggradation times can be long, care must be taken to collect data of terrace aggradation times over at least a full glacial-interglacial cycle or more (10^5 yr) to allow an accurate relationship between uplift and incision to be established.

5.3.2 How do climatic changes translate into the terrace record?

Whilst terraces can act as useful markers to constrain river incision rates over geological timescales, at a first order these landforms record a geomorphic response to climatic changes on top of background base-level lowering (§1.3.3). It has been demonstrated that river terraces form in response to changes in sediment generation and flux driven by changes in climate at various timescales, with a dominance of eccentricity driven cycles in the large lowland rivers sourced from high-relief ice-sheet influenced catchments of NW Europe (Bridgland and Westaway, 2008, 2014). However, the timing of terraces in response to climate is still equivocal with reports of incision during glacial, as well as interglacial stages or at transitions between those (Schanz et al., 2018). Furthermore, the timescale at which late Quaternary cyclic climatic forcing dominates over intrinsic geomorphic dynamics is another key area of debate (Vandenberghe, 1995, 2003). In NW Africa, orbitally-induced insolation maxima induce Green Sahara Periods which are spaced dominantly by precession and eccentricity (Tjallingii et al., 2008; Larrasoaña et al., 2013). The OSL results from the Mgoun terraces indicate a river-wide aggradation event during the interglacial maximum Green Sahara period (GSP) 110-130 ka. However, there is no such event in the following Green Sahara periods one and two precession cycles – ~ 26 and 52 kyr – later (Fig. 4.21). This observation introduces two key questions: 1) how do interglacial GSP conditions lead to river channel aggradation? 2) Why is there no one-to-one relationship between climate and river aggradation?

1. How do interglacial GSP conditions lead to river channel aggradation?

To answer the first question, I have to consider the regional climatic system and the place of the river catchment in it. As described in §1.4.2, the upland source area of the Mgoun catchment receives rain from winter-spring Mediterranean and Atlantic storms (Schulz et al., 2008), which result in an annual rainfall distribution of 500 mm yr^{-1} at the central peaks in the source area, rapidly reducing to < 300 mm yr^{-1} entering the wedge-top basin and < 200 mm yr^{-1} in the thrust front and foreland basin (Fig. 1.3; Hijmans et al., 2005). Thus, whilst the trunk stream has a perennial flow of water, the tributaries and channelised fans in the study area are ephemeral and less commonly activated to transport sediment (Dłużewski et al., 2013; Stokes and Mather, 2015; Mather et al., 2017; Rojan et al., 2020). Even occasional low magnitude storm events may not be enough to create connectivity throughout an ephemeral tributary catchment, due to transmission losses resulting from infiltration into unconsolidated alluvium (Thornes, 1977). During precession-driven interglacial Green Sahara periods, the shift of the ITCZ (Rossignol-Strick, 1985; Tuenter et al., 2003) and more frequent high magnitude tropical incursions of the type described by Knippertz (2003) and Knippertz et al. (2003b) result in more frequent activation and transport of sediment from lateral sources into the river channel, thus leading to aggradation in the trunk river channel (Fig. 5.6).

Studies of Late Pleistocene to Holocene sediment production and landscape response in arid environments such as the Negev (Enzel et al., 2012) and Mojave Deserts (Miller et al., 2010) have shown periods of higher frequency and magnitude of storms, which in the case of the Negev Desert are not necessarily linked to changes in mean climatic states (Enzel et al., 2012), led to increased sediment production on hillslopes and subsequent fan

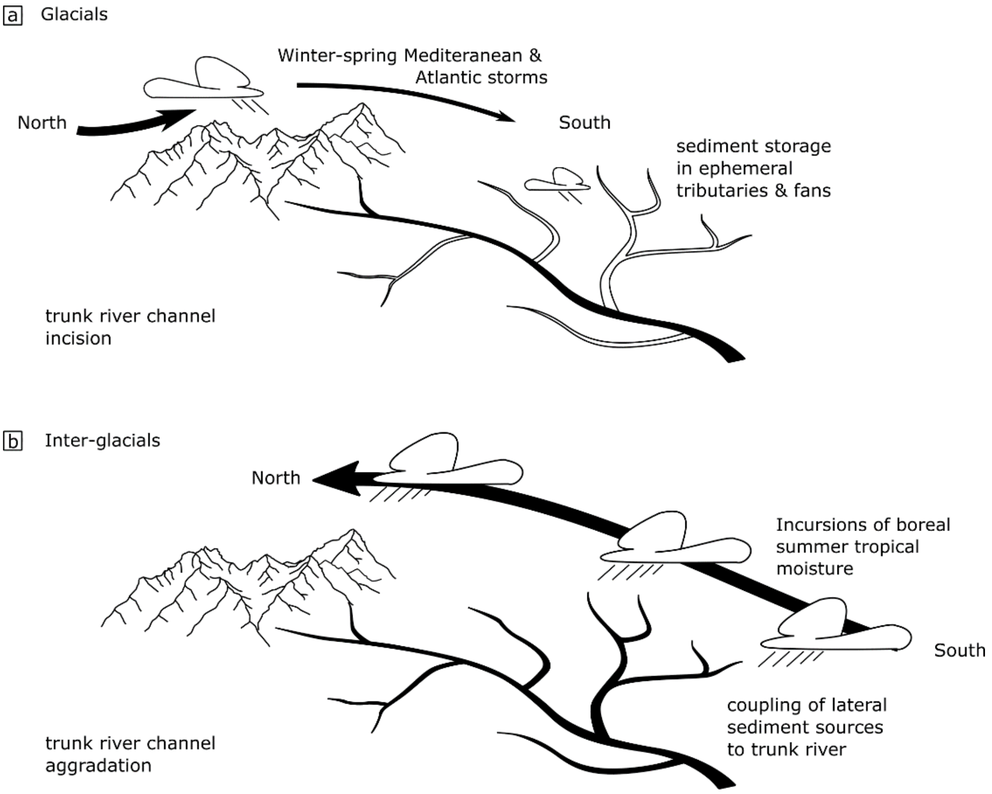

Figure 5.6 – Proposed climate-aggradation relationship for the southern High Atlas draining into the Ouarzazate basin. During dry periods, winter-spring storms from the Mediterranean and Atlantic dominate annual precipitation patterns, which rapidly decline southwards of the drainage divide (Schulz et al., 2008). Tributaries downstream of the upland fold and thrust belt are ephemeral and store sediment in their hillslopes, channels, and fans. (b) During interglacials, the northward shift of the ITCZ (Rossignol-Strick, 1985; Tuenter et al., 2003) brings more frequent incursions of boreal summer tropical storms, which cover the entire catchment and produce significant geomorphic work by activating hillslopes, channels and fans of tributaries (Knippertz, 2003; Knippertz et al., 2003b) leading to coupling to the axial river channel (Stokes and Mather, 2015; Mather et al., 2017).

aggradation. Furthermore, Anders et al. (2005) dated the colluvial mantles on hillslopes, tributary stream deposits, and fluvial terraces along the Colorado River, showing a disconnect and lag time between the mainstem and tributary response to climate. This lag time in geomorphic response is explained by the weathering-limited nature of hillslope sediment production in arid tributary catchments (Anders et al., 2005). The studies in the Negev, Majove Desert and in Colorado all evoke and constrain a model of weathering-controlled response of arid hillslopes to the frequency of high-intensity storms. Thus, it is likely that the effect of increased frequency and magnitude of tropical storm incursions in the southern High Atlas has had an effect on the coupling of lateral sources to the main stem of the Mgoun River, and that increased weathering and sediment production had a contributing role to river channel aggradation. While levels of the local Lake Isli in the High Atlas are consistent with a drier phase during terrace incision in the Last Glacial Maximum (Lamb et al., 1994; Valero-Garcés et al., 1998; Roberts et al., 2008), care must be taken when interpreting climatic controls on geomorphic processes from speleothem or lacustrine records as the controls on lake levels including total annual precipitation, evaporation and groundwater flow are different from climatic properties such as storm magnitude and frequency affecting geomorphic action. Furthermore, whilst comparison to other African or Mediterranean terrace records is tempting, care must be taken as the relation between the site-specific geomorphic system and local climate system is crucial as demonstrated in the example of the Mgoun River given here. Noticeably, regional compilations across the Mediterranean, whilst attempting correlation of terraces, have seen limited success due to limited age control and distinctive asynchronicity of river aggradation and incision displayed in these databases over the last 200 ka (Macklin et al., 2002; Santisteban and Schulte, 2007).

The role of vegetation

In addition to the influence of storm magnitude and frequency on sediment flux into the river channel, another potential influence is vegetation. Geomorphologists have often based the relationship between climate, vegetation, erosion and the formation of terraces on a relationship between annual precipitation and sediment yield published by Langbein and Schumm (1958). The Langbein-Schumm sediment-yield curve portrays a logical increase and decrease of sediment yield with increasing annual precipitation, with peak sediment yield at 400 – 500 mm of mean annual precipitation. Thus, along these lines, periods of increased precipitation such as MIS 5e in the High Atlas may result in more runoff and higher sediment yield in the downstream reaches with modern annual rainfall < 200 mm, whilst increasing vegetation in the headwaters which currently receive ~ 500 mm annual rainfall could see decreased sediment yield at the same time.

However, whilst the elegance and simplicity of the Langbein-Schumm relationship has led to widespread and persistent adoption by the geomorphological community, subsequent studies including increasingly larger datasets have derived sediment yield curves that are distinctly different, or do not find a clear relationship (Fournier, 1960; Tabuteau, 1960; Douglas, 1967; Wilson, 1969; Wilson, 1973; Dendy and Bolton, 1976; Walling and Kleo, 1979). Indeed, Langbein and Schumm (1958) acknowledge the problems inherent in developing their curve, such as the unequal geographic distribution of data points and influence of other factors such as geology, topography, land use and climatic seasonality. More importantly, however, biogeomorphic responses to climatic change have been shown to follow complex responses between vegetation cover, weather and soil production, runoff, hillslope erosion and soil depletion, and to lead to transient geomorphic signals caused by lags between these variables during transitional periods (Knox, 1972; Bull, 1991; Vandenberghe, 1995). The transience of such responses points out the futility of using general curves that directly relate sediment yield to effective precipitation, and points out the implicit assumption of equilibrium in hillslope and fluvial systems when using the Langbein-Schumm curve. An example of an interpretation of transient biogeomorphic responses to transitions in climate and vegetation supported by the data of terrace aggradation in the High Atlas could be built on the lags between climatic changes and vegetational response observed in the pollen records (Dupont and Hooghiemstra, 1989; Dupont and Agwu, 1992; Dupont, 1993). In the High Atlas, the lag between the humidification during the transition from MIS 6 to 5e and migration of the vegetational zone is correlated with the widespread aggradation of terraces in the Mgoun catchment (Fig 4.21). This could point to increased sediment yield in response to higher frequency and magnitude of storm events before an increase in vegetational stability returns the system to equilibrium. Subsequently the high-amplitude shift in Sahelian vegetation during stage 5d and c in response to precessional control on monsoonal strength whilst higher latitude Mediterranean vegetation persisted might explain the incision and aggradational hiatus recorded in the strath terraces (Fig. 4.21). Similarly, the incision and abandonment of terraces after MIS 4 is a possible response to the retreat of the Mediterranean-Saharan vegetational transition zone during MIS 3 and 2 (Fig. 4.21).

However, biogeomorphic mechanisms of terrace formation in the Mgoun catchment are all but conclusive, as terraces lack soil horizons or macroscopic palaeobotanical evidence suggesting vegetation might not have been a significant presence during the history of terrace formation. A study by Antinao and McDonald (2013) further demonstrates the ambiguous relation between changes in vegetation in a desert environment. Importantly, Antinao and McDonald (2013) synthesised palaeobotanical and alluvial fan stratigraphy in the Mojave desert and found that the onset of alluvial fan deposition over the late Pleistocene-Holocene climatic transition began well before changes in catchment vegetative cover. In addition, this increase in deposition across multiple altitudinal regions occurred during several possible combinations of vegetation change. Instead, changes in the frequency and magnitude of storms are probably more important (Antinao and McDonald, 2013). The importance of storm frequency over mean climatic conditions such as annual precipitation and vegetation is further supported by the analysis of diachronic deposition of fan and hillslope material in the Colorado river (Anders et al., 2005) and a recent study of aggradation at a catchment scale in the arid Negev Desert (Enzel et al., 2012) referred to in the previous section. I am not advocating for an abandonment of vegetation as a model of climatic control on terrace formation. Instead, I argue that a greater emphasis is placed on the integration of hydrologic and vegetation processes, and that the relationships between vegetation and hillslope sediment yield is explored further.

How well does terrace formation link to the climatic record?

Despite the synchronous aggradation of sediment across the catchment during the MIS 5e interglacial maximum, the record of aggradation and incision does not present a direct linkage with Milankovitch climatic cycles. Subsequent Green Sahara Periods during the interglacial MIS stages 5c and 5a are not linked to records of widespread aggradation, and the aggradation recorded on terraces is neither synchronous within the catchment, nor directly relatable to any climatic stage on this timescale (Fig. 4.21). Effectively, the aggradational terrace record of the Mgoun records solely a strong 100 kyr control of climate. Even more notable is the lack of correlation of terrace incision and abandonment within the catchment and with climatic stages. Over the last 200 ka, the Ait Said reach records the planation of T2 at ~ 180 ka, followed by incision and abandonment at ~100 ka, and abandonment of the following T1 terrace < 50 ka (Fig. 4.21). Conversely, the wedge-top basin records planation of T2 at ~130 ka and incision and abandonment at ~ 60 ka

(Fig. 4.21). Of these, only the planation of T2 in the wedge-top basin at the start of the MIS stage 5e interglacial maximum (~130 ka) can be related to changes in climate recorded in the marine oxygen isotope and NW African humidity record. Thus, from these results a pertinent question can be distilled: how come only the MIS 5e interglacial GSP forced a synchronously timed aggradation event in the terrace record?

2. *Why is there no one-to-one relationship between climate and river aggradation?*

Late Quaternary climatic fluctuations, such as reconstructed from global $\delta^{18}O$ records (Lisiecki and Raymo, 2005), can often be broken down in Milankovitch cycles with time periods of ~ 100 kyr (eccentricity) and 26 kyr (precession). The key to understanding the effect of climate on terrace formation is to examine the filters between Milankovitch cycles and the terrace record (Schanz et al., 2018). The first filter is that of the global and regional climate systems converting the orbital fluctuations of Milankovitch cycles into changes in climatic parameters. Whilst the details of the interference of the three cycles with differing periodicities – precession, obliquity and eccentricity – inherently produce a signal of orbital fluctuations that does not have a constant periodicity and amplitude (Fig. 5.7a), the spectral signature of this complex insolation pattern is precession-dominated, paced by longer term obliquity and eccentricity cycles (Fig. 5.7a; Berger and Loutre, 1991; Berger et al., 1999; Laskar et al., 2004). The late Quaternary is characterised by a non-linear response of global oceans and ice sheets: the precessional (~26 kyr) interglacial-glacial cycles are paced by eccentricity into a sawtooth pattern of rapid high amplitude glacial ice sheet melting, followed

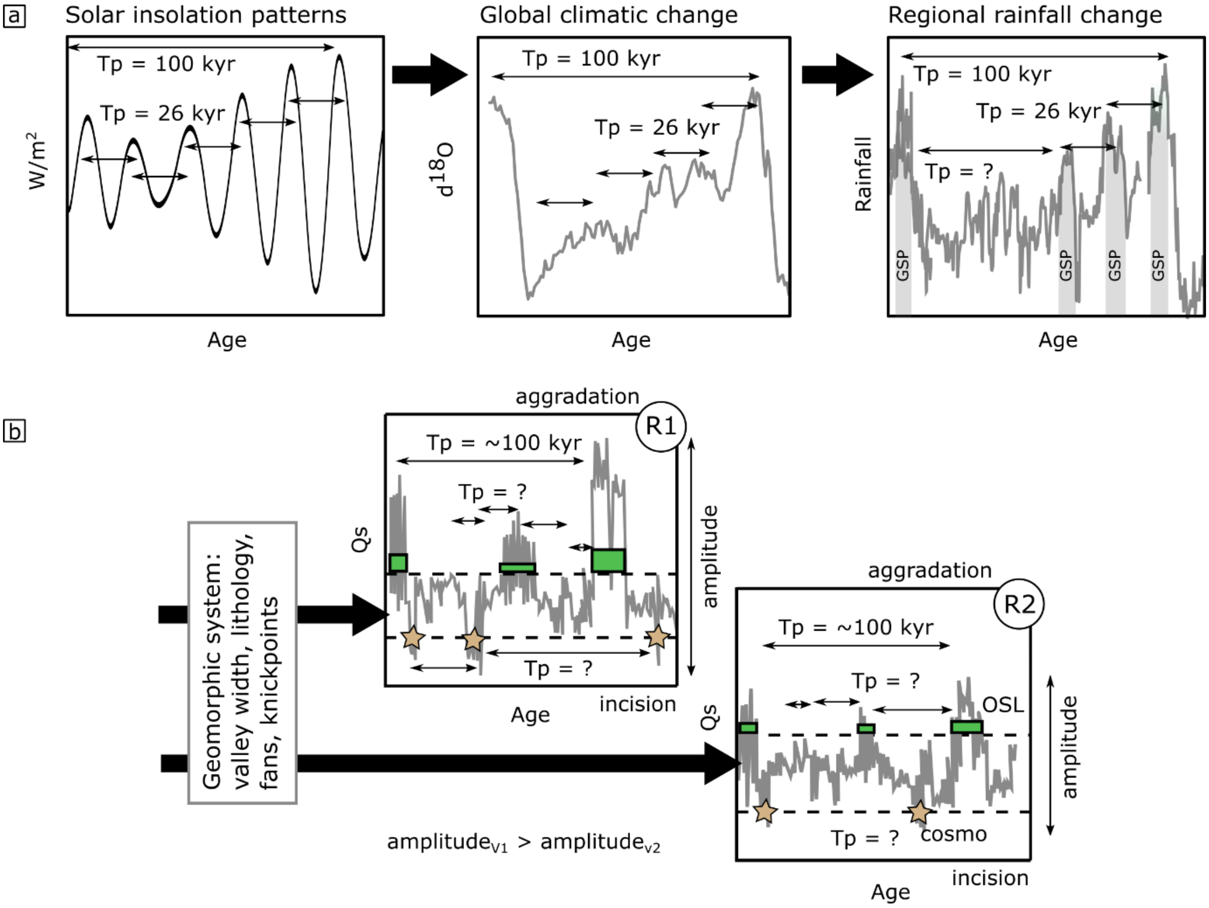

Figure 5.7– From Milankovitch cycles to the terrace record. Arrows from the top left to the bottom right represent the progression of the original orbital signal to the aggradation and incision patters recorded in terraces. (a) Progression from orbitally controlled solar insolation patterns to global δ^{18}O records (Lisiecki and Raymo, 2005), to the regional High Atlas humidity record (Tjallingii et al., 2008; Larrasoaña et al., 2013; Dixit et al., 2020). Tp = time period of signal. (b) Progress of the climatic signal through the geomorphic system and consequent aggradation and incision patters in reaches of a river system (R1 vs R2). The amplitude of local sediment flux (Qs) and thresholds (dashed lines) in the geomorphic system determine the timing of incision and aggradation, thus shredding the original orbitally forced climatic signal. OSL dates periods of aggradation (green boxes) and cosmogenic nuclides date the timing of incision (stars).

by a more gradual return from interglacial to glacial maximum conditions (Fig. 5.7a; Lisiecki and Raymo, 2005; Maslin and Ridgwell, 2005). On top of the non-linear response of the global climate system to Milankovitch orbital cycles, the resultant response of regional climate, in particular precipitation patterns, vary in direction and magnitude (Horowitz, 1989; Magee et al., 2004; Cohen et al., 2011; Cohen et al., 2012; Enzel et al., 2012). Northwest African climate humidity and Green Sahara Periods of the last glacial cycle follow a signal strongly controlled by precessional cycles (~ 26 kyr) albeit still paced by eccentricity (Tjallingii et al., 2008; Larrasoaña et al., 2013; Dixit et al., 2020). In essence, the global climatic curve derived from stacked marine oxygen isotope records (Lisiecki and Raymo, 2005) does not differ significantly from the record of northern Saharan humidity (Fig. 5.7a). The precessional signal is even more prominent in the record of regional climate (Fig. 5.7a). Thus, compared to records of eccentricity-controlled terrace formation in glaciated northwest Europe, the signal in the NW African terrace record would have been expected to show a stronger precessional control. In contrast to areas of high rate base-level lowering such as the Tibetan Plateau (0.87 mm yr^{-1}) where strath terrace levels record as high-resolution as 10^3 yr climatic fluctuations (Wang et al., 2015), lower base level lowering rates (~0.17 mm yr^{-1}, see §5.3.1) mean less vertical space for the formation and preservation of strath levels over time. Instead, the sedimentary fill on terraces may be expected to record such fluctuations, though they may not always preserve small-scale incisional events leading to internal erosion, such as documented in the repetition of overbank sands in the stratigraphy of T2 in the downstream Ait Said reach (TF). However, even accounting for such potential small-amplitude responses of the geomorphic system to precession-scale climatic signals, the relative amplitude of geomorphic action at ~10^5 yr timescales compared to negligible evidence for any response at a precessional timescale is inconsistent with the strength of the precessional signal in the climatic record (Fig. 5.7a). Thus, the lack of any precession signal in the strath terrace record, and the limited expression of an eccentricity-scale (100 kyr) signal, needs to be understood through the next filter: the geomorphic system (Fig. 5.7b).

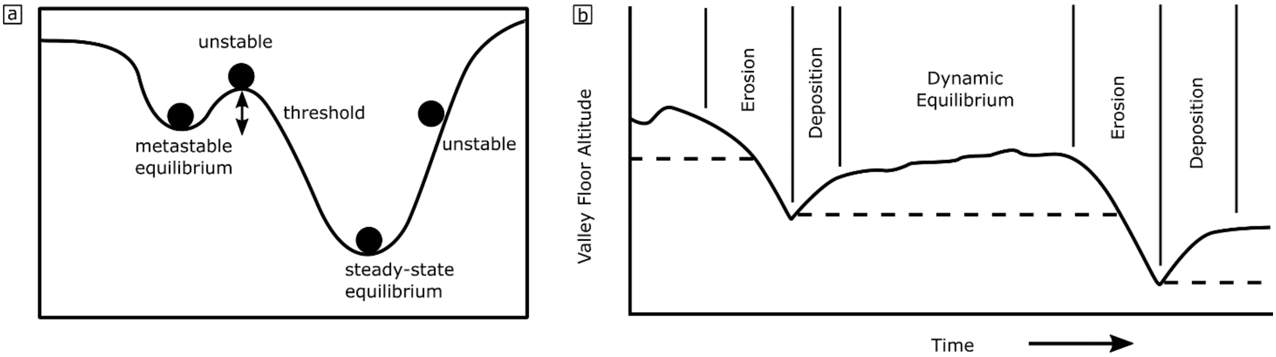

Figure 5.8 – The concept of metastable equilibrium, thresholds, incision, and deposition. (a) Concave shapes convey negative feedbacks keeping the system in (metastable) equilibrium, whilst convex shapes represent positive feedbacks promoting runaway aggradation or incision. The bump in between the metastable equilibrium and steady-state equilibrium conditions represents thresholds which need to be exceeded to push the system to the next state of equilibrium. Note that this diagram represents the relationship between equilibrium state and thresholds at one point in time and space. However, the thresholds as well as equilibrium positions change over time as well as spatially in a river system in response to allogenic forcing (e.g., climatic, and tectonic forcing) as well as the history of geomorphic response (e.g. aggradation, occupation and incision) and local conditions such as valley morphology and sediment flux. (b) Diagram modified from Schumm (1977), showing periods of instability when thresholds of erosion and deposition are subsequently triggered, separated by longer periods of dynamic metastable equilibrium.

A non-linear geomorphic response

One notable result which gives insight into the geomorphic system in the Mgoun River catchment is the long occupation time of terraces followed by episodic incision (see §5.3.1, Fig. 5.3). The concept of dynamic metastable equilibrium by Schumm (1973), wherein a river responding to sustained base-level lowering jumps from one metastable equilibrium (terrace occupation) to the next (Fig. 5.8a), through episodic incision rather than progressive steady state incision, is far from new. Geomorphologists in depositional settings have used models of intrinsic dynamics and complex response leading to increased recognition of autogenic dynamics in the last few decades (Paola et al., 2016; Hajek and Straub, 2017; Straub et al., 2020). However, the continued interpretations of incision rates from the abandonment ages of terraces and their elevations against the modern channel (Lavé and Avouac, 2000; Mukul, 2000; Hancock and Anderson, 2002; Fuller et al., 2009;

Pazzaglia, 2013) imply an assumption inherent in geological thought on erosional landscape evolution: one of progressive incision linked to base level lowering. In such a paradigm, mechanisms of geomorphic systems tending to equilibrium conditions are sought, with a bias towards negative feedbacks (Bull, 1979; Murray et al., 2014). In this school of thought observed transient and non-steady state conditions need an explanation of external forcing causing a temporary perturbation in the system (Hancock and Anderson, 2002; Fuller et al., 2009; Schanz et al., 2018). However, the continued occupation and aggradation of terraces over > 80 kyr in the Mgoun River during long-term geological uplift of the High Atlas is not a steady state equilibrium condition and does not correlate with a linear response to climatic changes. Similarly, the rates recorded here during periods of incision exceed an order of magnitude the background uplift rates, and can neither be considered in steady state equilibrium. Only by constraining over ~ 200 kyr of river behaviour can a long-term allogenic trend be accurately constrained (Figs. 5.3, 5.7). Since the behaviour of the Mgoun River cannot be explained by climatic forcing alone, I invoke the threshold and complex response model of geomorphology pioneered by Schumm (1973, 1977, 1979) and Bull (1979, 1990, 1991).

The concept of positive and negative feedback together with thresholds can be illustrated using the periods of rapid incision in between terrace occupation superimposed on a long-term surface lowering trend controlled by base level change or topographic degradation (Fig. 5.8b), such as observed throughout the High Atlas (Fig. 5.3). To start incision, an internal threshold needs to be triggered – e.g., by a change in sediment and water flux through climatic change -, after which the channels start transporting more material than they deposit. As channels deepen, the ratio of channel width to depth decrease, leading to more concentrated stream powers, and thus a self-enhancing feedback towards incision (Bull, 1979). As the riverbed is cleared of sediment to expose more bedrock, surface roughness decreases, in turn leading to narrower channels and more focused incision (e.g. experiment by Lamb et al., 2015). The resultant rapid incision continues, until the lowered local base level of the trunk channel leads to increased coupling with lateral sources of sediment, such as tributaries, fans and a gullied floodplain (Schumm and Parker, 1973; Schumm, 1977). Once a threshold is crossed, this increase in sediment input triggers a transition from incision to aggradation (Schumm and Parker, 1973; Schumm, 1977, 1979). As rivers start to aggrade, roughness increases, lateral erosion increases, the channel width to depth ratio increases: all positive feedbacks enhancing a rapid aggradation of the riverbed. Such positive and negative feedbacks together with internal thresholds could explain the parts of the pattern of incision and aggradation in the Mgoun River (Fig. 5.3a) which show a rapid change in operation of the geomorphic system (c.f. Fig. 5.8b). In turn, the concept of metastable equilibrium, a state of equilibrium away from steady state equilibrium, is one in which negative feedbacks keep a system in terrace occupation mode, whilst threshold exceedance can tip the system over to rapidly jump to another state closer to steady state equilibrium (Fig. 5.8a) – that is, a riverbed elevation adjusted to the build-up of gradual base level change. An example of negative feedbacks maintaining a metastable state is increased coupling and thus increased sediment load in response to channel lowering, whereas aggradation of the riverbed leads to an increase in local slope and thus an increase in stream power (Schumm, 1973, 1979). It becomes apparent from this model of thresholds that parts of the catchment, e.g., reaches within a river network, may have different thresholds and are at different proximity to these thresholds throughout their history. Thus, asynchronous aggradation and incision events within a river network such as the studied Mgoun reach (Fig. 4.21) can be explained, as well as large magnitude climatic events such as the transition from maximum glacial to maximum interglacial conditions (MIS 6/5e) leading to widespread threshold exceedance and consequent synchronous aggradation within the Mgoun River catchment. Lithological controls on local thresholds as well as inter-reach connectivity, in the form of gorges in the Mgoun River, are likely to contribute to such asynchronicity.

The record of asynchronous incision and aggradation out of sync with climatic transitions and the underlying concept of intrinsic thresholds on the timescale of interglacial-glacial cycles have implications for the interpretation of geomorphic landforms as well as downstream stratigraphy. Here I find that in particular incision, terrace abandonment and planation are asynchronous, whilst aggradation records a climatic influence in the system at a ~ 100 kyr timescale (Figs. 4.21; 5.7b). In turn, this means that cosmogenic exposure dating or conventional OSL overbank sand dating of terrace incision and radiocarbon dating of aggradation up to its limit of ~ 50 kyr would have been unlikely to have returned a climatic signal in the Mgoun terrace record at all (Fig. 5.7b). This points out at once the caution needed to be taken when interpreting terrace records as climatically forced with limited age control and over less than 100 kyr, in particular without dating at least two river reaches, as well as the challenge of obtaining an accurate climate signal with many conventional chronological tools. At a larger scale, the sediment flux signal exiting the erosional zone of the mountain belt influences the stratigraphy of any subsequent deposition such as in the foreland basin. In particular, models of alluvial river sediment transfer suggest Milankovitch scale signals of less than a few hundred thousand years are unlikely to propagate from mountain source areas through alluvial river systems more than 300 km long due to long intrinsic equilibrium timescales of the sedimentary system (Castelltort and Van Den Driessche, 2003; Armitage et al., 2013; Romans et al., 2016). Similarly, the non-linear and intrinsic dynamics of erosional zone geomorphic systems on Milankovitch timescales may lead to completely shredded and asynchronous depositional records such as terraces and distributary fan deposits in more proximal settings such foreland basins (e.g. Foster et al., 2017). Thus, even if some fluvial transport models allow the transference of high-frequency climatic signals from mountain sources to depositional basins further downstream (Simpson and Castelltort, 2012), the results presented here suggest the climatic record may be shredded before even reaching the mountain front.

The discussion on the extent of climatic, allogenic forcing, and the role of intrinsic behaviour of the geomorphic system is one that has been well-debated. Workers on European terrace records have weighed the evidence for and against climatically controlled river terrace formation (Vandenberghe, 1995, 2002, 2003; Gibbard and Lewin, 2009). In particular, Vandenberghe (1995) considered the evolution of river systems at the 10^2 – 10^3 year timescale to be controlled by intrinsic evolution and complex response as detailed by Schumm (1977) and Bull (1991), with fluvial evolution at 10^4 - 10^5 year timescales dominated by climatic fluctuations and its derivative effects on the geomorphic system. In this model, 10^4 – 10^5 year geomorphic processes result in long stable periods offset by periods of instability triggering incision and subsequent aggradation during climatic transitions (Vandenberghe, 1995). Such a view of glacial-interglacial climatic control on terrace formation at 100 kyr timescales has been further corroborated by reviews of Quaternary terrace staircases (Bridgland and Westaway, 2008, 2014). Notably, these propose an increase in continental denudation at the mid-Pleistocene transition from a dominant 41 kyr to a 100 kyr signature of global climate fluctuations, through harmonic resonance with river response time at a 10^5 yr timescale. On the one hand, the temperate climate as well as the strong forcing of ice sheets during glacial conditions may contribute to the higher river-hillslope and inter-reach connectivity, and ability of geomorphic systems to attain equilibrium conditions than in arid settings. However, even in temperate humid conditions, increased constraints on the chronologies of terrace formation reviewed by Vandenberghe (2003) have led to the conclusion that a direct relationship between interglacial-glacial climate and fluvial dynamics does not apply in all cases even at 100 kyr timescales. The question remains: what determines the timescales at which intrinsic thresholds and complex response control fluvial development? In the next section I will discuss the geomorphic and geological data of the Mgoun River catchment (1200 km^2) to explain the long timescales of asynchronous aggradation (>10^4 yr) and incision (>10^5 yr) along a 50 km long reach.

5.3.3 Diachronous or asynchronous? Timescales of local bedrock incision and knickpoint migration

The combination of terrace treads derived from DEM and field data (Ch. 3) and OSL ages (Ch. 4) allow terrace formation to be constrained in the context of river long profile evolution. Two knickpoints can be seen in the modern river profile (Fig. 5.9a). These two knickpoints coincide with gorges through resistant limestone bedrock, but not all gorges in resistant limestone bedrock coincide with knickpoints. Terrace treads of T1 and T2 abut against a knickpoint in the thrust front, upstream of which no strath incision has yet occurred after the deposition of the thick T2 sediment stack. The merging of erosional bedrock treads of T1 and T2 just downstream of this knickpoint

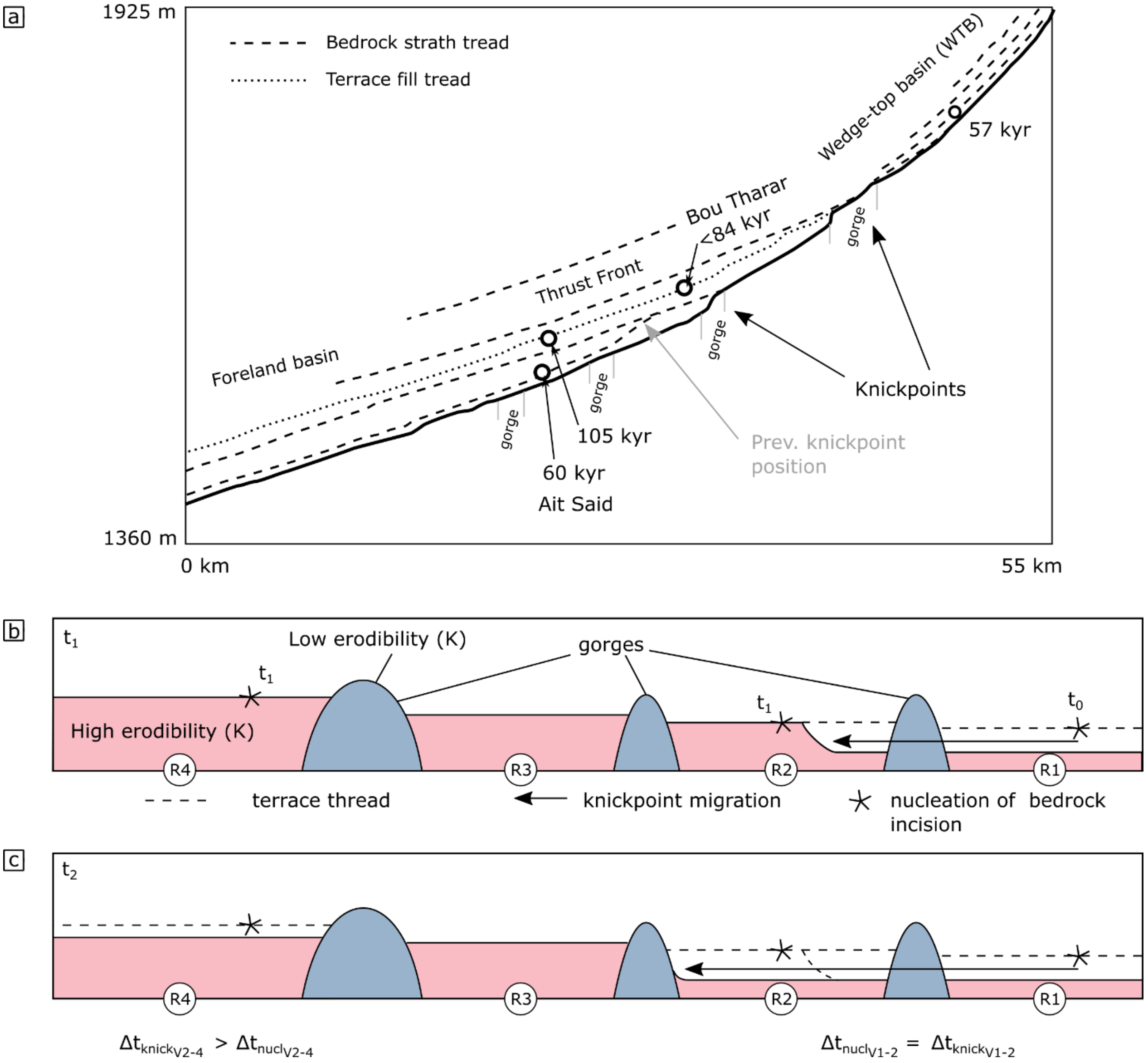

Figure 5.9– Terrace treads, abandonment ages and river profile evolution. (a) Modern river long profile of the Mgoun River with terrace treads and OSL dates of terrace abandonment. (b-c) Conceptual model distinguishing diachronous terrace formation due to knickpoint migration and distinct timing of incision nucleation. (b) t1 during the river profile evolution of a river eroding through erodible bedrock separated by gorges in resistant bedrock. A knickpoint nucleating incision downstream (in Reach 1) has propagated though one gorge and into the next reach upstream (R2). At the same time, during t1 supercritical knickpoints (Baynes et al., 2018) nucleate in the second (R2) and fourth reach (R4). (c) Terrace treads record the timing of abandonment. In the second reach, the difference in timing of incision nucleation is indistinguishable from the time needed to propagate the first knickpoint. However, the knickpoint has not yet reached the fourth reach, which enables the resolution of independent nucleation of incision in this reach.

constrains a previous position of the knickpoint before T1 incision (Fig. 5.9a). Based on this geomorphological evidence alone it is possible to identify river profile evolution through knickpoint migration. In addition, in the TF the top OSL dates constraining the age of abandonment show a decreasing age of T2 abandonment from the downstream Ait Said reach (105 ka) to the mid-stream Bou Tharar reach (<84 ka) 10 km upstream. Terrace formation through progressive knickpoint incision has been demonstrated in numerous field studies where tectonically-generated propagating knickpoints were identified including in northern California (Seidl and Dietrich, 1992), the Virginia Coastal Plain and Piedmont (Howard et al., 1994), the Rocky Mountains (Zaprowski et al., 2001), and additionally with in situ cosmogenic ^{10}Be in western Scotland (Jansen et al., 2011). The subsequent conceptual model of knickpoints propagating up from downstream perturbations of sea level or tectonic faults to form terrace treads (Finnegan, 2013) has led to further field evidence, dating and discussion on climatic modulation of tectonically generated knickpoint migration resulting in diachronous terraces (Anthony and Granger, 2007; Rixhon et al., 2011; Baynes et al., 2015; Beckers et al., 2015; DiBiase et al., 2015; Demoulin et al., 2017; Ortega-Becerril et al., 2018). However, the geomorphic and chronologic evidence of strath treads in the Mgoun present a challenge to the simple model of downstream knickpoint-controlled terrace abandonment and bedrock incision. The unfinished propagation of terrace abandonment initiated at 105 ka in the thrust front (Fig. 5.9a) demonstrates an erosional disconnect between river reaches in the thrust front and the wedge-top basin since that time. Whilst knickpoint migration from the thrust front is expected to migrate into the wedge-top basin eventually, the terrace abandonment of the stratigraphic T2 level in the wedge-top basin at 57 ka must be the product of incision starting independently from upstream propagation.

A physical experiment by Baynes et al. (2018) has shown that rivers can nucleate terrace incision and the formation of local bedrock knickpoints in response to changes in sediment flux in the absence of downstream perturbations in base level. Such climatically triggered knickpoint formation and strath formation of ~ 10 – 40 m height on the order of 10^4-10^5 years is of a different scale to knickpoints created by tectonic perturbations, often exhibiting a few hundred to thousand meters relief depending on the rate of baselevel fall, on the order of 10^6 years (e.g. Boulton et al., 2014 in the High Atlas). The logical extension of such a conceptual model is one that is demonstrated in the field data: multiple local nucleations of terrace and bedrock incision along a river long profile. The ability of the dataset to demonstrate local nucleations depends on the timescale of asynchronicity of the two mechanisms (Fig. 5.9b-c). It is only when the difference in time between incision through knickpoint propagation (Δt_{knick}) is longer than the difference in time between local nucleations of incision (Δt_{nucl}) that the two effects can be resolved (Fig. 5.9b-c). Knickpoint celerity has been shown to be affected up to an order of magnitude for a twofold difference in rock strength (Zondervan et al., 2020). Considering the up to an order of magnitude difference in rock strength between the erodible red beds and the resistant limestones along the Mgoun River (Table 3.1), the gorges of resistant bedrock are expected to play a major role in extending the Δt_{knick} between the Ait Said reach and the wedge-top basin to more than 10^5 yr. Whilst a catchment existing solely of resistant bedrock would also have a high Δt_{knick}, a preserved terrace record is most likely in weaker lithologies which enable lateral erosion (Montgomery, 2004; Schanz and Montgomery, 2016; Stokes et al., 2017) and consequently also a low Δt_{knick}. Thus, the most likely landscape to resolve separate nucleations of river incision in the terrace record is in a setting with weak bedrock separated by high-strength gorges where $\Delta t_{knick} > \Delta t_{nucl}$. In effect, the model proposed in Fig. 5.9 demonstrates an example where bedrock strength of the underlying lithologies and their stratigraphic and structural configuration in a mountain belt affect not only the formation and preservation of terraces (e.g. Stokes et al., 2017), but also the timing of terrace formation. The lithological and structural controls on the distribution of erodibilities along the Mgoun River present a direct control on the timescales of knickpoint propagation (Δt_{knick}), the timescale of terrace diachronicity, and the ability to resolve separate incision nucleation events in the terrace record. However, what controls Δt_{nucl}, the time difference between separate incision nucleation events along a river? To answer that question, I will next examine the sediment flux system of the Mgoun River catchment.

5.3.4 *The controls of valley bedrock structure and lithology on sediment flux*

The repetition of weak red beds and strong limestones in the High Atlas thrust front is responsible for the multiple gorges of the Mgoun River which slow down knickpoint propagation (Figs. 5.9 & 5.10). In addition to moderating the bottom-up control of terrace formation through knickpoint propagation, the top-down control of climate and its influence on sediment flux is moderated by lithology and structure. In particular, the distribution of weak (10 - 14 MPa) and strong (39 – 90 MPa) rock types in these thrust stacks (Fig. 5.10) forces valley widths varying from ~3.5 km in the upstream Ait Toumert reach (WTB) to ~150 m in the midstream Bou Tharar reach (TF) and ~750 m in the downstream Ait Said reach (TF). To consider the effect of these variable valley widths and the underlying hillslope lithologies on the timing of terrace aggradation and incision I will here discuss lateral and longitudinal

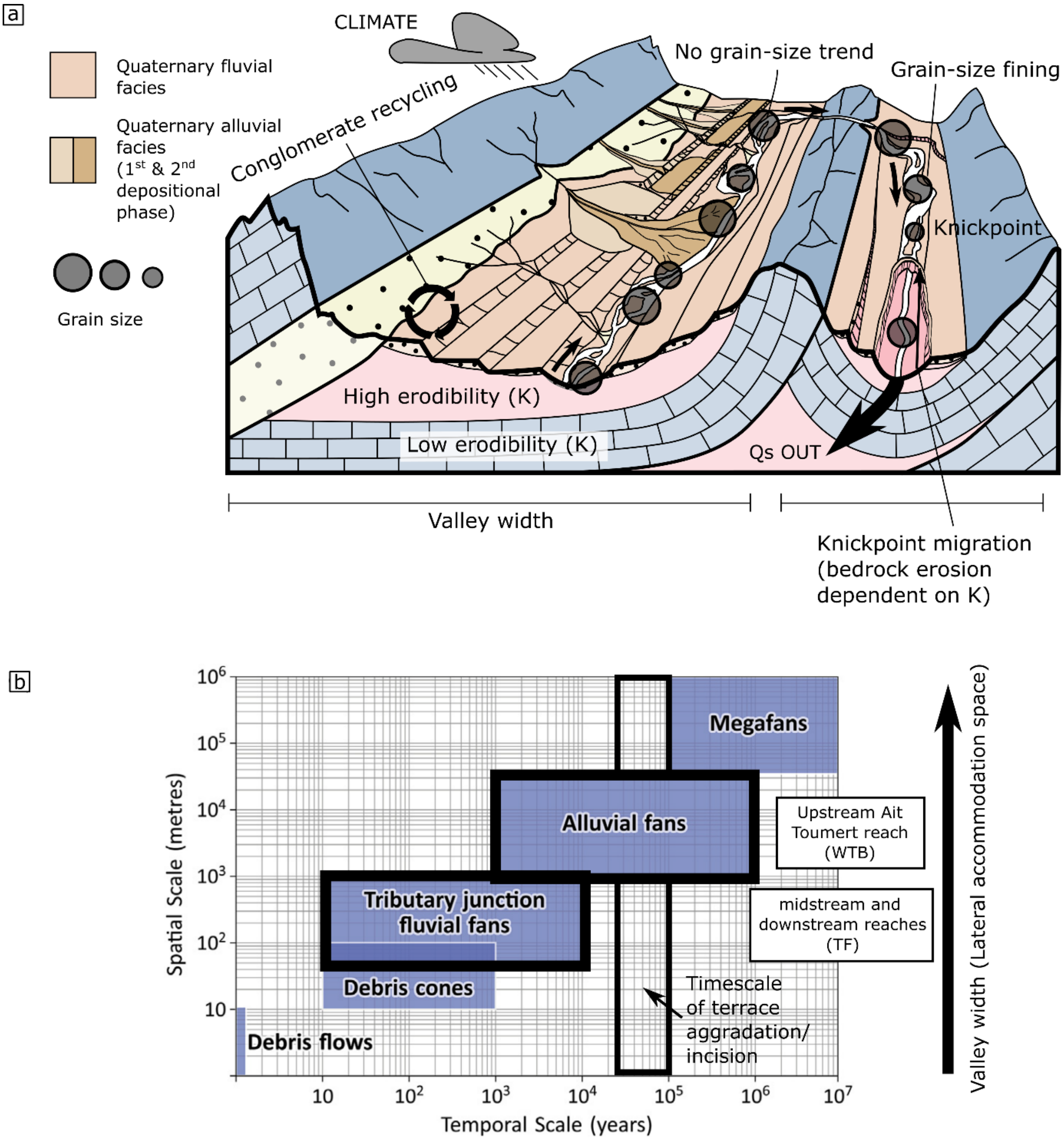

Figure 5.10 – Valley width controlled by lithological and passive tectonic structural controls and its effect on sediment flux. (a) Passive structural geology and lithology influences terrace formation in three ways: 1) The presence of structurally exposed conglomerates in certain valleys allows for recycling of clasts into Quaternary valley fill sediments. This effect can influence grain size, as well as the lithological signature and abundance of available sediments within valleys; 2) Spacing of thrusted low erodibility lithologies determines the width of valleys. Wider valleys can accommodate alluvial fans and extensive tributaries. Lateral sediment features buffer the coupling between hillslopes and the river channel in wide valleys, whilst in narrow valleys this coupling is more direct. Furthermore, extensive lateral input means bedload is supplied with coarse grained sediment, preventing downstream fining. Wider valleys can accommodate preservation of more terrace levels than narrower valleys. 3) The bedrock erodibility of lithologies along the length of the river influences knickpoint

migration speeds. Low erodibility gorges can act as significant blocks against the propagation and connectivity of terrace treads, keeping terrace formation processes local. (b) The typical spatial and temporal scales of distributive fluvial features coupling hillslope sediment generation with river channel transport (from Mather et al 2017). As valley width increases, features buffering between hillslopes and river channels increase in spatial and temporal scales. At the timescale of terrace formation in the High Atlas, the presence of alluvial fans is expected to make a significant impact on timing of formation.

sediment flux. Lateral sediment flux is considered in the cross-section of a valley from hillslope to river channel, whilst longitudinal flux is in the downstream direction along the length of the trunk river channel.

Firstly, the clast lithological and grain size data can be used to track the provenance and transport of sediment along the Mgoun River. The first control on local lateral sediment flux is the geological substrate of hillslopes. In the wedge-top basin and thrust front Pliocene and Mio-Pliocene conglomerates derived from parts of the central fold-thrust belt make up hillslopes (Fig. 5.10a) in all reaches except the midstream Bou Tharar reach in the TF (Figs. 3.1, 3.2, 3.8). Typically, terrace and modern gravel bars have a high percentage of limestone, a narrow grain size distribution and well-rounded pebbles, which likely results from clasts being recycled from conglomerates and terrace gravels (Quick et al., 2019). Noticeably, the similarity of clast lithological distributions of reaches with geographically and chronologically similar conglomerate deposits suggests conglomerate recycling is likely the dominant source of clasts within each reach overprinting any signature coming from upstream (Fig. 3.8). The narrow grain size distribution and well sorted, well-rounded ellipsoidal pebbles resulting from conglomerate recycling increase the threshold for bedload entrainment and thus increases the thresholds for fluvial incision (Komar and Li, 1986). Consequently, the effect of conglomerate recycling on sediment character may well contribute to the stochastic nature of terrace occupation and episodic incision observed in the Mgoun River (Fig. 5.3).

The dominance of lateral over longitudinal sediment flux is also noticeable in grain size trends. Unlike in longitudinally connected river systems where steady decrease in grain size along linear or exponential trends occur (Paola et al., 1992; Ferguson et al., 1996; Rice and Church, 2001; Attal and Lavé, 2006; Fedele and Paola, 2007; Duller et al., 2010), grain size trends are interrupted from reach to reach. Even in the midstream Bou Tharar reach, with the strongest fining trends, fining rates are lower than in other field studies (Fig. 3.8). Thus, the coarse grain size fraction of the studied Mgoun River reaches in the WTB and TF are dominated by lateral sediment flux recycled from conglomerates (Fig. 5.10). The relatively low longitudinal transport connectivity is likely the effect of unsaturated groundwater systems in porous sedimentary rocks and karstic aquifers which diminish hydrologic flow through infiltration in the Mgoun River channel (Cappy, 2006; de Jong et al., 2008). In addition, any geomorphic barriers to sediment flux such as valley constrictions, sediment slugs and over-widened channels may also contribute to low longitudinal connectivity (Fryirs et al., 2007; Fryirs, 2013).

Because the lateral sediment flux dominates the flux of coarse sediment bedload in the river channel, landforms buffering between hillslope sediment generation and delivery to the trunk river channel have a dominant role in the sediment content of the river channel over time. The width of the valley, determined through the distribution of erodibilities by lithology and passive tectonic structure of the thrust front (Fig. 5.10a), affects the magnitude of buffering landforms, their connectivity with the channel, and the timescale of stochastic sediment flux (Fig. 5.10b). In the confined 150 – 650 m wide valley of the Bou Tharar reach terraces preserve only stratified conglomerates characteristic of braided fluvial channel bars and bedforms in channels of at least three meters depth. Here, any input from hillslopes has been reworked by fluvial transport. In contrast, in the unconfined, ~ 3.5 km wide valley of the wedge-top basin, river terraces preserve inversely graded and massive conglomerate deposits recording sediment gravity flows derived from tributaries and distributary fans (Fig. 3.9). The stochastic nature of such flows as well as the buffered connection of tributary and alluvial fans to the river channel (Stokes and Mather, 2015; Mather et al., 2017; Mather and Stokes, 2018) introduce noise and extend response times between climatic effects on hillslopes and delivery of sediment into the channel. In addition, stochastic sediment flux has been shown to induce local knickpoints and terrace formation as sediment deposition can create a local armour layer preventing bedrock incision (Sklar and Dietrich, 2001; Korup, 2006; Ouimet et al., 2009; Korup et al., 2010; Scherler et al., 2016). Valley width both influences the size of buffering landforms such as fans, as well as their connectivity to the river channel (Stokes and Mather, 2015). In the 3.5 km wide wedge-top basin, large alluvial fans affect sediment flux to the river channel. These larger landforms buffer at timescales of 10^3-10^6 yr (Fig. 5.10b; Mather et al., 2017), the same timescale Milankovitch forced climatic fluctuations operate on. Contrastingly tributary fans and debris cones, more likely to be found in more confined valleys, affect channel conditions over timescales of less than 10^4 yr (Fig. 5.10b; Mather et al., 2017). Mather et al. (2017) show that alluvial fans in the High Atlas experienced limited coupling with the trunk river during fan-building periods, whilst periods of river incision induce a partial buffering by alluvial fans which connect via an active channel incising into the deposit. Thus, the effect of alluvial fans in the wedge-top basin is to extend the river response time to externally forced changes in sediment availability by buffering the hillslope-tributary to trunk river sediment transfer.

The implication of valley-width controlled stochasticity and timescales of buffering between hillslopes and the river channel in a setting where valley width is set by lithological and structural controls rather than hydrologic scaling (Fig. 5.10), is that the response to external forcing as well as the timescales of internal dynamics are expected to vary by orders of magnitude. Together with the dominance of lateral sediment flux and limited longitudinal connectivity in the Mgoun River, the result is the observed river incision occurring independently and asynchronously on the order of 10^4 years over ~ 30 km flow length of trunk river channel. Only through the emergent mechanisms and behaviours (Murray et al., 2014) of a whole-catchment model that links the behaviours of individual components such as the river channels, hillslopes, and fans (e.g. Fryirs, 2013) and its underlying contingent geological controls can the internal dynamics and asynchronous response of river channel incision and aggradation start to be understood. The models proposed in Figs. 5.9 and 5.10 enable underlying controls on asynchronous terrace formation such as lithology and structure to be understood and quantified.

5.3.5 *Asynchronous terraces: an anomaly or a fundamental concept?*

By combining the chronologic, geomorphic, sedimentologic and geological data of the Mgoun River catchment I have been able to demonstrate the influence of lithology and its stratigraphic and structural configuration on the response to climatic fluctuations and internal dynamics of incision and aggradation in the catchment. The stratigraphy of repeated thrust stacks with weak bedrock (10 - 14 MPa) making up valley floors enables terrace formation and preservation. The high strength bedrock (39 – 90 MPa) forms gorges and separates reaches of the river, lengthening the timescale at which the system equilibrates through knickpoint propagation (Fig. 5.9). Consequently, the asynchronous responses of several reaches to fluctuations in climate and internal dynamics on the order of 10^4 – 10^5 yr along 30 km of river channel are recorded within terraces. The lithologies and thrust stack structure resulting in variable spacing of high-contrasts in bedrock erodibility result in valleys with variable widths along the length of the Mgoun River (Fig. 5.10). These variable valley widths ranging from 150 m to 3.5 km introduce differences in the hillslopes to river channel connectivity in terms of response time and stochasticity of sediment flux. In addition, recycling of conglomerates in the thrust front increases the importance of lateral sources of sediment and affects sediment character. The result is river response to late Quaternary climate fluctuations on the order of 10^4 and 10^5 yr which documents only a limited synchronous signal of the catchment on the order of 10^5 yr (Figs. 5.6, 5.7) as well as asynchronous signals on the order of 10^4 to 10^5 yr controlled by internal dynamics (Figs. 5.7, 5.8). Due to the resultant metastable equilibrium conditions of stochastic occupation and incision in river channels (Fig. 5.8), terrace records require a chronology of occupation and abandonment up to 200 kyr to accurately derive meaningful denudation rates consistent with background uplift rates (Fig. 5.3). From the mechanisms explained above it emerges that the underlying conditions of the Mgoun River catchment play a significant role in setting the timescale of internal dynamics, asynchronous terrace formation and transience. The role of lithology and structure is most significant when there are large contrasts in bedrock erodibility, which is most likely in erosion through sedimentary units in thin skinned tectonic settings often found in the thrust front of a mountain belt (Fig. 5.11). Furthermore, the control of lateral sediment flux and thus local

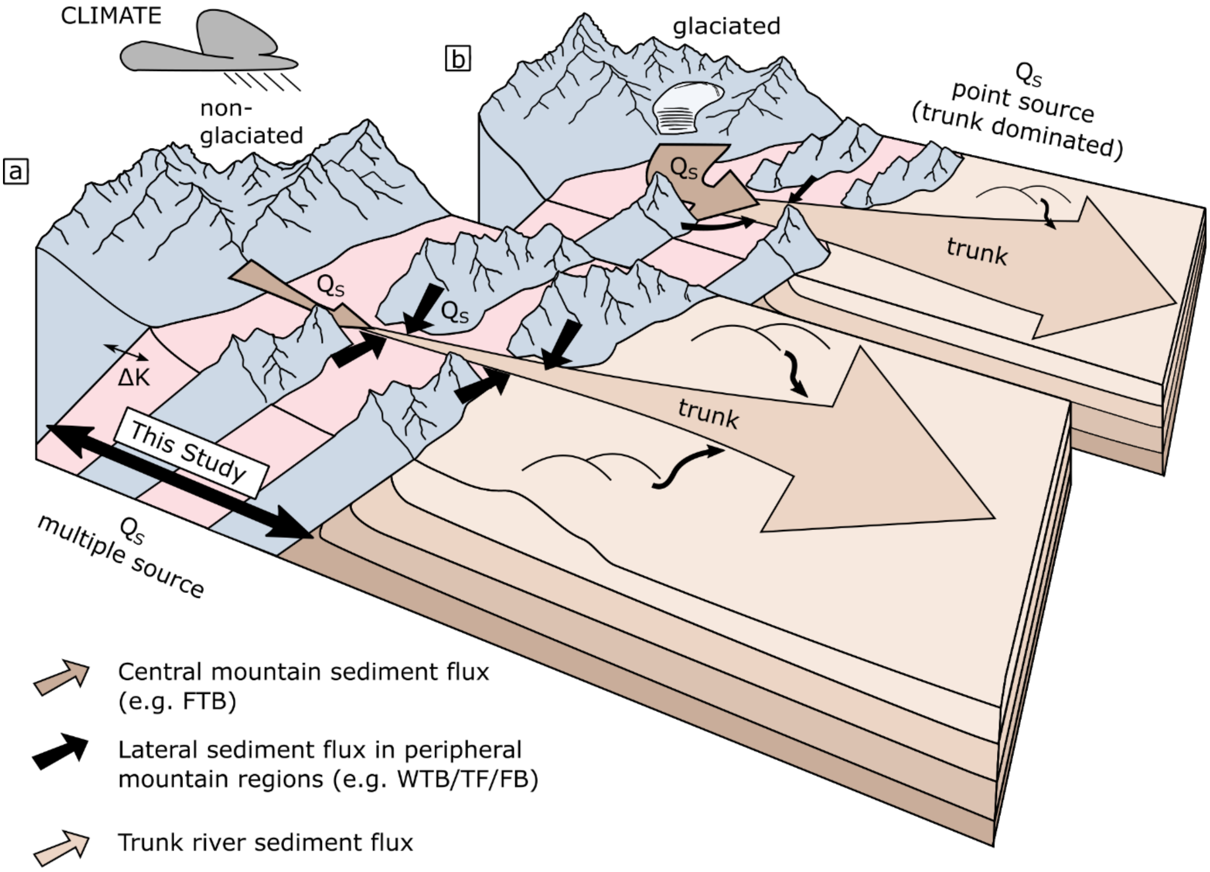

Figure 5.11 – Conceptual model of sediment flux from source to sink, in a non-glaciated and glaciated environment. (a) in the non-glaciated model, a trunk river traversing the centre of the mountain belt (including the fold-thrust belt) to the peripheral edges of the mountain belt (including wedge-top basins and the thrust front) increases its sediment flux, but lateral input is still relatively large enough to make an impact on local trunk river sediment flux. Once the ratio of lateral sediment fluxes to the trunk sediment flux decreases, the system can be treated as a point-source system. (b) in a glaciated environment, glacial activity over glacial-interglacial timescales dominates the sediment flux from a much more central position, and the peripheral mountain regions and foreland basin can be treated as being controlled by a point source. This study is situated in the peripheral mountain region in a non-glaciated setting, where lateral sediment fluxes are important, and where erodibility contrasts elicit dynamics described in sections above.

valley conditions are most significant when the ratio of longitudinal sediment flux to lateral sediment flux is lowest. In contrast to non-glaciated arid to semi-arid settings, mountain belts experiencing ice sheets in glacial periods often found in more temperate settings are more likely to experience sediment flux dominated by sourcing from the catchment headwaters and high longitudinal connectivity. Whilst this means the internal dynamics leading to stochastic incision and aggradation discussed in this study may not apply in temperate and depositional settings, other internal dynamics may still generate autogenic responses (Scheingross et al., 2020). For example, models of autogenic terrace formation through meander cut-off (Finnegan and Dietrich, 2011) and steady vertical erosion with irregular lateral migration (Merritts et al., 1994; Limaye and Lamb, 2014, 2016) are capable of predicting asynchronous terraces on the order of 10^4 yr. Thus whilst it is more likely that climatically controlled river terrace staircases occur in temperate glaciated catchments (Vandenberghe, 1995, 2002, 2003; Bridgland and Westaway, 2008; Gibbard and Lewin, 2009; Bridgland and Westaway, 2014), I recommend caution in extrapolating concepts derived from these field settings to areas with only limited constraints on geomorphic behaviour and catchment conditions.

5.4 SYNTHESIS

This thesis presents an integrated approach of quantitative geomorphology, sedimentology and geochronology through field, DEM, and lab-based techniques to investigate the effects of lithology and structure on fluvial archives originating in mountain belts. Fluvial archives including erosional topography and depositional landforms are used to derive direct information on the interrelationships between erosion, climate, and tectonic histories (§1.2). The need for a greater understanding of the effect of variable lithology and structure of bedrock on fluvial landscape evolution has been increasingly recognised as an outstanding challenge within the field of geoscience (§1.2 - §1.3). First, chapter 2 uses the High Atlas as a natural laboratory to assess the progressive mobility of the drainage divide in three lithologically and structurally distinct groups of bedrock. The approach here is to constrain the lithological, structural, and rock strength properties of lithostratigraphic units which increase in age from Mesozoic sedimentary cover to Palaeozoic crystalline basement east to west. These properties are then linked to topographic data on the mobility of the central drainage divide to constrain the controls of rock types and their passive tectonic structural configuration in a post-orogenic mountain belt on the mobility of the drainage network on the timescale of 10^6 – 10^7 years (§5.2). Whilst the dynamics that emerged from this work are compatible with the timescale at which tectonic changes affect landscape erosion and subsequent deposition into stratigraphic records, the dominant climatic signal during the Quaternary consists of 10^4-10^5 year orbital fluctuations (§1.4 & §5.3). Therefore, the insights on the bedrock lithologies and their stratigraphic and structural configuration in the mountain belt gained in chapter 2 (§5.2) are then applied to a catchment draining an area of the mountain chain. The Mgoun catchment exhibits the highest contrasts in rock erodibility and structural control, draining the wedge-top basin and the widest part of the thrust front with multiple thrust stacks. In chapter 3 geological, geomorphological, and sedimentological data from strath terraces and the modern river in the Mgoun catchment are collected and chapter 4 develops the necessary geochronological methodology to accurately date the occupation of these strath terraces. §5.3 integrates data from chapters 3 and 4 to: 1) constrain a 200 kyr history of river channel incision and aggradation; and 2) use these results to gain insight on the effect of lithology and structure on interactions between erosion, transport, deposition on hillslopes and in the river channel network and the timescales on which these occur. Important research contributions of this thesis include:

- Quantifying the relationship between lithology, rock strength, structure and geomorphic response of river channels and derivation of the range of erodibility within the High Atlas collisional mountain belt (Ch. 2, Ch. 5.2). These results allow calibration of the stream power model of erosion whilst at the same time demonstrating its limited ability to reflect the full response of river channels to rock strength and structure.

- Demonstrating how the physical properties of the mountain belt including lithology, rock strength, stratigraphy and passive tectonic structure control the mobility of the central drainage divide during the long-term erosion of a collisional mountain belt (Ch. 2, Ch. 5.2).
- Demonstrating that the timing of terrace abandonment is determined by the control of rock erodibility on the timescales of diachronous erosional connectivity through knickpoint migration as well as the timescale of asynchronous local initiations of incision along the river long profile (Ch. 3, Ch. 4, Ch. 5.3).
- Demonstrating how bedrock conglomerates recycled in thin-skinned tectonic structure and water flow through porous and jointed bedrock result in low river longitudinal connectivity and a dominance of coarse-grained lateral sediment flux from hillslopes to the river channel (Ch.3, Ch. 5.3).
- Showing that local timescales of hillslope to river channel coupling of sediment flux is mediated by lithology and thin-skinned tectonic structure through their effects on valley width and buffering landforms such as tributary and alluvial fans (Ch. 3, Ch. 4, Ch. 5.3).
- Demonstrating the cumulative effects of lithological and structural controls in the Mgoun catchment result in river channel incision and aggradation that is asynchronous on the order of 10^4-10^5 years, whilst there is still a signal of synchronous aggradation linked to 100 kyr

> climate fluctuations. This result also demonstrates the signal of fluctuations in the regional climate system is shredded and only preserved in a record that requires chronological control of ~ 200 kyr of terrace aggradation in multiple reaches to be accurately constrained.

Below I discuss the importance and implications of these contributions. Finally, I suggest some future work that is motivated by the findings in this thesis.

IMPORTANCE, IMPACT, IMPLICATIONS

Rock strength and structural controls on rock erodibility

The dataset of lithology, uniaxial compressive strength determined from field measurements, and normalised river channel steepness from topographic analysis of a DEM (Ch. 2) provide the first explicit quantitative characterisation of the relationship between rock strength, normalised channel steepness and rock erodibility (*K*). This is important, because this has enabled me to calibrate the stream power model of river erosion which has been effective at modelling landscape evolution on 10^6 – 10^7 year timescales. The extent to which lithological strength affects erodibility in the stream power model depends on the scaling of the slope term, *n* (Eq. 6; Whipple and Tucker, 1999; Lague, 2014; Perne et al., 2017). Through the comparison of normalised steepness and rock strength I constrained this parameter to $n \sim 2$, such that uniaxial compressive strength and normalised river channel steepness scale along a linear relationship. However, there is a difference in the range of rock erodibilities calculated through values of uniaxial compressive strength (one order of magnitude) and through normalised river steepness using the stream power model (two orders of magnitude). This difference reflects on the one hand the controls of weaknesses in rock mass generated by joints and fractures which are not accounted for in measures of uniaxial compressive strength (e.g. Anton et al., 2015; Baynes et al., 2015). On the other hand, dynamic effects such as channel width adjustment (e.g. Allen et al., 2013), are not accounted for in the simplified stream power model. Thus, whilst the results in this thesis allow for useful calibration of the stream power model and its erodibility parameter with rock properties measured in field settings, they also demonstrate the limits of the stream power model of fluvial erosion.

Drainage divide mobility driven by rock erodibility and tectonic structure

A key contribution of this thesis has been to provide a conceptual framework of lithological and structural controls on drainage divide mobility during the long-term erosion of a collisional mountain belt (Ch. 5.2). In particular, I show that in gently deformed horizontal sedimentary strata often found in the early stages of erosion through a mountain belt, the drainage divide is mobile (Ch. 2). Here, erosion through high contrasts in erodibility offset by faults or gentle folds result in transience of erosion rates in space and time. In more extensively faulted, folded, and metamorphosed bedrock lower contrasts in erodibility and near-vertical stratigraphy results in a stable drainage divide. Finally, when ultra-resistant crystalline basement is exhumed, the drainage divide migrates to the centre of the resistant body or rock. This means drainage divide reorganisation can be induced through rock properties alone without need for tectonic or climatic drivers, and that its effect is strongest in rock with high contrasts in erodibility, limited tectonic structural deformation as well as during the exhumation of crystalline basement. This is an important conclusion because drainage reorganisation asserts a first order control on landscape evolution, affecting discharge of water, sediment and the shape of river long profiles and thus the erosional processes and resultant stratigraphy in downstream basins (Bonnet, 2009; Giachetta et al., 2014).

Lithological control on erosional connectivity

A further significant result is the control of rock erodibility on the timescales and processes of river long profile evolution (Ch. 3, Ch. 4, Ch. 5.3). Once incision starts downstream, river terrace abandonment is progressively younger upstream as a wave of incision propagates (c.f. Finnegan, 2013; Demoulin et al., 2017). The timescale of this propagation along a 30 km length of the Mgoun River is 10^5 years. This means that at a timescale of $< 10^5$ years, incision responding to changes in sediment flux may initiate river incision elsewhere on the long profile independent from such knickpoint propagation. I observed such local initiation of river incision resulting in terrace abandonment ages that are not only diachronous in some reaches, but asynchronous along the entire length of the river profile on the order of 10^4 years. Effectively, the erosional connectivity of the river is too low for a consistent pattern of terrace incision. This is important because this means the effect of resistant bedrock is not just to slow landscape response in the form of knickpoint propagation (Zondervan et al., 2020), but to cause low erosional connectivity that fragments reaches of a river which are responding to climate in different ways. Thus, especially along long rivers with reaches of resistant bedrock, it is very likely that histories of incision and aggradation are asynchronous. Consequently, studies that constrain river incision by dating terraces in one reach of a river may not constrain the river's entire history of incision.

Lithological control on longitudinal and lateral sediment flux

The compartmentalisation of river reaches and their asynchronous terrace formation depend on the connectivity of sediment transport longitudinally along the river trunk channel (Ch. 3, Ch 5.3). The ratio of lateral to longitudinal sediment flux, where lateral sediment flux originates from hillslopes and buffering landforms such as alluvial fans (Mather et al., 2017), I found is controlled by lithology and structure in two ways. Firstly, longitudinal connectivity and transport through the river channel downstream may be hindered by geomorphic barriers thrown up by constrictions in strong bedrock and over-widened channels and sediment slugs in weak bedrock (c.f. Fryirs et al., 2007; Fryirs, 2013), whilst overground flow filtering through porous sedimentary bedrock and flowing into joints and fractures in limestone gorges (Cappy, 2006; de Jong et al., 2008) diminish a stream's capacity to transport sediment over long distances. Secondly, I observed the recycling of bedrock conglomerates common in thin-skinned tectonic settings (Dingle et al., 2016; Quick et al., 2019) causes coarse-grained sediment in the river channel to reflect local provenance. This means lithological and structural conditions influence the relative local contributions of downstream sediment flux and sediment flux from the hillslopes. This is important because a dominance of lateral sediment flux increases the isolation of response to climatic change from reach to reach. This in turn supports the controls of lithological and structural control on valley morphology, as wider valleys in widely spaced thrust stacks with weak valley-floor bedrock and strong valley walls affect the spatial and temporal scale of buffering landforms. I found alluvial and tributary fans in wide valleys introduce stochastic gravity flows into the river channel which get reworked in more confined valleys through fluvial processes. This means lithological and structural controls on valley morphology affect the timescale of buffering between hillslope sediment generation and the river channel, whilst also affecting the timescale at which the river reworks stochastic gravity deposits originating from lateral sources. Hence lithological and structural control on both longitudinal and lateral sediment flux into river channels influences the sensitivity of river reaches to external perturbations such as climate and internal dynamics spurred on by stochastic events. These ideas are important because internal dynamics and system sensitivity to external signals have been demonstrated to exert major influences on depositional geomorphology that limit their ability to record tectonic and climatic history (Castelltort and Van Den Driessche, 2003; Armitage et al., 2013; Romans et al., 2016). The same questions are now asked in the field of erosional geomorphology of mountain belts, with constraining spatial and temporal timescales of internal dynamics as a main challenge (Scheingross et al., 2020). Understanding that the timescales of internal dynamics and sensitivity to external perturbations is dependent on the underlying conditions of lithology and structure will help guide such inquiry.

Lithological and structural controls on geomorphic system response to Quaternary climate

A key motivator for this thesis was to investigate the timescales at which lithology and structure affect the response of the geomorphic system to external forcing such as Quaternary climate (Ch. 1). Whilst terrace stratigraphy with any sort of chronological control is routinely interpreted in terms of climatic changes, I have demonstrated that river terrace abandonment can be asynchronous on the order of 10^4 – 10^5 years, whilst terrace sediment aggradation can be asynchronous on the order of 10^4 years

(Ch. 4). In addition, the synchronous aggradation on the order of 10^5 years could only be resolved using extensive dating of terrace sediment over 200 kyr in at least two river reaches. This synchronous event was likely also a result of local climatic and geomorphic conditions, where sediment transport through ephemeral tributaries is boosted by higher storm frequencies during interglacial periods in the High Atlas (Ch. 5.3). This means the analysis of river terraces to deduce climatic changes is vulnerable to significant error if the timescales of internal dynamics are longer than Milankovitch cycles of climatic change.

5.5 SUGGESTIONS FOR FUTURE WORK

The success of this thesis in exploring the controls of lithology and structure on geomorphic landforms and processes in a mountain belt has depended on the integration of geomorphic, geologic, sedimentologic and chronologic datasets from field, digital and lab-based techniques. The pillars of the unique contributions of this thesis have been datasets on material properties such as *in situ* Schmidt Hammer measurements of rock strength and strong geochronologic control on terrace occupation and incision. I have at least two suggestions for further work on improving the insight gained from such datasets:

1. *Geologic controls on material properties and geomorphic process*

   A major challenge in characterising the effect of material properties on geomorphic processes on large scales is the ability to quantitatively characterise the structural properties of rock and their influence on rock mass strength, fluvial erodibility, and hillslope process. Many excellent contributions to the links between material properties and geology have been made in the field of structural geology and rock engineering. For example, Cosgrove and Hudson (2016) summarise and integrate the understanding from structural geology, tectonics, rock mechanics and engineering geology. In particular, lithology has a direct control on how tectonic stresses are expressed in structural deformation of rock. Furthermore, the interference of stratigraphy, geological structures and tectonic stresses influence the width spacing and pervasiveness of joints and fractures. Integrating understanding on how the geologic history of rock affects its material properties with theory on how these properties affect geomorphic processes will be key in making further progress in modelling the Earth surface.

2. *Timescales of large-scale emergent geomorphic behaviour*

   Apart from comparing geomorphic records to local rather than global record of climate, comparing records of various aspects of the geomorphic system, such as hillslopes, alluvial fans and river channels should become common practice in studies of climatic geomorphology. Whilst the integration of geomorphology and chronology of terrace formation in the High Atlas has provided insights into many links between geomorphic processes and landforms through a catchment and their timescales, further insight may be gained by constraining timescales of processes in tributaries, on tributary fans, alluvial fans, and other hillslope landforms. To transcend the gradualist steady state equilibrium approach of the stream power model of landscape evolution, I encourage field and experimental studies on the timescales of emergent behaviour stemming from the linkage between fluvial and non-fluvial processes occurring in high-relief catchments. Such emergent behaviours could include internal dynamics affecting the timescales at which the erosional landscape responds and transmits information on external perturbations such as climate and tectonics, or produces autogenic signals. Advances in the application of chronological tools to geological problems such as those developed in Ch. 4 of this thesis will help progress in this field of inquiry.

Next to these suggestions which may benefit progress in understanding through empirical approaches, the synthesis of this thesis also produced a number of ideas about landscape evolution that may be tested using numerical modelling as a powerful tool of induction.

- *Modelling erodibility and erosion in a collisional mountain belt*
  Drainage divide reorganisation can occur in response to erosion through rock of contrasting erodibility and passive tectonic structural organisation (Ch. 2, Ch. 5.2). The empirical approach followed in this thesis has provided a conceptual model of how these material properties change through the history of incision in a collisional mountain belt, as well as quantitative constraints on the magnitude of contrasts in rock erodibility. A stream power landscape evolution model with the organisation of erodibility drawn in the conceptual diagram of Fig. 5.2 might experiment with the outcomes when changing parameters such as erodibility contrasts, stratigraphy, and tectonic structure. Landscape evolution models that already enable such experiments include LithoCHILD (Forte et al., 2016) and Landlab (Barnhart et al., 2018). Such experiments may be able to show the dynamics of drainage reorganisation such as captures and their influence on smaller scale landforms such as river long profiles.
- *Modelling river long profile evolution with asynchronous local incision*
  Landscape evolution models such as CHILD and Landlab can also be deployed to evaluate the potential effects of a combination of

knickpoint retreat and asynchronous independent initiations of incision along the river long profile (e.g., Fig. 5.7). Whilst the physics of initiation of local incision may be explored in more detail following from the physical experiment by Baynes et al. (2018), integrating randomised initiations of incision along a river channel in a simplified model can already be used to evaluate its potential effects on river long profile evolution. The temporal and spatial scaling of such initiations and knickpoint propagation derived in the work of this thesis can be used to choose the right parameters for such models.

- *Modelling longitudinal and lateral sediment flux*

  The concept of longitudinal and lateral sediment connectivity, and of stochastic sediment flux from hillslopes with different temporal distributions may be integrated in sediment-flux-dependent river incision models. For example, alluvial fans and tributary fan inputs can be modelled using stochastic functions with different temporal distributions. Changing these parameters can then answer new questions such as: How does changing the ratios of longitudinal vs lateral sediment flux affect the timescale of catchment response to changes in boundary conditions? How does changing the temporal distribution of stochastic sediment flux affect this response? Again, the scales derived in this thesis can help constrain relevant parameters for such models and produce behaviours and landforms that can be tested in the field.
- *A strategy for understanding lithological and structural effects on landscape evolution*

  The relative complexity of lithological and structural effects on concepts such as longitudinal and lateral sediment flux could be more effectively modelled using simplified numerical models of their effects such as suggested above, rather than detailed physical models. This is because there is still limited understanding and modelling of hillslope processes on geological timescales which can feed into simplified landscape models. Furthermore, material properties of rock do not only influence the parameters in numerical models such as erodibility in the stream power model but can also affect which physical processes occur – e.g., plucking vs abrasion, diffusive soil flow or stochastic gravity flows, weathering generated sediment or rock toppling from hillslopes, overland flow, or infiltration into groundwater. Real-world stratigraphy and structural geology can also be complex and need significant simplification for modelling purposes. Addressing this challenge requires a strategic approach to the nexus of field studies, physics-based models of small-scale processes, and simplified numerical models integrating the observed effects into large-scale landscape evolution models with a focus on understanding and modelling hillslope process and catchment connectivity.

6

Conclusions

The post-orogenic dryland nature of the intracontinental High Atlas mountain belt has provided an ideal setting for investigating the lithological and climatic controls on fluvial landscape evolution, isolated from eustatic base-level changes, ice sheet influence or dominance of crustal thickening and local fault-controlled rock advection. At the scale of a mountain belt and 10^6-10^7 yr fluvial landscape evolution, mobility of the drainage divide varies with the age of bedrock and its associated tectonic architecture in the mountain belt, which increases from east to west in the study area. The main conclusions linked to the lithological and structural controls on fluvial landscape evolution at this scale are:

- A combination of *in situ* rock mass strength measurements and normalised river channel steepness (k_{sn}) derived from a digital elevation model constrain the contrasts in fluvial erodibility exhibited in the High Atlas to between a factor of 4 calculated through k_{sn} and two orders of magnitude calculated through uniaxial compressive strength (UCS).
- A regression of UCS and k_{sn} data yields a strong linear fit consistent with $n = 2$ in the stream power model, and I suggest that $n \sim 2$. Any difference between UCS and k_{sn}-derived normalised K values is likely due to effects such as weathering and structural discontinuities, and

responses of the landscape unaccounted for in the simple stream power model, such as changes in channel width, valley width and the efficiency of riverbed load in eroding underlying bedrock.

- In a collisional mountain belt, the drainage divide will be mobile in response to changes in erosion rates of rivers incising into gently dipping and deformed strata of contrasting erodibility in the sedimentary cover. Based on the values of erodibility contrast and numerical models I estimate the timescale of adjustment in response to changes in erodibility of exposed bedrock to be on the order of 10^6-10^7 years.
- When deformed meta-sediments become exhumed, the increase in dip and deformation of strata leads to more stable erosion as rivers incise, resulting in stable drainage divides as witnessed in the middle of the study area.
- Results show a transient stage of drainage divide migration in response to exhumation of crystalline basement, where today's drainage divide at the edge of the crystalline basement is expected to be stable in the centre of the strong crystalline basement, or might even continue reorganising within the basement to follow the exhumation of resistant plutons. Divide mobility can be driven by exhumation of basement that is only a factor of two less erodible than the overlying meta-sedimentary rock if calculated through k_{sn} (Fig. 4d), and a factor of three less erodible if calculated through UCS (Fig. 4c).

The mobility of the drainage divide in response to erosion through rock-types and their structural configuration in a mountain belt has implications for the perception of autogenic dynamism of drainage networks and fluvial erosion in mountain belts, and the interpretation of the geomorphology and downstream stratigraphy. The ensuing stochastic signals of sediment supply that drainage reorganisation events would generate are not resolvable in the ~ 200 kyr terrace record in this thesis, but the potential effect of drainage reorganisation, occurring stochastically on timescales of 10^6 – 10^7 years need to be considered when interpreting longer timescale terrace sequences. The findings on lithological and structural controls on rock erodibility provide a framework for landscape evolution at the catchment scale, where the Mgoun River catchment exhibits some of the highest contrasts in erodibility and variation in passive tectonic configuration.

Catchment system response to orbital climatic changes (10^4-10^5 yr) are strongly controlled by the high contrasts in rock erodibility and inherited tectonic structural configuration along the reaches of the Mgoun River draining the wedge-top basin and thrust front of the High Atlas. The main conclusions linked to the climatic, lithological, and structural controls on fluvial landscape evolution at the catchment scale are:

- Strath terraces in the High Atlas record punctuated bedrock incision spaced out by up to 80 kyr periods of terrace aggradation over the last 170 kyr. Accounting for such long periods without incision enable reinterpretation of previously published records which appear consistent with regional low-rate post-orogenic rock uplift rates.
- The record of terrace aggradation and incision in the Mgoun River catchment extends to 180 ka, but only includes one synchronous aggradation event during the last interglacial maximum MIS 5e (~124-110 ka). Such an influx of gravel into the perennial river channel is likely an effect of glacial build-up of sediment in valley hillslopes, ephemeral tributaries and alluvial fans, and subsequent

connectivity of these sources with the river channel during interglacial maximum, Green Sahara enhanced northward monsoon penetration.

- Strath terrace formation in the High Atlas records a non-linear threshold response of the geomorphic system to climatic changes. Whilst the NW African climate system shows a strong precessional signal (26 kyr), strath terraces aggrade and incise asynchronously along a 30 km trunk river length on this timescale and these events are not correlated with precessional cycles. The timescale at which intrinsic thresholds and complex response control fluvial landscape evolution are affected by contingent geomorphological and geological conditions of the catchment.
- Whilst strath terraces are formed only in weak bedrock (10-14 MPa) three gorges of strong limestone (39 – 90 MPa) separate 30 km of the river length into four reaches and slow the propagation of waves of incision propagating upstream. Such knickpoints propagate from one reach to the next over a timescale of ~ 10^5 years, leaving the upper reaches isolated from downstream incision. However, independent incision in upstream reaches result in terrace incision asynchronous on the order of 10^4 years.
- Clast lithological distribution and grain size trends in terraces dating back 200 kyr as well as the modern river plain reflect a low ratio of longitudinal to lateral sediment input. Lateral sediment input is dominated by the recycling of bedrock conglomerates whilst longitudinal sediment transport capacity is suppressed by waterflow infiltrating into porous sediment bedrock and fractures in limestone.
- Valley width along the four reaches is strongly controlled by lithological controls on erodibility and the passive tectonic structure

of the wedge-top and thrust front characterised by stacks of weak bedrock and strong limestone. Valley width ranging from 150 m to 3.5 km has a strong control on the spatial and temporal scale of hillslope to river channel buffering through tributaries and alluvial fans: up to 10^4 years. Terraces in the unconfined valley (3.5 km wide) record abundant gravity flow deposits, whilst terraces in confined valleys preserve only completely fluvially reworked deposits. The result is different timescales of river channel to hillslope coupling and a different timescale and influence of stochastic sediment gravity flows on river channel incision and aggradation from reach to reach.

The cumulative effects of lithological and structural controls on erosional and depositional connectivity of the river channel with the rest of the catchment results in internal and autogenic dynamics dominating the catchment fluvial archives on the order of 10^4 – 10^5 years with a 10^5 year response to regional climate.

Overall, the findings presented in this thesis demonstrate that lithological and structural properties of mountain belts affect the controls of internal dynamics and climatic changes on geomorphic response, at spatial scales which translate into landscape evolution over 10^4 – 10^7 yr timescales.

R

References

Agwu, C.O.C., Beug, H.J., 1982. Palynological studies of marine sediments off the West African coast. Meteor Forschungsergeb C 36, 1-30.

Aitken, M.J., 1985. Thermoluminescence dating. Academic press, London.

Allen, G.H., Barnes, J.B., Pavelsky, T.M., Kirby, E., 2013. Lithologic and tectonic controls on bedrock channel form at the northwest Himalayan front. Journal of Geophysical Research: Earth Surface 118, 1806-1825. doi:10.1002/jgrf.20113

Anders, M.D., Pederson, J.L., Rittenour, T.M., Sharp, W.D., Gosse, J.C., Karlstrom, K.E., Crossey, L.J., Goble, R.J., Stockli, L., Yang, G., 2005. Pleistocene geomorphology and geochronology of eastern Grand Canyon: linkages of landscape components during climate changes. Quaternary Science Reviews 24, 2428-2448. doi:10.1016/j.quascirev.2005.03.015

Anthony, D.M., Granger, D.E., 2007. An empirical stream power formulation for knickpoint retreat in Appalachian Plateau fluviokarst. Journal of Hydrology 343, 117-126. doi:10.1016/j.jhydrol.2007.06.013

Antinao, J.L., McDonald, E., 2013. A reduced relevance of vegetation change for alluvial aggradation in arid zones. Geology 41, 11-14. doi:10.1130/g33623.1

Anton, L., Mather, A.E., Stokes, M., Muñoz-Martin, A., De Vicente, G., 2015. Exceptional river gorge formation from unexceptional floods. Nature Communications 6, 7963. doi:10.1038/ncomms8963

Aoki, H., Matsukura, Y., 2007. A new technique for non-destructive field measurement of rock-surface strength: an application of the Equotip hardness tester to weathering studies. Earth Surface Processes and Landforms 32, 1759-1769. doi:10.1002/esp.1492

Arboleya, M.L., Babault, J., Owen, L.A., Teixell, A., Finkel, R.C., 2008. Timing and nature of Quaternary fluvial incision in the Ouarzazate foreland basin, Morocco. Journal of the Geological Society 165, 1059-1073. doi:10.1144/0016-76492007-151

Armitage, J.J., Dunkley Jones, T., Duller, R.A., Whittaker, A.C., Allen, P.A., 2013. Temporal buffering of climate-driven sediment flux cycles by transient catchment response. Earth and Planetary Science Letters 369-370, 200-210. doi:10.1016/j.epsl.2013.03.020

Attal, M., Mudd, S.M., Hurst, M.D., Weinman, B., Yoo, K., Naylor, M., 2015. Impact of change in erosion rate and landscape steepness on hillslope and fluvial sediments grain size in the Feather River basin (Sierra Nevada, California). Earth Surf. Dynam. 3, 201-222. doi:10.5194/esurf-3-201-2015

Attal, M., Tucker, G.E., Whittaker, A.C., Cowie, P.A., Roberts, G.P., 2008. Modeling fluvial incision and transient landscape evolution: Influence of dynamic channel adjustment. Journal of Geophysical Research 113. doi:10.1029/2007jf000893

Attal, M.l., Lavé, J.r.m., 2006. Changes of bedload characteristics along the Marsyandi River (central Nepal): Implications for understanding hillslope sediment supply, sediment load evolution along fluvial networks, and denudation in active orogenic belts, in: Willett, S.D., Hovius, N., Brandon, M.T., Fisher, D.M. (Eds.), Tectonics, Climate, and Landscape Evolution. Geological Society of America, p. 0.

Babault, J., Teixell, A., Arboleya, M.L., Charroud, M., 2008. A Late Cenozoic age for long-wavelength surface uplift of the Atlas Mountains of Morocco. Terra Nova 20, 102-107. doi:10.1111/j.1365-3121.2008.00794.x

Babault, J., Teixell, A., Struth, L., Van Den Driessche, J., Arboleya, M.L., Tesón, E., 2013. Shortening, structural relief and drainage evolution in inverted rifts: insights from the Atlas Mountains, the Eastern Cordillera of Colombia and the Pyrenees. Geological Society, London, Special Publications 377, 141-158. doi:10.1144/sp377.14

Babault, J., Van Den Driessche, J., Teixell, A., 2012. Longitudinal to transverse drainage network evolution in the High Atlas (Morocco): The role of tectonics. Tectonics 31, n/a-n/a. doi:10.1029/2011tc003015

Bailey, R.M., Arnold, L.J., 2006. Statistical modelling of single grain quartz De distributions and an assessment of procedures for estimating burial dose. Quaternary Science Reviews 25, 2475-2502. doi:10.1016/j.quascirev.2005.09.012

Baldwin, J.A., Whipple, K.X., Tucker, G.E., 2003. Implications of the shear stress river incision model for the timescale of postorogenic decay of topography. Journal of Geophysical Research: Solid Earth 108. doi:10.1029/2001jb000550

Barnhart, K.R., Hutton, E., Gasparini, N.M., Tucker, G.E., 2018. Lithology: A Landlab submodule for spatially variable rock properties. Journal of Open Source Software 3, 979.

Baynes, E.R.C., Attal, M., Niedermann, S., Kirstein, L.A., Dugmore, A.J., Naylor, M., 2015. Erosion during extreme flood events dominates Holocene canyon evolution in northeast Iceland. Proceedings of the National Academy of Sciences 112, 2355-2360. doi:10.1073/pnas.1415443112

Baynes, E.R.C., Lague, D., Kermarrec, J.-J., 2018. Supercritical river terraces generated by hydraulic and geomorphic interactions. Geology 46, 499-502. doi:10.1130/g40071.1

Beckers, A., Bovy, B., Hallot, E., Demoulin, A., 2015. Controls on knickpoint migration in a drainage network of the moderately uplifted Ardennes Plateau, Western Europe. Earth Surface Processes and Landforms 40, 357-374. doi:doi.org/10.1002/esp.3638

Beeson, H.W., McCoy, S.W., Keen-Zebert, A., 2017. Geometric disequilibrium of river basins produces long-lived transient landscapes. Earth and Planetary Science Letters 475, 34-43. doi:10.1016/j.epsl.2017.07.010

Berger, A., Li, X.S., Loutre, M.F., 1999. Modelling northern hemisphere ice volume over the last 3Ma. Quaternary Science Reviews 18, 1-11. doi:10.1016/S0277-3791(98)00033-X

Berger, A., Loutre, M.F., 1991. Insolation values for the climate of the last 10 million years. Quaternary Science Reviews 10, 297-317. doi:10.1016/0277-3791(91)90033-Q

Bernard, T., Sinclair, H.D., Gailleton, B., Mudd, S.M., Ford, M., 2019. Lithological control on the post-orogenic topography and erosion history of the Pyrenees. Earth and Planetary Science Letters 518, 53-66. doi:10.1016/j.epsl.2019.04.034

Bonnet, S., 2009. Shrinking and splitting of drainage basins in orogenic landscapes from the migration of the main drainage divide. Nature Geoscience 2, 766. doi:10.1038/ngeo666

Bøtter-Jensen, L., Thomsen, K.J., Jain, M., 2010. Review of optically stimulated luminescence (OSL) instrumental developments for retrospective dosimetry. Radiation Measurements 45, 253-257. doi:10.1016/j.radmeas.2009.11.030

Boulton, S.J., Stokes, M., 2018. Which DEM is best for analyzing fluvial landscape development in mountainous terrains? Geomorphology 310, 168-187. doi:10.1016/j.geomorph.2018.03.002

Boulton, S.J., Stokes, M., Mather, A.E., 2014. Transient fluvial incision as an indicator of active faulting and Plio-Quaternary uplift of the Moroccan High Atlas. Tectonophysics 633, 16-33. doi:10.1016/j.tecto.2014.06.032

Boulton, S.J., VanDeVelde, J.H., Grimes, S.T., 2019. Palaeoenvironmental and tectonic significance of Miocene lacustrine and palustrine carbonates (Aït Kandoula Formation) in the Ouarzazate Foreland Basin, Morocco. Sedimentary Geology 383, 195-215. doi:10.1016/j.sedgeo.2019.01.009

Bridgland, D.R., 2000. River terrace systems in north-west Europe: an archive of environmental change, uplift and early human occupation. Quaternary Science Reviews 19, 1293-1303. doi:10.1016/S0277-3791(99)00095-5

Bridgland, D.R., Westaway, R., 2008. Climatically controlled river terrace staircases: A worldwide Quaternary phenomenon. Geomorphology 98, 285-315. doi:10.1016/j.geomorph.2006.12.032

Bridgland, D.R., Westaway, R., 2014. Quaternary fluvial archives and landscape evolution: a global synthesis. Proceedings of the Geologists' Association 125, 600-629. doi:10.1016/j.pgeola.2014.10.009

Brocard, G.Y., van der Beek, P.A., 2006. Influence of incision rate, rock strength, and bedload supply on bedrock river gradients and valley-flat widths: Field-based evidence and calibrations from western Alpine rivers (southeast France). 398, 101-126. doi:10.1130/2006.2398(07)

Brocard, G.Y., van der Beek, P.A., Bourlès, D.L., Siame, L.L., Mugnier, J.L., 2003. Long-term fluvial incision rates and postglacial river relaxation time in the French Western Alps from 10Be dating of alluvial terraces with assessment of inheritance, soil development and wind ablation effects. Earth and Planetary Science Letters 209, 197-214. doi:10.1016/s0012-821x(03)00031-1

Bronk Ramsey, C., 2009. Bayesian Analysis of Radiocarbon Dates. Radiocarbon 51, 337-360. doi:10.1017/S0033822200033865

Brozovic, N., Burbank, D.W., 2000. Dynamic fluvial systems and gravel progradation in the Himalayan foreland. GSA Bulletin 112, 394-412. doi:10.1130/0016-7606(2000)112<394:Dfsagp>2.0.Co;2

Bryant, I.D., 1983. Facies sequences associated with some braided river deposits of Late Pleistocene age from southern Britain, Modern and ancient fluvial systems. Special Publications of the International Association of Sedimentologists, pp. 267-275.

Bull, W.B., 1979. Threshold of critical power in streams. GSA Bulletin 90, 453-464. doi:10.1130/0016-7606(1979)90<453:Tocpis>2.0.Co;2

Bull, W.B., 1990. Stream-terrace genesis: implications for soil development. Geomorphology 3, 351-367. doi:10.1016/0169-555X(90)90011-E

Bull, W.B., 1991. Geomorphic responses to climatic change. New York, NY (United States); Oxford University Press.

Burbank, D.W., Anderson, R.S., 2011. Tectonic geomorphology. John Wiley & Sons.

Bursztyn, N., Pederson, J.L., Tressler, C., Mackley, R.D., Mitchell, K.J., 2015. Rock strength along a fluvial transect of the Colorado Plateau – quantifying a fundamental control on geomorphology. Earth and Planetary Science Letters 429, 90-100. doi:10.1016/j.epsl.2015.07.042

Buylaert, J.-P., Jain, M., Murray, A.S., Thomsen, K.J., Thiel, C., Sohbati, R., 2012. A robust feldspar luminescence dating method for Middle and Late Pleistocene sediments. Boreas 41, 435-451. doi:10.1111/j.1502-3885.2012.00248.x

Buylaert, J.-P., Thiel, C., Murray, A., Vandenberghe, D., Yi, S., Lu, H., 2011. IRSL and post-IR IRSL residual doses recorded in modern dust samples from the Chinese Loess Plateau. Geochronometria 38, 432-440. doi:10.2478/s13386-011-0047-0

Buylaert, J.P., Murray, A.S., Thomsen, K.J., Jain, M., 2009. Testing the potential of an elevated temperature IRSL signal from K-feldspar. Radiation Measurements 44, 560-565. doi:10.1016/j.radmeas.2009.02.007

Cappy, S., 2006. Hydrogeological characterization of the Upper Draa catchment: Morocco. Unpublished PhD thesis, Geological Institute, Faculty of Mathematics and Natural Sciences, University of Bonn.

Carte Géologique du Maroc, 1975. Jbel Saghro-Dadès.

Castelltort, S., Van Den Driessche, J., 2003. How plausible are high-frequency sediment supply-driven cycles in the stratigraphic record? Sedimentary Geology 157, 3-13. doi:10.1016/s0037-0738(03)00066-6

Chapot, M.S., Sohbati, R., Murray, A.S., Pederson, J.L., Rittenour, T.M., 2012. Constraining the age of rock art by dating a rockfall event using sediment and rock-surface luminescence dating techniques. Quaternary Geochronology 13, 18-25. doi:10.1016/j.quageo.2012.08.005

Chittenden, H., Delunel, R., Schlunegger, F., Akçar, N., Kubik, P., 2014. The influence of bedrock orientation on the landscape evolution, surface morphology and denudation (10Be) at the Niesen, Switzerland. Earth Surface Processes and Landforms 39, 1153-1166. doi:10.1002/esp.3511

Clubb, F.J., Mudd, S.M., Milodowski, D.T., Hurst, M.D., Slater, L.J., 2014. Objective extraction of channel heads from high-resolution topographic data. Water Resources Research 50, 4283-4304. doi:10.1002/2013WR015167

Cohen, T.J., Nanson, G.C., Jansen, J.D., Jones, B.G., Jacobs, Z., Larsen, J.R., May, J.H., Treble, P., Price, D.M., Smith, A.M., 2012. Late Quaternary mega-lakes fed by the northern and southern river systems of central Australia: Varying moisture sources and increased continental aridity. Palaeogeography, Palaeoclimatology, Palaeoecology 356-357, 89-108. doi:10.1016/j.palaeo.2011.06.023

Cohen, T.J., Nanson, G.C., Jansen, J.D., Jones, B.G., Jacobs, Z., Treble, P., Price, D.M., May, J.-H., Smith, A.M., Ayliffe, L.K., Hellstrom, J.C., 2011. Continental aridification and the vanishing of Australia's megalakes. Geology 39, 167-170. doi:10.1130/g31518.1

Cook, K.L., Whipple, K.X., Heimsath, A.M., Hanks, T.C., 2009. Rapid incision of the Colorado River in Glen Canyon – insights from channel profiles, local incision rates, and modeling of lithologic controls. Earth Surface Processes and Landforms 34, 994-1010. doi:10.1002/esp.1790

Cordier, S., Harmand, D., Frechen, M., Beiner, M., 2006. Fluvial system response to Middle and Upper Pleistocene climate change in the Meurthe and Moselle valleys (Eastern Paris Basin and Rhenish Massif). Quaternary Science Reviews 25, 1460-1474. doi:10.1016/j.quascirev.2005.11.007

Cosgrove, J.W., Hudson, J.A., 2016. Structural geology and rock engineering. Imperial College Press, London.

Crosby, B.T., Whipple, K.X., 2006. Knickpoint initiation and distribution within fluvial networks: 236 waterfalls in the Waipaoa River, North Island, New Zealand. Geomorphology 82, 16-38. doi:10.1016/j.geomorph.2005.08.023

Cunningham, A.C., Murray, A.S., Armitage, S.J., Autzen, M., 2018. High-precision natural dose rate estimates through beta counting. Radiation Measurements 120, 209-214. doi:10.1016/j.radmeas.2018.04.008

Cunningham, A.C., Wallinga, J., 2010. Selection of integration time intervals for quartz OSL decay curves. Quaternary Geochronology 5, 657-666. doi:10.1016/j.quageo.2010.08.004

de Jong, C., Cappy, S., Finckh, M., Funk, D., 2008. A transdisciplinary analysis of water problems in the mountainous karst areas of Morocco. Engineering Geology 99, 228-238. doi:10.1016/j.enggeo.2007.11.021

DeCelles, P.G., Gray, M.B., Ridgway, K.D., Cole, R.B., Pivnik, D.A., Pequera, N., Srivastava, P., 1991. Controls on synorogenic alluvial-fan architecture, Beartooth Conglomerate (Palaeocene), Wyoming and Montana. Sedimentology 38, 567-590. doi:10.1111/j.1365-3091.1991.tb01009.x

deMenocal, P.B., Tierney, J.E., 2012. Green Sahara: African Humid Periods Paced by Earth's Orbital Changes. Nature Education Knowledge 3, 12.

Demoulin, A., Mather, A., Whittaker, A., 2017. Fluvial archives, a valuable record of vertical crustal deformation. Quaternary Science Reviews 166, 10-37. doi:10.1016/j.quascirev.2016.11.011

Dendy, F.E., Bolton, G.C., 1976. Sediment yield-runoff drainage area relationships in the United States. J. Soil Wat. Conserv. 32, 264-266.

DiBiase, R.A., Denn, A.R., Bierman, P.R., Kirby, E., West, N., Hidy, A.J., 2018. Stratigraphic control of landscape response to base-level fall, Young Womans Creek, Pennsylvania, USA. Earth and Planetary Science Letters 504, 163-173. doi:10.1016/j.epsl.2018.10.005

DiBiase, R.A., Whipple, K.X., Lamb, M.P., Heimsath, A.M., 2015. The role of waterfalls and knickzones in controlling the style and pace of landscape adjustment in the western San Gabriel Mountains, California. GSA Bulletin 127, 539-559. doi:10.1130/b31113.1

Dingle, E.H., Sinclair, H.D., Attal, M., Milodowski, D.T., Singh, V., 2016. Subsidence control on river morphology and grain size in the Ganga Plain. American Journal of Science 316, 778-812. doi:10.2475/08.2016.03

Dixit, Y., Toucanne, S., Fontanier, C., Pasquier, V., Lora, J.M., Jouet, G., Tripati, A., 2020. Enhanced western mediterranean rainfall during past interglacials driven by North Atlantic pressure changes. Quaternary International 553, 1-13. doi:10.1016/j.quaint.2020.08.017

Dłużewski, M., Krzemień, K., Rojan, E., Biejat, K., 2013. Stream channel development in the southern parts of the High Atlas Mountains, Morocco. Geografija 49.

Douglas, I., 1967. Man, Vegetation and the Sediment Yields of Rivers. Nature 215, 925-928. doi:10.1038/215925a0

Dubille, M., Lavé, J., 2015. Rapid grain size coarsening at sandstone/conglomerate transition: similar expression in Himalayan modern rivers and Pliocene molasse deposits. Basin Research 27, 26-42. doi:10.1111/bre.12071

Duller, R.A., Whittaker, A.C., Fedele, J.J., Whitchurch, A.L., Springett, J., Smithells, R., Fordyce, S., Allen, P.A., 2010. From grain size to tectonics. Journal of Geophysical Research 115. doi:10.1029/2009jf001495

Dupont, L., 2011. Orbital scale vegetation change in Africa. Quaternary Science Reviews 30, 3589-3602. doi:10.1016/j.quascirev.2011.09.019

Dupont, L.M., 1993. Vegetation zones in NW Africa during the brunhes chron reconstructed from marine palynological data. Quaternary Science Reviews 12, 189-202. doi:10.1016/0277-3791(93)90053-O

Dupont, L.M., Agwu, C.O.C., 1992. Latitudinal shifts of forest and savanna in N. W. Africa during the Brunhes chron: further marine palynological results from site M 16415 (9°;N 19°W). Vegetation History and Archaeobotany 1, 163-175. doi:10.1007/BF00191556

Dupont, L.M., Hooghiemstra, H., 1989. The Saharan–Sahelian boundary during the Brunhes chron. Acta Botanica Neerlandica 38, 405-415. doi:10.1111/j.1438-8677.1989.tb01372.x

Enzel, Y., Amit, R., Grodek, T., Ayalon, A., Lekach, J., Porat, N., Bierman, P., Blum, J.D., Erel, Y., 2012. Late Quaternary weathering, erosion, and deposition in Nahal Yael, Israel: An “impact of climatic change on an arid watershed”1? GSA Bulletin 124, 705-722. doi:10.1130/b30538.1

Errarhaoui, K., 1998. Structure du haut-atlas : plis et chevauchements du socle et de couverture (interpretations des donnees geophysiques et geologiques), p. 326 P.

Fedele, J.J., Paola, C., 2007. Similarity solutions for fluvial sediment fining by selective deposition. Journal of Geophysical Research: Earth Surface 112. doi:10.1029/2005jf000409

Ferguson, R., Hoey, T., Wathen, S., Werritty, A., 1996. Field evidence for rapid downstream fining of river gravels through selective transport. Geology 24, 179-182. doi:10.1130/0091-7613(1996)024<0179:Fefrdf>2.3.Co;2

Fick, S.E., Hijmans, R.J., 2017. WorldClim 2: new 1-km spatial resolution climate surfaces for global land areas. International Journal of Climatology 37, 4302-4315. doi:10.1002/joc.5086

Fink, A.H., Knippertz, P., 2003. An extreme precipitation event in southern Morocco in spring 2002 and some hydrological implications. Weather 58, 377-387. doi:10.1256/wea.256.02

Finnegan, N.J., 2013. Interpretation and downstream correlation of bedrock river terrace treads created from propagating knickpoints. Journal of Geophysical Research: Earth Surface 118, 54-64. doi:10.1029/2012jf002534

Finnegan, N.J., Dietrich, W.E., 2011. Episodic bedrock strath terrace formation due to meander migration and cutoff. Geology 39, 143-146. doi:10.1130/g31716.1

Finnegan, N.J., Schumer, R., Finnegan, S., 2014. A signature of transience in bedrock river incision rates over timescales of 104–107 years. Nature 505, 391-394. doi:10.1038/nature12913

Finnegan, N.J., Sklar, L.S., Fuller, T.K., 2007. Interplay of sediment supply, river incision, and channel morphology revealed by the transient evolution of an experimental bedrock channel. Journal of Geophysical Research: Earth Surface 112. doi:10.1029/2006jf000569

Flowers, R.M., Ehlers, T.A., 2018. Rock erodibility and the interpretation of low-temperature thermochronologic data. Earth and Planetary Science Letters 482, 312-323. doi:10.1016/j.epsl.2017.11.018

Forte, A.M., Whipple, K.X., 2018. Criteria and tools for determining drainage divide stability. Earth and Planetary Science Letters 493, 102-117. doi:10.1016/j.epsl.2018.04.026

Forte, A.M., Whipple, K.X., 2019. Short communication: The Topographic Analysis Kit (TAK) for TopoToolbox. Earth Surf. Dynam. 7, 87-95. doi:10.5194/esurf-7-87-2019

Forte, A.M., Whipple, K.X., Cowgill, E., 2015. Drainage network reveals patterns and history of active deformation in the eastern Greater Caucasus. Geosphere 11, 1343-1364. doi:10.1130/ges01121.1

Forte, A.M., Yanites, B.J., Whipple, K.X., 2016. Complexities of landscape evolution during incision through layered stratigraphy with contrasts in rock strength. Earth Surface Processes and Landforms 41, 1736-1757. doi:10.1002/esp.3947

Foster, M.A., Anderson, R.S., Gray, H.J., Mahan, S.A., 2017. Dating of river terraces along Lefthand Creek, western High Plains, Colorado, reveals punctuated incision. Geomorphology 295, 176-190. doi:10.1016/j.geomorph.2017.04.044

Fournier, F., 1960. Climat et érosion: la relation entre l'érosion du sol par l'eau et les précipitations atmosphériques. Presses universitaires de France.

Franklin, J.A., Chandra, R., 1972. The slake-durability test. International Journal of Rock Mechanics and Mining Sciences & Geomechanics Abstracts 9, 325-328. doi:10.1016/0148-9062(72)90001-0

Freiesleben, T., Sohbati, R., Murray, A., Jain, M., al Khasawneh, S., Hvidt, S., Jakobsen, B., 2015. Mathematical model quantifies multiple daylight exposure and burial events for rock surfaces using luminescence dating. Radiation Measurements 81, 16-22. doi:10.1016/j.radmeas.2015.02.004

Fryirs, K., 2013. (Dis)Connectivity in catchment sediment cascades: a fresh look at the sediment delivery problem. Earth Surface Processes and Landforms 38, 30-46. doi:10.1002/esp.3242

Fryirs, K.A., Brierley, G.J., Preston, N.J., Kasai, M., 2007. Buffers, barriers and blankets: The (dis)connectivity of catchment-scale sediment cascades. CATENA 70, 49-67. doi:10.1016/j.catena.2006.07.007

Fuller, T.K., Perg, L.A., Willenbring, J.K., Lepper, K., 2009. Field evidence for climate-driven changes in sediment supply leading to strath terrace formation. Geology 37, 467-470. doi:10.1130/g25487a.1

Galbraith, R.F., Roberts, R.G., 2012. Statistical aspects of equivalent dose and error calculation and display in OSL dating: An overview and some recommendations. Quaternary Geochronology 11, 1-27. doi:10.1016/j.quageo.2012.04.020

Galbraith, R.F., Roberts, R.G., Laslett, G.M., Yoshida, H., Olley, J.M., 1999. Optical dating of single and multiple grains of quartz from Jinmium rock shelter, northern Australia: Part I, experimental design and statistical models. Archaeometry 41, 339-364. doi:10.1111/j.1475-4754.1999.tb00987.x

Gallen, S.F., 2018. Lithologic controls on landscape dynamics and aquatic species evolution in post-orogenic mountains. Earth and Planetary Science Letters 493, 150-160. doi:10.1016/j.epsl.2018.04.029

Gallen, S.F., Pazzaglia, F.J., Wegmann, K.W., Pederson, J.L., Gardner, T.W., 2015. The dynamic reference frame of rivers and apparent transience in incision rates. Geology 43, 623-626. doi:10.1130/g36692.1

Giachetta, E., Refice, A., Capolongo, D., Gasparini, N.M., Pazzaglia, F.J., 2014. Orogen-scale drainage network evolution and response to erodibility changes: insights from numerical experiments. Earth Surface Processes and Landforms 39, 1259-1268. doi:10.1002/esp.3579

Gibbard, P.L., Lewin, J., 2009. River incision and terrace formation in the Late Cenozoic of Europe. Tectonophysics 474, 41-55. doi:doi.org/10.1016/j.tecto.2008.11.017

Gokceoglu, C., Aksoy, H., 2000. New approaches to the characterization of clay-bearing, densely jointed and weak rock masses. Engineering Geology 58, 1-23. doi:10.1016/S0013-7952(00)00032-6

Goktan, R.M., Gunes, N., 2005. A comparative study of Schmidt hammer testing procedures with reference to rock cutting machine performance prediction. International Journal of Rock Mechanics and Mining Sciences 42, 466-472. doi:10.1016/j.ijrmms.2004.12.002

Gosse, J.C., Phillips, F.M., 2001. Terrestrial in situ cosmogenic nuclides: theory and application. Quaternary Science Reviews 20, 1475-1560. doi:10.1016/S0277-3791(00)00171-2

Goudie, A.S., 2006. The Schmidt Hammer in geomorphological research. Progress in Physical Geography: Earth and Environment 30, 703-718. doi:10.1177/0309133306071954

Goudie, A.S., 2016. Quantification of rock control in geomorphology. Earth-Science Reviews 159, 374-387. doi:10.1016/j.earscirev.2016.06.012

Gray, H.J., Jain, M., Sawakuchi, A.O., Mahan, S.A., Tucker, G.E., 2019. Luminescence as a Sediment Tracer and Provenance Tool. Reviews of Geophysics 57, 987-1017. doi:10.1029/2019rg000646

Guérin, G., Mercier, N., Adamiec, G., 2011. Dose-rate conversion factors: update. Ancient TL 29, 5-8.

Hajek, E.A., Straub, K.M., 2017. Autogenic Sedimentation in Clastic Stratigraphy. Annual Review of Earth and Planetary Sciences 45, 681-709. doi:10.1146/annurev-earth-063016-015935

Hancock, G.S., Anderson, R.S., 2002. Numerical modeling of fluvial strath-terrace formation in response to oscillating climate. GSA Bulletin 114, 1131-1142. doi:10.1130/0016-7606(2002)114<1131:Nmofst>2.0.Co;2

Hein, F.J., Walker, R.G., 1977. Bar evolution and development of stratification in the gravelly, braided, Kicking Horse River, British Columbia. Canadian Journal of Earth Sciences 14, 562-570. doi:10.1139/e77-058

Hijmans, R.J., Cameron, S.E., Parra, J.L., Jones, P.G., Jarvis, A., 2005. Very high resolution interpolated climate surfaces for global land areas. International journal of climatology 25, 1965-1978.

Hooghiemstra, H., Stalling, H., Agwu, C.O.C., Dupont, L.M., 1992. Vegetational and climatic changes at the northern fringe of the sahara 250,000–5000 years BP: evidence from 4 marine pollen records located between Portugal and the Canary Islands. Review of Palaeobotany and Palynology 74, 1-53. doi:10.1016/0034-6667(92)90137-6

Horowitz, A., 1989. Continuous pollen diagrams for the last 3.5 m.y. from Israel: Vegetation, climate and correlation with the oxygen isotope record. Palaeogeography, Palaeoclimatology, Palaeoecology 72, 63-78. doi:10.1016/0031-0182(89)90132-6

Howard, A.D., Dietrich, W.E., Seidl, M.A., 1994. Modeling fluvial erosion on regional to continental scales. Journal of Geophysical Research: Solid Earth 99, 13971-13986. doi:10.1029/94jb00744

Hughes, P.D., Gibbard, P.L., Woodward, J.C., 2004. Quaternary glaciation in the Atlas Mountains of North Africa, in: Ehlers, J., Gibbard, P.L. (Eds.), Developments in Quaternary Sciences. Elsevier, pp. 255-260.

Hurst, M.D., Mudd, S.M., Yoo, K., Attal, M., Walcott, R., 2013. Influence of lithology on hillslope morphology and response to tectonic forcing in the northern Sierra Nevada of California. Journal of Geophysical Research: Earth Surface 118, 832-851. doi:10.1002/jgrf.20049

Jansen, J.D., Fabel, D., Bishop, P., Xu, S., Schnabel, C., Codilean, A.T., 2011. Does decreasing paraglacial sediment supply slow knickpoint retreat? Geology 39, 543-546. doi:10.1130/g32018.1

Jerolmack, D.J., Paola, C., 2010. Shredding of environmental signals by sediment transport. Geophysical Research Letters 37. doi:10.1029/2010gl044638

Johnson, J.P.L., Whipple, K.X., 2010. Evaluating the controls of shear stress, sediment supply, alluvial cover, and channel morphology on experimental bedrock incision rate. Journal of Geophysical Research: Earth Surface 115. doi:10.1029/2009jf001335

Johnson, K.N., Finnegan, N.J., 2015. A lithologic control on active meandering in bedrock channels. GSA Bulletin 127, 1766-1776. doi:10.1130/b31184.1

Kahraman, S., Fener, M., Gunaydin, O., 2002. Predicting the Schmidt hammer values of in-situ intact rock from core sample values. International Journal of Rock Mechanics and Mining Sciences 39, 395-399.

Kahraman, S., Fener, M., Kozman, E., 2012. Predicting the compressive and tensile strength of rocks from indentation hardness index. Journal of the Southern African Institute of Mining and Metallurgy 112, 331-339.

Karakus, M., Kumral, M., Kilic, O., 2005. Predicting elastic properties of intact rocks from index tests using multiple regression modelling.

International Journal of Rock Mechanics and Mining Sciences 42, 323-330. doi:10.1016/j.ijrmms.2004.08.005

Katz, O., Reches, Z., Roegiers, J.-C., 2000. Evaluation of mechanical rock properties using a Schmidt Hammer. International Journal of rock mechanics and mining sciences 37, 723-728.

Keen-Zebert, A., Hudson, M.R., Shepherd, S.L., Thaler, E.A., 2017. The effect of lithology on valley width, terrace distribution, and bedload provenance in a tectonically stable catchment with flat-lying stratigraphy. Earth Surface Processes and Landforms 42, 1573-1587. doi:10.1002/esp.4116

Kenworthy, M.K., Rittenour, T.M., Pierce, J.L., Sutfin, N.A., Sharp, W.D., 2014. Luminescence dating without sand lenses: An application of OSL to coarse-grained alluvial fan deposits of the Lost River Range, Idaho, USA. Quaternary Geochronology 23, 9-25. doi:10.1016/j.quageo.2014.03.004

Kirby, E., Whipple, K., 2001. Quantifying differential rock-uplift rates via stream profile analysis. Geology 29, 415-418. doi:10.1130/0091-7613(2001)029<0415:QDRURV>2.0.CO;2

Kirby, E., Whipple, K.X., 2012. Expression of active tectonics in erosional landscapes. Journal of Structural Geology 44, 54-75. doi:10.1016/j.jsg.2012.07.009

Knippertz, P., 2003. Tropical–Extratropical Interactions Causing Precipitation in Northwest Africa: Statistical Analysis and Seasonal Variations. Monthly Weather Review 131, 3069-3076. doi:10.1175/1520-0493(2003)131<3069:Ticpin>2.0.Co;2

Knippertz, P., Christoph, M., Speth, P., 2003a. Long-term precipitation variability in Morocco and the link to the large-scale circulation in recent and future climates. Meteorology and Atmospheric Physics 83, 67-88. doi:10.1007/s00703-002-0561-y

Knippertz, P., Fink, A.H., Reiner, A., Speth, P., 2003b. Three Late Summer/Early Autumn Cases of Tropical–Extratropical Interactions Causing Precipitation in Northwest Africa. Monthly Weather Review 131, 116-135. doi:10.1175/1520-0493(2003)131<0116:Tlseac>2.0.Co;2

Knox, J.C., 1972. Valley Alluviation in Southwestern Wisconsin. Annals of the Association of American Geographers 62, 401-410. doi:10.1111/j.1467-8306.1972.tb00872.x

Komar, P.D., Li, Z., 1986. Pivoting analyses of the selective entrainment of sediments by shape and size with application to gravel threshold. Sedimentology 33, 425-436. doi:10.1111/j.1365-3091.1986.tb00546.x

Korup, O., 2006. Rock-slope failure and the river long profile. Geology 34, 45-48. doi:10.1130/g21959.1

Korup, O., Densmore, A.L., Schlunegger, F., 2010. The role of landslides in mountain range evolution. Geomorphology 120, 77-90. doi:10.1016/j.geomorph.2009.09.017

Kutzbach, J.E., 1981. Monsoon Climate of the Early Holocene: Climate Experiment with the Earth's Orbital Parameters for 9000 Years Ago. Science 214, 59-61. doi:10.1126/science.214.4516.59

Lague, D., 2014. The stream power river incision model: evidence, theory and beyond. Earth Surface Processes and Landforms 39, 38-61. doi:10.1002/esp.3462

Lamb, H., Duigan, C., Gee, J., Kelts, K., Lister, G., Maxted, R., Merzouk, A., Niessen, F., Tahiri, M., Whittington, R., 1994. Lacustrine sedimentation in a high-altitude, semi-arid environment The palaeolimnological record of Lake Isli, High Atlas, Morocco. Environmental Change in Drylands Biogeographical and geomorphological perspectives (AC Millington, K Pye, eds) Wiley, London, 148-161.

Lamb, H.F., Eicher, U., Switsur, V.R., 1989. An 18,000-Year Record of Vegetation, Lake-Level and Climatic Change from Tigalmamine, Middle Atlas, Morocco. Journal of Biogeography 16, 65-74. doi:10.2307/2845311

Lamb, M.P., Dietrich, W.E., Sklar, L.S., 2008. A model for fluvial bedrock incision by impacting suspended and bed load sediment. Journal of Geophysical Research 113. doi:10.1029/2007jf000915

Lamb, M.P., Finnegan, N.J., Scheingross, J.S., Sklar, L.S., 2015. New insights into the mechanics of fluvial bedrock erosion through flume experiments and theory. Geomorphology 244, 33-55. doi:10.1016/j.geomorph.2015.03.003

Langbein, W.B., Schumm, S.A., 1958. Yield of sediment in relation to mean annual precipitation. Eos, Transactions American Geophysical Union 39, 1076-1084. doi:10.1029/TR039i006p01076

Larrasoaña, J.C., Roberts, A.P., Rohling, E.J., 2013. Dynamics of Green Sahara Periods and Their Role in Hominin Evolution. PLOS ONE 8, e76514. doi:10.1371/journal.pone.0076514

Laskar, J., Robutel, P., Joutel, F., Gastineau, M., Correia, A.C.M., Levrard, B., 2004. A long-term numerical solution for the insolation quantities of the Earth. A&A 428, 261-285. doi:10.1051/0004-6361:20041335

Lavé, J., Avouac, J.P., 2000. Active folding of fluvial terraces across the Siwaliks Hills, Himalayas of central Nepal. Journal of Geophysical Research: Solid Earth 105, 5735-5770. doi:10.1029/1999jb900292

Lepper, K., Larsen, N.A., McKeever, S.W.S., 2000. Equivalent dose distribution analysis of Holocene eolian and fluvial quartz sands from Central Oklahoma. Radiation Measurements 32, 603-608. doi:10.1016/S1350-4487(00)00093-7

Lewin, J., Gibbard, P.L., 2010. Quaternary river terraces in England: Forms, sediments and processes. Geomorphology 120, 293-311. doi:10.1016/j.geomorph.2010.04.002

Limaye, A.B.S., Lamb, M.P., 2014. Numerical simulations of bedrock valley evolution by meandering rivers with variable bank material. Journal of Geophysical Research: Earth Surface 119, 927-950. doi:10.1002/2013JF002997

Limaye, A.B.S., Lamb, M.P., 2016. Numerical model predictions of autogenic fluvial terraces and comparison to climate change expectations. Journal of Geophysical Research: Earth Surface 121, 512-544. doi:10.1002/2014JF003392

Lin, C.-M., Zhuo, H.-C., Gao, S., 2005. Sedimentary facies and evolution in the Qiantang River incised valley, eastern China. Marine Geology 219, 235-259. doi:10.1016/j.margeo.2005.06.009

Lindsey, D.A., Langer, W.H., Van Gosen, B.S., 2007. Using pebble lithology and roundness to interpret gravel provenance in piedmont fluvial systems of the Rocky Mountains, USA. Sedimentary Geology 199, 223-232. doi:10.1016/j.sedgeo.2007.02.006

Lisiecki, L.E., Raymo, M.E., 2005. (Appendix 1) Global Plio-Pleistocene stack of benthic oxygen isotope records, In supplement to: Lisiecki, LE; Raymo, ME (2005): A Pliocene-Pleistocene stack of 57 globally distributed benthic d18O records. Paleoceanography, 20, PA1003, doi:10.1029/2004PA001071. PANGAEA.

Liu, J., Cui, F., Murray, A.S., Sohbati, R., Jain, M., Gao, H., Li, W., Li, C., Li, P., Zhou, T., Chen, J., 2019. Resetting of the luminescence signal in modern riverbed cobbles along the course of the Shiyang River, China. Quaternary Geochronology 49, 184-190. doi:10.1016/j.quageo.2018.04.004

Lomax, J., Hilgers, A., Twidale, C.R., Bourne, J.A., Radtke, U., 2007. Treatment of broad palaeodose distributions in OSL dating of dune sands from the western Murray Basin, South Australia. Quaternary Geochronology 2, 51-56. doi:10.1016/j.quageo.2006.05.015

Macklin, M.G., Fuller, I.C., Lewin, J., Maas, G.S., Passmore, D.G., Rose, J., Woodward, J.C., Black, S., Hamlin, R.H.B., Rowan, J.S., 2002. Correlation of fluvial sequences in the Mediterranean basin over the last 200ka and their relationship to climate change. Quaternary Science Reviews 21, 1633-1641. doi:10.1016/S0277-3791(01)00147-0

Maddy, D., 1997. Uplift-driven valley incision and river terrace formation in southern England. Journal of Quaternary Science 12, 539-545. doi:10.1002/(sici)1099-1417(199711/12)12:6<539::Aid-jqs350>3.0.Co;2-t

Magee, J.W., Miller, G.H., Spooner, N.A., Questiaux, D., 2004. Continuous 150 k.y. monsoon record from Lake Eyre, Australia: Insolation-forcing implications and unexpected Holocene failure. Geology 32, 885-888. doi:10.1130/g20672.1

Marsaglia, K.M., DeVaughn, A.M., James, D.E., Marden, M., 2010. Provenance of fluvial terrace sediments within the Waipaoa sedimentary system and their importance to New Zealand source-to-sink studies. Marine Geology 270, 84-93. doi:10.1016/j.margeo.2009.10.017

Maslin, M.A., Ridgwell, A.J., 2005. Mid-Pleistocene revolution and the 'eccentricity myth'. Geological Society, London, Special Publications 247, 19-34. doi:10.1144/gsl.Sp.2005.247.01.02

Massari, F., 1983. Tabular cross-bedding in Messinian fluvial channel conglomerates, Southern Alps, Italy, in: Collinson, J.D., Lewin, J. (Eds.), Modern and ancient fluvial systems. International Association of Sedimentologists, pp. 287-300.

Mather, A., Stokes, M., 2016. Extracting palaeoflood data from coarse-grained Pleistocene river terrace archives: an example from SE Spain. Earth Surface Processes and Landforms 41, 1991-2004. doi:10.1002/esp.4001

Mather, A.E., Hartley, A., 2005. Flow events on a hyper-arid alluvial fan: Quebrada Tambores, Salar de Atacama, northern Chile. Geological Society, London, Special Publications 251, 9-24. doi:10.1144/gsl.Sp.2005.251.01.02

Mather, A.E., Stokes, M., 2018. Bedrock structural control on catchment-scale connectivity and alluvial fan processes, High Atlas Mountains, Morocco. Geological Society, London, Special Publications 440, 103-128. doi:10.1144/sp440.15

Mather, A.E., Stokes, M., Whitfield, E., 2017. River terraces and alluvial fans: The case for an integrated Quaternary fluvial archive. Quaternary Science Reviews 166, 74-90. doi:10.1016/j.quascirev.2016.09.022

McGregor, H.V., Dupont, L., Stuut, J.-B.W., Kuhlmann, H., 2009. Vegetation change, goats, and religion: a 2000-year history of land use in southern Morocco. Quaternary Science Reviews 28, 1434-1448. doi:10.1016/j.quascirev.2009.02.012

Merritts, D.J., Vincent, K.R., Wohl, E.E., 1994. Long river profiles, tectonism, and eustasy: A guide to interpreting fluvial terraces. Journal of Geophysical Research: Solid Earth 99, 14031-14050. doi:10.1029/94JB00857

Meyer, M.C., Gliganic, L.A., Jain, M., Sohbati, R., Schmidmair, D., 2018. Lithological controls on light penetration into rock surfaces – Implications for OSL and IRSL surface exposure dating. Radiation Measurements 120, 298-304. doi:10.1016/j.radmeas.2018.03.004

Miall, A.D., 1977. A review of the braided-river depositional environment. Earth-Science Reviews 13, 1-62. doi:10.1016/0012-8252(77)90055-1

Miall, A.D., 1978. Lithofacies types and vertical profile models in braided river deposits: a summary, in: Miall, A.D. (Ed.), Fluvial Sedimentology. Canadian Society of Petroleum Geologists.

Miall, A.D., 1985. Architectural-element analysis: A new method of facies analysis applied to fluvial deposits. Earth-Science Reviews 22, 261-308. doi:10.1016/0012-8252(85)90001-7

Miall, A.D., 1996. Methods of Architectural-Element Analysis, The Geology of Fluvial Deposits: Sedimentary Facies, Basin Analysis, and Petroleum Geology. Springer Berlin Heidelberg, Berlin, Heidelberg, pp. 75-98.

Miller, D.M., Schmidt, K.M., Mahan, S.A., McGeehin, J.P., Owen, L.A., Barron, J.A., Lehmkuhl, F., Löhrer, R., 2010. Holocene landscape response to seasonality of storms in the Mojave Desert. Quaternary International 215, 45-61. doi:10.1016/j.quaint.2009.10.001

Miller, J.R., 1991. The Influence of Bedrock Geology on Knickpoint Development and Channel-Bed Degradation along Downcutting Streams in South-Central Indiana. The Journal of Geology 99, 591-605.

Molnar, P., Anderson, R.S., Anderson, S.P., 2007. Tectonics, fracturing of rock, and erosion. Journal of Geophysical Research 112. doi:10.1029/2005jf000433

Montgomery, D.R., 2004. Observations on the role of lithology in strath terrace formation and bedrock channel width. American Journal of Science 304, 454-476. doi:10.2475/ajs.304.5.454

Mukul, M., 2000. The geometry and kinematics of the Main Boundary Thrust and related neotectonics in the Darjiling Himalayan fold-and-thrust belt, West Bengal, India. Journal of Structural Geology 22, 1261-1283. doi:10.1016/S0191-8141(00)00032-8

Murray, A., Marten, R., Johnston, A., Martin, P., 1987. Analysis for naturally occuring radionuclides at environmental concentrations by gamma spectrometry. Journal of Radioanalytical and Nuclear Chemistry 115, 263-288. doi:10.1007/bf02037443

Murray, A.B., Coco, G., Goldstein, E.B., 2014. Cause and effect in geomorphic systems: Complex systems perspectives. Geomorphology 214, 1-9. doi:10.1016/j.geomorph.2014.03.001

Murray, A.S., Thomsen, K.J., Masuda, N., Buylaert, J.P., Jain, M., 2012. Identifying well-bleached quartz using the different bleaching rates of quartz and feldspar luminescence signals. Radiation Measurements 47, 688-695. doi:10.1016/j.radmeas.2012.05.006

Murray, A.S., Wintle, A.G., 2000. Luminescence dating of quartz using an improved single-aliquot regenerative-dose protocol. Radiation Measurements 32, 57-73. doi:10.1016/S1350-4487(99)00253-X

Murray, A.S., Wintle, A.G., 2003. The single aliquot regenerative dose protocol: potential for improvements in reliability. Radiation Measurements 37, 377-381. doi:10.1016/S1350-4487(03)00053-2

Nathan, R.P., Thomas, P.J., Jain, M., Murray, A.S., Rhodes, E.J., 2003. Environmental dose rate heterogeneity of beta radiation and its implications for luminescence dating: Monte Carlo modelling and experimental validation. Radiation Measurements 37, 305-313. doi:10.1016/S1350-4487(03)00008-8

Nazir, R., Momeni, E., Armaghani, D.J., Amin, M.M., 2013. Correlation between unconfined compressive strength and indirect tensile strength of limestone rock samples. Electronic Journal of Geotechnical Engineering 18, 1737-1746.

Nicholson, S.E., 1996. A review of climate dynamics and climate variability in eastern Africa, in: Johnson, T.C., Odada, E.O. (Eds.), The Limnology, Climatology, and Paleoclimatology of the East African Lakes. Gordon and Breach Publ., Amsterdam, pp. 25-56.

Ortega-Becerril, J.A., Garzón, G., Tejero, R., Meriaux, A.-S., Delunel, R., Merchel, S., Rugel, G., 2018. Controls on strath terrace formation and evolution: The lower Guadiana River, Pulo do Lobo, Portugal. Geomorphology 319, 62-77. doi:10.1016/j.geomorph.2018.07.015

Ouimet, W.B., Whipple, K.X., Granger, D.E., 2009. Beyond threshold hillslopes: Channel adjustment to base-level fall in tectonically active mountain ranges. Geology 37, 579-582. doi:10.1130/g30013a.1

Paola, C., Budd, D.A., Hajek, E.A., Purkis, S.J., 2016. A Mind of Their Own: Recent Advances in Autogenic Dynamics in Rivers and Deltas, Autogenic Dynamics and Self-Organization in Sedimentary Systems. SEPM Society for Sedimentary Geology, p. 0.

Paola, C., Mohrig, D., 1996. Palaeohydraulics revisited: palaeoslope estimation in coarse-grained braided rivers. Basin Research 8, 243-254. doi:10.1046/j.1365-2117.1996.00253.x

Paola, C., Parker, G., Seal, R., Sinha, S.K., Southard, J.B., Wilcock, P.R., 1992. Downstream Fining by Selective Deposition in a Laboratory Flume. Science 258, 1757-1760. doi:10.1126/science.258.5089.1757

Pastor, A., Babault, J., Teixell, A., Arboleya, M.L., 2012a. Intrinsic stream-capture control of stepped fan pediments in the High Atlas piedmont of Ouarzazate (Morocco). Geomorphology 173-174, 88-103. doi:10.1016/j.geomorph.2012.05.032

Pastor, À., Teixell, A., Arboleya, M.L., 2012b. Rates of Quaternary deformation in the Ouarzazate Basin (Southern Atlas Front, Morocco). 2013 55. doi:10.4401/ag-4940

Pausata, F.S.R., Gaetani, M., Messori, G., Berg, A., Maia de Souza, D., Sage, R.F., deMenocal, P.B., 2020. The Greening of the Sahara: Past Changes and Future Implications. One Earth 2, 235-250. doi:10.1016/j.oneear.2020.03.002

Pazzaglia, F.J., 2013. 9.22 Fluvial Terraces, in: Shroder, J.F. (Ed.), Treatise on Geomorphology. Academic Press, San Diego, pp. 379-412.

Pechlivanidou, S., Cowie, P.A., Duclaux, G., Nixon, C.W., Gawthorpe, R.L., Salles, T., 2019. Tipping the balance: Shifts in sediment production in an active rift setting. Geology 47, 259-262. doi:10.1130/g45589.1

Perne, M., Covington, M.D., Thaler, E.A., Myre, J.M., 2017. Steady state, erosional continuity, and the topography of landscapes developed in layered rocks. Earth Surf. Dynam. 5, 85-100. doi:10.5194/esurf-5-85-2017

Perron, J.T., Royden, L., 2013. An integral approach to bedrock river profile analysis. Earth Surface Processes and Landforms 38, 570-576. doi:10.1002/esp.3302

Pierson, T.C., 1980. Erosion and deposition by debris flows at Mt Thomas, North Canterbury, New Zealand. Earth Surface Processes 5, 227-247. doi:10.1002/esp.3760050302

Pierson, T.C., 2005. Hyperconcentrated flow — transitional process between water flow and debris flow, Debris-flow Hazards and Related Phenomena. Springer Berlin Heidelberg, Berlin, Heidelberg, pp. 159-202.

Prescott, J.R., Hutton, J.T., 1995. Environmental dose rates and radioactive disequilibrium from some Australian luminescence dating sites. Quaternary Science Reviews 14, 439-448. doi:10.1016/0277-3791(95)00037-2

Pye, K., Goudie, A.S., Watson, A., 1986. Petrological influence on differential weathering and inselberg development in the Kora area of central Kenya. Earth Surface Processes and Landforms 11, 41-52. doi:10.1002/esp.3290110106

Quick, L., Sinclair, H.D., Attal, M., Singh, V., 2019. Conglomerate recycling in the Himalayan foreland basin: Implications for grain size and provenance. GSA Bulletin 132, 1639-1656. doi:10.1130/b35334.1

Rades, E.F., Sohbati, R., Lüthgens, C., Jain, M., Murray, A.S., 2018. First luminescence-depth profiles from boulders from moraine deposits: Insights into glaciation chronology and transport dynamics in Malta valley, Austria. Radiation Measurements 120, 281-289. doi:10.1016/j.radmeas.2018.08.011

Reichart, G.-J., 1997. Late Quaternary variability of the Arabian Sea monsoon and oxygen minimum zone. Utrecht University.

Rhodes, E.J., Bronk Ramsey, C., Outram, Z., Batt, C., Willis, L., Dockrill, S., Bond, J., 2003. Bayesian methods applied to the interpretation of multiple OSL dates: high precision sediment ages from Old Scatness Broch excavations, Shetland Isles. Quaternary Science Reviews 22, 1231-1244. doi:10.1016/S0277-3791(03)00046-5

Rice, S.P., Church, M., 2001. Longitudinal profiles in simple alluvial systems. Water Resources Research 37, 417-426. doi:10.1029/2000wr900266

Rixhon, G., Braucher, R., Bourlès, D., Siame, L., Bovy, B., Demoulin, A., 2011. Quaternary river incision in NE Ardennes (Belgium)–Insights from 10Be/26Al dating of river terraces. Quaternary Geochronology 6, 273-284. doi:10.1016/j.quageo.2010.11.001

Rixhon, G., Briant, R.M., Cordier, S., Duval, M., Jones, A., Scholz, D., 2017. Revealing the pace of river landscape evolution during the Quaternary: recent developments in numerical dating methods. Quaternary Science Reviews 166, 91-113. doi:10.1016/j.quascirev.2016.08.016

Rizza, M., Mahan, S., Ritz, J.F., Nazari, H., Hollingsworth, J., Salamati, R., 2011. Using luminescence dating of coarse matrix material to estimate the slip rate of the Astaneh fault, Iran. Quaternary Geochronology 6, 390-406. doi:10.1016/j.quageo.2011.03.001

Roberts, N., Jones, M.D., Benkaddour, A., Eastwood, W.J., Filippi, M.L., Frogley, M.R., Lamb, H.F., Leng, M.J., Reed, J.M., Stein, M., Stevens, L., Valero-Garcés, B., Zanchetta, G., 2008. Stable isotope records of Late

Quaternary climate and hydrology from Mediterranean lakes: the ISOMED synthesis. Quaternary Science Reviews 27, 2426-2441. doi:10.1016/j.quascirev.2008.09.005

Roberts, R.G., Galbraith, R.F., Yoshida, H., Laslett, G.M., Olley, J.M., 2000. Distinguishing dose populations in sediment mixtures: a test of single-grain optical dating procedures using mixtures of laboratory-dosed quartz. Radiation Measurements 32, 459-465. doi:10.1016/S1350-4487(00)00104-9

Rojan, E., Dłużewski, M., Krzemień, K., 2020. Sediment budget of high mountain stream channels in an arid zone (High Atlas mountains, Morocco). CATENA 190, 104530. doi:10.1016/j.catena.2020.104530

Romans, B.W., Castelltort, S., Covault, J.A., Fildani, A., Walsh, J.P., 2016. Environmental signal propagation in sedimentary systems across timescales. Earth-Science Reviews 153, 7-29. doi:10.1016/j.earscirev.2015.07.012

Rossignol-Strick, M., 1985. Mediterranean Quaternary sapropels, an immediate response of the African monsoon to variation of insolation. Palaeogeography, Palaeoclimatology, Palaeoecology 49, 237-263. doi:10.1016/0031-0182(85)90056-2

Roy, S.G., Koons, P.O., Upton, P., Tucker, G.E., 2015. The influence of crustal strength fields on the patterns and rates of fluvial incision. Journal of Geophysical Research: Earth Surface 120, 275-299. doi:10.1002/2014JF003281

Rust, B.R., 1978. Depositional models for braided alluvium, in: MIall, A.D. (Ed.), Fluvial sedimentology. Canadian Society of Petroleum Geologists.

Saadi, M., Hilali, E.A., Bensaid, M., Boudda, A., Dahmani, M., 1985. Carte Géologique du Maroc Notes et mémoires (Morocco. Service Géologique). Editions du Service Géologique du Maroc.

Sadler, P.M., 1981. Sediment Accumulation Rates and the Completeness of Stratigraphic Sections. The Journal of Geology 89, 569-584. doi:10.1086/628623

Santisteban, J.I., Schulte, L., 2007. Fluvial networks of the Iberian Peninsula: a chronological framework. Quaternary Science Reviews 26, 2738-2757. doi:10.1016/j.quascirev.2006.12.019

Sawakuchi, A.O., Jain, M., Mineli, T.D., Nogueira, L., Bertassoli, D.J., Häggi, C., Sawakuchi, H.O., Pupim, F.N., Grohmann, C.H., Chiessi, C.M., Zabel, M., Mulitza, S., Mazoca, C.E.M., Cunha, D.F., 2018. Luminescence of quartz and feldspar fingerprints provenance and correlates with the source area denudation in the Amazon River basin. Earth and Planetary Science Letters 492, 152-162. doi:10.1016/j.epsl.2018.04.006

Sawakuchi, A.O., Rodrigues, F.C.G., Mineli, T.D., Mendes, V.R., Melo, D.B., Chiessi, C.M., Giannini, P.C.F., 2020. Optically Stimulated Luminescence Sensitivity of Quartz for Provenance Analysis. Methods and Protocols 3, 6. doi:10.3390/mps3010006

Schanz, S.A., Montgomery, D.R., 2016. Lithologic controls on valley width and strath terrace formation. Geomorphology 258, 58-68. doi:10.1016/j.geomorph.2016.01.015

Schanz, S.A., Montgomery, D.R., Collins, B.D., Duvall, A.R., 2018. Multiple paths to straths: A review and reassessment of terrace genesis. Geomorphology 312, 12-23. doi:10.1016/j.geomorph.2018.03.028

Scheingross, J.S., Limaye, A.B., McCoy, S.W., Whittaker, A.C., 2020. The shaping of erosional landscapes by internal dynamics. Nature Reviews Earth & Environment. doi:10.1038/s43017-020-0096-0

Scherler, D., Lamb, M.P., Rhodes, E.J., Avouac, J.-P., 2016. Climate-change versus landslide origin of fill terraces in a rapidly eroding bedrock landscape: San Gabriel River, California. GSA Bulletin 128, 1228-1248. doi:10.1130/b31356.1

Scherler, D., Schwanghart, W., 2020. Drainage divide networks – Part 2: Response to perturbations. Earth Surf. Dynam. 8, 261-274. doi:10.5194/esurf-8-261-2020

Schulz, O., Busche, H., Benbouziane, A., 2008. Decadal Precipitation Variances and Reservoir Inflow in the Semi-Arid Upper Drâa Basin (South-Eastern Morocco), in: Zereini, F., Hötzl, H. (Eds.), Climatic Changes and Water Resources in the Middle East and North Africa. Springer Berlin Heidelberg, Berlin, Heidelberg, pp. 165-178.

Schumm, S.A., 1973. Geomorphic thresholds and complex response of drainage systems. Fluvial geomorphology 6, 69-85.

Schumm, S.A., 1977. The fluvial system. John Wiley and Sons, New York.

Schumm, S.A., 1979. Geomorphic Thresholds: The Concept and Its Applications. Transactions of the Institute of British Geographers 4, 485-515. doi:10.2307/622211

Schumm, S.A., Parker, R.S., 1973. Implications of Complex Response of Drainage Systems for Quaternary Alluvial Stratigraphy. Nature Physical Science 243, 99-100. doi:10.1038/physci243099a0

Schwanghart, W., Scherler, D., 2014. Short Communication: TopoToolbox 2 – MATLAB-based software for topographic analysis and modeling in Earth surface sciences. Earth Surface Dynamics 2, 1-7. doi:10.5194/esurf-2-1-2014

Seidl, M., Dietrich, W., 1992. The problem of channel erosion into bedrock. Functional geomorphology, 101-124.

Selby, M., 1980. A rock mass strength classification for geomorphic purposes: with tests from Antarctica and New Zealand. Zeit. fur Geomorph., NF 24, 31-51.

Selby, M., 1993. Hillslope Materials and Processes Oxford Univ. Press. Oxford.

Simpson, G., Castelltort, S., 2012. Model shows that rivers transmit high-frequency climate cycles to the sedimentary record. Geology 40, 1131-1134. doi:10.1130/g33451.1

Sklar, L.S., Dietrich, W.E., 2001. Sediment and rock strength controls on river incision into bedrock. Geology 29, 1087-1090. doi:10.1130/0091-7613(2001)029<1087:sarsco>2.0.co;2

Skonieczny, C., McGee, D., Winckler, G., Bory, A., Bradtmiller, L.I., Kinsley, C.W., Polissar, P.J., De Pol-Holz, R., Rossignol, L., Malaizé, B., 2019. Monsoon-driven Saharan dust variability over the past 240,000 years. Science Advances 5, eaav1887. doi:10.1126/sciadv.aav1887

Smith, G.A., 1986. Coarse-grained nonmarine volcaniclastic sediment: Terminology and depositional process. GSA Bulletin 97, 1-10. doi:10.1130/0016-7606(1986)97<1:Cnvsta>2.0.Co;2

Sohbati, R., Murray, A.S., Buylaert, J.-P., Almeida, N.A.C., Cunha, P.P., 2012a. Optically stimulated luminescence (OSL) dating of quartzite cobbles from the Tapada do Montinho archaeological site (east-central Portugal). Boreas 41, 452-462. doi:10.1111/j.1502-3885.2012.00249.x

Sohbati, R., Murray, A.S., Chapot, M.S., Jain, M., Pederson, J., 2012b. Optically stimulated luminescence (OSL) as a chronometer for surface exposure dating. Journal of Geophysical Research: Solid Earth 117. doi:doi:10.1029/2012JB009383

Sohbati, R., Murray, A.S., Porat, N., Jain, M., Avner, U., 2015. Age of a prehistoric “Rodedian” cult site constrained by sediment and rock surface luminescence dating techniques. Quaternary Geochronology 30, 90-99. doi:10.1016/j.quageo.2015.09.002

Starkel, L., 2003. Climatically controlled terraces in uplifting mountain areas. Quaternary Science Reviews 22, 2189-2198. doi:10.1016/S0277-3791(03)00148-3

Sternberg, H., 1875. Untersuchungen über längen-und querprofil geschiebeführender flüsse. Zeitshrift für Bauwesen 25, 483-506.

Stock, J.D., Montgomery, D.R., 1999. Geologic constraints on bedrock river incision using the stream power law. Journal of Geophysical Research. B 104, 4983-4993.

Stokes, M., Cunha, P.P., Martins, A.A., 2012. Techniques for analysing Late Cenozoic river terrace sequences. Geomorphology 165–166, 1-6. doi:10.1016/j.geomorph.2012.03.022

Stokes, M., Mather, A.E., 2015. Controls on modern tributary-junction alluvial fan occurrence and morphology: High Atlas Mountains, Morocco. Geomorphology 248, 344-362. doi:10.1016/j.geomorph.2015.08.003

Stokes, M., Mather, A.E., Belfoul, A., Farik, F., 2008. Active and passive tectonic controls for transverse drainage and river gorge development in a collisional mountain belt (Dades Gorges, High Atlas Mountains, Morocco). Geomorphology 102, 2-20. doi:10.1016/j.geomorph.2007.06.015

Stokes, M., Mather, A.E., Belfoul, M., Faik, F., Bouzid, S., Geach, M.R., Cunha, P.P., Boulton, S.J., Thiel, C., 2017. Controls on dryland mountain landscape development along the NW Saharan desert margin: Insights from Quaternary river terrace sequences (Dadès River, south-central High Atlas, Morocco). Quaternary Science Reviews 166, 363-379. doi:10.1016/j.quascirev.2017.04.017

Straub, K.M., Duller, R.A., Foreman, B.Z., Hajek, E.A., 2020. Buffered, Incomplete, and Shredded: The Challenges of Reading an Imperfect Stratigraphic Record. Journal of Geophysical Research: Earth Surface 125, e2019JF005079. doi:10.1029/2019jf005079

Strong, C.M., Attal, M., Mudd, S.M., Sinclair, H.D., 2019. Lithological control on the geomorphic evolution of the Shillong Plateau in Northeast India. Geomorphology 330, 133-150. doi:10.1016/j.geomorph.2019.01.016

Struth, L., Babault, J., Teixell, A., 2015. Drainage reorganization during mountain building in the river system of the Eastern Cordillera of the Colombian Andes. Geomorphology 250, 370-383. doi:10.1016/j.geomorph.2015.09.012

Tabuteau, M., 1960. Etude graphique pour les conséquences hydro-érosives du climat méditerranéen (avec un exemple d'Algérie). Bulletin de l'Association de Géographes Français 295-5, 130-142.

Tadono, T., Ishida, H., Oda, F., Naito, S., Minakawa, K., Iwamoto, H., 2014. Precise global DEM generation by ALOS PRISM. ISPRS Annals of the Photogrammetry, Remote Sensing and Spatial Information Sciences 2, 71.

Teixell, A., Arboleya, M.-L., Julivert, M., Charroud, M., 2003. Tectonic shortening and topography in the central High Atlas (Morocco). Tectonics 22, n/a-n/a. doi:10.1029/2002tc001460

Tesón, E., Pueyo, E.L., Teixell, A., Barnolas, A., Agustí, J., Furió, M., 2010. Magnetostratigraphy of the Ouarzazate Basin: Implications for the timing of deformation and mountain building in the High Atlas Mountains of Morocco. Geodinamica Acta 23, 151-165. doi:10.3166/ga.23.151-165

Tesón, E., Teixell, A., 2008. Sequence of thrusting and syntectonic sedimentation in the eastern Sub-Atlas thrust belt (Dadès and Mgoun valleys, Morocco). International Journal of Earth Sciences 97, 103-113. doi:10.1007/s00531-006-0151-1

Thaler, E.A., Covington, M.D., 2016. The influence of sandstone caprock material on bedrock channel steepness within a tectonically passive setting: Buffalo National River Basin, Arkansas, USA. Journal of Geophysical Research: Earth Surface 121, 1635-1650. doi:10.1002/2015jf003771

Thomsen, K.J., Murray, A., Jain, M., 2012. The dose dependency of the over-dispersion of quartz OSL single grain dose distributions. Radiation Measurements 47, 732-739. doi:10.1016/j.radmeas.2012.02.015

Thornes, J., 1977. Channel changes in ephemeral streams: observations, problems and models, in: Gregory, K.J. (Ed.), River Channel Changes. Wiley, Chichester, pp. 317-335.

Tjallingii, R., Claussen, M., Stuut, J.-B.W., Fohlmeister, J., Jahn, A., Bickert, T., Lamy, F., Röhl, U., 2008. Coherent high- and low-latitude control of the northwest African hydrological balance. Nature Geoscience 1, 670. doi:10.1038/ngeo289

Tucker, G.E., van der Beek, P., 2013. A model for post-orogenic development of a mountain range and its foreland. Basin Research 25, 241-259. doi:10.1111/j.1365-2117.2012.00559.x

Tuenter, E., Weber, S.L., Hilgen, F.J., Lourens, L.J., 2003. The response of the African summer monsoon to remote and local forcing due to precession and obliquity. Global and Planetary Change 36, 219-235. doi:10.1016/S0921-8181(02)00196-0

Valero-Garcés, B., Zeroual, E., Kelts, K., 1998. Arid phases in the western Mediterranean region during the last glacial cycle reconstructed from lacustrine records. Paleohydrology and Environmental Change, 67-80.

Valla, P.G., van der Beek, P.A., Shuster, D.L., Braun, J., Herman, F., Tassan-Got, L., Gautheron, C., 2012. Late Neogene exhumation and relief development of the Aar and Aiguilles Rouges massifs (Swiss Alps) from low-temperature thermochronology modeling and 4He/3He thermochronometry. Journal of Geophysical Research: Earth Surface 117. doi:10.1029/2011JF002043

Vandenberghe, D., Hossain, S.M., De Corte, F., Van den haute, P., 2003. Investigations on the origin of the equivalent dose distribution in a Dutch coversand. Radiation Measurements 37, 433-439. doi:10.1016/S1350-4487(03)00051-9

Vandenberghe, J., 1995. Timescales, climate and river development. Quaternary Science Reviews 14, 631-638. doi:10.1016/0277-3791(95)00043-O

Vandenberghe, J., 2002. The relation between climate and river processes, landforms and deposits during the Quaternary. Quaternary International 91, 17-23. doi:10.1016/S1040-6182(01)00098-2

Vandenberghe, J., 2003. Climate forcing of fluvial system development: an evolution of ideas. Quaternary Science Reviews 22, 2053-2060. doi:10.1016/s0277-3791(03)00213-0

Viles, H., Goudie, A., Grab, S., Lalley, J., 2011. The use of the Schmidt Hammer and Equotip for rock hardness assessment in geomorphology and heritage science: a comparative analysis. Earth Surface Processes and Landforms 36, 320-333. doi:10.1002/esp.2040

Vos, R.G., Tankard, A.J., 1981. Braided fluvial sedimentation in the lower paleozoic cape basin, South Africa. Sedimentary Geology 29, 171-193. doi:10.1016/0037-0738(81)90006-3

Vutukuri, V.S., Lama, R.D., Saluja, S.S., 1974. Handbook on mechanical properties of rocks. Trans Tech Publications,Clausthal, Germany;.

Walling, D.E., Kleo, A.H.A., 1979. Sediment yields of rivers in areas of low precipitation: a global view, Proceedings of the Canberra Symposium, December 1979. International Association of Hydrological Sciences.

Wang, X., Vandenberghe, J., Yi, S., Van Balen, R., Lu, H., 2015. Climate-dependent fluvial architecture and processes on a suborbital timescale in areas of rapid tectonic uplift: An example from the NE Tibetan Plateau. Global and Planetary Change 133, 318-329. doi:10.1016/j.gloplacha.2015.09.009

Ward, D.J., 2019. Dip, layer spacing, and incision rate controls on the formation of strike valleys, cuestas, and cliffbands in heterogeneous stratigraphy. Lithosphere 11, 697-707. doi:10.1130/l1056.1

Ward, D.J., Spotila, J.A., Hancock, G.S., Galbraith, J.M., 2005. New constraints on the late Cenozoic incision history of the New River, Virginia. Geomorphology 72, 54-72. doi:10.1016/j.geomorph.2005.05.002

Wegmann, K.W., Pazzaglia, F.J., 2002. Holocene strath terraces, climate change, and active tectonics: The Clearwater River basin, Olympic Peninsula, Washington State. GSA Bulletin 114, 731-744. doi:10.1130/0016-7606(2002)114<0731:Hstcca>2.0.Co;2

Wegmann, K.W., Pazzaglia, F.J., 2009. Late Quaternary fluvial terraces of the Romagna and Marche Apennines, Italy: Climatic, lithologic, and tectonic controls on terrace genesis in an active orogen. Quaternary Science Reviews 28, 137-165. doi:10.1016/j.quascirev.2008.10.006

Weissel, J.K., Seidl, M.A., 1997. Influence of rock strength properties on escarpment retreat across passive continental margins. Geology 25, 631-634. doi:10.1130/0091-7613(1997)025<0631:Iorspo>2.3.Co;2

Whipple, K.X., Snyder, N.P., Dollenmayer, K., 2000. Rates and processes of bedrock incision by the Upper Ukak River since the 1912 Novarupta ash flow in the Valley of Ten Thousand Smokes, Alaska. Geology 28, 835-838. doi:10.1130/0091-7613(2000)28<835:Rapobi>2.0.Co;2

Whipple, K.X., Tucker, G.E., 1999. Dynamics of the stream-power river incision model: Implications for height limits of mountain ranges, landscape response timescales, and research needs. Journal of Geophysical Research: Solid Earth 104, 17661-17674. doi:10.1029/1999jb900120

Whittaker, A.C., 2012. How do landscapes record tectonics and climate? Lithosphere 4, 160-164. doi:10.1130/rf.l003.1

Whittaker, A.C., Attal, M., Allen, P.A., 2010. Characterising the origin, nature and fate of sediment exported from catchments perturbed by active tectonics. Basin Research 22, 809-828. doi:10.1111/j.1365-2117.2009.00447.x

Whittaker, A.C., Boulton, S.J., 2012. Tectonic and climatic controls on knickpoint retreat rates and landscape response times. Journal of Geophysical Research: Earth Surface 117. doi:10.1029/2011jf002157

Whittaker, A.C., Cowie, P.A., Attal, M., Tucker, G.E., Roberts, G.P., 2007a. Bedrock channel adjustment to tectonic forcing: Implications for predicting river incision rates. Geology 35, 103-106. doi:10.1130/g23106a.1

Whittaker, A.C., Cowie, P.A., Attal, M., Tucker, G.E., Roberts, G.P., 2007b. Contrasting transient and steady-state rivers crossing active normal faults: new field observations from the Central Apennines, Italy. Basin Research 19, 529-556. doi:10.1111/j.1365-2117.2007.00337.x

Whittaker, A.C., Duller, R.A., Springett, J., Smithells, R.A., Whitchurch, A.L., Allen, P.A., 2011. Decoding downstream trends in stratigraphic grain size as a function of tectonic subsidence and sediment supply. GSA Bulletin 123, 1363-1382. doi:10.1130/b30351.1

Willett, S.D., McCoy, S.W., Perron, J.T., Goren, L., Chen, C.-Y., 2014. Dynamic Reorganization of River Basins. Science 343. doi:10.1126/science.1248765

Willett, S.D., Slingerland, R., Hovius, N., 2001. Uplift, Shortening, and Steady State Topography in Active Mountain Belts. American Journal of Science 301, 455-485. doi:10.2475/ajs.301.4-5.455

Williams, P.F., Rust, B.R., 1969. The sedimentology of a braided river. Journal of Sedimentary Research 39, 649-679. doi:10.1306/74d71cf3-2b21-11d7-8648000102c1865d

Wilson, L., 1969. Les relations entre les processus geomorphologiques et le climat moderne comme methode de paleoclimatologie sér. 2. Rev. Géogr. Physique Geol. Dynamique 11, 309-314.

Wilson, L., 1973. Variations in mean annual sediment yield as a function of mean annual precipitation. American Journal of Science 273, 335-349. doi:10.2475/ajs.273.4.335

Wintle, A.G., Murray, A.S., 2006. A review of quartz optically stimulated luminescence characteristics and their relevance in single-aliquot regeneration dating protocols. Radiation Measurements 41, 369-391. doi:10.1016/j.radmeas.2005.11.001

Wobus, C., Whipple, K.X., Kirby, E., Snyder, N., Johnson, J., Spyropolou, K., Crosby, B., Sheehan, D., 2006. Tectonics from topography: Procedures, promise, and pitfalls, in: Willett, S.D., Hovius, N., Brandon, M.T., Fisher, D.M. (Eds.), Tectonics, Climate, and Landscape Evolution. Geological Society of America.

Wohl, E.E., Merritt, D.M., 2001. Bedrock channel morphology. Geological Society of America Bulletin 113, 1205-1212.

Wolman, M.G., 1954. A method of sampling coarse river-bed material. Eos, Transactions American Geophysical Union 35, 951-956. doi:10.1029/TR035i006p00951

Yanites, B.J., Becker, J.K., Madritsch, H., Schnellmann, M., Ehlers, T.A., 2017. Lithologic Effects on Landscape Response to Base Level Changes: A Modeling Study in the Context of the Eastern Jura Mountains, Switzerland. Journal of Geophysical Research: Earth Surface 122, 2196-2222. doi:10.1002/2016jf004101

Zaprowski, B.J., Evenson, E.B., Pazzaglia, F.J., Epstein, J.B., 2001. Knickzone propagation in the Black Hills and northern High Plains: A different perspective on the late Cenozoic exhumation of the Laramide Rocky Mountains. Geology 29, 547-550. doi:10.1130/0091-7613(2001)029<0547:Kpitbh>2.0.Co;2

Ziegler, M., Tuenter, E., Lourens, L.J., 2010. The precession phase of the boreal summer monsoon as viewed from the eastern Mediterranean (ODP Site 968). Quaternary Science Reviews 29, 1481-1490. doi:10.1016/j.quascirev.2010.03.011

Zinke, R., Dolan, J.F., Rhodes, E.J., Van Dissen, R., McGuire, C.P., 2017. Highly Variable Latest Pleistocene-Holocene Incremental Slip Rates on the Awatere Fault at Saxton River, South Island, New Zealand, Revealed by Lidar Mapping and Luminescence Dating. Geophysical Research Letters 44, 11,301-311,310. doi:10.1002/2017gl075048

Zondervan, J.R., Whittaker, A.C., Bell, R.E., Watkins, S.E., Brooke, S.A.S., Hann, M.G., 2020. New constraints on bedrock erodibility and landscape response times upstream of an active fault. Geomorphology 351, 106937. doi:10.1016/j.geomorph.2019.106937

S

Supplementary material

CHAPTER 2

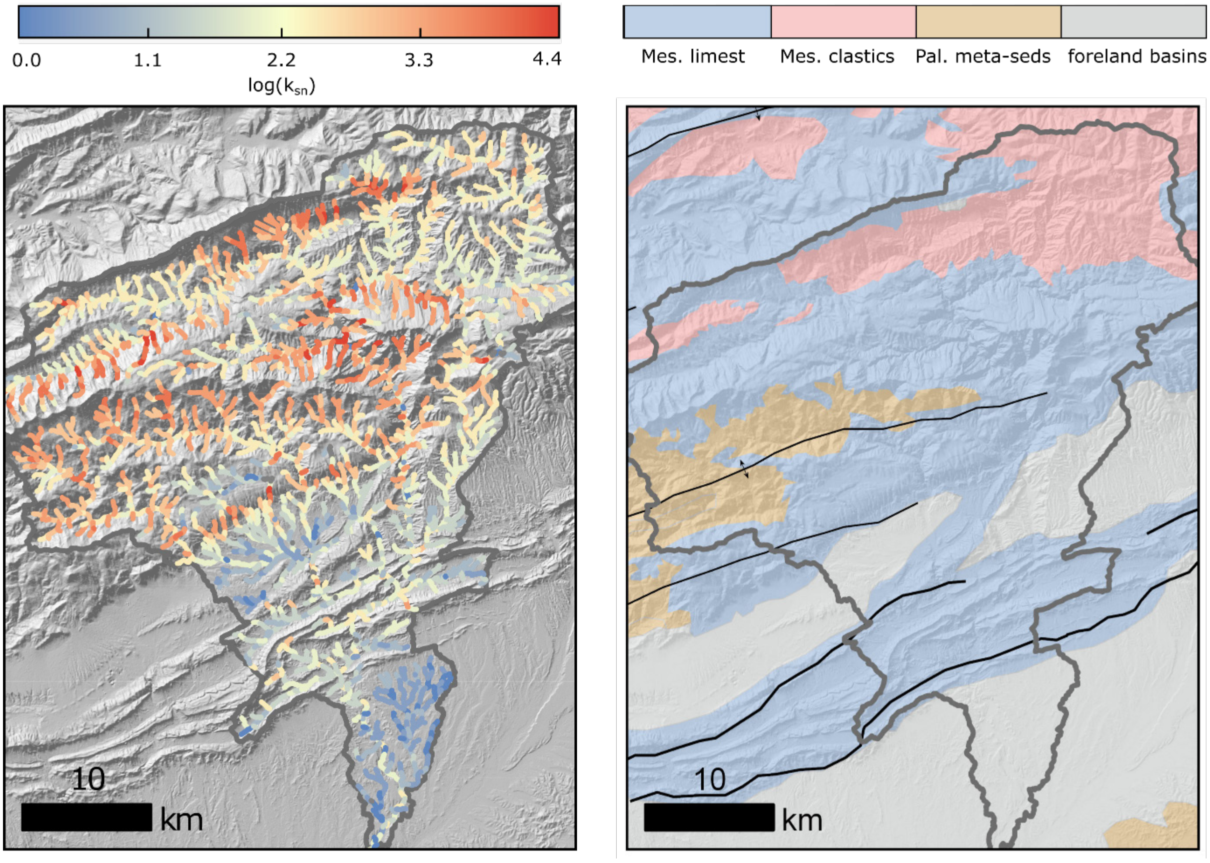

Figure S2.1 – Relation between topography, lithology and k_{sn} in a catchment example. Left panel is a map of ksn for the Mgoun catchment on top of shaded topographic relief. The right panel corresponds to the same area but with the lithology represented in colours. Black lines correspond to main faults, and a black line with arrows indicates a synclinal axis.

Table S2.1 – Schmidt Hammer Rebound and UCS data for each geological unit, with their respective lithologies and chronolithological groupings (as in Fig 2.4).

Mesozoic	Geological unit	Lithology	period	R range	R av	R std	UCS av	UCS std	citation
limestones	Middle Lias	limestone and marl	Mesozoic		43	15	44	15	This Study
	Bajocian	oolitic limestone and marls	Mesozoic		46	15	54	18	This Study
	Lower Lias	limestone and dolomite	Mesozoic	40-60	50	10	73	15	Sachpazis (1990)
sand-siltstones and conglomerates	Upper Lias (Toarcian, Aalenian), Continental Permo-Triassic, Bathonian, and Upper Bajocian	silts, marls, sandstones	Mesozoic		41	13	38	13	This Study
red beds	Continental Senonian	red marls with calcite and gypsum	Mesozoic		22	15	10	7	This Study
	Continental Upper Lias, Continental Jurassic, Continental Lower Cretaceous	red sst, conglomerates and marls	Mesozoic		26	13	14	7	This Study
	Continental Mio-Pliocene	red beds	Mesozoic		25	14	12	7	This Study

Palaeozoic	Geological unit	Lithology	period	R range	R av	R unc	UCS av	UCS av	citation
meta-sediments	Ordovician schists	schist	Palaeozoic	40.0–43.7	42	2	41	2	Gökçeogˇ lu and Aksoy (2000)
	schists, Sericite schists, sandstone	schist	Palaeozoic	49.5-51.5	51	1	76	2	Gökçeogˇ lu and Aksoy (2000)
	Continental Permian	sandstone	Palaeozoic	34.2-55	45	10	50	12	Goudie (2006)
	Middle Devonian, Upper Visean, Acadian, Tournaisian - Visean seriea of Betaïna, Silurian	shales, sandstone, schist	Palaeozoic	30-64	47	17	59	21	Goktan and Gunes (2005)
granites	Migmatites	migmatite	Palaeozoic	47.3–50.6	49	2	68	2	Pye et al. (1986)
	Diorites injected by granite, Biotite granites, granodiorites etc.	granodiorite	Palaeozoic	57.0–63.3	60	3	149	8	Kahraman et al. (2002)
	Microgranites related to rhyolites, Leucocratic granites, High Atlas pink granite	granite	Palaeozoic	48-73.4	61	13	155	32	Goudie (2006)

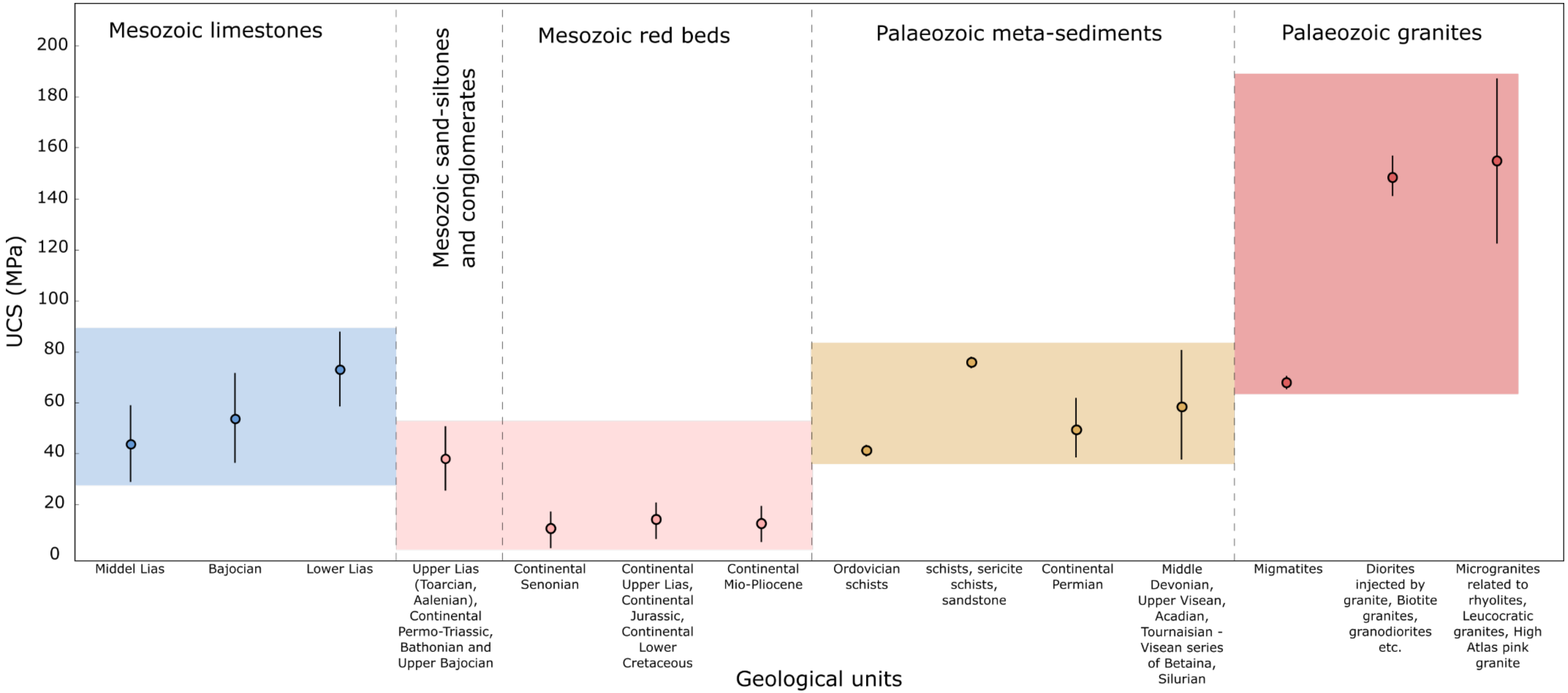

Figure S2.2 - Average and standard deviation of uniaxial compressive strength for every geological unit. See table 2.1 for corresponding data.

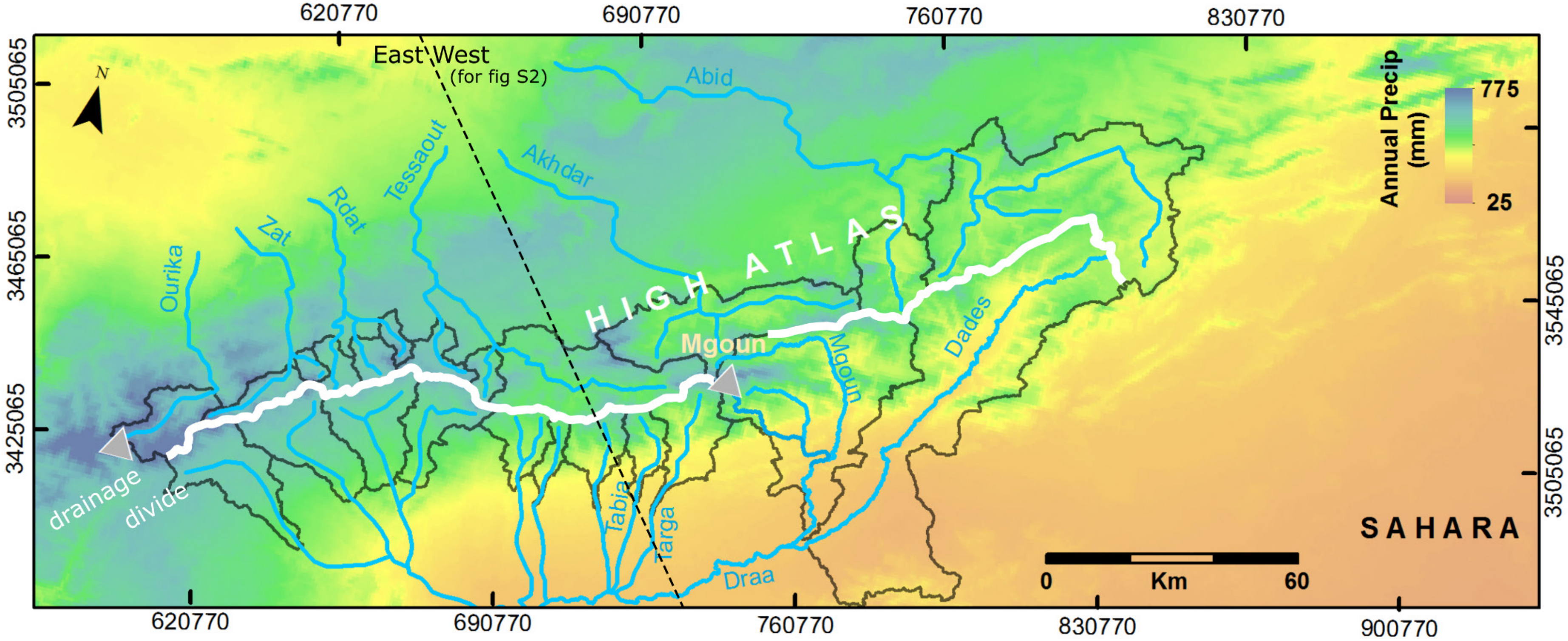

Figure S2.3 - Map of annual rainfall from Worldclim 2 (Fick and Hijmans, 2017) showing north-south and west-east trends of declining rainfall. The highest rainfall (775 mm) falls on the peaks, Toubkal in the west and Mgoun in the east. Driest conditions are towards the Sahara Desert in the southwest with annual rainfall of ~25mm.

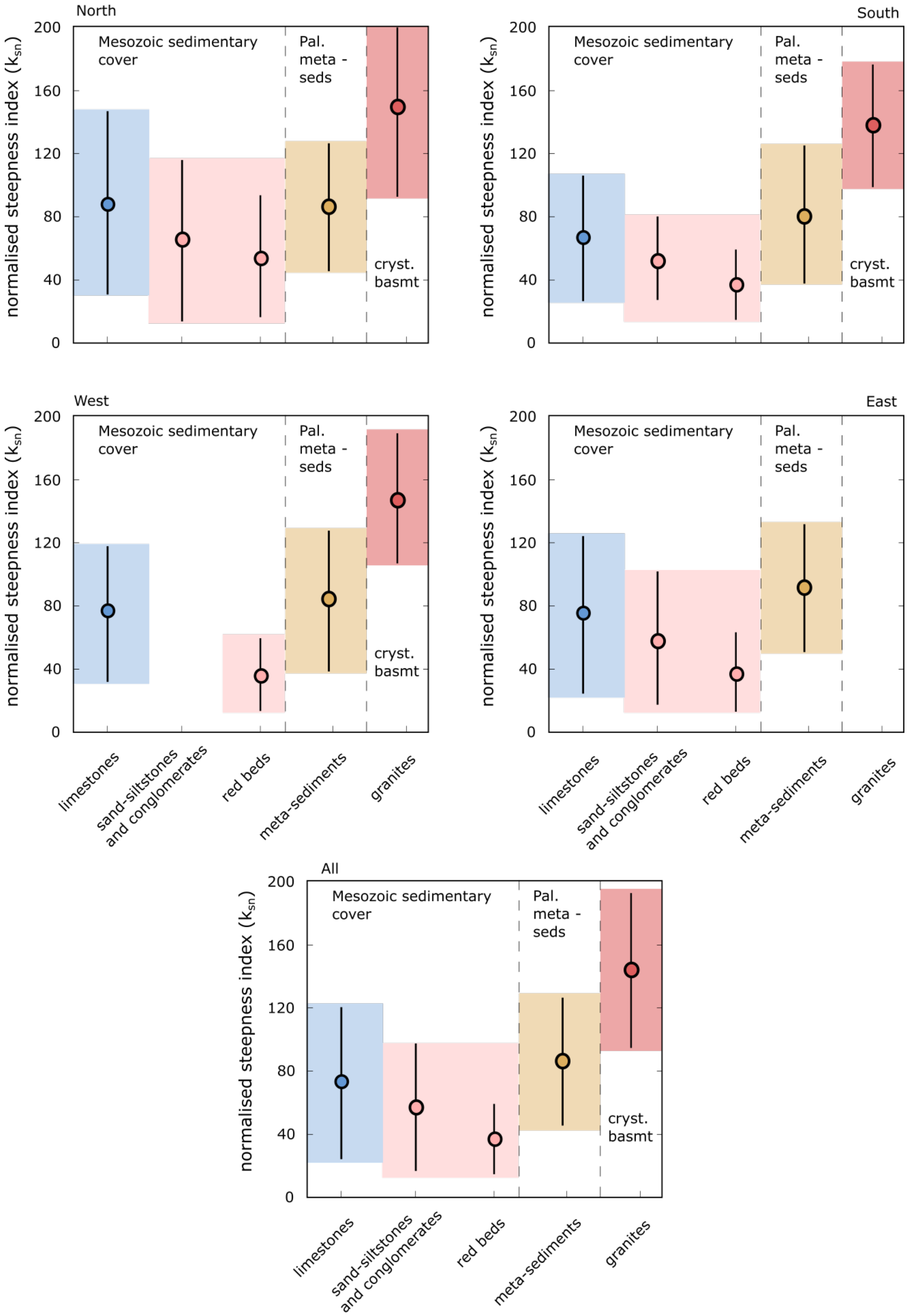

Figure S2.4 – Set of panels showing the average and standard deviation of k_{sn} for every chronolithological unit in the northern, southern, eastern, and western High Atlas(see area definitions on Figure S2.1). The northern and southern High Atlas correspond to the channels in the study area north and south of the drainage divide (see Fig 2.1)

CHAPTER 3

Detailed facies descriptions and interpretation

Facies Gh – Clast-supported conglomerate

Facies Gh consist of moderately well-sorted, tightly-packed, clast-supported pebble-cobble conglomerate with very well rounded clasts. Clast sizes range from pebble to cobble size with occasional boulders, and the matrix consists of poorly-sorted mud-granule-sized particles. Weak horizontal bedding to massive architecture is common, as well as clast imbrication and otherwise an absence of sedimentary structures or preserved sand bars. Grain size changes, where present, are abrupt and not systematic. The base of Gh units are sharp and erosional, with the thickness of bodies varying between 2 to 10 m, laterally extensive over the extent of exposed terraces, up to 3 km in width along stream and 300 m width perpendicular to the river channel.

Interpretation

The association of imbricated, crudely horizontally stratified pebble and cobble conglomerate indicates deposition as gravel sheets, lag deposits and sieve deposits as described by many workers (Williams and Rust, 1969; Hein and Walker, 1977; Miall, 1977). The lack of preserved sand bars within conglomerates suggests reworking during a sustained period of valley floor aggradation. The reason for the absence of cross-stratification may be explained by the low ratio of water depth to mean clast size, which inhibits the development of slip faces (Rust, 1978).

Facies Gci – Inversely graded conglomerate

Facies Gci is recorded in one terrace deposit on T2 in the wedge-top basin. This poorly-sorted, clast-supported pebble to boulder conglomerate exhibits inverse grading from pebble to boulder clasts (Fig. 3.10b). Clasts are sub-angular to sub-rounded, disc-shaped to spherical and clast imbrication is common and pervasive in all grainsizes. The base of these deposits is erosional, with a sharp, stepping boundary along beds of more resistant evaporates within red marl bedrock. Reversely graded sequences are about 2 m thick and laterally extensive over the ~ 150 m width of the terrace. The terrace in which facies Gci is deposited stretches ~500 m upslope to a modern tributary.

Interpretation

The reverse grading and presence of imbricated coarse clasts indicate more hyperconcentrated flow with a high concentration of sediment boulder clasts in suspension on top of bedload transported pebbles and cobbles (Mather and Hartley, 2005; Pierson, 2005; Mather and Stokes, 2016; Mather and Stokes, 2018). Since this deposit is linked to an abandoned fork of a tributary and the section studied is incised by the modern river plain, this deposit is interpreted as being linked to infrequent high sediment concentrated flows through ephemeral tributaries with possible reworking by high-river flows at a tributary junction.

Facies Gcg – Graded moderately poorly-sorted conglomerate

Facies Gcg consist of moderately poorly-sorted, clast-supported pebble-cobble conglomerate with sub-angular to well-rounded spherical to discoidal clasts. The matrix consists of poorly-sorted red mud-granule-sized particles. Weak horizontal bedding to massive architecture is common, as well as clast imbrication and normal grading of beds ~2 to 3 m in thickness. The base of Gcg units are sharp and erosional, and bodies are laterally extensive over the extent of exposed terraces, up to 2 km in width along stream and 300 m width perpendicular to the river channel.

Interpretation

The association of imbricated, crudely horizontally stratified pebble and cobble conglomerate indicates deposition as gravel sheets, lag deposits and sieve deposits as described by many workers (Williams and Rust, 1969; Hein and Walker, 1977; Miall, 1977). The generally coarse-grainsizes, and poor sorting suggests that deposition occurred primarily during floods (DeCelles et al., 1991). The upward-fining trends present within the gravel bodies probably resulted from waning flow velocity following floods (Williams and Rust, 1969; Vos and Tankard, 1981; DeCelles et al., 1991).

Facies Gp – Cross-stratified conglomerate

Facies Gp is characterised by clast-supported, moderately well-sorted, pebble-cobble conglomerate exhibiting several meter-scale planar cross beds (Fig. 3.12). Internal surfaces dip moderately, between 10° and 20°, and dip parallel to the modern flow direction. This facies occurs as 1 to 2 m thick deposits with erosional bases directly on top of bedrock strath surfaces.

Interpretation

The planar cross stratification and dip direction indicate progradational deposition of gravels by longitudinal and transverse bars (Massari, 1983). The preferential preservation of this facies directly above the strath surface may indicate limited reworking during initial aggradation on the strath due to high aggradation rates.

Facies Gt – Trough-stratified conglomerate

Facies Gt is characterised by clast-supported, moderately well-sorted, pebble-cobble conglomerate. Trough-stratification and clast imbrication are common. Lenticular bodies of Gt range from 0.3 to 1 m in thickness and typically extend 2 to 10 m laterally (Fig. 3.12). Bodies of Gt have erosional bases.

Interpretation

The erosional bases and amalgamated lenticular shapes of bodies of Gt indicate deposition in channels. Deposition could occur either during high-water stage avulsion or bar dissection at falling-water stage (Miall, 1978).

Facies Fl – Fine clay - sand

Facies Fl includes clay to medium-grained tan-coloured sandstone with crude horizontal lamination or a massive architecture (Fig. 3.14). Beds of facies Fl are 1-2 m thick, tabular, can be traced laterally for hundreds of metres in large outcrops, and occur wedged in-between beds of facies Gm in a fluvial terrace and Gm4 in an alluvial terrace. The basal contacts of Fl units are gradational and non-erosional. Facies Fl is observed as overbank deposits in the modern river plain in the most downstream valley in the thrust front.

Interpretation

Because of its extensive tabular geometry and association with fluvial channel facies and observation in the modern environment, facies Fl is interpreted to represent vertical accretion when the terrace on top of the flood plain during floods, from now on referred to as overbank deposits (Wegmann and Pazzaglia, 2002; Pazzaglia, 2013; Stokes et al., 2017).

Facies Gcm – Clast and matrix-supported conglomerate

Facies Gcm consist of moderately well-sorted, clast and matrix-supported pebble-cobble conglomerate with sub-angular to well-rounded clasts. The matrix consists of moderately well-sorted silt-sand-sized particles. The conglomerate is massive. Facies Gcm is interbedded with facies Fl in an alluvial fan terrace where the river exits a gorge into the wedge-top basin (Fig. 3.14). Gravels with angular clasts of a composition derived from local bedrock geology drape as aprons on the valley sides and an extensive terrace in the thrust front (Fig. 3.14).

Interpretation

The lobate shape of the deposit in the wide plains of the wedge-top basin and association with preserved facies Fl points to deposition in a fluvial distributary system. The preservation of fines and the presence of sub-angular clasts point to lower reworking than in Gh and Gcg, and is interpreted to be typical of the river flood plain edge where it was deposited. The textural immaturity gravel aprons of Gcm covering terraces indicate localised gravity driven slope deposits (Stokes et al., 2012; Mather et al., 2017). Where this facies caps Fl in a fluvial terrace it acts as a valuable marker constraining the end of river activity.

CHAPTER 4

Corr_lum_dose_rate python script

Calculates the Ḋ of luminescence samples, and corrects for changes in the water table. The model assumes saturation water content until the water table drops below the samples at an age specified by the user, after which the wet water content measured in the lab is used to correct Ḋ values.

Requirements

This code is written in Python 3

Usage

1. Calculate the external gamma Ḋ added to the samples by cosmic rays. This depends on the altitude and geographical location of the samples, as well as the depth of samples. This can be done in a standard luminescence spreadsheet, for example the one provided by Risø
2. Complete a csv file with sample name, *a priori* age (optional), end of saturation age (time of water table lowering below the sample), saturation water content, wet water content, dry gamma Ḋ, dry beta Ḋ, conglomerate correction (if applicable), external gamma Ḋ and the dose.
3. run the code for quartz and/or feldspar luminescence ages

The output is a printout of the corrected luminescence ages and Ḋ values based on the water content model, and also gives the precision only error (leaving out systematic errors related to measurement uncertainties shared by all samples)

DOI:10.5281/zenodo.3833822.

Cite as: Jesse Zondervan. (2020, May 19).
jessezondervan/corr_lum_dose_rate v1.0 (Version v1.0). Zenodo.
http://doi.org/10.5281/zenodo.3833823

See https://github.com/jessezondervan/corr_lum_dose_rate for the source files.

MIT License

Copyright © 2019 Jesse Zondervan

Permission is hereby granted, free of charge, to any person obtaining a copy of this software and associated documentation files (the "Software"), to deal in the Software without restriction, including without limitation the rights to use, copy, modify, merge, publish, distribute, sublicense, and/or sell copies of the Software, and to permit persons to whom the Software is furnished to do so, subject to the following conditions:
The above copyright notice and this permission notice shall be included in all copies or substantial portions of the Software.

THE SOFTWARE IS PROVIDED "AS IS", WITHOUT WARRANTY OF ANY KIND, EXPRESS OR IMPLIED, INCLUDING BUT NOT LIMITED TO THE WARRANTIES OF MERCHANTABILITY, FITNESS FOR A PARTICULAR PURPOSE AND NONINFRINGEMENT. IN NO EVENT SHALL THE AUTHORS OR COPYRIGHT HOLDERS BE LIABLE FOR ANY CLAIM, DAMAGES OR OTHER LIABILITY, WHETHER IN AN ACTION OF CONTRACT, TORT OR OTHERWISE, ARISING FROM, OUT OF OR IN CONNECTION WITH THE SOFTWARE OR THE USE OR OTHER DEALINGS IN THE SOFTWARE.

```
###quartz
### calculate the age based on a model for water content in terrace sediments
##need file with input data, see example csv file
fil = open('<path to file>')

#set the following variables: water content error (fractional), grain attenuation of beta Ḋ (fractional),
#internal Ḋ (Gy/ky) and error (fractional), beta calibration error (fractional)

wc_err = 0.04
grain_att = 0.887355
internal = 0.02
internal_se = 0.01
beta_calib = 0.02

#####################################################################################################
# Function written by Jesse R. Zondervan - Updated : 24/06/19
```

```
##################################################################
##################################

#read the csv header
fil.readline()

#prepare lists
sample_numbers = []

age_samples = []
age_ends = []

wc_sats = []
wc_wets = []

gamma_drys = []
g_ses = []
beta_drys = []
b_ses = []
conglom_corrs = []

external_gammas = []
ext_ses = []

Des = []
De_ses = []

#fill the lists using data in the csv:
for line in fil:
    sample_numbers.append(line.split(',')[0])
    age_samples.append(float(line.split(',')[1]))
    age_ends.append(float(line.split(',')[2]))
    wc_sats.append(float(line.split(',')[3]))
    wc_wets.append(float(line.split(',')[4]))
    gamma_drys.append(float(line.split(',')[5]))
    g_ses.append(float(line.split(',')[6]))
    beta_drys.append(float(line.split(',')[7]))
    b_ses.append(float(line.split(',')[8]))
    conglom_corrs.append(float(line.split(',')[9]))
    external_gammas.append(float(line.split(',')[10]))
    ext_ses.append(float(line.split(',')[11]))
    Des.append(float(line.split(',')[12]))
    De_ses.append(float(line.split(',')[13]))
```

```
#import numpy
import numpy as np

##for every sample calculate the ages of the samples using their
dose, dry Ḋ and by iteratively
#modelling the time of water saturation in the sediment
for i in range(0,len(age_samples)):

    #set the apriori sample age and the terrace abandonement age
    age_sample = age_samples[i]
    age_end = age_ends[i]

    #set the water content measurements in percentages
    wc_sat = wc_sats[i]/100
    wc_wet = wc_wets[i]/100

    #take the values for this sample out of the lists
    gamma_dry = gamma_drys[i]
    g_se = g_ses[i]
    beta_dry = beta_drys[i]
    b_se = b_ses[i]
    conglom_corr = conglom_corrs[i]
    beta_dry = beta_dry *conglom_corr
    b_se = b_se*conglom_corr

    external_gamma = external_gammas[i]
    ext_se = ext_ses[i]

    De = Des[i]
    De_se = De_ses[i]


    #calculate the apriori amount of time the sample has been
    saturated and the time since abandonement during which
    #the sediment is assumed to have a water content similar to the
    wet sediment measurement
    time_sat = age_sample - age_end
    time_wet = age_end

    #calculate the attentuation of Ḋ depending on the measured
    water contents of the sample
    wc_att_gamma_sat = 1/(1+(1.14*wc_sat))
    wc_att_gamma_wet = 1/(1+(1.14*wc_wet))
    wc_att_beta_sat = 1/(1+(1.25*wc_sat))
```

```
wc_att_beta_wet = 1/(1+(1.25*wc_wet))

#calculate the attentuated gamma and beta rates for saturated
and wet conditions
gamma_sat = gamma_dry*wc_att_gamma_sat + external_gamma
gamma_wet = gamma_dry*wc_att_gamma_wet + external_gamma
beta_sat = beta_dry*wc_att_beta_sat * grain_att
beta_wet = beta_dry*wc_att_beta_wet * grain_att

#calculate the total rates for saturated and wet conditions
tot_rate_sat = gamma_sat + beta_sat + internal
tot_rate_wet = gamma_wet + beta_wet + internal

#calculate the average Ḋ over the timespan of the terrace
weighted_rate = (tot_rate_sat * (time_sat/age_sample)) +
(tot_rate_wet * (time_wet/age_sample))

#calculate a corrected age for the sample
age_corr = De/weighted_rate

#loop which continues the process iteratively until the
correction is equal to or smaller than 2 kyr
while abs(age_corr - age_sample) > 2:
    age_sample = age_corr
    time_sat = age_sample - age_end
    time_wet = age_end

    gamma_sat = gamma_dry*wc_att_gamma_sat + external_gamma
    gamma_wet = gamma_dry*wc_att_gamma_wet + external_gamma
    beta_sat = beta_dry*wc_att_beta_sat * grain_att
    beta_wet = beta_dry*wc_att_beta_wet * grain_att

    tot_rate_sat = gamma_sat + beta_sat + internal
    tot_rate_wet = gamma_wet + beta_wet + internal

    weighted_rate = (tot_rate_sat * (time_sat/age_sample)) +
    (tot_rate_wet * (time_wet/age_sample))

    age_corr = De/weighted_rate

#carrying over the error on dry Ḋ to the calculated Ḋ
gamma_sat_se = np.sqrt((g_se*wc_att_gamma_sat)**2+ext_se**2)
beta_sat_se = b_se*wc_att_beta_sat*grain_att
gamma_wet_se = np.sqrt((g_se*wc_att_gamma_wet)**2+ext_se**2)
```

```
beta_wet_se = b_se*wc_att_beta_wet*grain_att
tot_rate_sat_se                                                       =
np.sqrt(gamma_sat_se**2+beta_sat_se**2+internal_se**2)
tot_rate_wet_se                                                       =
np.sqrt(gamma_wet_se**2+beta_wet_se**2+internal_se**2)


#now calculate the water content error
wc_sat = wc_sat+wc_err
wc_wet = wc_wet+wc_err

time_sat = age_sample - age_end
time_wet = age_end

wc_att_gamma_sat = 1/(1+(1.14*wc_sat))
wc_att_gamma_wet = 1/(1+(1.14*wc_wet))
wc_att_beta_sat = 1/(1+(1.25*wc_sat))
wc_att_beta_wet = 1/(1+(1.25*wc_wet))

gamma_sat = gamma_dry*wc_att_gamma_sat + external_gamma
gamma_wet = gamma_dry*wc_att_gamma_wet + external_gamma
beta_sat = beta_dry*wc_att_beta_sat * grain_att
beta_wet = beta_dry*wc_att_beta_wet * grain_att

tot_rate_sat = gamma_sat + beta_sat + internal
tot_rate_wet = gamma_wet + beta_wet + internal

weighted_rate_xtra = (tot_rate_sat * (time_sat/age_sample)) +
(tot_rate_wet * (time_wet/age_sample))

age_corr_xtra = De/weighted_rate_xtra

while abs(age_corr_xtra - age_sample) > 5:
    age_sample = age_corr_xtra
    time_sat = age_sample - age_end
    time_wet = age_end

    gamma_sat = gamma_dry*wc_att_gamma_sat + external_gamma
    gamma_wet = gamma_dry*wc_att_gamma_wet + external_gamma
    beta_sat = beta_dry*wc_att_beta_sat * grain_att
    beta_wet = beta_dry*wc_att_beta_wet * grain_att

    tot_rate_sat = gamma_sat + beta_sat + internal
    tot_rate_wet = gamma_wet + beta_wet + internal
```

```
     weighted_rate_xtra = (tot_rate_sat *
     (time_sat/age_sample)) + (tot_rate_wet *
     (time_wet/age_sample))

     age_corr_xtra = De/weighted_rate_xtra

wat_cont_err = abs(age_corr_xtra-age_corr)/age_corr

weighted_rate_se =
np.sqrt(tot_rate_sat_se**2+tot_rate_wet_se**2)

age_corr_se_prec_only =
np.sqrt((De_se/De)**2+weighted_rate_se**2)*age_corr
age_corr_se_all =
np.sqrt((De_se/De)**2+weighted_rate_se**2+beta_calib**2+wat_c
ont_err**2)*age_corr

print (sample_numbers[i])
print ('the corrected age is %.f +- %.f kyr (prec only error
is %.f kyr)' % (age_corr, age_corr_se_all,
age_corr_se_prec_only))
print ('the corrected weighted rate is %.2f +- %.2f Gy/kyr' %
(weighted_rate, weighted_rate_se))
```